Rydberg interactions in subwavelength atomic arrays and Hubbard systems

Kritsana Srakaew

SIGILL. UNIVERSITAT. LUDOVIC. MAXIM.

München 2024

Rydberg interactions in subwavelength atomic arrays and Hubbard systems

Kritsana Srakaew

Dissertation
an der Fakultät für Physik
der Ludwig-Maximilians-Universität
München

vorgelegt von

Kritsana Srakaew

geboren in Nan, Thailand

München, 24. September 2024

Erstgutachter:
Prof. Dr. Immanuel Bloch

Zweitgutachter:
Prof. Dr. Thomas Pohl

Weitere Prüfungskommissionsmitglieder:
Prof. Dr. Lode Pollet
Prof. Dr. Alexander Högele

Tag der mündlichen Prüfung:
6. November 2024

Zusammenfassung

Rydberg-Atome zeichnen sich durch langreichweitige dipolare Wechselwirkungen aus, welche optisch kontrolliert und eingestellt werden können, was sie zu einem idealen Baustein für Quantenforschung und -technologien macht, mit Anwendungsmöglichkeiten von Quantensimulation über Quantencomputer bis hin zu Quanteninformation. In dieser Dissertation untersuchen wir diese langreichweitigen Rydberg-Wechselwirkungen mittels eines Quantengasmikroskops mit Einzelplatzkontrolle und -auflösung unter Verwendung von bosonischen ^{87}Rb-Atomen. Dies ermöglicht es uns, die Dynamik von Vielteilchensystemen zu erforschen, in denen langreichweitige Wechselwirkungen auftreten.

In einem ersten Experiment ordnen wir Atome in einem zweidimensionalen, optischen Subwellenlängen-Gitter an. In solchen Anordnungen treten starke photonische Wechselwirkungen auf wodurch sie effiziente Licht-Materie-Schnittstellen mit hohem Reflexionsgrad bilden. Wir manipulieren diese Licht-Materie-Schnittstelle mithilfe von kontrollierten Rydberg-Wechselwirkungen. Dazu nutzen wir elektromagnetisch induzierte Transparenz in Verbindung mit einem Rydberg-Zustand und realisieren dadurch zunächst eine für die Photonen transparente Konfiguration. Mit zunehmender Rydberg-Population kollabiert das Transparenzfenster und das System wird aufgrund der Rydberg-Wechselwirkungen wieder reflektierend. Durch die lokale Anregung einzelner Rydberg-Atome, demonstrieren wir darüber hinaus kontrollierte "Rydberg-Blockaden", welche der EIT entgegenwirken, und Schaltprozesse für einzelne Photonen zulassen. Zudem demonstrieren wir Korrelationen zwischen einzelnen atomaren und photonischen Zuständen, was ein erster Schritt auf dem Weg zur Erzeugung deterministischer Verschränkung zwischen den Atomen und Photonen ist.

In einem zweiten Experiment koppeln wir mittels sogenannter "Rydberg-Bei-mischung" verstimmt an Rydberg-Zustände, was zu einer langreichweitigen Wechselwirkung führt. Mithilfe dieser realisieren wir ein eindimensionales erweitertes Bose-Hubbard Model unter Verwendung eines stroboskopischen Protokolls, bei dem die Rydberg-Wechselwirkungen periodisch gepulst werden, und erreichen so eine wesentlich längere Lebensdauer, welche kompatibel mit den Tunnelzeitskalen des Hubbard-Modellss sind. Mit dieser Technik können wir die Existenz abstoßend-gebundener Zustände zweier Atome, sowie die Stabilisierung einer Ladungsdichtewelle im Nichtgleichgewicht nachweisen. Schließlich beobachten wir korrelierte Dichteanordnungen innerhalb eines niederenergetischen Ensembles bei halber Füllung, wenn dieses durch kontrolliertes Anschalten der langreichweitigen Wechselwirkungsstärke einen Phasenübergang nahe dem Gleichgewicht durchläuft, was den Weg für die Untersuchung komplexer Phasenübergänge einschließlich von Quantenfestkörpern ebnet.

Rydberg interactions in subwavelength atomic arrays and Hubbard systems

Abstract

Rydberg atoms provide long-range dipolar interactions that can be tuned and switched using optical coupling, rendering them an ideal choice for quantum science and technologies, which encompass a range of applications from quantum simulations, quantum computing, and quantum information. In this dissertation, we incorporate long-range Rydberg interactions into a quantum gas microscope of bosonic ^{87}Rb atoms with single-site control and resolution. This approach allows us to explore the dynamics of many-body systems that feature long-range interactions.

In a first set of experiments, trapped atoms are arranged in a two-dimensional periodic array with subwavelength spacing. Such arrays give rise to photon-mediated interactions and form strong light-matter interfaces with specular reflection. We manipulate this light-matter interface using Rydberg interactions. We make use of electromagnetically induced transparency (EIT) coupled to a Rydberg state, turning the array transparent to probe photons. With increasing Rydberg population, the transparency window collapses and the array becomes reflective again due to the Rydberg interactions. We further demonstrate a controlled way of optical switching using a single Rydberg atom. Here, the single Rydberg atom causes a controlled "Rydberg blockade" within the array, which destroys EIT and renders the system reflective. Moreover, correlations of the single atomic and photonic states are observed, which is a precursor to creating deterministic entanglement between the atom and the photons.

In a second set of experiments, we off-resonantly couple to the Rydberg states, known as "Rydberg dressing", which results in a long-range interaction strength compatible with the itinerant Hubbard model. Here, we realize the one-dimensional (1D) extended Bose-Hubbard model (eBHM) use a stroboscopic scheme, periodically pulsing the Rydberg interactions, and demonstrate substantially enhanced lifetimes, surpassing the timescales relevant for the Hubbard model. With this technique, we observe the existence of repulsively-bound states of atomic pairs as well as the stabilization of a charge density wave state in out-of-equilibrium dynamics. Finally, we find density ordering of low-energy ensembles at half-filling when undergoing a near-equilibrium phase transition upon ramping the long-range interactions, paving the way to study complex phase transitions including quantum solids.

Contents

Chapter 1

Introduction

The development of laser cooling techniques [1–5] has rapidly expanded the fields of atomic, molecular and laser physics. The achievement of ultralow temperatures required for making Bose-Einstein condensates (BECs) [6–8] and reaching Fermi degeneracy [9–11] opens new avenues for research in the strongly correlated regime. Ultracold atoms provide both excellent control and isolated systems for simulating certain sets of strongly correlated quantum problems [12–14], which are relevant for the field of solid state and condensed matter physics [15–20], high-energy physics [21, 22], and cosmology [23, 24]. The advancement of quantum gas microscopy has facilitated the extraction of local information, giving access to correlations of the quantum system [25–34]. Microscopic control down to the single-site level [35] offers further benefits for preparing out-of-equilibrium states and studying their dynamics [36–41].

Interactions of ultracold atoms are typically short-range, which can be tuned using Feshbach resonances [42]. Additional long-range interactions are predicted to host a rich variety of novel phases and quantum phenomena [43, 44], prompting a focus of recent research on exploring the influence of these long-range interactions. Several experimental platforms have been developed to address these interests [44, 45]. Magnetic atoms provide permanent magnetic dipolar interactions at close distances [46–50], whereas ground state molecules have a permanent electric dipole moment, featuring strong dipolar interactions [51–56]. Furthermore, electronically-excited Rydberg atoms offer the strongest electric dipolar interaction via optical coupling [57].

Rydberg atoms are uniquely suited for a range of applications in quantum many-body systems [58–63]. In the regime of resonant optical coupling, the interplay between long-range interactions and optical coupling strength leads to an excitation blockade, known as "Rydberg blockade". This provides a nonlinear behavior that has been utilized for quantum simulations [64–67], quantum computing [68–74], or quantum optics [68–75]. In a first set of experiments in this dissertation, we combine the Rydberg blockade with the strong light-matter interactions offered by subwavelength atomic arrays [76–78]. Such arrays provide high-efficiency light-matter interaction in free space, where scattered photons are restricted solely to the reflection mode. We tune the array to transparent by coupling it to a Rydberg state using an electromagnetically induced transparency (EIT). As the Rydberg population rises, the array becomes nonlinear and starts reflecting photons. However, a single ancilla atom can be employed to control the optical properties of the array through the Rydberg blockade mechanism. We finally realize a switch for photons the between two strong scattering modes of transmission and reflection by optically controlling the state of the ancilla.

The timescales related to the Rydberg interactions are generally faster than the atomic motion by three orders of magnitude in the resonant regime. This limits most of the research to the "frozen gas" regime[79, 80]. By operating off-resonantly from the Rydberg states, known as "Rydberg dressing", the mismatch of both timescales can be bridged. In a second set of experiments, we incorporate Rydberg dressing into our quantum gas microscope to realize the one-dimensional (1D) extended Bose-Hubbard model (eBHM). Here, we overcome the challenge of interaction-induced avalanche losses [81], through stroboscopic Rydberg dressing where interactions are periodically pulsed. Using this technique, we improve the atomic lifetimes to more than one hundred milliseconds, which is ten times longer than the motional timescale in Hubbard parameters, while maintaining comparable long-range interactions. We then measure key features of the eBHM by probing the out-of-equilibrium dynamics of repulsive-bound atomic pairs. We observe the stabilization of a charge density wave (CDW) state during the dynamics due to the influence of nearest-neighbor interactions. Finally, we observe density ordering of a low-energy ensemble resulting from the interplay of dominant nearest-neighbor interactions over the tunneling energy.

Outline

This dissertation begins with an overview of the presented experiments in Chapter 1. Chapter 2 introduces a brief of Rydberg atoms, the origin of their interactions, and the most relevant properties. Then, two key mechanisms relevant for the experiments performed in this dissertation, namely "Rydberg blockade" and "Rydberg dressing", are explained in detail. Chapter 3 describes the experimental setup of our quantum gas microscope, which is employed for microscopic control and read-out the quantum system. After an overview of the new optical lattice setups that were constructed during the framework of this dissertation, we present the various laser systems related to the Rydberg excitations, along with the calibration of the most relevant parameters. Furthermore, fast manipulation of hyperfine ground state is demonstrated using Raman transitions. In Chapter 4, we utilize the Rydberg blockade to control the strong light-matter coupling of subwavelength atomic arrays. Employing the Rydberg blockade from a deterministically controlled single Rydberg atom, we counteract the effect of Rydberg EIT, leading to the breakdown of transparency and changing the properties of the array from reflective to transmissive. Finally, in Chapter 5, Rydberg dressing is incorporated with itinerant atoms in an optical lattice, thus introducing long-range interactions to realize an eBHM. We investigate the eBHM in one-dimension by exploring the out-of-equilibrium dynamics of repulsively-bound pairs and the stability of a CDW under the effects of nearest-neighbor interactions. Moreover, we observe long-range density-density correlations of a half-filled system in near-equilibrium dynamics, indicators for the emergence of a novel quantum solid phase. We present a summary with a brief perspective on extensions of the experiments presented here in Chapter 6.

Publications

The following articles have been published in refereed journals in the context of this thesis. The articles most relevant to this dissertation are shown in bold font.

- Rydberg Molecules Bound by Strong Light Fields.
  S. Hollerith, V. Walther, K. Srakaew, D. Wei, D. Adler, S. Agrawal, P. Weckesser, I. Bloch, J. Zeiher.
  PRX Quantum **5**, 030335 (2024).
- Observation of brane parity order in programmable optical lattices.
  D. Wei, D. Adler, K. Srakaew, S. Agrawal, P. Weckesser, I. Bloch, J. Zeiher.
  Phys. Rev. X **13**, 021042 (2023).
- **A subwavelength atomic array switched by a single Rydberg atom.**
  K. Srakaew, P. Weckesser, S. Hollerith, D. Wei, D. Adler, I. Bloch, J. Zeiher.
  Nat. Phys. **19**, 714–719 (2023).
- Quantum gas microscopy of Kardar–Parisi–Zhang superdiffusion.
  D. Wei, A. Rubio-Abadal, B. Ye, F. Machado, J. Kemp, K. Srakaew, S. Hollerith, J. Rui, S. Gopalakrishnan, N. Y. Yao, I. Bloch, J. Zeiher.
  Science **376**, 716–720 (2022).
- Realizing distance-selective interactions in a Rydberg-dressed atom array.
  S. Hollerith, K. Srakaew, D. Wei, A. Rubio-Abadal, D. Adler, P. Weckesser, A. Kruckenhauser, V. Walther, R. van Bijnen, J. Rui, C. Gross, I. Bloch, J. Zeiher.
  Phys. Rev. Lett. **128**, 113602 (2022).
- Microscopic electronic structure tomography of Rydberg macrodimers.
  S. Hollerith, J. Rui, A. Rubio-Abadal, K. Srakaew, D. Wei, J. Zeiher, C. Gross, I. Bloch.
  Phys. Rev. Research **3**, 013252 (2021).

Preprints

- **Realization of a Rydberg-dressed extended Bose Hubbard model.**
  P. Weckesser, K. Srakaew, T. Blatz, D. Wei, D. Adler, S. Agrawal, A. Bohrdt, I. Bloch, J. Zeiher.
  arXiv:2405.20128 (2024).
- Observation of Hilbert-space fragmentation and fractonic excitations in two-dimensional Hubbard systems.
  D. Adler, D. Wei, M. Will, K. Srakaew, S. Agrawal, P. Weckesser, R. Moessner, F. Pollmann, I. Bloch, J. Zeiher.
  arXiv:2404.14896 (2024).

Chapter 2

Rydberg atoms

2.1 Introduction

This chapter provides an overview of Rydberg atoms and their intriguing properties. We cover concise calculations and derive the relevant scalings of Rydberg properties. Next, we examine the interactions between two Rydberg atoms and demonstrate the various interaction processes. We further introduce the important concepts of "Rydberg blockade" and "Rydberg dressing", which become relevant in a quantum many body system driven by light. Lastly, we highlight stroboscopic Rydberg dressing and demonstrated its suitability for realizing long-range interactions in an itinerant lattice-based quantum simulator.

2.2 Properties and scalings of Rydberg atoms

Rydberg atoms are an intriging quantum system where at least one valence electron is excited to a high principle quantum number n far from the nucleus [57]. The large separation between the ion core and the excited electron provides huge electric dipole moments, making Rydberg atoms strongly interact with external fields and display strong, long-range interactions with nearby Rydberg atoms. Importantly, their unique properties can be controlled via optical coupling. These characteristics make Rydberg atoms useful for quantum science applications [82] such as quantum simulators or quantum computing [64, 83, 84], quantum information [85], quantum nonlinear optics [86], quantum sensing [87–90], and single-photon sources for quantum communication [91].

The valence electron of an alkali Rydberg atom resembles an electron in the hydrogen atom and can be calculated with high accuracy. Understanding the characteristic properties of Rydberg atoms and their scaling is essential to estimate and design the interaction for Rydberg experiments. The valence electron of a Rydberg atom is in an orbit that is far away from the ion core. The closed inner electron shells and the ion core can be viewed as a single positive charge, which features a hydrogen-like behavior especially for large orbital angular momentum $L > 3$. For small L, the penetration and polarization between the inner electron shells and the ion core cause deviations from the simple hydrogenic model. In those cases, "quantum defect theory" is used to apply additional corrections to the hydrogenic model [92–95].

2.2.1 Binding energy

The principle quantum number dependent binding energy of the electron in the hydrogen atom is given by $E_n = -R_\infty/n^2$, where $R_\infty = e^4 m_e/16\pi^2\epsilon_0^2\hbar^2$ is the Rydberg constant [57, 93]. Alkali atoms, featuring additionally closed shells, are described by a corrected formula derived from quantum defect theory as

$$E_{nLJ} = -\frac{R^*}{(n^*)^2}, \tag{2.1}$$

where $R^* = m_{\mathrm{Rb}}/(m_{\mathrm{Rb}} + m_e) \cdot R_\infty$ is the modified Rydberg constant, m_{Rb} is the ionic core mass of Rubidium, and m_e is the electron mass. For ^{87}Rb, the modified Rydberg constant is $R^* = h \times 3289.821\,194\,66(2)\,\mathrm{THz}$ [96, 97]. The binding energy is parametrized by an effective principle quantum number $n^* = (n - \delta_{nLJ})$ with

$$\delta_{nLJ} = \delta_0 + \left(\frac{\delta_2}{n-\delta_0}\right)^2 + \left(\frac{\delta_4}{n-\delta_0}\right)^2 + \dots. \tag{2.2}$$

Here, δ_{nLJ} is the quantum defect, which depends on n, L, and the total angular momentum $J = L + S$ with J is the spin-orbit coupling of L and the electron spin S. The quantum defects are empirically determined by fitting the spectroscopy measurements [94, 96, 97]. They depend significantly on L but weakly on n and J.

2.2.2 Rydberg wavefunction

The Rydberg state is defined by its quantum numbers of the valence electron $|nLJm_J\rangle$ with their corresponding energy of E_{nLJ}. Here, coupling between the total angular momentum J with the nuclear spin I of the Rydberg state is usually negligible. As a consequence, the fine-structure basis provides a set of well-defined quantum numbers for the Rydberg states. Many Rydberg atom properties require detailed calculation of the Rydberg state, such as the dipole moment and the coupling between Rydberg states. Assuming a spherical symmetric potential for the electron, the Rydberg wave function can be separated into a real space function and an angular-dependent function $\Psi(r,\theta,\phi) = R_{nLJ}(r)Y_{LJm_J}(\theta,\phi)$. Here, $R_{nLJ}(r)$ represents the radial wavefunction while $Y_{LJm_J}(\theta,\phi)$ contains the angular-dependent part. With this assumption, the two terms can be solved independently. Including the centrifugal barrier, one can derive the following radial wavefunction from Schrödinger equation,

$$\left[-\frac{1}{2\mu}\left(\frac{\mathrm{d}^2}{\mathrm{d}r^2} + \frac{2}{r}\frac{\mathrm{d}}{\mathrm{d}r}\right) + \frac{L(L+1)}{2\mu r^2} + V_{\mathrm{mod}}(r)\right] R_{nLJ} = E_{nLJ} R_{nLJ}, \tag{2.3}$$

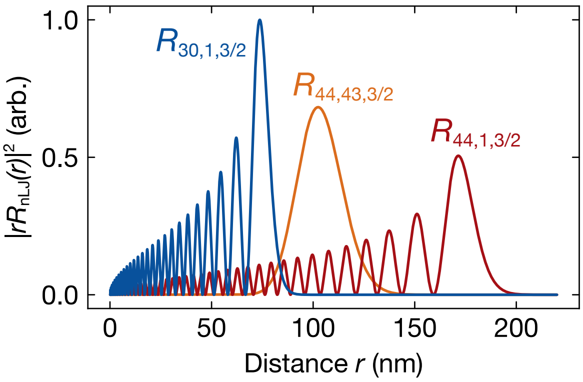

Figure 2.1: Radial wavefunctions of Rydberg states. The Rydberg radial wavefunctions are numerally calculated from the Schrödinger equation Eq. (2.3) and illustrated as relative probability distributions $|rR_{nLJ}(r)|^2$. The plot illustrates the solutions for $R_{30,1,3/2}$ (blue), $R_{44,1,3/2}$ (red), and $R_{44,43,3/2}$ (orange). The wavefunction expands farther away from the ion core with increasing n. The circular Rydberg state with maximum $L = n - 1$, see $R_{44,43,3/2}$ (orange), has a vanish probability at a short distance.

with the reduced mass $\mu = m_{\mathrm{Rb}} m_e / (m_{\mathrm{Rb}} + m_e)$ and the binding energy from Eq. (2.1). The atomic potential includes a species-dependent-modification [98, 99],

$$V_{\mathrm{mod}}(r) = V_C(r) + V_P(r) + V_{\mathrm{S.O.}}(r). \tag{2.4}$$

Here, $V_C(r)$ is the modified Coulomb potential capturing the screening of the core charge by the inner electron shells,

$$V_C(r) = -\frac{1 + (Z-1)e^{-\alpha_1 r} - r(\alpha_3 + \alpha_4 r)e^{-\alpha_2 r}}{r}, \tag{2.5}$$

with $Z = 37$ for ^{87}Rb, and L-dependent parameters $\alpha_{1..4}$ [100]. The $V_P(r)$ describes the core polarization due to the valence electron,

$$V_P(r) = -\frac{\alpha_d}{2r^4}\left[1 - e^{-(r/r_{\mathrm{core}})^6}\right], \tag{2.6}$$

where r_{core} is the effective core radius. Finally, the $V_{\mathrm{S.O.}}(r)$ is the core polarizability and the spin-orbit interaction [101] with effective expression

$$V_{\mathrm{S.O.}}(r > r_{\mathrm{core}}) = \left(\frac{g_s}{4m_e^2 c^2}\right)\frac{L \cdot S}{r^3}, \tag{2.7}$$

where g_s is the electron spin. However, this expression is only valid for $r > r_{\mathrm{core}}$. For a smaller distance, one has to derive this modification using the Dirac equation [99].

Many Rydberg properties are based on the wavefunction of the Rydberg state. Since the angular dependence of the wavefunction has an analytic solution, the calculated accuracy of the Rydberg properties depends primarily on the numerical accuracy of the radial wavefunction. Most available Rydberg calculations such as *Pairinteraction* [98] and *ARC* [102] rely on the preceding approach to compute the Rydberg wavefunctions, which are then used to estimate other Rydberg properties. Fig. 2.1 illustrates the relative probability distribution of the radial wavefunction, which expands farther away from the ion core with increasing n.

2.2.3 Dipole matrix elements

Transition dipole matrix elements play a crucial role in determining various properties of Rydberg atoms, such as the optical coupling rate with the ground state, radiative lifetimes, and interactions with other Rydberg atoms. The dipole operator is defined as

$$\hat{d} = e\hat{r} = e\sum_q r_q \hat{e}^q. \tag{2.8}$$

Here, the index $q = (-1, 0, +1)$ labels the projection of $\hat{r}$ on the spherical basis with $\hat{e}^0 = \hat{e}^z$ and $\hat{e}^{\pm 1} = \mp\frac{1}{\sqrt{2}}(\hat{e}^x \mp i\hat{e}^y)$, corresponding to π, and $\sigma^\pm$ transitions, respectively. The dipole matrix elements that couple between the initial state $|i\rangle = |nLJm_J\rangle$ and then the final state $|j\rangle = |n'L'J'm'_J\rangle$ are given by $d^{ji} = \langle j|\hat{d}|i\rangle$. With the separability of the radial and angular wavefunction, the dipole matrix elements can be expressed by

$$\begin{aligned} d_q^{ji} &= \langle n'L'J'm'_J|er_q|nLJm_J\rangle \\ &= e\mathcal{R}_{nLJ\to n'L'J'}(-1)^{J'+J+L'+S-m'_J+1}\sqrt{(2J'+1)(2J+1)}\begin{Bmatrix} L & L' & 1 \\ J' & J & S \end{Bmatrix}\begin{pmatrix} J' & 1 & J \\ -m'_J & q & m_J \end{pmatrix}. \end{aligned} \tag{2.9}$$

The radial component of the dipolar coupling $\mathcal{R}_{nLJ\to n'L'J'}$ is a radial integral of the initial and final radial wavefunctions, which is obtained by numerical calculation in Sec. 2.2.2,

$$\mathcal{R}_{nLJ\to n'L'J'} = \int_0^\infty r^3 R_{nLJ}(r)R_{n'L'J'}(r)\mathrm{d}r. \tag{2.10}$$

The angular component can be calculated using the Wigner-Eckart theorem [103, 104], which involves the use of the Wigner-3J (Wigner-6J) symbol, denoted by a round (curly) bracket. These result in the Clebsch-Gordan coefficients, ensuring the selection rules for angular momentum conservation. For dipole transitions, the selection rules dictate that the transitions are possible when $\Delta J = J' - J = 0, \pm 1$ and $\Delta m_J = m'_J - m_J = 0, \pm 1$. However, the transitions are forbidden when $J = 0 \leftrightarrow J' = 0$ or $m_J = 0 \leftrightarrow m'_J = 0$ if $\Delta J = 0$.

2.2.4 Rydberg excitation from the ground state

Coherent coupling from the ground to the Rydberg states allows us to control the atomic properties between two distinct regimes. For the ground state, the angular momentum J couples with the nuclear spin I, resulting in the total angular momentum $F = J + I$. Consequently, the ground state is best characterized by the total angular momentum F, which is expressed on the basis $|nLJFm_F\rangle$. It can be expanded to an uncoupled spin basis in $|nLJFm_F\rangle = \sum_{m_J,m_I} |nLJm_Jm_I\rangle\langle nLJm_Jm_I|nLJFm_F\rangle$. Here, $\langle nLJm_Jm_I|nLJFm_F\rangle$ are the Clebsch-Gordan coefficients. Note that the Rydberg excitation leaves the nuclear spin projection unaffected (i.e. $m_I = m'_I$), as the Rydberg state has negligible coupling to the nuclear spin. Finally, the optical coupling strength between the ground states and the Rydberg state can be calculated by

$$\hbar\Omega_{ji} = E_0\langle j|\hat{d}\cdot\hat{\epsilon}|i\rangle, \tag{2.11}$$

where Ω is the Rabi frequency and $E_0 = (2I/c\epsilon_0)^{1/2}$ is the amplitude of the light field with intensity I. The $\hat{\epsilon} = \sum_q \epsilon_q\hat{e}^q$ is the polarization vector of light on a spherical basis with $q = (-1, 0, +1)$. Following the expression in [59, 105], the Rabi frequency that couples the ground state $|i\rangle = |nLJFm_F\rangle$ to the Rydberg state $|f\rangle = |n'L'J'm'_Jm'_I\rangle$ can be computed as

$$\begin{aligned}
\Omega_{rg} &= \frac{eE_0}{\hbar}\sum_q \langle n'L'J'm'_Jm'_I|r_q\epsilon^q|nLJFm_F\rangle \\
&= \frac{eE_0}{\hbar}\mathcal{R}_{nLJ\to n'L'J'}(-1)^{J+2J'+S+m_F+m'_J-I+1+\max[L,L']} \\
&\times \sqrt{(2F+1)(2J+1)(2J'+1)\max[L,L']} \\
&\times \begin{Bmatrix} L & L' & 1 \\ J' & J & S \end{Bmatrix} \sum_q \epsilon^q \begin{pmatrix} J & I & F \\ m'_J - q & m_F - m'_J + q & -m_F \end{pmatrix} \begin{pmatrix} J' & 1 & J \\ m'_J & -q & -m'_J + q \end{pmatrix}.
\end{aligned} \tag{2.12}$$

The same argument as in Eq. (2.9) holds, as the radial component determines the over all coupling strength while the angular component captures the selection rules given by the Clebsch-Gordan coefficients. The ground and the Rydberg states have small spatial overlap between their wavefunctions. The coupling strength is thus smaller by several orders of magnitude compared to the transition from the ground to the first excited states.

2.2.5 Lifetime of the Rydberg atoms

One of the important and intriuging properties of Rydberg atoms is the extended lifetimes compared to the first excited state. This timescale is crucial to estimate the feasibility of a given Rydberg system. There are two main processes by which

Rydberg atoms can decay [57]. The first process involves radiative decay from the Rydberg state to the electronic ground state with a decay rate Γ_{rad} [106]. Alternatively, microwave (MW) photons due to thermal black-body radiation can trigger transitions to neighboring Rydberg of opposite parity with a rate Γ_{BB}. Both processes contribute to the final Rydberg decay rate of $\Gamma_{\mathrm{ryd}} = \Gamma_{\mathrm{rad}} + \Gamma_{\mathrm{BB}}$, with the corresponding lifetime $\tau = 1/\Gamma_{\mathrm{rad}}$.

Radiative decay is a depopulation mechanism due to available vacuum modes. This causes a direct decay into lower-lying states upon emission of a visible or ultraviolet (UV) photon. The radiative decay rate is obtained by summing all possible decay paths using the Einstein-A coefficient [57, 59, 107] from an initial state $|i\rangle = |nLJm_J\rangle$ to a final state $|j\rangle = |nLJFm_F\rangle$ as

$$\begin{aligned}\Gamma_{\mathrm{rad}} &= \sum_j A_{i\to j} \\ &= \sum_{F',m'_F} \frac{\left|\langle n'L'J'F'm'_F|\hat{\boldsymbol{d}}|nLJm_J\rangle\right|^2 \omega^3_{nLJm_J\to n'L'J'F'm'_F}}{3\pi\epsilon_0\hbar c^3},\end{aligned} \tag{2.13}$$

where $\omega_{nLJm_J\to n'L'J'F'm'_F}$ is the transition frequency between the Rydberg and the respective ground state. The $\omega_{nLJm_J\to n'L'J'F'm'_F}$ is approximately independent of n as the energy splitting of the ground states is much smaller than the large energy splitting between the Rydberg and ground states. As a consequence, the radiative decay rate depends mainly depends on the radial integral$\mathcal{R}_{nLJ\to n'L'J'} \propto (n^*)^{-3}$, see Sec. 2.2.4. Therefore, the radiative decay rate scales as $\Gamma_{\mathrm{rad}} \propto (n^*)^{-3}$. One can view this as the overlap between the ground and Rydberg wavefunctions. As the principal quantum number n increases, the Rydberg state wave function spreads further from the ion core, leading to decreased overlap with the ground state wavefunction, which is concentrated near the ion core.

The radiative decay to neighboring Rydberg states is comparably weak due to the small energy differences between the states, which correspond to small transition frequencies $\omega_{nLJm_J\to n'L'J'm'_J} \propto (n^*)^{-3}$. However, the black-body radiation at room temperature contains photons at a frequency close to the transition frequencies of the neighboring Rydberg states. These enhanced stimulated transitions cause black-body-induced decay, which can be estimated by multiplying the transition rate with the photon density $n(\omega_{i\to j}, T)$ as

$$\begin{aligned}\Gamma_{\mathrm{BB}} &= \sum_j A_{i\to j} n(\omega_{i\to j}, T) \\ &= \sum_{n',L',J',m_J'} \frac{\left|\langle n'L'J'm_J'|\hat{\boldsymbol{d}}|nLJm_J\rangle\right|^2 \omega^3_{nLJm_J\to n'L'J'm_J'}}{3\pi\epsilon_0\hbar c^3} \times \frac{1}{e^{\hbar\omega_{nLJm_J\to n'L'J'm_J'}/k_B T}-1},\end{aligned} \tag{2.14}$$

where k_B is the Boltzmann constant and T is the black-body temperature. In the regime where $e^{\hbar\omega_{nLJm_J\to n'L'J'm_J'}/k_B T} \approx 1 + \hbar\omega_{nLJm_J\to n'L'J'm_J'}/k_B T$, the black-body-induced decay rate scales as $\Gamma_{\mathrm{BB}} \propto \mathcal{R}^2_{nLJ\to n'L'J'}\omega^2_{nLJm_J\to n'L'J'm_J'}$. Therefore, this results in a scaling of $\Gamma_{\mathrm{BB}} \propto (n^*)^4 \cdot (n^*)^{-6} \propto (n^*)^{-2}$ [57, 102, 107].

The estimated scaling of the Rydberg decay rate suggests that the Rydberg lifetime $\tau = 1/\Gamma_{\mathrm{ryd}}$ generally increases with higher n. The Rydberg decay rate is influenced by two distinct mechanisms, which determine the dominant decay process depending on n. At low n, the radiative decay is the primary mechanism, while at high n, the black-body-induced decay becomes more significant. For ^{87}Rb, the two decay rates become equal around $n \approx 29$. Several methods are being explored to enhance the Rydberg lifetime. By operating in circular Rydberg states, the radiative decay can be diminished due to the vanishing transition dipole matrix elements to the ground state [108, 109]. Black-body-induced decay can be further suppressed in a cryogenic environment, where the population of photon modes is drastically decreased [110–112].

2.3 Interactions between two Rydberg atoms

The standard treatment of two interacting Rydberg atoms is discussed discussed in detail in the following references [98, 113–116]. Here, we summarize the most important steps. Consider the case where the interaction between two atoms is dominated by the strong Rydberg interaction, where the electrostatic Hamiltonian is described by $H(R) = H_1 + H_2 + H_{\mathrm{int}}(R)$ with R being the interatomic distance. Here, the term $H_{1,2}$ accounts for the individual Rydberg states while $H_{\mathrm{int}}(R)$ describes their interaction. For the calculation, we introduce the pair basis $|i,j\rangle = |n_1L_1J_1m_{J_1}\rangle \otimes |n_2L_2J_2m_{J_2}\rangle$. We assume that the interatomic distance is large compared to the electronic wavefunction, such that the overlap of the electronic wavefunctions can be neglected. Therefore, the two valence electrons can be treated as distinguishable particles. The resulting electrostatic interaction Hamiltonian is given by

$$H_{\mathrm{int}}(R) = \frac{e^2}{4\pi\epsilon_0}\left(\frac{1}{|R|} + \frac{1}{|R+\hat{r}_2-\hat{r}_1|} - \frac{1}{|R-\hat{r}_1|} - \frac{1}{|R+\hat{r}_2|}\right), \tag{2.15}$$

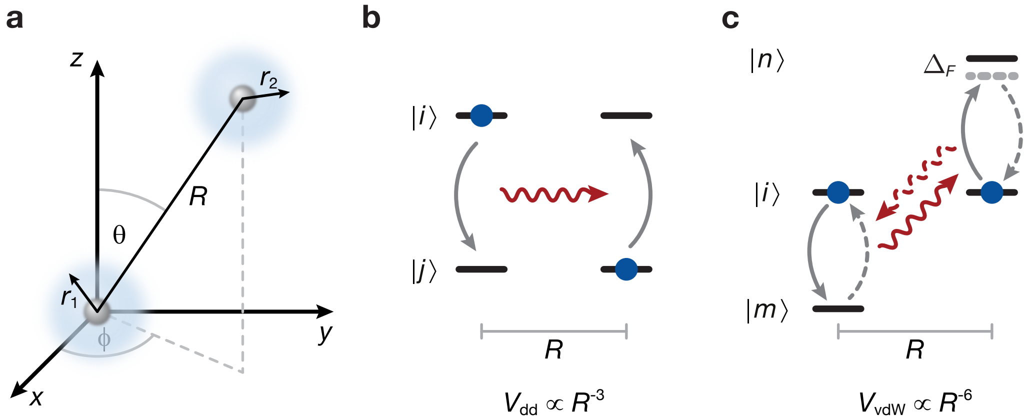

Figure 2.2: Interactions between Rydberg atoms. (**a**) Coordinate system. The interatomic axis can be expressed by the angles θ and ϕ with respect to the quantization axis z. (**b**) Resonant dipole-dipole interactions. Due to the degenerate energies of $|i,j\rangle$ and $|j,i\rangle$, both states are directly coupled by the interaction strength of $|V_{\mathrm{dd}}(R,\theta)| = |C_3|D(\theta)/R^3$. Two atoms that are initialized in $|i,j\rangle$ thus undergo coherent oscillations $|i,j\rangle \leftrightarrow |j,i\rangle$ with a frequency of $2V_{\mathrm{dd}}/h$. (**c**) Off-resonant van der Waals interactions. When two atoms are initialized in the same state $|i,i\rangle$, these can interact by coupling to a nearby pair state $|m,n\rangle$ with the off-resonant Förster defect $\Delta_F = E_m + E_n - 2E_i$. The coupling only occurs through a second-order process, resulting in the characteristic van der Waals interaction with strength $|V_{\mathrm{vdW}}(R,\theta)| = |C_6|D(\theta)/R^6$.

where $\hat{r}_{1,2}$ is the position of the Rydberg electrons. The first and second terms represent the repulsive interaction of both ion cores and both Rydberg electrons, respectively. The last two terms describe the attractive interaction between Rydberg electrons with the ion core of the other Rydberg atom. The $H_{\mathrm{int}}(R)$ can be rewritten in the multipole expansion form [117–119] as

$$H_{\mathrm{int}}(R) = \sum_{\kappa_1,\kappa_2=1}^{\infty} \frac{V_{\kappa_1,\kappa_2}}{4\pi\epsilon_0 |R|^{\kappa_1+\kappa_2+1}}. \tag{2.16}$$

Choosing the spherical multipole operators such that the quantization axis z points along the interatomic distance $\boldsymbol{R}$, the V_{κ_1,κ_2} term can be expressed as

$$\begin{aligned} V_{\kappa_1,\kappa_2} = {} & \frac{4\pi e^2(-1)^{\kappa_2}}{\sqrt{(2\kappa_1+1)(2\kappa_2+1)}} \sum_{q=-\kappa_<}^{\kappa_<} \sqrt{\binom{\kappa_1+\kappa_2}{\kappa_1+q}\binom{\kappa_1+\kappa_2}{\kappa_2+q}} \\ & \times \hat{r}_1^{\kappa_1} \hat{r}_2^{\kappa_2} Y_{\kappa_1}^{q}(\theta_1,\phi_1)\, Y_{\kappa_2}^{-q}(\theta_2,\phi_2)\,, \end{aligned} \tag{2.17}$$

where $Y_{\kappa}^{q}(\theta,\phi)$ are the spherical harmonics and $\kappa_< = \min[\kappa_1,\kappa_2]$. This expansion simplifies the calculation to a single particle problem. In addition, the independent order κ can be evaluated separately depending on the desired accuracy for larger regime. The higher order κ decreases rapidly with greater distance $\boldsymbol{R}$. However, higher order term are required to properly capture the strong mixing regime at shorter distances. When the quantization axis z is not oriented along the interatomic axis R, see Fig. 2.2a, the atomic states $|nLJm_J\rangle$ can be transformed using the Wigner D matrices $\mathcal{D}(\theta,\phi)$. In that way, the interatomic axis is aligned with the quantization axis and the coupling can be calculated with a new rotated state $\mathcal{D}(\theta,\phi)|nLJm_J\rangle$.

2.3.1 Dipole-dipole interaction between two atoms

The lowest order in multipole expansion is given by $\kappa_1 = \kappa_2 = 1$, corresponding to the dipole-dipole interaction. The interaction Hamiltonian in Eq. (2.16) reduces to

$$H_{\text{int}}(R) \approx H_{\text{dd}}(R) = \frac{\hat{d}_1\hat{d}_2 - 3\left(\hat{d}_1 \cdot e_R\right)\left(\hat{d}_2 \cdot e_R\right)}{4\pi\epsilon_0|R|^3}, \tag{2.18}$$

where $\hat{d}_{1,2}$ are the dipole operators for each atom and $e_R = R/|R|$ is the unit vector along the interatomic axis. The dipole-dipole interaction, represented by equation Eq. (2.18), accounts for most of the interaction strength in the asymptotic region, where the interaction shifts are smaller than the energy splitting between paired states. For the special configuration of aligned dipoles $\hat{d}_1 = \hat{d}_2 = \hat{d}$, having the same orientation $\hat{d}_1 \cdot e_R = \cos\theta$, the Hamiltonian becomes

$$H_{\text{dd}}(R,\theta) = \frac{\hat{d}^2}{4\pi\epsilon_0|R|^3}\left(1 - 3\cos^2\theta\right). \tag{2.19}$$

Since the interaction scales with the square of the dipole matrix elements, the dipole-dipole interaction scales as $H_{\text{dd}} \propto (n^*)^4$. The complete description of the dipole-dipole interaction is captured by $H = H_1 + H_2 + H_{\text{int}}$ with the pair basis $|i,j\rangle$. Here, the isolated Rydberg states $(H_1 + H_2)$ have eigenenergies $\langle i,j|H_1 + H_2|i,j\rangle = E_i + E_j$, where $E_{i,j}$ is obtained from Eq. (2.1). The dipole-dipole interaction is given by $\langle i|H_{\text{int}}|j\rangle = V_{\text{dd}}$. By introducing the new energy references $E_i = 0$ and $E_j = \Delta$, we can write the Hamiltonian as,

$$H = \begin{array}{c} \\ |i,i\rangle \\ |i,j\rangle \\ |j,i\rangle \\ |j,j\rangle \end{array} \begin{array}{c} \begin{array}{cccc} \langle i,i| & \langle i,j| & \langle j,i| & \langle j,j| \end{array} \\ \begin{pmatrix} 0 & 0 & 0 & V_{\text{dd}} \\ 0 & \hbar\Delta & V_{\text{dd}} & 0 \\ 0 & V_{\text{dd}}^* & \hbar\Delta & 0 \\ V_{\text{dd}}^* & 0 & 0 & 2\hbar\Delta \end{pmatrix} \end{array}. \tag{2.20}$$

This matrix exhibits two possible processes depending on the initial state, which will be discussed in the following sections.

Resonance dipole-dipole interactions

Let first assume that the two atoms are initialized in a different states, such as $|i,j\rangle$ or $|j,i\rangle$, where both states have the same energy $E = \hbar\Delta$. The dynamics is restricted only in the subspace of $|i,j\rangle$ and $|j,i\rangle$. Here, the Hamiltonian becomes

$$H_{\text{exchange}} = \begin{array}{c c} & \begin{array}{cc} \langle i,j| & \langle j,i| \end{array} \\ \begin{array}{c} |i,j\rangle \\ |j,i\rangle \end{array} & \begin{pmatrix} \hbar\Delta & V_{\text{dd}} \\ V_{\text{dd}}^* & \hbar\Delta \end{pmatrix} \end{array}. \tag{2.21}$$

The eigenstates are $|\pm\rangle = 1/\sqrt{2}\,(|i,j\rangle \pm |j,i\rangle)$. As a consequence, the initial state $|i,j\rangle$ is not an eigenstate of the system. Its evolution can be obtained from Schrödinger equation,

$$|\Psi\rangle(t) = \cos\left(\frac{V_{\text{dd}}t}{\hbar}\right)|i,j\rangle + i\sin\left(\frac{V_{\text{dd}}t}{\hbar}\right)|j,i\rangle. \tag{2.22}$$

This shows that the initial state $|i,j\rangle$ coherently oscillates between $|i,j\rangle$ and $|j,i\rangle$. The probability of finding the system in $|i,j\rangle$ is

$$|\langle i,j|\Psi\rangle(t)|^2 = \cos^2\left(\frac{V_{\text{dd}}t}{\hbar}\right) = \frac{1}{2}\left[1 + \cos\left(2\pi\frac{2V_{\text{dd}}t}{h}\right)\right], \tag{2.23}$$

with oscillation frequency $2V_{\text{dd}}/h$ [120–123], see Fig. 2.2b. Experimentally, this can be achieved by preparing two neighboring Rydberg states of opposite parity, such as the Rydberg S and P states ($|S,P\rangle$).

Off-resonant Van der Waals interactions

Another situation arises when when both atoms are in the same Rydberg state $|i,i\rangle$ or $|j,j\rangle$. These two pair states have an energy difference by $\Delta_F = 2E_j - 2E_i = 2\hbar\Delta$, the so-called Förster defect. Here, the pair states are coupled via virtual second-order processes, as illustrated in Fig. 2.2c. The Hamiltonian in this subspace is

$$H_{\text{vdW}} = \begin{array}{c c} & \begin{array}{cc} \langle i,i| & \langle j,j| \end{array} \\ \begin{array}{c} |i,i\rangle \\ |j,j\rangle \end{array} & \begin{pmatrix} 0 & V_{\text{dd}} \\ V_{\text{dd}}^* & 2\hbar\Delta \end{pmatrix} \end{array}. \tag{2.24}$$

This hamiltonian only holds true for large detunings $V_{\text{dd}} \ll \Delta$, resulting in the following eigenenergies by $E_\pm = \hbar\Delta \mp \sqrt{(\hbar\Delta)^2 + |V_{\text{dd}}|^2}$. The energy shifts from the noninteracting energy in this case are known as *van der Waals* interaction,

$$\Delta E = V_{\text{vdW}}(\boldsymbol{R}, \boldsymbol{\theta}) = -\frac{|V_{\text{dd}}|^2}{32\pi^2\epsilon_0\hbar\Delta R^6} = -\frac{C_6}{R^6}D(\theta). \tag{2.25}$$

The "C_6-coefficient" quantifies the strength of the interaction, which contains all radial matrix elements between the initial and intermediate states. The $D(\theta)$ contains all

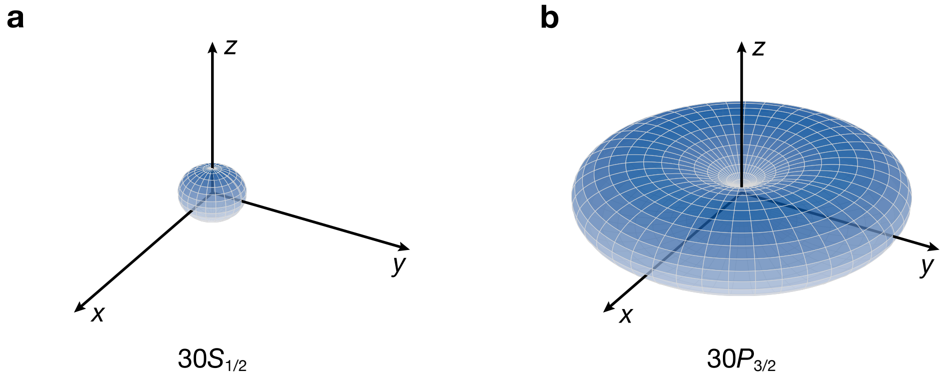

Figure 2.3: Rydberg interactions of the $30S_{1/2}$ and $30P_{3/2}$ states. Comparison of the interaction strength expressed by the C_6-coefficient versus three-dimensional (3D) interaction angles. The length from the center to the plot surface indicates the magnitude of the C_6-coefficient. (**a**) For the $30S_{1/2}$ state, the interaction is nearly symmetric for all interaction angles. Although the van der Waals interaction of an individual channel is angular dependent, the aggregation of all possible channels leads to an almost symmetric interaction for $30S_{1/2}$. (**b**) For the $30P_{3/2}$ state, there is only one significant transition involved. Therefore, it shows an anisotropic interaction with respect to θ while featuring a symmetric interaction along ϕ. The interaction is maximum when $\theta = 90°$ and vanishes for $\theta = 0°$. Moreover, the maximum interaction of $30P_{3/2}$ is much larger than $30S_{1/2}$ by a factor of 4.5.

the angular momentum properties of the states [124, 125]. The C_6 scaling can be deduced from the scaling of the Förster defect $\Delta_F \propto (n^*)^{-3}$ and the scaling of the dipole-dipole interaction $V_{\mathrm{dd}} \propto (n^*)^4$. Thus, the C_6-coefficient exhibits an overall scaling of $C_6 \propto (n^*)^{11}$. Furthermore, the interaction depends on the sign of $\Delta = E_j - E_i$. A positive value for $\Delta = |\Delta|$ results in an attractive interaction, while a negative value $\Delta = -|\Delta|$ results in a repulsive interaction.

The derivation in Eq. (2.24) only considers the two Rydberg states, $|i\rangle$ and $|j\rangle$. The general expression of the van der Waals interaction accounts for all possible states with comparable Förster defects Δ_F of the same order. The van der Waals interaction of $|i,i\rangle$ is given by

$$V_{\mathrm{vdW}}^{i,i}(\boldsymbol{R},\boldsymbol{\theta}) = -\sum_{m,n} \frac{|\langle i,i|H_{\mathrm{dd}}|m,n\rangle|^2}{\Delta_F^{m,n}} = -\frac{C_6}{R^6} D(\theta) \tag{2.26}$$

with $\Delta_F^{m,n} = E_m + E_n - 2E_i$. For ^{87}Rb, we can compare two interesting cases of van der Waals interactions. First, the pair state $|i,i\rangle = |nS\frac{1}{2}m_J, nS\frac{1}{2}m_J\rangle$ can couple to $|m,n\rangle = |nPJ'm_J', (n-1)PJ''m_J''\rangle$. Due to a large Förster defect $\Delta_F^{m,n}$ compared to the splitting of the fine structure, all intermediate pair states with $J', J'' = (1/2, 3/2)$ have

Property	Symbol	Scaling
Binding energy	E_{nLJ}	$(n^*)^{-2}$
Energy splitting	ΔE_{nLJ}	$(n^*)^{-3}$
Radial coupling $\lvert g\rangle \leftrightarrow \lvert r'\rangle$	$\mathcal{R}_{5S1/2\rightarrow n'L'J'}$	$(n^*)^{-3/2}$
Radial coupling $\lvert r\rangle \leftrightarrow \lvert r'\rangle$	$\mathcal{R}_{nLJ\rightarrow n'L'J'}$	$(n^*)^{2}$
Radiative decay rate	Γ_{rad}	$(n^*)^{-3}$
Black body decay rate	Γ_{BB}	$(n^*)^{-2}$
C_6 -coefficient	C_6	$(n^*)^{11}$
Rydberg blockade	r_b, r_c	$(n^*)^{11/6}$

Table 2.1: Scaling of relevant Rydberg properties. Approximate scaling of the relevant Rydberg properties with respect to the effective principle quantum number $n^* = n - \delta_{nLJ}$, where δ_{nLJ} is the quantum defect.

approximately the same Förster defect. As a result, the sum of all intermediate pair states results in close to angular-independent interaction $V_{\mathrm{vdW}}(\boldsymbol{R}) \approx -C_6 D/R^3$ [124], see Fig. 2.3a. In contrast, the specific pair state $|i,i\rangle = |nP\frac{3}{2}\frac{3}{2}, nP\frac{3}{2}\frac{3}{2}\rangle$ has only one significant transition to $|m,n\rangle = |nS\frac{1}{2}\frac{1}{2}, (n-1)S\frac{1}{2}\frac{1}{2}\rangle$. Other possible pair states have a significantly larger Förster defect Δ_F, resulting in negligible contributions to the interaction. This results in a strong angular dependence of $V_{\mathrm{vdW}}(\boldsymbol{R}, \boldsymbol{\theta}) \approx -C_6 \sin^4(\theta)/R^3$, see Fig. 2.3b. In conclusion, the choice of Rydberg state strongly affects the van der Waals interaction, making it a suitable tool for various applications. The Rydberg S state yields an isotropic interaction that is advantageous for experiments requiring uniform interactions in all directions. Conversely, operating with the Rydberg P state offers the possibility of customizing the interaction by adjusting a quantization field relative to the interatomic axis θ [126].

Finally, we summarize all previously discussed effects and their respective scaling with respect to the effective principle quantum number n^* in Tab. 2.1.

2.4 Rydberg interactions in the presence of a light field

Up until this point, the focus has been solely on the Rydberg interaction. In the following sections, we will extend this discussion by including optical coupling between the ground and Rydberg states. This will lead to two important mechanisms of experiments in this dissertation. First, we discuss the resonant coupling resulting in the "Rydberg blockade". It causes a volume in which only one Rydberg atom can be excited. The Rydberg blockade concept will be utilized in Chapter 4. Secondly, off-resonant coupling to the Rydberg states, the so-called "Rydberg dressing", provides long-range interactions between ground state atoms. Here, long-range interactions can be exploited despite the atoms mostly in their electronic ground state, making them suitable for itinerant long-range models explored in Chapter 5.

Consider the optical coupling from a single ground state $|g\rangle$ to a single Rydberg state $|r\rangle$. The light field associated with this coupling has Rabi frequency Ω and a frequency detuning Δ to the Rydberg state. When multiple atoms are in the Rydberg state, a van der Waals interaction appears as $V_{i,j}(R) = -C_6/R_{i,j}^6$ with $R_{i,j} = |R_i - R_j|$. For simplicity and without loss of generality, we assume an isotropic interaction which can be experimentally obtained by applying a quantization field orthogonal to the interatomic axis. We can write the Hamiltonian describing the two-level system of N atoms in presence of a light field and the long-range van der Waals interaction as [127–130]

$$\begin{aligned} H &= H_{\mathrm{L}} + H_0 + H_{\mathrm{int}} \\ &= \frac{\hbar\Omega}{2}\sum_i^N \left(|g\rangle_i\langle r|_i + |r\rangle_i\langle g|_i\right) - \hbar\Delta\sum_i^N |r\rangle_i\langle r|_i + \sum_{i<j}^N V_{i,j}(R)|r\rangle_i\langle r|_i|r\rangle_j\langle r|_j. \end{aligned} \tag{2.27}$$

The size of the Hamiltonian's Hilbert space increases exponentially with atom number N, requiring heavy computational resources to derive an exact solution. For simplicity, we first focus on the problem with $N = 2$ atoms, where the Hamiltonian becomes

$$H = \begin{array}{c c} & \begin{array}{cccc} \langle g,g| & \langle g,r| & \langle r,g| & \langle r,r| \end{array} \\ \begin{array}{c} |g,g\rangle \\ |g,r\rangle \\ |r,g\rangle \\ |r,r\rangle \end{array} & \begin{pmatrix} 0 & \hbar\Omega/2 & \hbar\Omega/2 & 0 \\ \hbar\Omega/2 & -\hbar\Delta & 0 & \hbar\Omega/2 \\ \hbar\Omega/2 & 0 & -\hbar\Delta & \hbar\Omega/2 \\ 0 & \hbar\Omega/2 & \hbar\Omega/2 & -2\hbar\Delta + V(R) \end{pmatrix} \end{array}. \tag{2.28}$$

This matrix has the symmetric coupling from $|g,r\rangle$ and $|r,g\rangle$ to $|g,g\rangle$ and $|r,r\rangle$, motivating the symmetric and antisymmetric basis $|\pm\rangle = 1/\sqrt{2}\left(|g,r\rangle \pm |r,g\rangle\right)$. The antisymmetric state is uncoupled and equivalent to a dark state with $\langle g,g|H|-\rangle = \langle r,r|H|-\rangle = 0$. However, the symmetric state experiences an enhanced coupling of $\langle g,g|H|+\rangle = \langle r,r|H|+\rangle = \sqrt{2}\hbar\Omega/2$. Making use of these states, one can simplify the

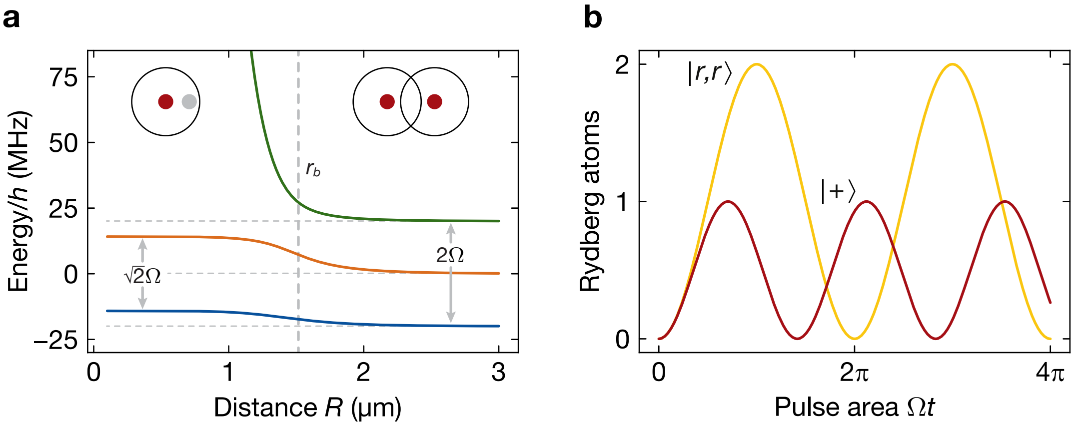

Figure 2.4: Rydberg blockade and enhanced Rabi frequency. (**a**) Eigenenergies of the Hamiltonian in Eq. (2.29) presented for $\Delta = 2\pi \times 0\,\text{MHz}$, $\Omega = 2\pi \times 20\,\text{MHz}$, and $C_6 = -1.3\,\text{GHz}\,\mu\text{m}^6$. The blockade radius $r_b = 1.5\,\mu\text{m}$ separates the non-interacting ($R > r_b$) and strong interacting ($R < r_b$) regimes. The insets illustrate either that both atoms are independently excited (see the right inset) or that only one atom can be excited in the blockade volume at the strong interacting regime. (**b**) Enhanced Rabi frequency in the Rydberg blockaded regime. For $R > r_b$ (yellow), the two atoms independently oscillate between $|g, g\rangle$ and $|r, r\rangle$ with Rabi frequency Ω. For $R < r_b$ (red), the large interaction prevents a subsequent excitation, so that only one excitation is possible. The $|g, g\rangle$ state is coupled to $|+\rangle$ with the enhanced Rabi frequency $\sqrt{2}\Omega$.

Hamiltonian as

$$H = \begin{array}{c} \\ |g,g\rangle \\ |+\rangle \\ |r,r\rangle \end{array} \begin{array}{c} \begin{array}{ccc} \langle g,g| & \langle +| & \langle r,r| \end{array} \\ \begin{pmatrix} 0 & \sqrt{2}\hbar\Omega/2 & 0 \\ \sqrt{2}\hbar\Omega/2 & -\hbar\Delta & \sqrt{2}\hbar\Omega/2 \\ 0 & \sqrt{2}\hbar\Omega/2 & -2\hbar\Delta + V(R) \end{pmatrix} \end{array} . \tag{2.29}$$

2.4.1 Rydberg blockade

Considering the case when $\Delta = 0$, diagonalizing the Hamiltonian in Eq. (2.29) results in new eigenenergies, which depends on the interatomic distance R, see Fig. 2.4a. In the limit of large interatomic distances R, where $V(R) \approx 0$, each atom will undergo trivial independent Rabi oscillations $|g\rangle \leftrightarrow |r\rangle$. For small distances R where $V(R) \gg \Omega$, the strong van der Waals interaction shifts the energy of $|r, r\rangle$ out of resonance. The latter effectively forms an effective two-level system in the subspace of $|g,g\rangle$ and $|+\rangle$,

$$H = \begin{array}{c c} & \begin{array}{cc} \langle g,g| & \langle +| \end{array} \\ \begin{array}{c} |g,g\rangle \\ |+\rangle \end{array} & \begin{pmatrix} 0 & \sqrt{2}\hbar\Omega/2 & 0 \\ \sqrt{2}\hbar\Omega/2 & 0 \end{pmatrix} \end{array}, \tag{2.30}$$

with eigenstates $1/\sqrt{2}\,(|g,g\rangle \pm |+\rangle)$. Starting at $|g,g\rangle$, this yields a Rabi oscillation between $|g,g\rangle$ and $|+\rangle$, with an enhanced Rabi frequency of $\sqrt{2}\Omega$, see Fig. 2.4b. It can be generalized to N atoms system where the enhanced Rabi frequency is $\sqrt{N}\Omega$ [131–134]. Additionally, the dynamics is restricted with a maximum of one single Rydberg atom, which is known as the "Rydberg blockade". The blockade radius r_b characterizes the transition point between the regimes of strong and weak interaction $V(R)$, where the power broadening Ω equals the magnitude of the interaction $V(R)$,

$$r_b = \left(\frac{|C_6|}{\hbar\Omega}\right)^{1/6}. \tag{2.31}$$

The concept of Rydberg blockade has been observed experimentally [127, 132] and has demonstrated substantial potential for various applications [63, 72].

2.4.2 Rydberg dressing

Here, we focus on the case of far-detuned off-resonant coupling $|\Delta| \gg \Omega$. In the regime of large interatomic distances where $V(R) = 0$, the ground eigenstate is simply a product of two independent dressed states that are coupled by the light field,

$$|\tilde{g},\tilde{g}\rangle \approx (|g\rangle - \beta|r\rangle) \otimes (|g\rangle - \beta|r\rangle)\,, \tag{2.32}$$

where $\beta = \Omega/2|\Delta| \ll 1$ is the admixture with β^2 being the probability to find the dressed atom in the Rydberg state $|r\rangle$ in the dressed state $|\tilde{g}\rangle$. Diagonalizing the Hamiltonian for variable interatomic distances results in Fig. 2.5a, where $\Delta < 0$ and $C_6 < 0$ are assumed. The $|\tilde{g},\tilde{g}\rangle$ state has a distance-dependent eigenenergy due to the dipole interactions of the Rydberg state admixture. The additional energy, compared with the non-interacting limit at large distances, is called "dressed interaction" $U(R)$ and can be approximated using a perturbative approach, as detailed in the works of [105, 135–139]. This is based on the limit where $\Delta \ll \Omega$ so that the light field can be treated perturbatively. Then, determining the energy of $|\tilde{g},\tilde{g}\rangle$ from the correction energies of $|g,g\rangle$, as $E_{\tilde{g}\tilde{g}} = \sum_i E^{(i)}_{gg}$, to the point where the interaction $V(R)$ becomes

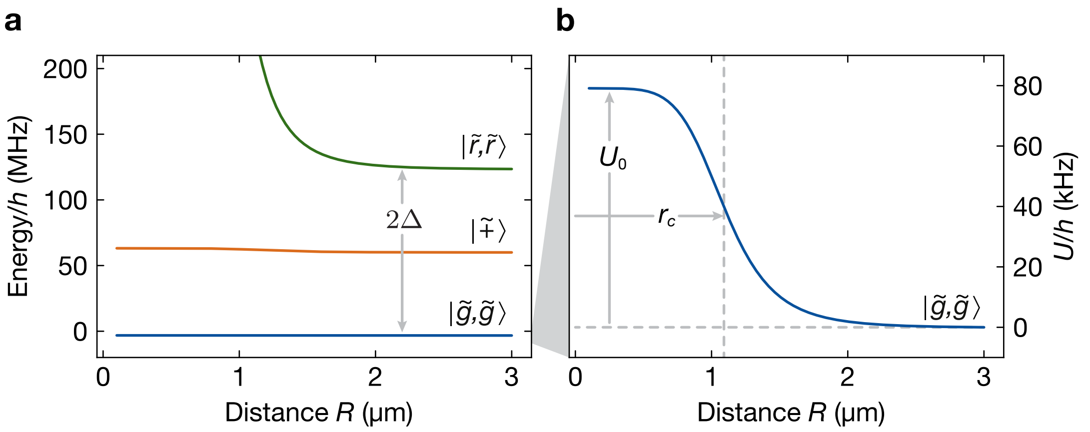

Figure 2.5: Dressed interaction potential of two Rydberg atoms. (**a**) Eigenenergies of the Hamiltonian in Eq. (2.29) calculated for $\Delta = 2\pi \times -60\,\text{MHz}$, $\Omega = 2\pi \times 20\,\text{MHz}$, and $C_6 = -1.3\,\text{GHz}\,\mu\text{m}^6$. The interatomic axis orients with θ and ϕ with respect to the quantization axis z. (**b**) A zoom to the lowest eigenenergy. The dressed interaction $U(R) = E_{\tilde{g}\tilde{g}}(R) - E_{\tilde{g}\tilde{g}}(R=\infty)$ shows a distance-dependent potential. The dressed interaction strength $U_0 = \hbar\Omega^4/8\Delta^3$ is independent of the chosen Rydberg state but only relates to the optical coupling parameters. The cut-off distance $r_c = (|C_6|/2\hbar|\Delta|)^{1/6}$ can be tuned by the choice of Rydberg state and detuning.

significant. The correction energies can be calculated as

$$\begin{aligned}
E_{gg}^{(1)} &= E_{gg}^{(3)} = 0\\
E_{gg}^{(2)} &= \frac{|\langle g,g|H_L|+\rangle|^2}{-E_+} = \frac{\hbar\Omega^2}{2\Delta}\\
E_{gg}^{(4)} &= \frac{|\langle g,g|H_L|+\rangle\langle +|H_L|r,r\rangle|}{E_+^2\cdot(-E_{rr})} - \frac{|\langle g,g|H_L|+\rangle|^4}{E_+^2\cdot(-E_+)} = \frac{\hbar\Omega^4}{4\Delta^2(2\Delta - V(R)/\hbar)} - \frac{\hbar\Omega^4}{4\Delta^3}.
\end{aligned} \tag{2.33}$$

We can see that the correction up to fourth order contains the Rydberg interaction $V(R)$. The energy of $|\tilde{g},\tilde{g}\rangle$ is

$$E_{\tilde{g}\tilde{g}}(R) = \frac{\hbar\Omega^4}{4\Delta^2(2\Delta - V(R)/\hbar)} - \frac{\hbar\Omega^4}{4\Delta^3} + \frac{\hbar\Omega^2}{2\Delta}. \tag{2.34}$$

The distance-independent offset potential corresponds to the light-induced AC Stark shift of two independent atoms. The dressed interaction potential $U(R)$ can simply be derived by subtracting asymptotic energy from $E_{\tilde{g}\tilde{g}}(R)$, yielding

$$\begin{aligned} U(R) &= E_{\tilde{g},\tilde{g}}(R) - E_{\tilde{g},\tilde{g}}(R=\infty) \\ &= \frac{\hbar\Omega^4}{4\Delta^2(2\Delta - V(R)/\hbar)} \\ &= \frac{U_0}{1+(R/R_c)^6}. \end{aligned} \tag{2.35}$$

In the last step of Eq. (2.35), we assume that the Rydberg interaction is repulsive $V(R) = |C_6|/R^6$ and the detuning is negative $\Delta = -|\Delta|$. This assumption ensures that the resonant condition $-2\Delta + V(R) = 0$ is avoided. The $U(R)$ expresses a softcore shape with a maximum of

$$U_0 = 2\hbar\Delta\beta^4 = \frac{\hbar\Omega^4}{8\Delta^3}, \tag{2.36}$$

with r_c is the cut-off distance, defined when the Rydberg interaction $V(R)$ equates with the power broadening of $\sqrt{\Omega^2 + (2\Delta)^2} \approx 2|\Delta|$,

$$R_c = \left(\frac{|C_6|}{2\hbar|\Delta|}\right)^{1/6}. \tag{2.37}$$

Fig. 2.5b shown the softcore shape of $U(R)$ for $\Delta = 2\pi \times -60\,\mathrm{MHz}$, $\Omega = 2\pi \times 20\,\mathrm{MHz}$, and $C_6 = h \times -1.3\,\mathrm{GHz}\,\mu\mathrm{m}^6$. It is evident that the optical coupling Ω and the detuning Δ are the sole determinants of the dressed interaction strength U_0, with the Rydberg interaction C_6 having no effect. However, the range of dressed interaction R_c is dictated by the magnitude of Rydberg interaction C_6 and detuning $|\Delta|$. These two parameters, U_0 and R_c, are crucial to customizing the Rydberg-dressed interaction. Moreover, the interaction strength can be tuned with the orientation of the quantization field due to the orientation-dependent interaction of Rydberg P state [140].

Continuous vs stroboscopic Rydberg dressing

To combine long-range Rydberg interactions with an itinerant lattice based quantum system, the Rydberg lifetime has to be longer than the timescale associated with the atomic motion. However, the usual Rydberg lifetime of several microseconds is significantly shorter than the few milliseconds characteristic of moving atoms in optical lattices. Rydberg dressing is introduced to overcome this short lifetime of bare Rydberg state. The off-resonant admixing of the Rydberg state into the ground state effectively increases the lifetime, surpassing the motional timescale while providing a substantial extended-range interaction on the nearest lattice site. In the limit of $\Delta \gg \Omega$, we summarize the relevant scaling parameters for the Rydberg dressing, where the light field continuously drives the system,

$$\begin{aligned} U_C &= U_0 = \frac{\Omega^4}{8\Delta^3} = \beta^3\Omega \\ \tau_C &= \frac{4\Delta^2}{\Omega^2}\tau_{\text{ryd}} = \frac{\tau_{\text{ryd}}}{\beta^2}. \end{aligned} \tag{2.38}$$

The important parameter to quantify the applicability is "quality factor" Q. It represents the ratio between the coherent to incoherent portion of the coupling. For continuous Rydberg dressing, the quality factor is given by [141]

$$Q_C = U_C \cdot \tau_C = \beta\Omega\tau_{\text{ryd}} = \frac{\Omega^2\tau_{\text{ryd}}}{2\Delta}. \tag{2.39}$$

This shows that larger Rabi frequency and smaller detuning give better quality factor as soon as we are still in the limit of $\Delta \gg \Omega$.

One can further improve the quality factor and thus the effective lifetime by applying a "stroboscopic Rydberg dressing" by pulsing light into the system. Following the derivation in [105], the dressed interaction strength of U_S, with the associated lifetime of τ_S, is pulsed on for a duration t. The interval T between each pulse results in the duty cycle $D = t/(t+T) < 1$. In a regime where the pulse period is much shorter than the external timescale, e.g. the motional timescale in the optical lattice, the stroboscopic dressed interaction and lifetime are simply become average properties over the duty cycle,

$$\begin{aligned} U_{S,\text{avg}} &= \langle U_0 \rangle_t = D U_S \\ \tau_{S,\text{avg}} &= \frac{\tau_S}{D}. \end{aligned} \tag{2.40}$$

The average interaction strength $U_{S,\text{avg}}$ reduces as the duty cycle decreases, whereas the average lifetime $\tau_{S,\text{avg}}$ extends proportionally. If the same parameters are used in the stroboscopic dressing, $\Omega_S = \Omega$ and $\Delta_S = \Delta$, the quality factor remains unchanged,

$$Q_{S,\text{avg}} = U_{S,\text{avg}} \cdot \tau_{S,\text{avg}} = \beta_S\Omega_S\tau_S = \beta\Omega\tau_{\text{ryd}} = Q_C. \tag{2.41}$$

This approach appears to offer no enhancement when utilizing the dressing pulses. However, we can operate with a larger admixture $\beta_S > \beta$ where the stroboscopic dressed interaction is equated to the continuous dressed interaction. Assuming the same optical coupling $\Omega_S = \Omega$ but $\Delta_S < \Delta$, we can find the admixture relation as

$$\begin{aligned} U_{S,\text{avg}} &= U_C \\ D\beta_S^3\Omega &= \beta^3\Omega \\ \beta_S &= \frac{\beta}{D^{1/3}} \end{aligned} \tag{2.42}$$

This relation shows that the same dressed interaction can be reached by increase admixture of the stroboscopic dressing by a factor of $D^{-1/3}$. Applying this relation, the lifetime of the stroboscopic dressing is expressed as

$$\tau_{S,\mathrm{avg}} = \frac{\tau_{\mathrm{ryd}}}{D\beta_S^2} = \frac{\tau_{\mathrm{ryd}}}{D^{1/3}\beta^2} = \frac{\tau_C}{D^{1/3}}. \tag{2.43}$$

Since the duty cycle is less than unity $D < 1$, the stroboscopic dressed lifetime is longer compared with the continuous dressed lifetime despite offering the same interaction strength. Analyzing the quality factor in these configurations, we observe an enhancement of

$$Q_{S,\mathrm{avg}} = U_{S,\mathrm{avg}} \cdot \tau_{S,\mathrm{avg}} = U_C \cdot \frac{\tau_C}{D^{1/3}} = \frac{Q_C}{D^{1/3}}. \tag{2.44}$$

In summary, operating with stroboscopic Rydberg dressing while having the same time-averaged interaction strength, enhances the lifetime by a factor of $D^{-1/3}$. This extended lifetime is experimentally observed and then utilized to achieve extended-range interactions between atoms in optical lattices, discussed in Chapter 5.

2.5 Summary

This chapter has discussed the physics of Rydberg atoms. We started from calculating the energy and wavefunction on the basis of quantum defect theory. It provides an understanding of the Rydberg properties, such as coupling strength and lifetime. Tab. 2.1 outlines the relevant Rydberg characteristics that are proportional to the effective principal quantum number n^*, which are essential for the planning of experiments. Most calculations in this dissertation benefit from open source calculation scripts of the ARC [102] and Pairinteraction [98] packages. In addition, incorporating light-matter interactions within a Rydberg system introduces the concepts of Rydberg blockade and Rydberg dressing. Due to their versatile control with external light fields, Rydberg atoms play a crucial role in quantum simulation [64–67], engineering of the quantum gate [68–74], and quantum optics experiments [142–146].

Chapter 3

Experimental platform

3.1 Introduction

Ultracold atoms have become an established platform for quantum simulation of interacting many-body system [13, 14, 147]. Ultracold atoms in optical lattices, particularly, can realize a many-body Hamiltonian, the so-called Bose-Hubbard model (BHM) which can be used to simulate problems in many fields such as condensed matter physics, high energy physics, and astrophysics [14, 16, 148, 149]. They offer excellent tunable and controllable system parameters while being isolated from the environment. With quantum gas microscopes, accessibility to microscopic information can be reached at the single-atom level [150–152]. This also provides local control over the system, allowing one to study out-of-equilibrium phenomena [36, 37, 40, 153–155]. Moreover, incorporating the strong and controllable interaction of Rydberg atoms into the system introduces an additional energy scale over large distances. This makes the platform versatile for a wide range of studies, including many-body physics in strongly correlated regimes [61, 64, 65, 127, 140], quantum optics [86, 156], and quantum computing applications [68, 85].

This chapter describes the experimental setup and protocol used in this dissertation. The discussion starts with the preparation and detection of the quantum gas in an upgraded optical lattice setup, which offers a larger system size and tunable lattice geometry. Then, we benchmark our Rydberg single-photon and two-photon setups and compare to the previous setup [105, 113, 128]. Finally, a Raman setup to achieve fast ground state manipulation is presented. More technical information can be found at an earlier dissertations [105, 113, 157–162].

3.2 Ultracold atoms in optical lattices

In our experiment, a ^{87}Rb atomic gas is first cooled down to the quantum degeneracy. The atoms are trapped in a two-dimensional (2D) periodic potential formed by interference with off-resonant laser beams. This realizes the 2D Bose-Hubbard

Hamiltonian [163]

$$H_{\mathrm{BM}} = -J \sum_{\langle i,j \rangle} \hat{a}_i^{\dagger} \hat{a}_j + \frac{U}{2} \sum_i \hat{n}_i \left(\hat{n}_i - 1 \right) - \mu \sum_i \hat{n}_i, \tag{3.1}$$

where $\hat{a}_i$ $\left(\hat{a}_i^{\dagger}\right)$ is the annihilation (creation) operator of an atom at site i, $\hat{n}_i = \hat{a}_i \hat{a}_i^{\dagger}$ is the atom number operator at site i, and $\langle i, j \rangle$ denotes summing over the nearest-neighbor site i, j. The hopping energy J describes the coherent tunneling rate of an atom from site j to neighboring site i. The onsite interaction energy U is the interaction energy shift of the interaction of two atoms at the same site i. A chemical potential μ describes the spatial distribution of the site offset potential in the system, which is determined by the trapping potential or can be engineered using the local control capability.

The BHM is not analytically solvable. However, we can still describe its properties in the two extreme limits of $J \gg U$ and $J \ll U$ that feature the two quantum phases of a superfluid (SF) and a Mott insulator (MI), respectively. Those two regimes can be experimentally accessed by adiabatically tuning the lattice depth, revealing the SF-MI phase transition [164, 165]. For the non-interacting limit where $J \gg U$, the ground state is given by a Bose-Einstein condensate (BEC). The hopping energy is dominant and allows the atom to delocalize throughout the system. In the thermodynamic limit, where the atom number is large, the ground state is described by a product of local coherent states [147]

$$|\Psi\rangle_{\mathrm{SF}} = \prod_i |\alpha\rangle_i = \prod_i \left(e^{-|\alpha|^2/2} \sum_{n=0}^{\infty} \frac{\alpha^n}{\sqrt{n!}} |n\rangle_i \right), \tag{3.2}$$

where $\alpha^2 = \langle n \rangle$ is the mean occupation in one site, $|n\rangle_i$ is the Fock state in site i, and n is the single-site atom number. For the strongly interacting limit where $J \ll U$, the onsite interaction energy is much larger than the tunneling energy, thus, the hopping processes to sites j with $n_j \geq n_i$ are negligible. The ground state is simply the tensor product of all Fock states on the individual sites [147],

$$|\Psi\rangle_{\mathrm{MI}} = \prod_i |n\rangle_i = \frac{1}{\sqrt{n!}} \prod_i \left(\hat{a}_i^{\dagger} \right)^n |0\rangle. \tag{3.3}$$

Each particle is restricted to an individual lattice site therefore the variance vanishes $\sigma_i^2 = 0$ [166]. This described an isolating phase, called the MI.

3.3 The rubidium quantum gas microscope

The key feature of a "quantum gas microscope" is the microscopic accessibility of the local occupation of particles in the system by collecting fluorescence light with a high-resolution objective [150–152, 167–173]. The results in this dissertation have been performed with a quantum gas microscope using bosonic ^{87}Rb [151]. In this section, we will summarize the four main experimental protocols; preparing a cold ensemble and unity-filled MIs in the optical lattices, the actual experimental sequences, and the site-resolved detection. Moreover, we will discuss our capability to perform single-site addressing of atomic configurations and the ability to tune our lattice geometries.

3.3.1 Preparation of cold atomic ensembles and 2D unity-filled systems

To achieve ultracold temperatures of the atomic ensemble, we perform many cooling stages. First, a thermal rubidium gas is loaded into a 2D magneto-optical trap (MOT). This creates an atomic beam of ^{87}Rb atoms, which travel through a differential pumping to an intermediate chamber with ultrahigh vacuum. At this stage, a three-dimensional (3D) MOT is loaded, followed by a compressed MOT and molasses cooling, respectively. The atoms are then loaded into a magnetic trap generated by a quadrupole magnetic field. Using a microwave (MW) to transfer from trapped $|F = 2, m_F = -1\rangle$ to untrapped $|F = 2, m_F = -2\rangle$ hyperfine ground states, we perform a forced evaporation by sweeping the MW frequency to remove hot atoms from the trap. After that, the cold ensemble is loaded to a focused far-detuned dipole trap, and then a translation stage transports the atoms to the science chamber where the objective and optical lattice are located. In the science chamber, we load the atoms into a crossed optical dipole trap formed by blocking the retro-reflection of the horizontal lattice beams. A subsequent evaporation by lowering the trap depth further decreases the temperature of the ensemble. We transfer the atoms into $|F = 2, m_F = -2\rangle$ with a MW Landau-Zener sweep that provides a vertical force that cancels gravity using a vertical magnetic gradient. This keeps the atoms trapped at the center of the crossed dipole trap before loading into the vertical physics lattice, retro-reflected at the lower vacuum window, containing approximately $10 - 15$ 2D layers. We then transfer to the vertical pinning lattice with a smaller waist and simultaneously ramp the magnetic gradient to generate a Zeeman shift of $2\pi \times 4.5\,\text{kHz}$ between the adjacent layers with a spacing of 532 nm. In the next step, the so-called "slicing", we apply a narrow MW frequency sweep of $2\pi \times 2\,\text{kHz}$ to transfer only a single target layer to $|F = 2, m_F = -1\rangle$ and remove the remaining layers of $|F = 2, m_F = -2\rangle$ by a resonant push-out. The final evaporation step is performed by shifting the zero-field position of the quadrupole field away from the optical trap along the horizontal direction but vertically aligned to generate a maximum in-plane gradient. To increase the rethermalization rate during evaporation, a small trapping volume of a dimple trap is added by passing through the defocused objective. Lowering both the pinning lattice and dimple trap depths in the in-plane gradient results in the 2D ultralow temperature ensemble near a BEC with a tunable atom number upto 3000 atoms.

We then proceed to the next step of preparing one atom per lattice site, which is the essential starting point of all experiments performed in this dissertation. After preparing the ultracold ensemble, two horizontal optical lattices are adiabatically ramped up across the phase transition where the system changes from the SF to the MI phase [164, 165]. The ramp is a double s-shape with a slow change at the transition point until it reaches the atomic limit at a horizontal/vertical lattice depth of $40/60\ E_r$. After the ramp, we end up with a unity-filled atomic array of $200 - 2000$ atoms in $|F = 2, m_F = -1\rangle$ with a typical filling of $0.93 - 0.97$.

3.3.2 Potential engineering and single-site addressing

Up to now, the explained procedure in the previous section generates a spin-polarized state of $|F = 2, m_F = -1\rangle$ with the atomic array in a circular shape defined by the Gaussian trap potential of the vertical lattice. We can further add off-resonant light together with a digital micromirror device (DMD) to perform potential engineering [174, 175] and single-site spin addressing [35]. Details of the procedure and the underlying technology can be found in [157, 161, 162].

We engineer the optical potential using temporally incoherent light at a wavelength of 670 nm to illuminate the DMD. The light is then overlapped with the imaging path, passed through the objective lens, and is focused down to the atomic plane. Compared to fluorescence imaging at 780 nm, the objective must be shifted by approximately 15.7 µm so that the focus is in the atomic plane due to chromatic shifts.

To compensate for chromatic shifts, the objective must be shifted by approximately 15.7 µm when switching from fluorescence imaging at 780 nm to potential engineering light at 670 nm. Since the light is blue detuned from the D_2 transition, the light generates a repulsive potential onto the atoms. With DMD, we can engineer almost arbitrary patterns with spatially variable potential strengths, up to three times the onsite interaction potential U, during the SF-MI transition. Thereby, we can achieve consistently filled atomic arrays in a well-defined shape by lowering the entropy in a target region [174, 175].

Once the unity-filled atomic array is achieved, adding local control over the internal degrees of freedom of the atoms with single-site precision introduces numerous features for the experiments. For example, it can be used for initial state preparation, which is often employed in measurements discussed in this dissertation. To obtain this, a spatially programmable light pattern, generated by the same DMD, is projected to the atomic plane by the high-resolution objective. Starting from the spin polarized state of $|F = 2, m_f = -1\rangle$, the "tune-out" wavelength of 787.56 nm with σ^- polarization creates AC-Stark shifts on $|F = 2, m_F = -2\rangle$ whereas $|F = 2, m_F = -1\rangle$ is unaffected [35, 176]. The DMD generates differential AC-Stark shifts between the two states of up to $2\pi \times 200$ kHz. At the same time, a MW sweep, on-resonant with the differential shifts, is applied to only transfer the target atoms to $|F = 2, m_f = -2\rangle$. In the opposite way, applying a MW sweep on-resonant with the unshifted energy, can transfer the non-targeted atoms to $|F = 2, m_f = -2\rangle$ while the targeted atoms remain in $|F = 2, m_f = -1\rangle$. One challenge of this scheme is the relative phase drift between the projected light and the optical lattice phase. We address this issue by finding the lattice phase from the previous shots and feed-forward this to the projected on the DMD. Therefore, slow relative phase drifts due to temperature and alignment changes can be diminished.

3.3.3 Site-resolved fluorescence imaging and spin-selective detection

To detect the atomic distribution after an experiment, the horizontal lattices and the pinning lattice are simultaneously ramped up to a depth of $\approx 2000\, E_r$ per lattice. Then, optical molasses cooling and repumping on the D_2 transition in the $\sigma^+ - \sigma_-$ configuration along the horizontal axes and the vertical σ^+ beam are applied to the atoms. Due to light-assisted collisions [177–180], the imaging only has access to the parity of the atom number on a single site of the lattice. The large lattice depth freezes the dynamics of the atoms during the imaging. We collect the fluorescence light from the atoms using our high-resolution objective with a numerical aperture (NA) of 0.68 and image the atomic plane on the electron multiplying charge-coupled device (EMCCD). Afterward, a reconstruction algorithm [159, 162] yields the number of local occupations in the optical lattice. The resolution of the imaging system is approximately 700 nm, which is larger than the lattice spacing of $a_{\mathrm{lat}} = 532\,\mathrm{nm}$. However, the predetermined structure of the lattice still allows for a full reconstruction. Since cooling and repumping light scatters with all hyperfine states of atoms, the imaging detects atoms in both $|F = 1\rangle$ and $|F = 2\rangle$. We can selectively remove the atoms in $|F = 2\rangle$ using resonant push-out light on the D_2 transition, so that only the $|F = 1\rangle$ atoms are left for imaging. The $|F = 2\rangle$ atoms can be detected by applying a global MW transfer to flip the states before the resonant push-out.

3.3.4 Enlarging system size

Quantum simulation in optical lattices is often limited by the small available system size. A small system size restricts the dynamics to short timescales until the boundary of the system affects the main phenomena. The size of the array trapped in the optical lattices is given by the harmonic confinement of the Gaussian beam. An obvious way to increase system size is to increase the beam waist, so that the harmonic confinement is reduced. However, a higher power is required to retain the same trap depth when enlarging the beam. We use two different approaches for the horizontal and vertical lattices to achieve low confinement while using the same power budget. The upgrade, implemented during this dissertation, is described in detail as follows.

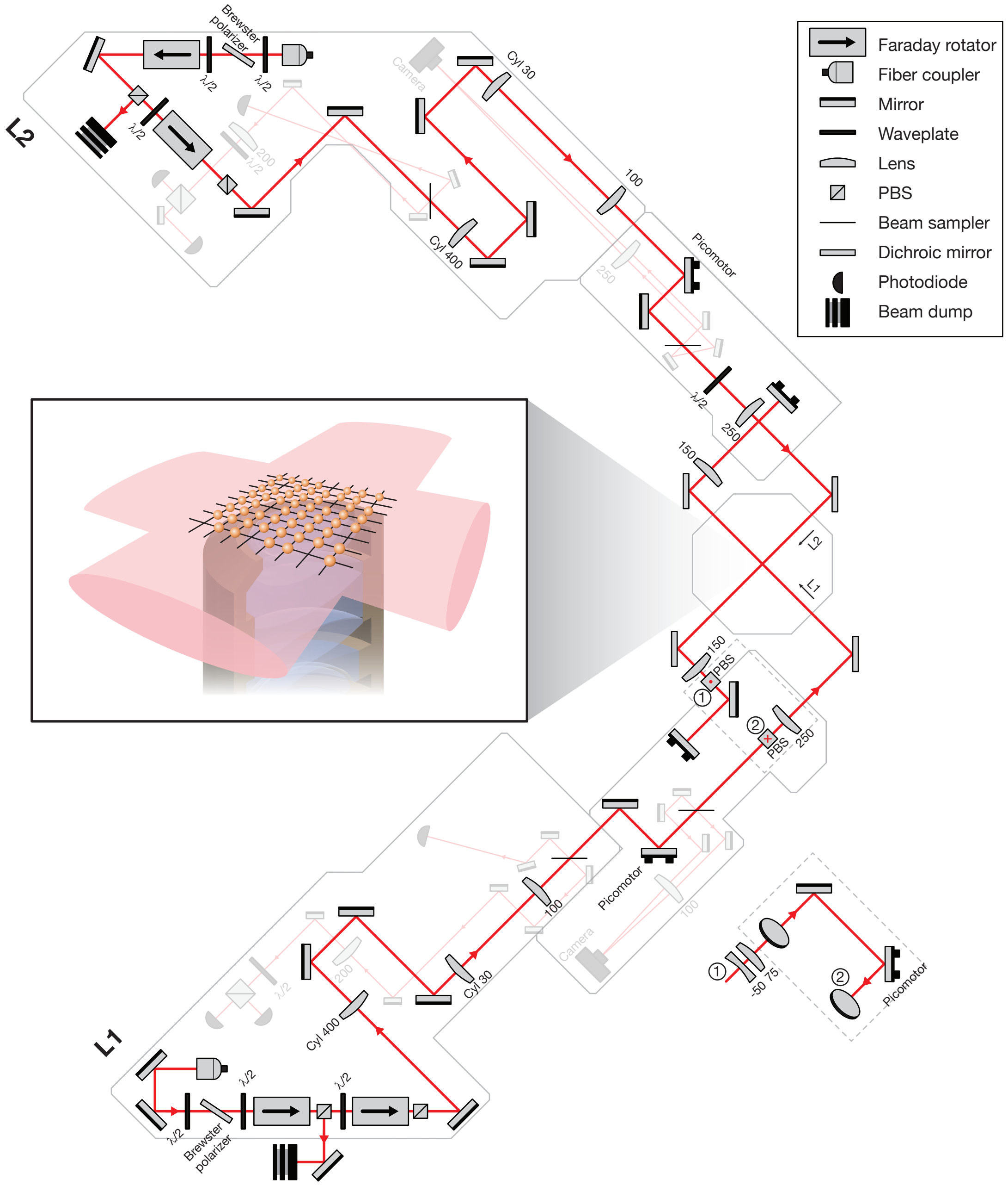

Figure 3.1: Optical layout of the horizontal lattices. The two horizontal lattices *L*1 (bottom) and *L*2 (top) are designed to generate an elliptic beam shape at the atomic position. Both beams are aligned orthogonal at the science chamber and are retro-reflected back to their original paths, forming a 2D periodic potential. The beams have a slight frequency difference, such that the two orthogonal optical lattice axes do not interfere. Changing to the folded scheme, the *L*1 is switched off while the polarization of *L*2 is tuned from horizontal to vertical linear polarization. The *L*2 beam, after entering the chamber, is altered to overlap with the incoming *L*1 beam path and is retro-reflected. The opaque optical components denote the primary optical lattice beam path, while the transparent optical components are used to monitor the power and position of the beams. The inset illustrates the elliptical beam shape with a size of 33 µm and 330 µm along the vertical and horizontal axis, respectively, forming the square optical lattices.

Horizontal lattice

For most of the experiments in our setup, we typically trap the atoms in a single horizontal plane, while the atoms in the other layers are removed. Since the vertical volume is insignificant, we introduce a strong ellipticity to the beam shape with a large waist along the horizontal axis. Therefore, the confinement in the horizontal plane is diminished without a strong intensity reduction. The horizontal beams originate from a 50 W laser source (Mephisto, Coherent), operating at a wavelength of 1064 nm. The beam is split into two paths for the two horizontal lattices (labeled $L1$ and $L2$) which are designed to have almost identical optical elements. Each beam path is frequency detuned by an acousto-optical modulator (AOM) before being guided to the experimental setup by a photonic crystal fiber (LMA-PM-15, ALPhANOV). Note that $L1$ and $L2$ do not interfere due to a frequency difference introduced by the AOMs. On the experimental table, a 20 mm lens (HFTLSQ-12-20PF1, OptoSigma) out-couples the beam with a circular beam waist of 500 µm. Two sets of Brewster polarizers and optical rotators (PAVOS 1010-1080nm (EOT.189.22223), EOTech) are used to block the retro-reflected light with a total isolation of 60 dB. Here, the polarization is set to the linear polarization along the horizontal axis. Then, a 400 mm and 30 mm cylindrical lens focus the beam along the horizontal and vertical axes respectively onto the same image plane before being collimated with a 100 mm lens. A focusing lens with a focal length of 250 mm focuses the beam into the chamber at the atomic position resulting in an elliptic shape with a waist of 330 µm and 33 µm along the horizontal and vertical axes, respectively. To form the optical lattice, a 250 mm lens in $4f$ configuration images the beam onto a mirror that retro-reflects the beam back with an identical shape. Picomotor actuated mounts are used for fine alignment of the beam to the atomic position. The optical layout of the horizontal lattices with respect to the science chamber are illustrated in Fig. 3.1. To compare with the previous horizontal lattice with a circular waist of 75 µm, our new cylindrical lattice has an area larger by a factor of two. Therefore, the maximum lattice depth reduces from 3000 E_r to 2000 E_r at the same laser power, which is sufficient to freeze the dynamics of the atoms during imaging.

With the same setup, we can switch from the non-interfering $L1$ and $L2$ to an interfering folded lattice scheme [162, 181] that uses only $L2$. This can be achieved by changing the polarization of $L2$ to linear polarization along the vertical axis using a half waveplate. The beam, after passing through the chamber, is routed to a telescope containing a 75 mm and a -50 mm lens to ensure that it maintains the same beam size for focusing it onto the atoms. The beam is then overlapped with the $L1$ optical path, which allows one to generate different optical lattice structures, see Sec. 3.3.5.

Vertical lattice

Unlike the horizontal lattices, the vertical lattice has to be enlarged symmetrically to reduce the confinement over the whole system. This causes a significant reduction of the lattice depth given the same laser power. In addition, the low confinement reduces the evaporation efficiency in the prior cooling step. Therefore, we set up a hybrid solution having two vertical lattices with different beam size. The "physics lattice" with a large beam waist is used when low confinement is required, such as for the SF-MI transition and when probing dynamics, where we usually operate at low lattice depth. The "pinning lattice" with a smaller waist is used when large confinement or large lattice depth is needed during the evaporation and the imaging process.

The laser setup is designed to deliver switchable full power from a single laser to both the physics and the pinning lattice. A 1064 nm laser (Mephisto, Coherent) with a power of 40 W is passed through a shear mode AOM (I-M080-2S2G-3-LV11, G&H) which is driven at a frequency of 80 MHz. This AOM is also used for intensity stabilization for the physics lattice. The $+1^{\text{st}}$ order from the AOM is sent to a telescope and then coupled to a fiber (LMA-PM-40, NKT) which afterward goes to the physics lattice optical beam path. Note that the LMA-PM-40 fiber required to be in a fixed and straight shape to avoid power loss after the fiber. The 0^{th} order from the same AOM is sent to a second AOM (3110-191, G&H), a telescope, and then coupled to a fiber (LMA-PM-15, ALPhANOV) for the pinning lattice. The second AOM, driven at a frequency of 110 MHz, is used for stabilizing the intensity of the pinning lattice. In this way, switching full power between the physics and pinning lattice can be controlled by the first AOM.

The fibers guide the beams to breadboards placed on top of the experimental chamber. These breadboards contain five different beam paths, see Fig. 3.2, that are combined before being sent to the atoms from the top:

- **The physics lattice (red):** a 40 mm lens (HFTLSQ-30-40PF1, OptoSigma) outcouples the beam from the LMA-PM-40 fiber at the second layer of the breadboards, resulting in a beam waist of 500 µm. After that, two sets of Brewster polarizers and optical isolators (PAVOS 1010-1080nm (EOT.189.22223), EOTech) provide isolation of 60 dB before the beam is sent down to the lower breadboard. The beam is then sent through a telescope containing lenses with focal lengths of 150, 100, and 100 mm, respectively, before being focused down to 350 µm at the atom position with a 400 mm lens. The bottom window, ≈ 5 mm below the atoms, is coated for high reflection at the wavelength of 1064 nm, therefore, the physics lattice is retro-reflected to the same path.

- **The pinning lattice (orange):** the beam from the LMA-PM-15 fiber is collimated with a 20 mm lens (HFTLSQ-12-20PF1, OptoSigma), resulting in a beam waist of 500 µm. The beam passes through an optical isolator (FI-1060-5TI, Linos) with 60 dB isolation, and then through a telescope with 50, 100 and 150 mm lenses to increase the beam waist to 1.8 mm. The pinning lattice has vertical polarization, orthogonal to the physics lattice, allowing it to be combined with the physics lattice using a Brewster polarizer.

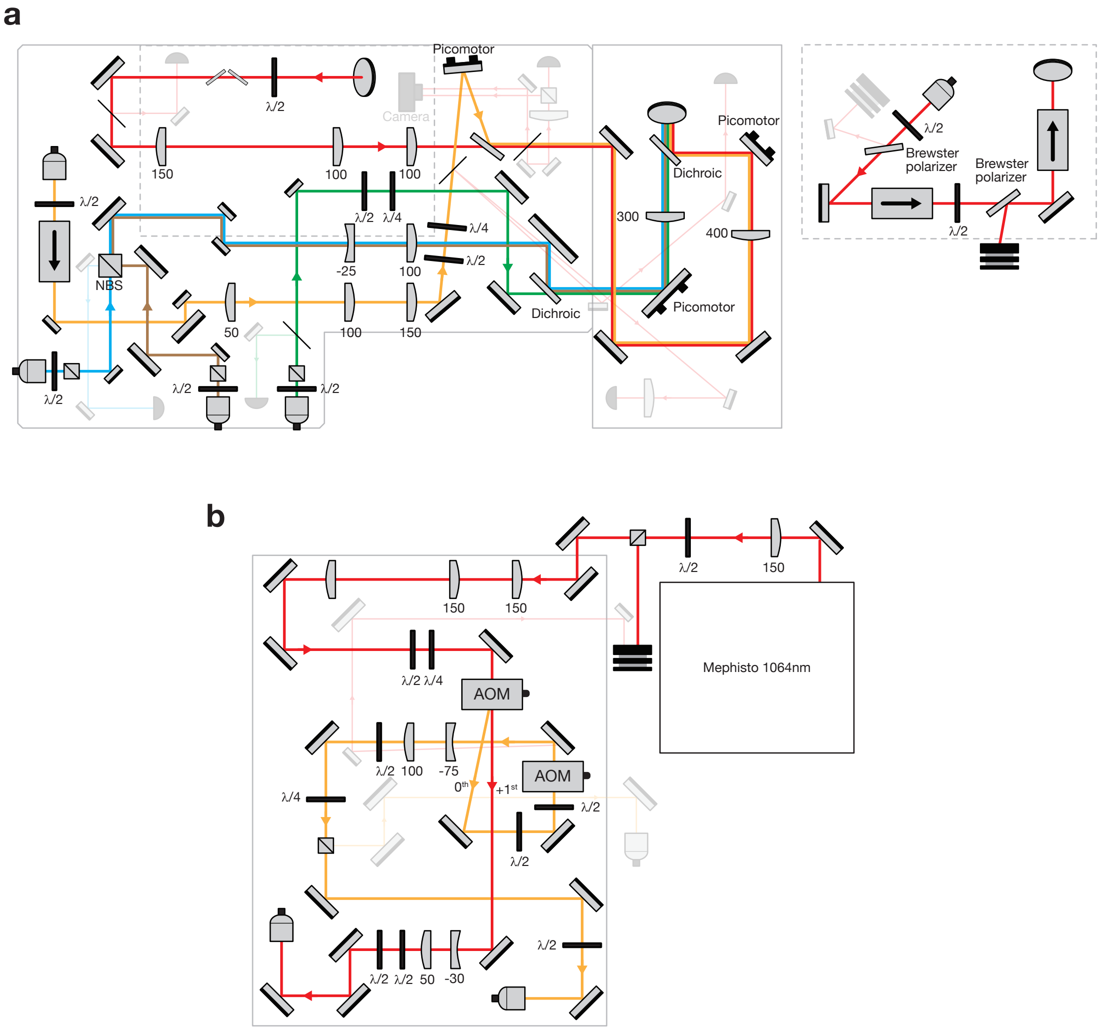

Figure 3.2: Optical layout of the vertical lattices. (**a**) The breadboards contain the physics lattice beam (red), the pinning lattice beam (orange), the push beam (blue), the probe beam (brown), and the vertical Raman beam (green). The 1064 nm physics and pinning lattices are overlapped on a Brewster polarizer with orthogonal polarization and focused on the atoms with waists of 350 µm and 75 µm, respectively. The 780 nm push and probe beams, used for removing $|F = 2, m_F = -2\rangle$ and sending weak light, respectively, are overlapped using a non-polarizing beam splitter (NPBS) before being combined with the vertical lattices with a dichroic mirror. The 795 nm vertical Raman beam is combined with the push and probe beams with a dichroic mirror. (**b**) The breadboard for distributing the 1064 nm laser to the physics and pinning lattices. The 1^{st} order of the first AOM is sent with full power to the physics lattice fiber. To switch from the physics to the pinning lattices, the first AOM is switched off, so that the 0^{th} order passes through the second AOM and the pinning lattice fiber with full power. The opaque optical components denote the primary optical lattice beam path, while the transparent optical components are used to monitor the beams' power and position.

Finally, the 400 mm lens focuses the beam to a waist of 75 µm onto the atoms, after which it is retro-reflected by the bottom window.

- **The push beam (blue) and the probe beam (brown):** the push beam, used for removing $|F = 2\rangle$ atoms, and the probe beam, used for sending weak light, have a wavelength of 780 nm. Both beams are combined with a 50 : 50 NPBS before passing through a telescope of 250 and -200 mm lenses. The beams are focused with a 300 mm lens and combined with the physics and pinning lattice by a dichroic mirror (FF930-SDi01, Semrock). The beam waists of the push and probe beam in the atomic position are 55 and 20 µm, respectively.
- **The vertical Raman beam (green):** the Raman beam at a wavelength of 795 nm is planned for driving $D1$ transition of the atoms. The beam is overlapped with the push and the probe beams by a dichroic mirror (LPD02-785RU, Samrock). After focusing with the 300 mm lens, the beam waist on the atomic position is 50 µm.

When ramping across the SF-MI transition to achieve unity-filled MI, the atoms will explore and form the MI at the local potential minima. Therefore, the cloud shape and size are strongly influenced by the beam shape and harmonic confinement of the vertical lattice beam. For example, an ideal Gaussian beam results in a circular MI shape. However, we found that the physics lattice beam with low confinement has speckles caused by disorder due to scattered particles on the bottom window. These speckles, with a typical size of 10 µm, are smaller than the confinement of the physics lattice, resulting in many local potential minima with an energy scale comparable to that of the BHM. This leads to the formation of multiple MIs with the same size as the speckles, see Fig. 3.3a. In contrast, the pinning lattice has stronger confinement than the speckles due to the smaller beam waist. The pinning lattice confinement remains the dominant factor in the potential, ensuring a circular MI shape. To overcome this speckles issue, we use the DMD to engineer the potential on top of the physics lattice potential to realize an almost homogeneous system with the remaining speckles potential smaller than the interaction energy scale U, see Sec. 3.3.2.

3.3.5 Tunable lattice geometries

The typical optical lattices in our setup are created by three retro-reflecting beams, where the frequencies of each lattice axis differ by approximately 100 MHz to prevent interference between the different axes. The lattice beams have a wavelength of 1064 nm resulting in 3D optical lattices with a lattice spacing of $a_{\mathrm{lat}} = 532$ nm. In this dissertation, we call this geometry the "square lattice" since the lattice structure orients the optical lattice beams. For a novel approach, we fold the horizontal lattice beam $L2$ into the orthogonal axis of $L1$ before retro-reflecting it back through the same path, thus realizing a bow-tie lattice [182], as discussed in Sec. 3.3.4. In this configuration, the interference of the two arms forms a square lattice oriented at 45 degrees with respect

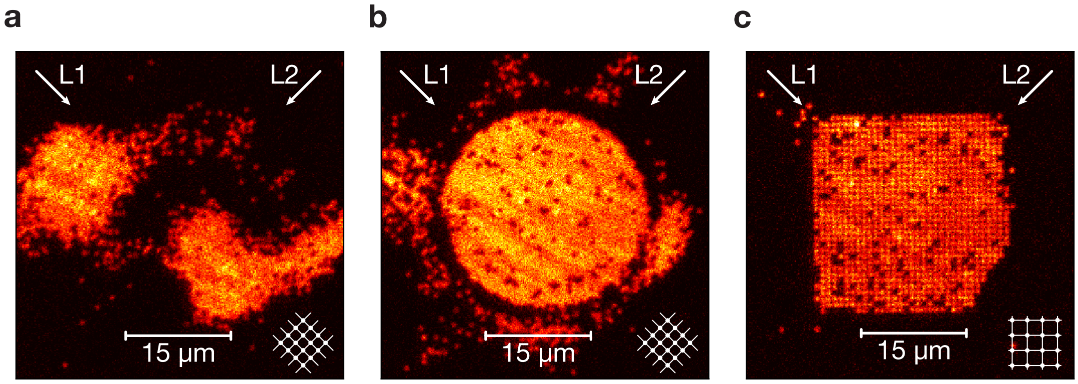

Figure 3.3: Fluorescence images of the Mott insulator. (**a**) MI in the physics lattice without any potential correction. The MI forms in separate sectors where the local potential minima are. This disorder potential is caused by the scattering of scattered particles in the bottom window. (**b**) MI of around 1500 atoms in the square lattice. The square lattice with a lattice spacing of $a_{\text{lat}} = 532\,\text{nm}$ is formed by two orthogonal independent retro-reflected beams. The orientation of the lattice structure aligns with the direction of the beam. (**c**) MI of around 1000 atoms in the diagonal lattice. The diagonal lattice is generated by a folded scheme, resulting in a 45° angle with respect to the beam direction, with a lattice spacing of $a_{\text{lat}} = 752\,\text{nm}$. The shape of the MI in **b** and **c** is engineered by a repulsive potential of 670 nm light projected to the DMD before focusing on the atoms with the objective.

to the beams' direction, with a lattice spacing of $a_{\text{lat}} = \sqrt{2} \cdot 532\,\text{nm} = 752\,\text{nm}$, while the vertical lattice spacing remains unchanged. A detailed analysis of the structural phase stability of both lattice configurations is discussed in [162]. We refer to this folded scheme as the "diagonal lattice" since the lattice structure orients diagonally compared to the square lattice. Figs. 3.3 b,c show fluorescence images of MIs in the square and diagonal lattice, respectively. With the imaging resolution of 700 nm, the square lattice with the spacing of $a_{\text{lat}} = 532\,\text{nm}$ cannot be resolved during imaging. The diagonal lattice has a larger spacing of $a_{\text{lat}} = 752\,\text{nm}$, causing a clear separation between each lattice site. The square lattice is predominantly used in most measurements in Chapter 4, while the diagonal lattice is used in Chapter 5.

3.4 Excitation of Rydberg *S* and *P* states

Exciting atoms from ground states to a target Rydberg state can provide long-range and strong interactions that are essential for quantum science [82]. There are several schemes that have been used for Rydberg excitation [59, 183–185]. We will focus on the simplest schemes of using purely optical excitation. First, Rydberg single-photon and two-photon excitation schemes will be compared, then experimental benchmarks of both excitation schemes in our setup are discussed.

Due to the dipole selection rules, ground S states can be directly excited to Rydberg P states with a single-photon excitation scheme, see Fig. 3.4a. In contrast, exciting from ground S states to Rydberg S states requires a two-photon excitation scheme, which is typically detuned from an intermediate state, see Fig. 3.4b. Both schemes have various advantages and disadvantages, as well as technical and fundamental limitations. For ^{87}Rb, the single-photon excitation scheme is in the ultraviolet (UV) regime with a wavelength of 298 nm. Such a laser system faces many challenges, such as strong material degradation, unavailability of suitable fibers, and high loss at optical components. In addition, the Rydberg P states have anisotropy and are more sensitive to external perturbations than the Rydberg S states, therefore, experimental parameters must be carefully selected [186]. However, the single photon coupling provides larger achievable Rabi frequencies by up to an order of magnitude compared to the two-photon coupling. This is essential for the Rydberg dressing interaction discussed in Chapter 5 because the dressed interaction strength scales with $V \propto \Omega^4$. In contrast, the two-photon excitation scheme usually features more accessible wavelengths of 780 nm + 480 nm or of 420 nm + 1013 nm depending on the chosen intermediate state. For the limit of large intermediate state detuning $\Delta \gg \Omega_r, \Omega_b$, the intermediate can be eliminated, resulting in an effective two-level system [159, 187, 188] with an effective Rabi frequency of

$$\Omega_{\text{eff}} = \frac{\Omega_r \Omega_b}{2\,|\Delta|}. \tag{3.4}$$

Usually, the limitation to achieving high effective Rabi frequency is the upper transition Ω_b since its dipole matrix coupling is much smaller for the lower transition. Moreover, the different coupling strength between the upper and lower transition causes an AC-Stark shift on the Rydberg transition that can be described as an effective detuning

$$\delta_{\text{eff}} = \delta + \frac{\Omega_b^2}{4\,(\Delta - \delta)} - \frac{\Omega_r^2}{4\Delta}. \tag{3.5}$$

Therefore, one has to take into account this AC-Stark shift when the lower and upper transitions have different coupling strength. The effective dephasing Γ_{dep} of both schemes can be described by

$$\Gamma_{\text{dep}} = \frac{1}{2}\gamma_{\text{dep}} + \frac{3}{4}\Gamma_{\text{dec}}, \tag{3.6}$$

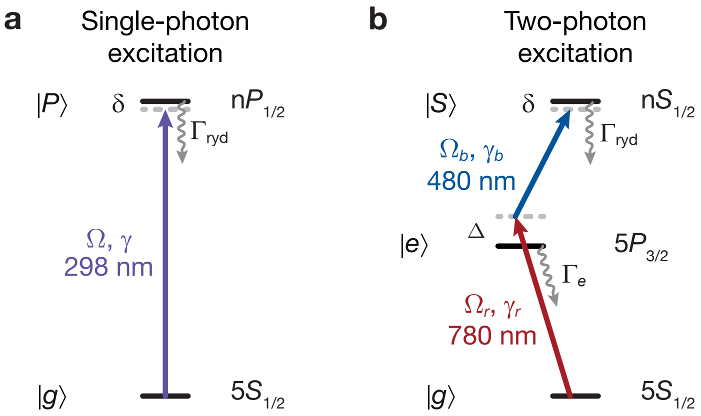

Figure 3.4: Rydberg excitation schemes of ^{87}Rb. (**a**) Single-photon excitation to Rydberg *P* states use a wavelength of 298 nm. It has a high Rabi frequency coupling. The main dephasing sources are laser noise and Rydberg decay. (**b**) Two-photon excitation to Rydberg *S* states use two lasers at wavelengths of 780 nm and 480 nm that off-resonantly detuned from the intermediate state $|e\rangle$. The effective Rabi frequency $\Omega = \Omega_r\Omega_b/2\Delta$ is usually limited by the upper transition due to smaller dipole matrix coupling and available laser power. The dephasing sources include the off-resonant scattering from the intermediate state $\Gamma_e\Omega_r^2/4\Delta^2$ in addition to laser noise and Rydberg decay.

where γ_{dep} contains all dephasing sources and Γ_{dec} all sources of decoherence. The single-photon scheme, see Fig. 3.4a, has $\gamma_{\text{dep}} = \gamma$ and $\Gamma_{\text{dec}} = \Gamma_{\text{ryd}}$. In comparison, the two-photon scheme, see Fig. 3.4b, has $\gamma_{\text{dep}} = \Gamma_e\Omega_r^2/4\Delta^2 + \gamma_r + \gamma_b$ and $\Gamma_{\text{dec}} = \Gamma_e\Omega_b^2/4\Delta^2 + \Gamma_{\text{ryd}}$. These show that the two-photon excitation scheme has additional dephasing and decoherence from off-resonant scattering of the intermediate state compared to the single-photon excitation scheme. This can be diminished by operating with larger detuning. Higher laser power is then required to keep the effective two-photon Rabi frequency the same.

In our experimental setup, we have both excitation schemes available. By locally preparing the atoms in different hyperfine ground states and then using our addressing technique described in Sec. 3.3.2, we can simultaneously address the Rydberg *S* and *P* states. Therefore, we can exploit the strong interaction of Rydberg *S* and *P* states, which is used in the experiments presented in Chapter 4.

3.4.1 Single-photon excitation scheme

The direct Rydberg excitation scheme, using a single-photon transition, can directly couple ground states to Rydberg states. This solution eliminates the scattering of the intermediate state, and significantly decreases the decoherence rate of the system. With a large dipole matrix coupling, single-photon excitation has a large Rabi frequency coupling, which is beneficial for the Rydberg dressing experiments presented in Chapter 5. Moreover, it allows access to Rydberg P states, which are inaccessible with the two-photon excitation scheme, opening various research directions [189–192]. The UV laser has been developed in several groups [192–198] but recently also high-power laser systems have become commercially available. In this section, we briefly introduce our UV laser setup focused on frequency and power stabilization protocols, spectroscopy of Rydberg P states, driving Rabi oscillation, and the effect of stray electric charges on Rydberg states.

Setup and operation of the single-photon excitation laser

Due to an unavailability of high-power commercial UV lasers at that time, we constructed a home-built laser system to meet our specific requirements. The laser system had been built together with Simon Hollerith and Simon Evered. The design and optical layout of the laser are discussed in details in [113]. The laser setup involves frequency quadrupling a laser source operating at a wavelength of 1192 nm using two stages of bow-tie type second harmonic generation (SHG) cavities [198, 199]. An external cavity diode laser at 1192 nm is frequency-referenced to an ultra-low expansion (ULE) cavity with a free-spectral range of 1496.66 MHz. A frequency-tunable radio frequency (RF) source up to 750 MHz generates tunable sidebands via an electro-optic modulator (EOM). An additional fixed 15 MHz RF source is combined with the tunable RF source to create an error signal for locking the sideband of the laser to the ULE cavity. Thus, the frequency of the 1192 nm laser is stabilized to the ULE cavity with tunable frequency by varying the RF during experiments. The 1192 nm is then used to seed a Raman fiber amplifier, amplifying the optical power up to 6 W. Next, the first SHG cavity generates light at a wavelength of 596 nm with up to 3 W of optical power. The beam is sent to an AOM and then to the second SHG cavity, thus achieving a 298 nm laser with a maximum optical power of 1 W. Both SHG cavities are locked using the Pound-Drever-Hall (PDH) technique [200] by modulating the current of the 1192 nm laser with a 20 MHz RF. The reflected light from the cavity is collected by photodiodes and mixed with the 20 MHz RF reference signal to generate the PDH error signal used for cavity locking. In our setup, the modulated sideband of the first SHG cavity is carried by the 596 nm laser and is large enough to generate the PDH error signal for the second SHG cavity without requiring additional components. Two mirrors in each SHG cavity are mounted with piezo stacks for fast and slow modulation at a resonant frequency around 500 kHz and 50 kHz, respectively [113]. To lock the SHG cavity with the error signal, a field programmable gate array (FPGA) (STEMlab 125-14, Red Pitaya) processes the error signal digitally and applies a proportional-integral-derivative (PID) filter which is then feedbacked to the cavity piezo stacks. FPGAs and microcontrollers have become popular to employ as feedback controllers due to being universally applicable and easily connectable to laboratory infrastructure [198, 201–203]. The

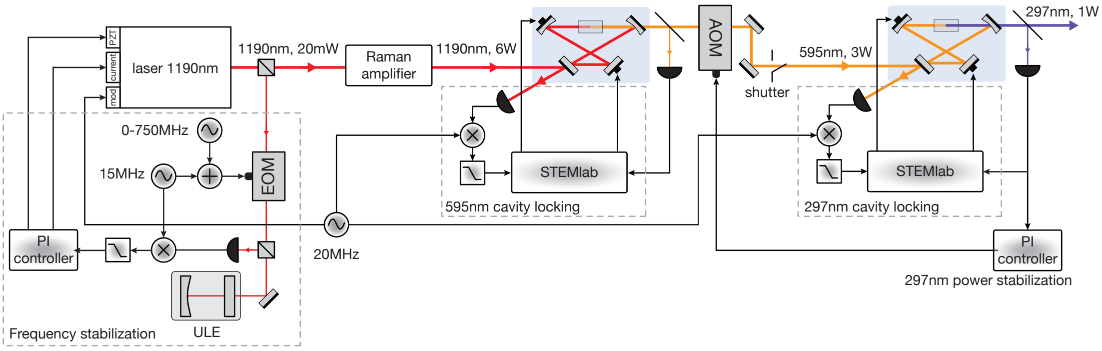

Figure 3.5: Schematic of the 298 nm **laser and locking scheme.** The 1192 nm external cavity diode laser is frequency stabilized to an ULE cavity and seeds the Raman amplifier, which generates up to 6 W at 1192 nm. Two sets of the doubling cavities sequentially double the frequency, yielding a 298 nm laser with a power up to 1 W. Each doubling cavity is stabilized using the PDH technique with an FPGA for PID feedback. The first cavity continuously operates in locked mode. The second cavity is locked a few tens of milliseconds before use. The 298 nm laser is power stabilized by altering the input power before entering the second cavity by PI feedback to the AOM in the 596 nm path.

STEMlab locking device has a limited analog output voltage range of ±1 V, which is insufficient to drive the piezo stacks. Therefore, two outputs from the locking device are amplified with inverting operational amplifiers (OP07C) with gains of 5.6 and 10 for the fast and slow feedback channels, respectively, before driving the cavity piezo stacks. The feedback bandwidth is currently limited by the operational amplifiers to around 30 kHz and 750 Hz for the fast and slow channels. Future improvements could be achieved by choosing faster operational amplifiers. The STEMlab locking devices offer several advantages, including automatic cavity relocking and remote operation capabilities. A beam sampler positioned at the cavities' output monitors the output power and initiates automatic relocking when the cavity is scanned to its resonance or loses lock. An open-source software allows for tuning PID parameters and configuring the automatic relocking threshold [204]. Throughout the operation of the laser setup, the first SHG cavity consistently operates in a locked mode, ensuring a stable output at 596 nm. In contrast, the UV lasers are known to cause degradation of optics and nonlinear crystals [205–207]. Therefore, a shutter blocks the 596 nm light going to the second SHG cavity. Just before the UV laser is required, the shutter is opened, allowing the second cavity to autolock a few tens of milliseconds beforehand. Once the second cavity is locked, we stabilize the output power using a photodiode and provide feedback to the AOM in the 596 nm path to control the incoming power into the cavity. An AOM in the 298 nm path is used for creating fast pulses with a rise

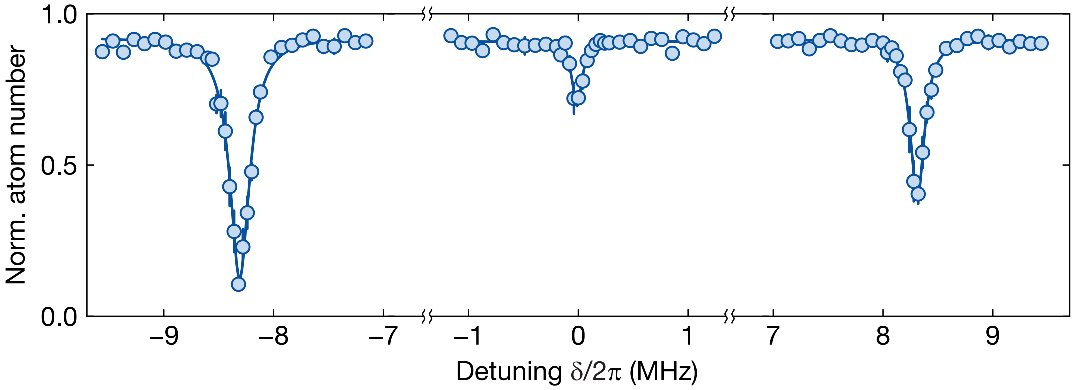

Figure 3.6: Rydberg resonances of $30P_{3/2}$ state. Rydberg spectroscopy of the $30P_{3/2}$ state using a MI trapped in the optical lattices and initialized in $|F = 2, m_F = -2\rangle$. The three Rydberg resonances of $m'_J = [-3/2, -1/2, 1/2]$ have linewidths of $2\pi \times$ [216(9), 111(13), 154(6)]kHz, respectively. The resonances are spaced equally corresponding to the Zeeman shifts of the magnetic field. With the ground state of $m_J = -1/2$, the $\sigma^+ - \sigma^-$ polarization causes a strong coupling to the Rydberg state of $m'_J = -3/2$ and $m'_J = 1/2$, whereas the $m'_J = -1/2$ coupling is weaker.

time of 100 ns. Finally, the 298 nm laser is sent to a pinhold for a spatial mode cleaning before focusing onto the atoms with a maximum power of 500 mW.

Single-photon Rydberg spectroscopy

We spectroscopically probe Rydberg P states by observing atomic loss while the atoms are trapped in the optical lattices. The UV laser is aligned within the atomic plane, while the bias magnetic field is perpendicular to the plane. The polarization of the UV laser is linear and perpendicular to the magnetic field, causing a $\sigma^+ - \sigma^-$ polarization configuration. The MI of around 100 atoms, initialized in $|5S_{1/2}, F = 2, m_F = -2\rangle$ with a hyperfine Zeeman sublevel of $m_J = -1/2$, can couple only to $m'_J = -3/2$ and $m'_J = 1/2$ with σ^- and σ^- polarization, respectively. To minimize power broadening, only very low power is applied for 0.5 ms. Fig. 3.6 presents the $30P_{1/2}$ Rydberg resonance of $m'_J = -3/2$, $m'_J = -1/2$, and $m'_J = 1/2$ where the $m'_J = -1/2$ coupling is diminished compared to the other states. The frequency difference between each resonance of $\Delta_z = 2\pi \times 8.31(1)$ MHz matches the expected Zeeman energy splitting of the set magnetic field. The extracted full width at half maximums (FWHMs) are $2\pi \times 216(9)$ kHz, $2\pi \times 111(13)$ kHz, and $2\pi \times 154(6)$ kHz for $m'_J = -3/2$, $m'_J = -1/2$, and $m'_J = 1/2$, respectively. The width of the resonances is still dominated by the power broadening of the collectively enhanced coupling for many atoms, as seen in Sec. 3.4.2.

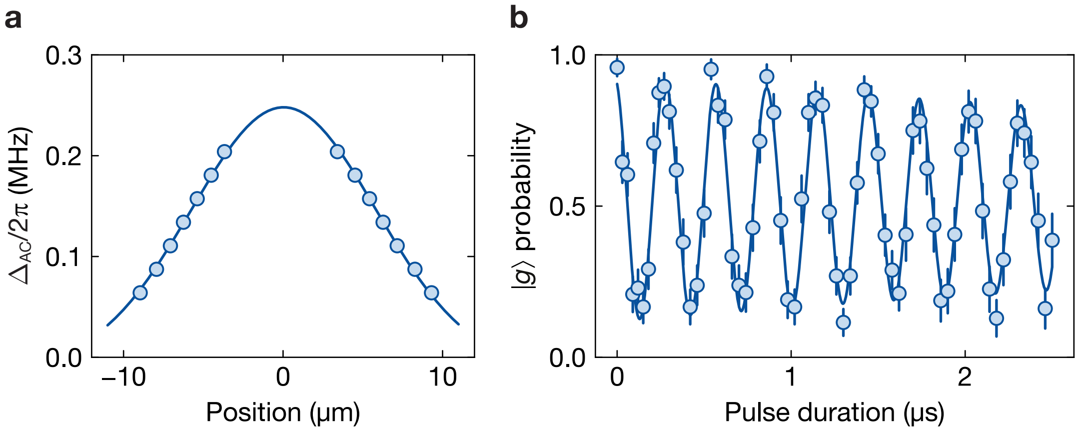

Figure 3.7: Calibration of the 298 nm **laser and single atom Rabi oscillations.** (**a**) The off-resonant 298 nm laser causes a spatial AC-Stark shift on the ground state, which can be measured using MW spectroscopy. The spatial AC-Stark shift is employed to align the laser in the center of the atomic cloud and to calibrate the Rabi frequency and the beam waist of the laser. (**b**) Single atom Rabi oscillation to the $36P_{1/2}$ state. The measured Rabi frequency is $\Omega = 2\pi \times 3.42(1)$ MHz with an exponential decay of 9(3) μs.

Calibration of the UV Rabi frequency and beam waist

The AC-Stark shift of off-resonant light can be used to determine the Rabi frequency of the single-photon excitation transition, as well as laser beam alignment. The energy shift of the ground state atoms is given by $\Delta_{AC} = \Omega^2/4\Delta$ for a large detuning compared with the Rabi frequency $\Delta \gg \Omega$. Therefore, it induces a differential shift between two-ground states which can be probed by MW spectroscopy. Moreover, by expanding the atomic could to a large size, we can spatially resolve the shift due to the intensity gradient of the beam shape and use this to align the beam to the atoms. The UV laser is detuned by $\Delta = 2\pi \times 720$ MHz and $2\pi \times 703$ MHz from $|30P_{3/2}, m'_J = 3/2\rangle$ and $|30P_{3/2}, m_J = -1/2\rangle$ for σ^+ and σ^- polarization, respectively. We expand the atomic cloud in the 2D plane to larger than 20 μm before measuring the spatial differential shift of the ground states $|F = 2, m_F = -2\rangle \leftrightarrow |F = 1, m_F = -1\rangle$. The resonance appears as two lines along the beam propagation between the beam center, see Fig. 3.7a. Here, these two resonance lines are used to center the beam along the in-plane direction, while the vertical direction is optimized for a maximum energy shift. With that, we extracted a maximal Rabi frequency of $\Omega = 2\pi \times 23.7(5)$ MHz and a beam waist of 11.6(6) μm from a Gaussian fit function.

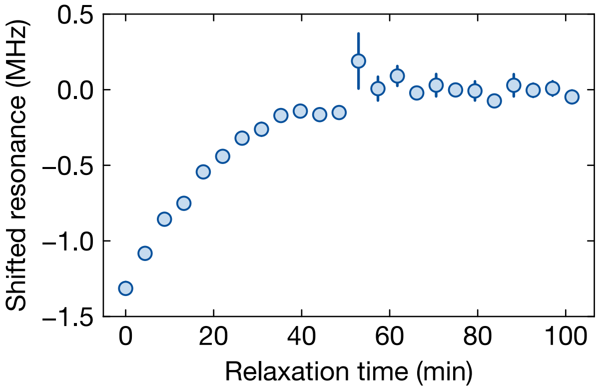

Figure 3.8: Influence of surface effects on Rydberg resonances. The resonance of the Rydberg $44P_{3/2}$ state is shifted after illumination of the 480 nm laser, which hits the bottom window, for more than 30 s. Once the 480 nm laser is turned off, the Rydberg resonance slowly drifts back to its original position. The drift is most likely caused by the accumulation path charges on the dielectrically coated window, located about 5 mm from the atomic position.

Single-photon Rabi oscillation

After identifying the Rydberg resonances and aligning the beam to the atoms, we drive a single-photon Rabi oscillation to Rydberg the $36P$ states. The single atom Rabi oscillation of the $|5S_{1/2}, F = 2, m_F = -2\rangle \leftrightarrow |36P_{1/2}, m'_J = -1/2\rangle$ transition is shown in Fig. 3.7b. We extract a Rabi frequency of $\Omega = 2\pi \times 3.42(1)$ MHz with an exponential decay time of $\tau = 1/\Gamma_{\text{dep}} = 9(3)$ µs. Considering only the laser linewidth γ and the decay of the Rydberg state Γ_{ryd} as sources of dephasing for Eq. (3.6), we find a maximum upper bound for the laser linewidth of $\gamma = 2\pi \times 30$ kHz. Furthermore, the quality factor, the ratio of coherent versus incoherent processes, of $Q = \Omega/\Gamma_{\text{dep}} = 193$ is larger than the two-photon excitation scheme, see Sec. 3.4.2.

Influence of surface effects on Rydberg resonance

Rydberg states are highly sensitive to external fields due to their large electric dipole moment. This makes them a good candidate for magnetic and electric sensors [87, 90]. However, any uncontrolled field or stray fields from nearby components can affect measurements and Rydberg state properties. We observe stray field effects through the resonance drift of Rydberg P state, see Fig. 3.8. Here, the resonance of $|44P_{3/2}, m_J = 3/2\rangle$ significantly shifts after the 480 nm laser is turned on for more than 30 s. By spectroscopically probing the resonance over time, we observe the Rydberg resonance to slowly relax to a stable point. This could be caused by accumulation of patch charges [208] on the dielectric surface of the bottom window, as our optical lattice position is located 5 mm away from the window. Simultaneously operating the single-photon and two-photon excitation lasers might encounter this issue. Nevertheless, the resonance drift is slow and only happens after long illumination times of the 480 nm laser. Operating with periodic sequences and short laser pulses should thus not affect the Rydberg resonances.

3.4.2 Two-photon excitation scheme

The commonly used scheme to optically excite alkali atoms to Rydberg S states involves two-photon excitation via an off-resonant intermediate state. For rubidium, there are two possible intermediate states accessible with reasonable optical power. The first intermediate state $5P_{3/2}$ requires lasers at a wavelength of 780 nm to couple $5S_{1/2} \leftrightarrow 5P_{3/2}$ and 480 nm to couple $5P_{3/2} \leftrightarrow n'S_{1/2}$, where n' is the principal quantum number of the targeted Rydberg state. This scheme is frequently used because 780 nm is usually used for standard laser cooling. However, off-resonant scattering from the intermediate state requires a large detuning and a high coupling strength of the 480 nm transition to maintain the same two-photon Rabi coupling. Therefore, the alternative intermediate state $6P_{3/2}$ is also often used [64, 209, 210]. The required wavelengths are 420 nm for $5S_{1/2} \leftrightarrow 6P_{3/2}$ and 1013 nm for $6P_{3/2} \leftrightarrow n'S_{1/2}$. The advantages of this scheme are reduced intermediate state scattering and significantly higher optical power available for the 1013 nm transition.

In this dissertation, we use the first scheme to couple a ground state $|5S_{1/2}, F = 2, m_F = -2\rangle$ with a 780 nm (lower coupling) laser of σ^- polarization to the intermediate state $|5P_{3/2}, F = 3, m_F = -3\rangle$. Then, a 480 nm laser of σ^+ polarization couples the intermediate state to the Rydberg states $|n'S_{1/2}, m'_J = -1/2, m'_I = -3/2\rangle$ (upper coupling), with a typical used principle quantum number of $n = 30 - 45$. This choice of "stretched" states ensures maximum coupling and is insensitive to the magnetic field due to the identical angular momentum projection of $m_J = m'_J = -1/2$ and $m_I = m'_I = -3/2$.

Two-photon Rydberg spectroscopy

To perform spectroscopy of the Rydberg S state with a two-photon excitation, we prepare a single atom or unity-filled MI trapped in the diagonal optical lattice. The atoms are initialized in $|F = 2, m_F = -2\rangle$ with a bias magnetic field of $B_z = 30G$, aligned perpendicular to the atomic plane. The intermediate state detuning is set to $\Delta = 2\pi \times 200\,\text{MHz}$. The 480 nm laser is first turned on and sent to the atoms from the bottom through the objective with a Rabi frequency of $\Omega_b = 2\pi \times 20.2\,\text{MHz}$. Subsequently, the 780 nm laser is applied along the same direction with the same Rabi frequency for a duration of 4 µs, which is longer than the two-photon Rabi oscillation timescale. By varying the 480 nm laser frequency, a dip in the detected atom number indicates resonances to the Rydberg state. Fig. 3.9 shows a Rydberg resonance of $|30S_{1/2}, m_J = -1/2\rangle$ for a single atom and unity-filled MI of around 100

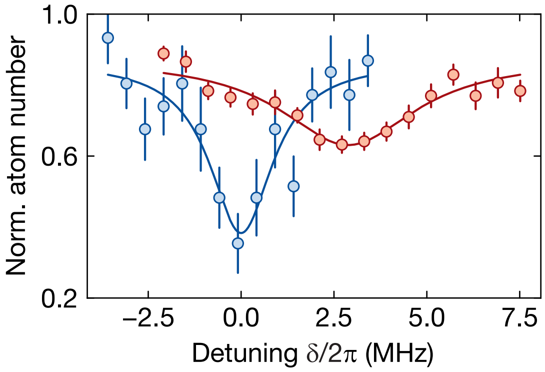

Figure 3.9: Rydberg resonance of the $30S_{1/2}$ state. Rydberg spectroscopy of the $|5S_{1/2}, F = 2, m_F = -2\rangle \rightarrow |30S_{1/2}, m_J = -1/2\rangle$ transition starting with a single atom (blue) or MI (red) trapped in the optical lattice. The resonance of a single atom (blue) has a width of $2\pi \times 2.0\,\mathrm{MHz}$. Initiate with a MI (red), the resonance shifts by $2\pi \times 2.9\,\mathrm{MHz}$ and has a broadened width of $2\pi \times 4.5\,\mathrm{MHz}$, indicating a Rydberg interaction induced shift and enhanced coupling.

atoms. The FWHM is approximately $2\pi \times 2.0\,\mathrm{MHz}$ for a single atom, which is larger than the expected two-photon Rabi frequency of $\Omega = 2\pi \times 1.0\,\mathrm{MHz}$. This discrepancy could come from imperfect preparation of single atoms, where many atoms may remain within the blockade radius. This results in Rydberg interaction-induced energy shifts and collectively enhanced coupling, as also observed in [105]. For the MI, we observed a shifted resonance of $2\pi \times 2.9\,\mathrm{MHz}$, which features a broader width of $2\pi \times 4.5\,\mathrm{MHz}$, which is a factor of 4.5 times larger than the expected single particle width. Focusing on width broadening, we consider the enhanced Rabi frequency of $\sqrt{N}$ factor [68, 134, 211], where N is the atom number with in the blockade radius. Taking into account approximately 20 atoms within the blockade radius, we can compare using the theoretical expectation for the C_6-coefficient of $C_6 = h \times 26\,\mathrm{MHz} \cdot \mu\mathrm{m}^6$ for $|30S_{1/2}, m_J = -1/2\rangle$ and a two-photon Rabi frequency of $\Omega = 2\pi \times 1.0\,\mathrm{MHz}$, which gives an estimated blockade radius of $r_b = 2.9\,\mu\mathrm{m}$. This corresponds to approximately 17 atoms in the blockade radius, in good agreement with the measurements.

Two-photon Rabi frequency calibration

Here, we present a method for calibrating the Rabi frequency of the $5S_{1/2} \leftrightarrow 5P_{3/2}$ (lower coupling) and the $5P_{3/2} \leftrightarrow nS_{1/2}$ (upper coupling) transitions. The lower coupling calibration is based on light-induced AC-Stark shifts due to off-resonant coupling. We measure the energy shift of the ground state atoms while applying an off-resonant 780 nm laser, which is given by $\Delta_{AC} = \Omega_r^2/4\Delta$. We start with atoms in $|F = 2, m_F = -2\rangle$ and illuminate them with the laser detuned by $\Delta = 2\pi \times 742\,\mathrm{MHz}$ from the $|5S_{1/2}, F = 2, m_F = -2\rangle \leftrightarrow |5P_{3/2}, F = 3, m_F = -3\rangle$ transition. Simultaneously, we

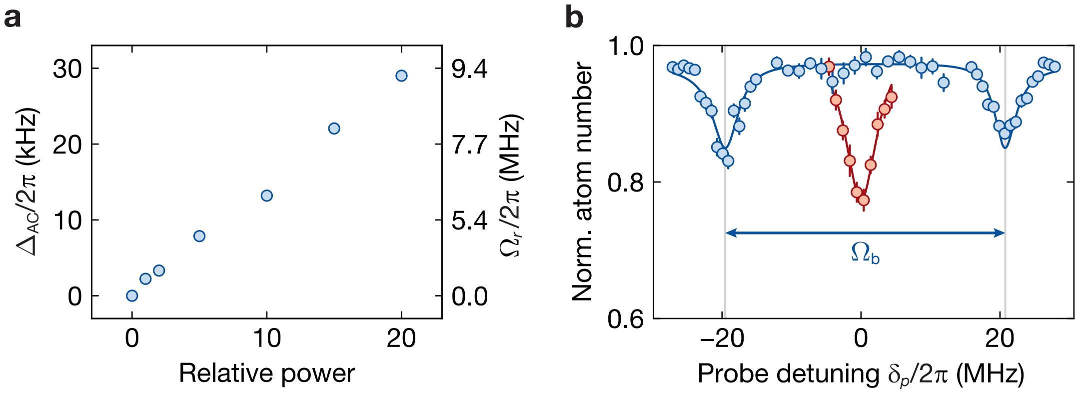

Figure 3.10: Rabi frequency calibration. (**a**) Rabi frequency calibration of the lower transition. The AC-Stark shift Δ_{AC} of the ground state is measured while the 780 nm laser is detuned from the intermediate state $|5P_{3/2}, F = 3, m_F = -3\rangle$ by $\Delta = 2\pi \times 742$ MHz. The AC-Stark shift can be mapped to the Rabi frequency using $\Delta_{AC} = \Omega_r^2/4\Delta$. (**b**) The Rabi frequency of the upper transition is measured by splitting of the resonance due to EIT. The 480 nm laser is tuned to resonance with the $|5P_{3/2}, F = 3, m_F = -3\rangle \leftrightarrow |36S_{1/2}, m_J = -1/2, m_I = -3/2\rangle$ transition, causing the resonance to split into two dips. The energy splitting between the two dips is equivalent to the Rabi frequency Ω_b.

apply a MW sweep to transfer the atoms from $|5S_{1/2}, F = 2, m_F = -2\rangle$ to $|5S_{1/2}, F = 1, m_F = -1\rangle$ before removing the atoms in $|5S_{1/2}, F = 2, m_F = -2\rangle$ with a push-out pulse. By scanning the MW frequency, we observe the energy shift as a function of the optical power, which is used to estimate the Rabi frequency Ω_r, see Fig. 3.10a.

The same method cannot be used with the 480 nm laser because its large detuning to the $5P_{3/2}$ transition results in a tiny energy shift that is challenging to measure accurately. Therefore, we exploit an electromagnetically induced transparency (EIT) [212] to calibrate the Rabi frequency of the upper transition. The atoms, initialized in $|5S_{1/2}, F = 2, m_F = -2\rangle$, are simultaneously illuminated with both the 480 nm and the 780 nm lasers. The 480 nm laser is set resonant to the $|5P_{3/2}, F = 3, m_F = -3\rangle \leftrightarrow |36S_{1/2}, m_J = -1/2, m_I = -3/2\rangle$ transition with high power. In contrast, the 780 nm laser is spectroscopically scanned near the resonance with very weak power to avoid many Rydberg excitations at the same time. The illumination time is set such that the intermediate scattering causes atom loss from the optical lattices. The 480 nm laser will cause the intermediate state resonance to split into two distinct dips, with the splitting equivalent to the Rabi frequency Ω_b of the $|5P_{3/2}, F = 3, m_F = -3\rangle \leftrightarrow |36S_{1/2}, m_J = -1/2, m_I = -3/2\rangle$ transition, see Fig. 3.10b.

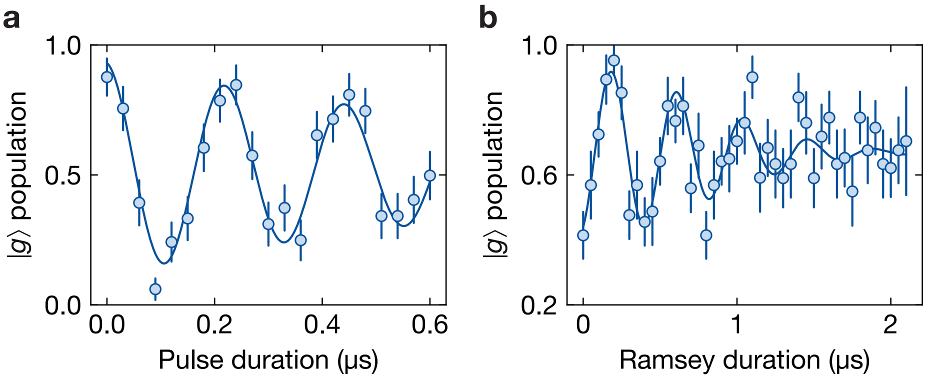

Figure 3.11: Two-photon Rabi oscillations and atom-laser dephasing. (**a**) Single atom Rabi oscillations to the $30S_{1/2}$ state via two-photon excitation pulses. The measured Rabi frequency is $\Omega = 2\pi \times 4.50(8)$ MHz with an exponential decay of $0.9(4)$ μs. (**b**) Ramsey measurement of the atom-laser coherence. The oscillation frequency of the $|g\rangle$ population is determined by the AC-Stark shift of the 480 nm light, which is kept constant during evolution. The decay contrast with a time constant of $0.8(1)$ μs is caused by laser frequency and intensity noise.

Two-photon Rabi oscillations

With known Rydberg resonances and proper calibration of the coupling strength, see the previous section, one can measure Rabi oscillations with the two-photon excitation scheme. We drive Rabi oscillations of a single atom between $|5S_{1/2}, F = 2, m_F = -2\rangle$ and $|30S_{1/2}, m_J = -1/2, m_I = -3/2\rangle$. The Rabi frequencies of the lower and upper transitions are set to be identical at $\Omega_r = \Omega_b = 2\pi \times 42$ MHz with an intermediate state detuning of $\Delta = 2\pi \times 200$ MHz. As for the loss of Rydberg atoms from the optical lattices, we observe Rabi oscillations on the detected atom number, see Fig. 3.11a. We fit the results with a sinusoidal with exponential decay function. The fitted Rabi frequency of $\Omega = 2\pi \times 4.50(8)$ MHz is in excellent agreement with the estimated two-photon Rabi frequency of $\Omega = \Omega_r\Omega_b/(2\Delta) = 2\pi \times 4.41$ MHz. An exponential decay rate can be estimated by $\tau = 1/\Gamma_{\text{dep}}$ from Eq. (3.6), where $\gamma_r = 2\pi \times 20$ kHz is the 780 nm laser linewidth, $\gamma_b = 2\pi \times 15$ kHz is the 480 nm laser linewidth, $\Gamma_e\Omega_r^2/(4\Delta^2) = 2\pi \times 70$ kHz is the off-resonant intermediate state dephasing, and $\Gamma_{\text{ryd}} = 2\pi \times 10$ kHz is the natural linewidth if the Rydberg state. With these experimental parameters, we estimate the exponential decay of $\tau = 2.7$ μs. However, the extracted exponential decay of $0.9(4)$ μs from the measurements is faster than the estimated value by a factor of 3. The model does not take into account intensity fluctuations of the excitation pulses, which can cause further dephasing. The coherent versus incoherent ratio $\Omega/\Gamma_{\text{dep}} = 25$ from these measurements is markedly improved by a factor of 4 compared to the one observed in [159] with the same laser system, where the substantial gain is due to the higher

Rabi frequency Ω_b of the upper transition. However, the coherent versus incoherent ratio is a factor of 2 lower than the single-photon excitation scheme, see Sec. 3.4.1.

Two-photon Ramsey spectroscopy

The dephasing of the atom-laser coherence due to laser noise can be determined with a Ramsey experiment. A single atom is driven to a superposition of $|g\rangle$ and $|S\rangle$ with a two-photon $\pi/2$ pulse $t = \pi/(2\Omega)$. Since the 480 nm beam switching time is very slow, it remains in place during evolution. Then, the atom evolves under 480 nm light for a variable duration before finishing with a second $\pi/2$ pulse, mapping the accumulated phase to the atomic population. The oscillation of the $|g\rangle$ population in Fig. 3.11b is given by the AC-Stark shift of the 480 nm light. The results are fit with a sinusoidal with Gaussian decay. The measured oscillation frequency of $\Delta_{\mathrm{AC}} = 2\pi \times 2.33(6)\,\mathrm{MHz}$ is in agreement with the estimated AC-Stark shift of $\Delta_{\mathrm{AC}} = 2\pi \times 2.2\,\mathrm{MHz}$. The decay of the contrast with a time constant of $0.8(1)\,\mu\mathrm{s}$ is caused by laser frequency and intensity noise. Here, the random intensity in each shot results in a random AC-Stark shift for the Ramsey detuning. This dephasing time from the Ramsey measurements is in good agreement with the dephasing time from the Rabi oscillation measurements, confirming that the main dephasing channel is due to the lasers.

3.5 Ground states manipulation via Raman transition

Fundamental units for exploring quantum science and technologies are quantum bits (qbit). For trapped atoms, one can encode qubits in long-lived states where information can be stored before loss. For this application, hyperfine ground state manifolds or metastable states are commonly considered. Encoding in the hyperfine qubit is usually chosen for alkali atoms because its splitting range is in the microwave regime. For ^{87}Rb, the hyperfine splitting between two ground states is around $\omega_{\mathrm{HF}} = 2\pi \times 6.84\,\mathrm{GHz}$. The conventional driving with a MW field is typically limited by a MW coupling strength on the order of a few ten kilohertz. Moreover, due to the large length scale of the field, driving with a MW is a global operation that affects the entire system.

An alternative approach to manipulating hyperfine qubits is offered by exploiting a two-photon Raman process. Here, two hyperfine ground states are optically coupled via an off-resonant intermediate state. This increases the Rabi frequency coupling to the megahertz regime and allows for local optical addressing of the individual qubits. A typical Raman transition setup uses two lasers phase-locked with a frequency difference equal to the hyperfine splitting. Another way is to use a single laser with phase modulation from an EOM, generating sidebands resonant to the hyperfine splitting. However, a cavity filter is additionally required to remove either a sideband or a carrier to prevent destructive interference. All of these approaches are based on active stabilization of phase-locked or cavity filtering.

In [213], a novel technique based on phase modulation with a highly dispersive optical element was demonstrated. The phase difference of the modulated sidebands is shifted by a dispersive element in a frequency-dependent fashion, such that the destructive interference turns into constructive interference. Therefore, this realizes an amplitude modulation that can be used for passively stable Raman transitions with high efficiency.

3.5.1 Stimulated Raman transitions

Stimulated Raman transitions for hyperfine qubits are conventionally implemented using a three-level atom in a Λ configuration. Two ground states, $|g\rangle$ and $|g'\rangle$, with hyperfine splitting ω_{HF} are coupled to an intermediate state $|e\rangle$ by two laser fields, $E_1 \cos \omega_1 t$ and $E_2 \cos \omega_2 t$. The system can be described by the following Hamiltonian in the rotating frame in the basis $(|g\rangle, |g'\rangle, |e\rangle)$:

$$H = \frac{\hbar}{2} \begin{pmatrix} 0 & 0 & \Omega_1 \\ 0 & 2\delta & \Omega_2 \\ \Omega_1^* & \Omega_2^* & 2\Delta \end{pmatrix}, \tag{3.7}$$

where $\Delta = \omega_1 - \omega_{eg}$ is the detuning from the intermediate state $|e\rangle$, ω_{eg} is the atomic transition frequency, and $\delta = (\omega_2 - \omega_1) - \omega_{\mathrm{HF}}$ is the differential detuning. When far-detuned from the intermediate state $\Delta \gg \Omega_1, \Omega_2$, this results in an effective two-level system

$$H_R = \frac{\hbar}{2}\begin{pmatrix} 0 & \Omega_{\mathrm{eff}} \\ \Omega^*_{\mathrm{eff}} & 2\delta_{\mathrm{eff}} \end{pmatrix}, \tag{3.8}$$

where $\Omega_{\mathrm{eff}} = \Omega_1\Omega_2^*/2\Delta$ is the effective Rabi frequency and $\delta_{\mathrm{eff}} = \delta + \left|\Omega_1^2\right|/4\Delta - \left|\Omega_2^2\right|/4\Delta$ is the effective detuning. For the resonant case where $\delta_{\mathrm{eff}} = 0$, the Raman Rabi frequency is $\Omega_R = \Omega_1\Omega_2^*/2\Delta$ and couples $|g\rangle$ and $|g'\rangle$ with a negligible population in $|e\rangle$. For identical Rabi frequencies $\Omega_1 = \Omega_2$, the resonant condition is met when the frequency difference between the fields matches the hyperfine splitting, $\omega_2 - \omega_1 = \omega_{\mathrm{HF}}$. In other words, two laser fields with the frequency difference of ω_{HF} result in the amplitude modulation of the combined field with oscillation frequency ω_{HF}, driving the Raman transition between $|g\rangle$ and $|g'\rangle$. Extending from two laser frequencies to multiple frequency components, usually arises when the laser is modulated, is discussed in detail in [209, 214]. Multiple laser frequency components with regular frequency spacing can be described by $\Omega = \Omega_0 \sum_n a_n e^{in\omega t}$, where the amplitude of all components are normalized such that $\sum_n a_n = 1$. The amplitude modulation of all components is thus

$$\begin{aligned} |\Omega|^2 &= |\Omega_0|^2 \sum_{n,m} a_n^* a_m e^{i(m-n)\omega t} \\ &= |\Omega_0|^2 \sum_k e^{ik\omega t}\left[\sum_n a_n^* a_{n+k}\right], \end{aligned} \tag{3.9}$$

where the indices n, m are changed to n, k with $k = m - n$. Considering the resonant condition when $k\omega = \omega_{\mathrm{HF}}$ ($k = 1$), the amplitude modulation driven by $e^{i\omega_{\mathrm{HF}}t}$ is thus given by the usual expression [215, 216] as

$$\Omega_R^2 = \frac{|\Omega_0|^2}{2\Delta}\sum_n a_n^* a_{n+1}. \tag{3.10}$$

The amplitude modulation depends on the distribution of power in the frequency components and their relative phase. One can define a modulation efficiency $\eta^{\mathrm{AM}} = \left|\sum_n a_n^* a_{n+1}\right|$, which is less than unity $\eta^{\mathrm{AM}} < 1$. In Sec. 3.5.2, we will show that the modulation efficiency vanished, i.e., $\eta^{\mathrm{AM}} = 0$ for a laser with phase modulation and how to address this issue using a dispersive optical component.

To consider the effect of the polarization of the laser field on the Raman transition, one can treat it as a light-induced fictitious magnetic field [217]. Since the scalar polarizability does not depend on the hyperfine structure F, the tensor polarizability vanishes for the $J = 1/2$ states (the ground states of alkali atoms). The off-resonant effective field of the Raman laser induces purely vector light shifts, acting as a fictitious magnetic field $B_{\mathrm{fict}} \propto \mathrm{Im}\left[\hat{\epsilon}^* \times \hat{\epsilon}\right]$ with $\hat{\epsilon} = \sum_q \epsilon_q \hat{e}^q$ being the polarization vector of the laser field [217–221]. For example, using circular polarization $\hat{\epsilon}^+ = -\frac{1}{\sqrt{2}}(\hat{e}^x - i\hat{e}^x)$ for both lasers causes the fictitious magnetic field along $-\hat{\mathbf{e}}^z$, which can drive a π transition with $\Delta m_F = 0$ between ground states. In contrast, using linear polarization for both lasers results in a zero fictitious magnetic field $B_{\text{fict}} = 0$, making it impossible to drive any transition. For our experiment, we want to drive the transition between $|g\rangle = |F = 2, m_F = -2\rangle$ and $|g'\rangle = |F = 1, m_F = -1\rangle$, which has $\Delta m_F = \pm 1$. Therefore, each laser component needs both circular and linear polarization so that the transitions with $\Delta m_F = \pm 1$ are possible. Since this setting allows for all $\Delta m_F = 0, \pm 1$, we use a large magnetic field to generate large Zeeman splitting such that each transition is isolated from the others through a large energy separation.

3.5.2 Amplitude modulation with a volumetric chirped Bragg grating

This section will demonstrate that sidebands from pure phase modulation cannot cause amplitude modulation and highlight how a chirped Bragg grating (CBG) can lead to amplitude modulation. The details of the derivation presented in the following can be found in [209, 213].

The sidebands of the laser are generated by sinusoidal phase modulation from an EOM. With a modulation frequency equal to the hyperfine splitting ω_{HF}, the coupling can be expressed using the Jacobi-Anger expansion as

$$\Omega = \Omega_0 e^{i\beta \sin \omega_{\text{HF}} t} = \Omega_0 \sum_{n=-\infty}^{\infty} \mathcal{J}_n(\beta) e^{in\omega_{\text{HF}} t}, \tag{3.11}$$

where $\mathcal{J}_n$ are the Bessel functions of the first kind and β is the modulation depth. Following the same steps as in Eq. (3.9) and (3.10), the Raman Rabi frequency becomes

$$\Omega_R = \frac{|\Omega|^2}{2\Delta} = \frac{|\Omega_0|^2}{2\Delta} \cdot \eta^{\text{AM}} = \frac{|\Omega_0|^2}{2\Delta} \cdot \sum_{n=-\infty}^{\infty} \mathcal{J}_n(\beta)^* \mathcal{J}_{n+1}(\beta). \tag{3.12}$$

It can be seen that the amplitude modulation vanishes due to the fact that the sidebands are destructively interfering since $\eta^{\text{AM}} = \sum_{n=-\infty}^{\infty} \mathcal{J}_n(\beta)^* \mathcal{J}_{n+1}(\beta) = 0$ [213]. Therefore, a single laser with phase modulation cannot drive Raman transitions. Several methods based on filtering out some components of phase-modulated light are commonly used to avoid this destructive interference [72, 222–224]. Rather than filtering the spectral components, we use a dispersive optical component to change the relative phase of the spectral components. Due to its group delay dispersion (GDD) with $GDD = \frac{\partial^2 \phi}{\partial \omega^2}$, this produces a quadratic frequency-dependent phase shift of the form:

$$\Omega = \Omega_0 \sum_{n=-\infty}^{\infty} \mathcal{J}_n(\beta) e^{in\omega_{\text{HF}} t} e^{i\alpha n^2}, \tag{3.13}$$

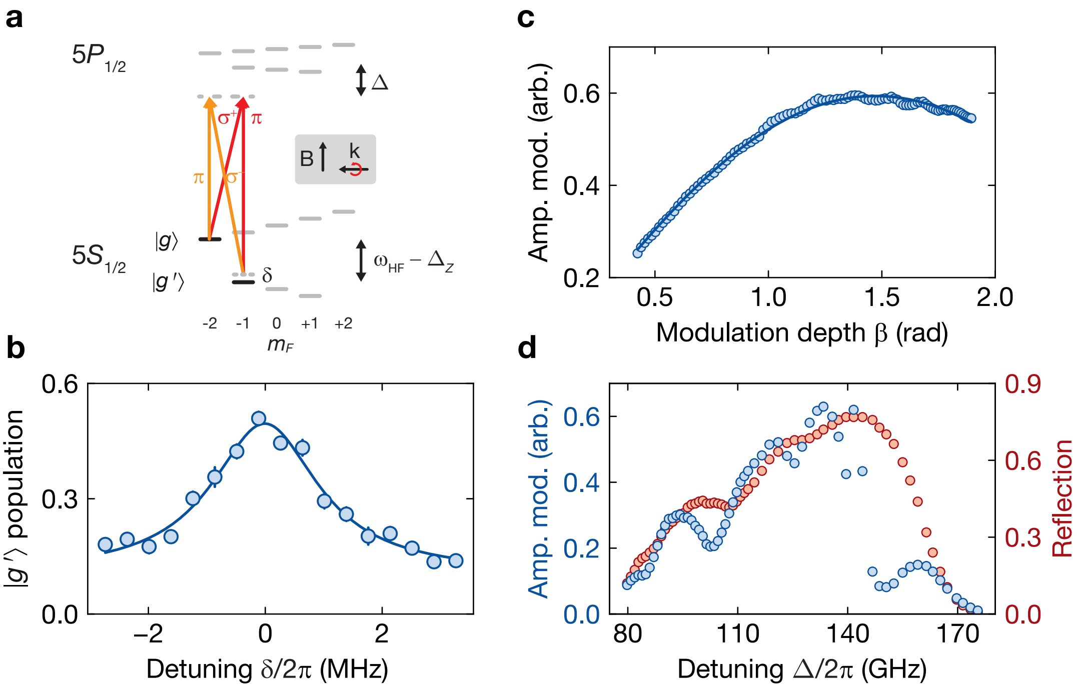

Figure 3.12: Raman laser with volumetric chirped Bragg grating. (**a**) The Raman beam with circular polarization propagates perpendicular to a magnetic field and thus has σ^+, σ^-, and π polarizations. These allow us to drive transitions from $|g\rangle$ to $|g'\rangle$ with $\Delta m_F = \pm 1$. There are two possible paths, $\pi - \sigma^-$ (orange) and $\pi - \sigma^+$, that contribute to the coupling. (**b**) Raman sideband spectroscopy. By varying the EOM sideband frequency, we find a resonance at a frequency of $\omega_{\mathrm{HF}} - \Delta_Z$. (**c**) An amplitude modulation of the laser field as a function of the EOM modulation depth β after passing through the CBG. The measured amplitude follows $\mathcal{J}_1(2\beta \sin\alpha)$, which yields a fitted $\alpha = 0.68(1)$. The maximum amplitude modulation is at $\beta \approx 1.5$. (**d**) Amplitude modulation strength (blue) and optical efficiency (red) of the CBG versus laser frequency. The efficiency is around 70 − 75 % in the range of 30 GHz. However, the amplitude modulation has a sharp reduction for higher frequency, which could be caused by non-uniform CBG dispersion over the bandwidth.

where $\alpha = GDD \cdot \omega_{\mathrm{HF}}^2/2$ is the phase curvature. The result is an effective Raman frequency of

$$\Omega_R = \frac{|\Omega_0|^2}{2\Delta} \cdot |\mathcal{J}_1(2\beta \sin\alpha)| \,. \tag{3.14}$$

The modulation efficiency $\eta^{\mathrm{AM}} = |\mathcal{J}_1(2\beta \sin\alpha)|$ depends on the modulation depth β and phase curvature α [213]. It has a maximum achievable efficiency of $\eta^{\mathrm{AM}} = 0.582$ when $\beta \sin\alpha = 0.92$. In practice, the modulation depth of the EOM is limited at $\beta \lesssim \pi$, and therefore a large GDD is required. For example, an EOM with modulation depth of $\beta = \pi/2$ needs a GDD of $GDD \approx 7 \times 10^8\,\mathrm{fs}^2$ to fulfill the maximum condition of $\mathcal{J}_1$. This large GDD is typically hard to reach. Standard telecom fibers with zero dispersion wavelength around 1310 nm have $GDD = 4 \times 10^4\,\mathrm{fs}^2$ per meter at 795 nm [225, 226]. To reach the target, one would need a fiber with a length of 20 km, which consequently causes a significant power loss. Another dispersive element, called a chirped Bragg mirror, has $GDD = 1300\,\mathrm{fs}^2$ per reflection, so many reflections are needed to fulfill the target GDD. Here, a volumetric chirped Bragg grating (CBG, CBG-795-90, OptiGrate) is used [227]. Due to its grating period gradually changing over the spatial distance [228], the CBG offers enormous GDD on the order of $GDD \approx 4 \times 10^8\,\mathrm{fs}^2$ for a length scale of $\approx 10\,\mathrm{cm}$. By reflecting twice on the same CBG, the GDD is doubled, giving close to the target values. However, the CBG has a bandwidth of around 50 GHz and the GDD not be uniform. Therefore, it is convenient to mount the CBG in a rotational mount, allowing for better maximization of the amplitude modulation.

3.5.3 Raman laser setup

The Raman laser setup, constructed during this dissertation, is shown in Fig. 3.13. A 532 nm laser (Verdi V18, Coherent) with optical power of 15 W pumps a titanium sapphire (Ti:Sa) laser (MBR110, Coherent), giving a power of 2.2 W at a wavelength of 795 nm near the $D1$ transition of ^{87}Rb. The beam is sent to an optical isolator before it is guided to the Raman setup breadboard by an end-capped fiber (FC PM630HP FC/APC EC FU, FiberCableConnect). After coupling out of the fiber, the beam with a power of 1.2 W is phase modulated by an EOM (PM-Rb_6.8, QUBIG). A small portion of the beam after the EOM is coupled out with a polarizing beam splitter and sent to a Fabry-Perot cavity for characterization of the sidebands. The main beam is sent to the CBG and retro-reflected back to the same path, experiencing twice frequency-dependent phase shifts and converting phase modulation to amplitude modulation of the laser field. The reflection from the CBG has an angle dependent on the laser frequency. Hence, the CBG and a mirror are mounted on the rotational stage such that the retro-reflection retains the same direction while tuning the CBG angle. A telescope before the CBG expands the beam size, reducing the intensity at the CBG. After passing through the CBG, a small amount of the power of the amplitude modulated beam is fiber coupled to a fast photodiode detector (DXM12CF, Thorlabs) for analysis of the amplitude modulation. The main beam is reshaped to its original size before being focused down to an AOM (3080-125, Crystal Technology) for fast switching pulses. Then, a second fiber guides the beam to the main experimental setup. The beam propagates in the atomic plane with circular polarization and is focused down with a 750 mm lens to a beam waist of 150 µm with a maximum power of 245 mW at the atoms.

To drive the EOM sidebands, a RF signal generator at a frequency of 2.28 GHz is

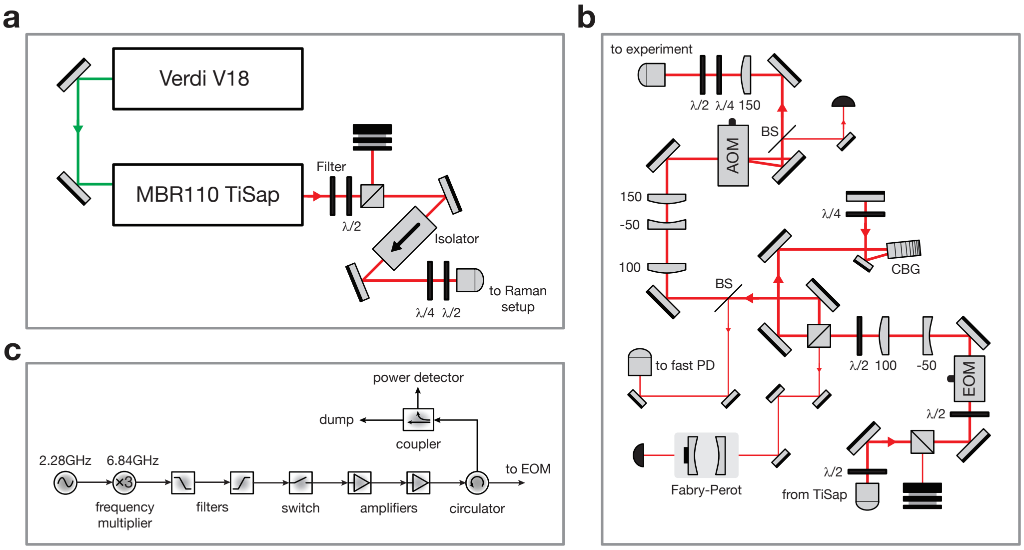

Figure 3.13: Schematic of the Raman laser system. (**a**) Laser source setup. The 532 nm laser with a power of 15 W pumps the titanium sapphire laser, generating a 795 nm laser with a power of 2.2 W. Then, the laser is guided to the setup shown in (b) with an end-capped fiber. (**b**) The 795 nm laser is phase-modulated with the EOM before converting to amplitude modulation by double passing through the CBG. Then, an AOM is used for fast switching before sending the light to the atoms via an optical fiber. (**c**) The RF circuits for driving the EOM. An RF at 2.28 GHz is frequency tripled. The signal is then sent through a series of filters and amplifiers, resulting in a 6.84 GHz signal with a power of up to 35 dBm. The circulator prevents back reflections of the RF signal from the EOM. The back reflection can also be used to optimize the EOM's resonant circuit.

frequency tripled with a frequency multiplier. A series of filters filter out unwanted frequencies, leaving a pure RF at 6.84 GHz to match the hyperfine energy splitting of ^{87}Rb. A preamplifier and a high-power amplifier amplify the RF power up to 35 dBm. The EOM has a tunable resonant circuit that offers a high Q factor, but has a narrow bandwidth of 23 MHz. Applying the RF outside the bandwidth range will cause the full RF power to be reflected back to the amplifiers and cause damage. Therefore, the RF signal is passed through a circulator before being sent to the EOM so that the reflected power is altered to an RF dump. Additionally, we can use the reflected power to optimize the resonant circuit to maximize RF coupling to the EOM by minimizing the reflection.

After this optimization procedure, we measure the dependence of the amplitude modulation after the CBG on the EOM phase modulation depth β, see Fig. 3.12 c. The amplitude modulation increases with the modulation depth β as a function of

$\mathcal{J}_1(2\beta\sin\alpha)$ as expected. The maximum amplitude modulation is around $\beta = 1.5$ with an extracted dispersion coefficient of $\alpha = 0.68(1)$ rad. This is lower than in other work [209, 213] where a coefficient of $\alpha = 0.93(1)$ rad was observed with a maximum modulation at $\beta = 1.2$. By scanning the laser frequency, the CBG has a stable reflection efficiency of $70 - 75\%$ over a range of ≈ 30 GHz, see Fig. 3.12 d (red). The amplitude modulation follows the reflection efficiency but has a sharp reduction at higher frequencies, see Fig. 3.12 d (blue). However, we do not see a strong decrease at the center of the bandwidth as observed in [213]. This observed variation of the amplitude modulation with laser frequency could be caused by nonuniform dispersion over the bandwidth of the CBG which can be differ for each CBG. The center frequency of the CBG's bandwidth can be changed by changing the alignment angle of the CBG.

The Raman laser can be coarsely aligned to the atoms using near-resonant light to push out the atoms. Due to space constraints, the final mirror of the Raman beam is ≈ 700 mm away from the atoms. This mirror is mounted on a picomotor-actuated mirror mount which allows for fine-tuning of the beam alignment. Once the beam is aligned to the atoms, the procedure in the following can be used to operate the Raman laser:

1. **Initial setup and pre-optimization:** The laser is set to the target detuning Δ with an estimated sideband frequency of $\omega_{\mathrm{HF}} - \Delta_Z$, where ω_{HF} is the hyperfine splitting and Δ_Z is the differential Zeeman shift of the target states. The next step is to optimize the resonant circuit of the EOM by minimizing the reflected RF power from the circulator. By monitoring on the fast photodiode, the CBG can be pre-optimized to get strong amplitude modulation.

2. **Searching for the EOM sideband resonance:** First, the atoms are prepared in $|g\rangle$. The Raman beam is then sent to the atoms for a duration longer than the estimated Rabi oscillation timescale so that the atoms reach the dephased regime, which has the same population of both $|g\rangle$ and $|g'\rangle$. The $|g'\rangle$ is detected after applying a resonant push out to remove atoms in $|g\rangle$. By varying the EOM sideband frequency, we find the sideband resonance as shown in Fig. 3.12 b. If the resonance cannot be found within the EOM resonant circuit bandwidth of 23 MHz, the first procedure has to be repeated to retain the high EOM sideband coupling.

3. **Optimizing the amplitude modulation with the CBG alignment:** With the correct sideband frequency, the EOM resonant circuit can be fine-tuned. Finally, maximum amplitude modulation can be achieved by adjusting the angle of the CBG and the modulation depth β of the EOM.

Once the amplitude modulation is optimized, Rabi oscillations between $|g\rangle$ and $|g'\rangle$ can be observed. Fine alignment of the Raman beam can be achieved by maximizing the Rabi frequency while adjusting the beam alignment and focus of the Raman beam.

Initially, we sent the Raman beam from the top of the chamber perpendicular to the atomic plane. Unfortunately, this direction caused significant atomic loss from the trap within $< 10\,\text{ms}$. We also observed the loss in a spatially periodic pattern. Since sending the beam from the top of the chamber means that the beam afterwards goes through the imaging path which has a few filters that can reflect light at 795 nm, we believe that this residual retro-reflection of the Raman beam causes interference in the atomic plane. Therefore, we changed the direction of the Raman beam to the atomic plane, oriented at 45° with respect to the optical lattice beams. In the absence of scattering in the optical path, we successfully observed the Raman population transfer signal and a much lower heating rate, which is discussed in the next section.

3.5.4 Fast ground states manipulation

To drive the transition between $|g\rangle$ and $|g'\rangle$, we set a circular polarization along the atomic plane with the bias magnetic field applied along the vertical direction perpendicular to the atomic plane. Since this configuration can drive all possible $\Delta m_F = 0, \pm 1$, a large magnetic field is used to isolate all transitions through a large energy separation so that each transition is decoupled. We spectroscopically probe the Raman resonance of the sidebands by varying the EOM modulation frequency, while the carrier is detuned from the $D1$ transition line of ^{87}Rb by $\Delta = 2\pi \times 146\,\text{GHz}$. The atoms are initialized in $|g\rangle$ and then illuminated for $300\,\mu\text{s}$ with a full power of around 245 mW. The atoms in $|g'\rangle$ are detected after atoms in $|g\rangle$ are pushed out. We found the sideband resonance at the frequency equivalent to the hyperfine splitting subtracted by the differential Zeeman shift, see Fig. 3.12a. With $B_z = 8.7G$, the hyperfine transitions splitting of $2\pi \times 6\,\text{MHz}$ is larger than the transition width of $2\pi \times 2.2(3)\,\text{MHz}$, so that the atoms are forbidden to populate the other ground state manifolds. Driving Raman Rabi oscillations between $|g\rangle \leftrightarrow |g'\rangle$, we observe a Rabi frequency of $\Omega_R = 2\pi \times 1.04(1)\,\text{MHz}$ with a high efficient population transfer of $\approx 99\%$, see Fig. 3.14b. Performing Rabi oscillations on a longer timescale, as shown in Fig. 3.14a, we extract the exponential decay of $100(38)\,\mu\text{s}$. Measurement of off-resonant scattering of the Raman laser yields a scattering rate of $\Gamma_{\text{sc}} = 2\pi \times 7.8(2)\,\text{kHz}$.

These results demonstrate highly efficient and fast population transfer using a passively stable Raman laser setup based on an EOM and a CBG. This presents a significant reduction in complexity compared with active frequency stabilization or cavity filtering, making the setup more stable and reliable to operate with. Having this upgrade paves the way for versatile future experiments. For example, integrating the setup with a DMD would give access to local manipulation of hyperfine ground state qubits on a fast timescale [229, 230]. Moreover, combining with the Rydberg dressing, this could be used to realize a transverse-field Ising model [231–234], which typically has a small transverse coupling limited by the low MW Rabi frequency.

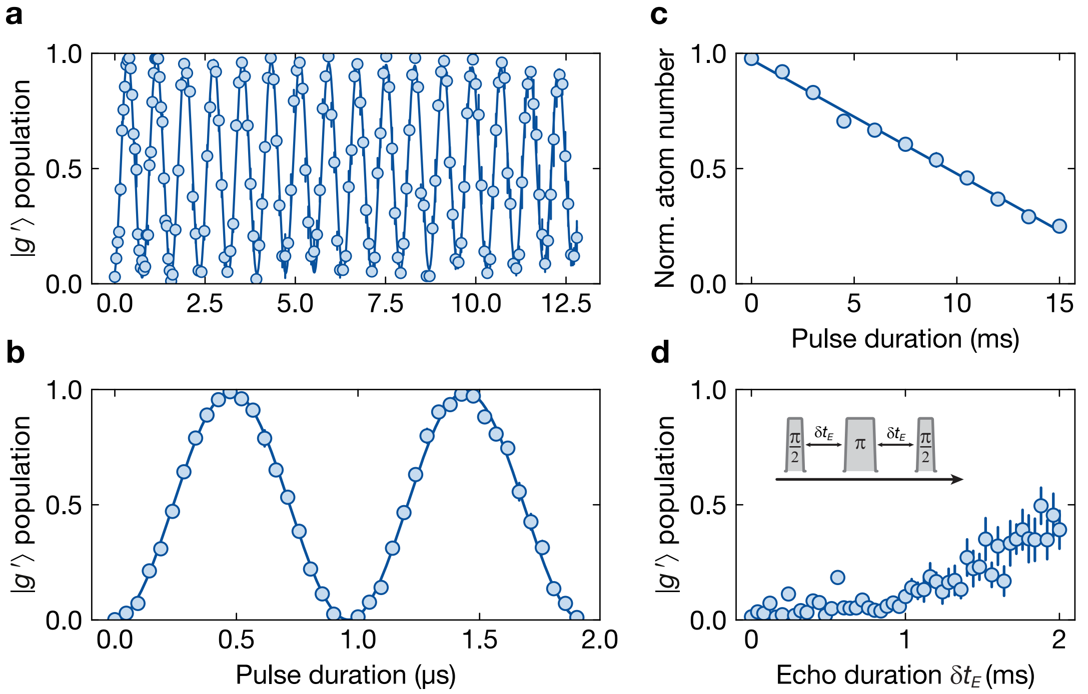

Figure 3.14: Hyperfine ground state transitions with the Raman setup. (**a**) Rabi oscillations of the $|g\rangle = |F = 2, m_F = -2\rangle \leftrightarrow |g'\rangle = |F = 1, m_F = -1\rangle$ transition, averaged over 25 atoms trapped in the diagonal lattice. The laser is frequency detuned by $\Delta = 2\pi \times 146\,\text{GHz}$ from the $D1$ transition. The measured Rabi frequency is $\Omega = 2\pi \times 1.26(1)\,\text{MHz}$ with a decay constant at $1/e$ of $100(38)\,\mu\text{s}$. (**b**) Rabi oscillations at a Rabi frequency of $\Omega = 2\pi \times 1.04(1)\,\text{MHz}$. we observe a highly efficient population transfer of $\approx 99\%$. (**c**) Off-resonant scattering of the Raman laser. The measured scattering rate of $\Gamma_{\text{sc}} = 2\pi \times 7.8(2)\,\text{kHz}$ is much slower than the Raman Rabi frequency. There is negligible atomic loss throughout the Rabi oscillations below $20\,\mu\text{s}$. (**d**) Echo measurement with Raman pulses. The dephasing kicks in at $\delta t_E \approx 1\,\text{ms}$, originating from magnetic field noise. This dephasing timescale agrees with an echo measurement using MW pulses.

3.6 Summary

In this chapter, we presented the experimental setup and protocols. The single atom control and detection of our ^{87}Rb quantum gas microscope is explained, along with the newly upgraded optical lattice that supports large system sizes and configurable lattice geometries. Then, two Rydberg excitation schemes and setups were compared, including the characterization of relevant parameters. These Rydberg excitation setups offer independent optical control to two Rydberg states, enabling dynamic manipulation of long-range interactions. Both the quantum gas microscope and Rydberg state control will be incorporated and used in subsequent experimental chapters. Finally, the Raman laser setup was introduced for fast hyperfine ground state transfers with passive operation, which is advantageous for future experimental work.

Chapter 4

Subwavelength atomic array switched by a single Rydberg atom

4.1 Introduction

In this chapter, we leverage the effects of the Rydberg blockade in conjunction with an electromagnetically induced transparency (EIT) to demonstrate spatial control over the optical response of subwavelength arrays. In the following, we describe the properties of subwavelength arrays and their advantage towards realizing quantum interfaces. We then explore the EIT nonlinearlity, identifying a regime where the transparent window breaks down due to Rydberg interactions. Finally, we realize the switching behavior of arrays using the Rydberg blockade via a single controlled ancilla atom. Broad aspects such as spectroscopic signatures, coherent manipulation, distribution of scattered photon number, and analysis of switching area are covered. The experimental results presented in this chapter follow the publication [235].

4.2 Light scattering in subwavelength atomic arrays

When the interatomic distances within an atomic quantum system is small compared to the emitted wavelength, the system can be described as a single composite entity as the scattering coherently occurs across the entire ensemble. This causes cooperative effects that can dramatically change the radiative properties of the ensemble [236]. In this chapter, we focus on the coupling between two-dimensional (2D) atomic arrays and an external near-resonant light field, particularly for the in-phase spin wave when the light impinges perpendicularly to the array. Following the derivation in [77], the identical pointlike atoms exhibit a linear and isotropic polarizability [237]

$$\alpha(\delta_p) = -\alpha_0 \frac{\Gamma_e}{2\delta_p + i(\Gamma_e + \gamma_{\text{loss}})}, \tag{4.1}$$

where $\alpha_0 = \frac{3}{4\pi^2}\epsilon_0\lambda_{\text{eg}}^3$. Here, $\delta_p = \omega_p - \omega_{\text{eg}}$ is the detuning between the angular frequency of the probe laser $\omega_p = 2\pi c/\lambda_p$ and the resonance frequency of the atoms $\omega_{\text{eg}} = 2\pi c/\lambda_{\text{eg}}$, and $\Gamma_e(\gamma_{\text{loss}})$ is the natural radiative (loss) rate. For many atoms, a single atom experiences a combination of a driving field with a radiation field from surrounding atoms, depending on the strength of the radiation field and its phase relative to the atom. This can be intuitively interpreted as photons scattered on an atom are re-scattered with different atoms in the array. The eigenstates of the atomic array, which interacts with the radiation field, are given by the collective eigenmodes of the spin waves [77, 238, 239]. Each mode has a different width and lamb shift, which are modified by multiple scattering processes. Considering the atomic arrays with small lattice spacing compared to the wavelength $a_{\mathrm{lat}} < \lambda_p$, the eigenstate is dominated by the lowest order of the collective eigenmodes. This is reminiscent of a diffraction grating, where light diffracts to many diffraction orders. As the grating spacing decreases, the higher order fractions also decrease. They eventually confine to the lowest order when the grating spacing is sufficiently small. The scattering amplitude S of the normal incidence photons is given by a self-consistent solution of multiple scattering [77]

$$S(\delta_p) = -\frac{i(\Gamma_e + \Gamma)}{2(\delta_p - \Delta) + i(\Gamma_e + \gamma_{\mathrm{loss}} + \Gamma)}. \tag{4.2}$$

By comparing this with the form of Eq. (4.1), we can deduce that the dipolar interactions among the atoms alter the width Γ_e and the resonance frequency ω_{eg} through the cooperative counterparts Γ and Δ_p,

$$\begin{aligned} \Gamma &= \Gamma_e \frac{3}{4\pi} \left(\frac{\lambda_p}{a_{\mathrm{lat}}} \right)^2 - \Gamma_e \\ \Delta &= -\frac{3}{2} \Gamma_e \lambda \sum_{n \neq 0} G\left(0, r_n\right) + \frac{i}{2} \Gamma. \end{aligned} \tag{4.3}$$

Here, $G\left(0, r_n\right)$ is the transverse (in-plane) component of the dyadic Green's function of electrodynamics in free space. This scattering amplitude specifies the scattering strength between the photons and the array, which is related to the transmittance (reflectance) as $T = |1 + S|^2 (R = |S|^2)$. Operating on the cooperative resonance $\delta_p = \Delta$ and choosing a closed cycling transition, where the loss rate is negligible $\gamma_{\mathrm{loss}} = 0$, one obtains the maximal scattering $S = -1$, resulting in a perfect reflection of the photons $R = 1$. For a finite loss rate $\gamma_{\mathrm{loss}} \neq 0$, the scattering amplitude becomes $S = -(\Gamma_e + \Gamma)/(\Gamma_e + \Gamma + \gamma_{\mathrm{loss}})$. Therefore, condition $\Gamma_e + \Gamma \gg \gamma_{\mathrm{loss}}$ needs to be fulfilled to reach a high level of reflection. Since $\Gamma_e + \Gamma \propto (\lambda_p / a_{\mathrm{lat}})^2$, strong interactions can be achieved by choosing a sufficiently small lattice spacing. The experimental measurements with our setup of $\lambda_p / a_{\mathrm{lat}} = 0.68$ show strong couplings between the photons and the 2D atomic array, resulting in the transmission and reflection of $T = 0.23(1)$ and $R = 0.58(3)$, respectively [78]. Furthermore, the "subradiant state" has been observed, as the cooperative width $\Gamma_e + \Gamma$ of the arrays is significantly reduced compared to the natural width Γ_e.

4.3 Quantum interfaces with subwavelength atomic arrays

Efficient and versatile light-matter interfaces are essential building-blocks for photon-bases quantum information processing [236, 240]. The main challenge in achieving strong light-matter coupling is the small interaction cross section between atoms and photons. A tightly focused beam on an individual particle was demonstrated for a molecule [241], an atom [242–245], and a quantum dot [246]. In those settings, the highest reported absorption efficiency for a particle is up to 10%. Here, the limitation is set by the diffraction limit of the focal area [247]. Several approaches have been developed to overcome this challenge: for instance, high-finesse optical cavities [248–254] increase the effective interaction strength by a number of photon round trips to a single atom. Waveguides [236, 255–258] strongly confine optical fields and engineer a dispersion and modal properties of light. In optical cavities, the optical response can be altered from transmitting to reflecting for incoming photons depending on whether a strongly coupled atom is present or absent. This serves as the foundation for robust photon-photon gates [254, 259–261]. However, the cavities feature strong mode selection, accommodating only a single spatial mode for the photons, thereby restricting their utility in spatial light shaping. Alternatively, high density ensembles [262–266] improve the chance of atom-photon scattering. The probability of scattering has an exponential attenuation due to scattering into other directions $\propto \exp(-\mathrm{OD})$, where OD is the *optical depth* that depends linearly on the number of atoms N. Such atomic ensembles typically enable efficient light-matter interactions at the cost of making the system highly linear. Strong nonlinear interactions can be achieved by coupling electronically, highly-lying Rydberg states through EIT [212]. In the presence of many photons, the strong interactions between two Rydberg atoms shifts the two-photon transition out of resonance, resulting in absorption [86, 142–144, 267–269].

Recently, ordered subwavelength atomic arrays have emerged as an alternative approach to realize strong light-matter coupling [76, 77, 238, 270–274]. Here, the atoms are periodically arranged at distances below the transition wavelength of the atoms, resulting in highly cooperative responses due to light-mediated dipole-dipole interactions. This suppressed the scattering in unwanted directions and results in a strong and directional light-matter interface [78]. Using such atomic arrays together with the strong interactions of Rydberg states was recently proposed [156, 275, 276]. The cooperative arrays in free space significantly reduce mode restrictions, allowing for the spatial manipulation of the modes of single photons interacting with the array. Introduced in [156], the properties of the arrays can be altered through the excitation of a single atom to a Rydberg state, realizing a "quantum-controlled metamaterial", in which the optical response of the system can be changed in a spatially controlled way, illustrated in Fig. 4.1. In contrast to schemes based on disordered ensembles, where the

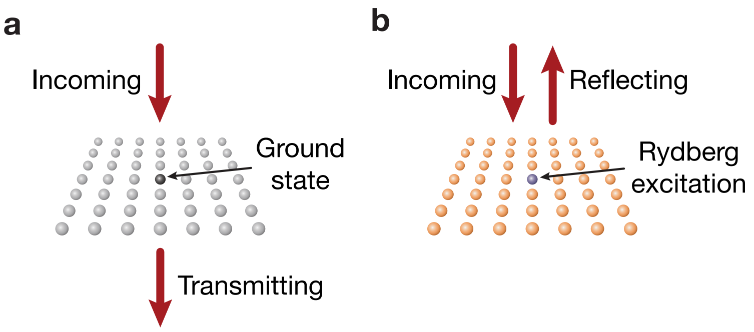

Figure 4.1: Illustration of photon switching with atomic array. The optical response of the array, which is coupled through the Rydberg EIT, is controlled by the single ancilla atom. (**a**) When the ancilla atom is in its ground state, the EIT transparent window permits the transmission of photons. (**b**) When the ancilla atom is excited to a Rydberg state, the EIT condition breaks down, resulting in the reflection of the photons.

decay couples stochastically from the input mode into numerous modes through free-space scattering, the cooperative array allows for coherent switching of the directional modes, such as the transmission and reflection of the arrays. In addition, the strong light-matter coupling of the arrays significantly reduces the number of required atoms compared to that of disordered ensembles. For example, a 4×4 atomic array is comparable with an optical depth of $OD \approx 600$ to achieve the same efficiency for photon storage, which requires around $10^6 - 10^7$ atoms for disordered ensembles [275, 277], and can mitigate some known limitations at large optical depths [143, 278]. This level of control opens up a novel method for engineering photonic states in free space, with potential applications for quantum information processing [156, 279, 280], photon storage [277], photonic gates [156, 275], and deterministic control of photonic modes [281, 282].

4.4 Experimental protocol

As described in Sec. 4.2, the cooperative response occurs when the interatomic spacing within the array is below the transition wavelength of the dipole oscillators. Our near unity-filled atomic array trapped in the square lattice naturally results in subwavelength regime.Comparing the $D2$ transition wavelength $\lambda_p = 780\,\text{nm}$ of ^{87}Rb with lattice spacing $a_{\text{lat}} = 532\,\text{nm}$, we realize a ratio of $a_{\text{lat}}/\lambda_p = 0.68$ [78]. With the array prepared, we use the single-site addressing technique [35, 36] to initially prepare a single ancilla atom, located at the center of the array, in a $|g'\rangle = |5S_{1/2}, F = 2, m_F = -2\rangle$ state while the remaining atomic array is prepared in a $|g\rangle = |5S_{1/2}, F = 1, m_F = -1\rangle$

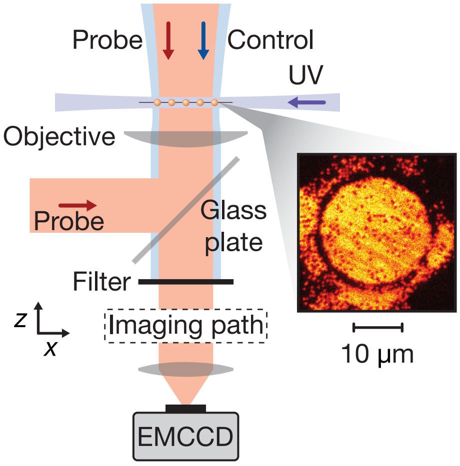

Figure 4.2: Schematic of the experiment. Atomic array and laser light orientations. The transmission (reflection) probe light is overlapped and co- (counter-) propagating with the control light along $-\hat{z}$ $(+\hat{z})$. The probe light is collected with the electron multiplying charge-coupled device (EMCCD), while the control light is filtered out. The inset shows an exemplary site-resolved fluorescence image of the atomic array with approximately 1500 atoms.

state. More details of the state preparation are described in Sec. 4.4.1. The schematic of the light orientations and couplings are shown in Fig. 4.2 and Fig. 4.3. We set a bias magnetic field $B_z = 28.5G$ perpendicular to the atomic plane. The probe light couples the atomic array from $|g\rangle$ to $|e\rangle = |5P_{3/2}, F = 3, m_F = -3\rangle$ with Rabi frequency Ω_p and wavelength $\lambda_p = 780\,\text{nm}$. The chosen states and polarization guarantee that the population is confined only within $|g\rangle$ and $|e\rangle$, since we are driving a closed cycling transition on the stretched states. In addition, we apply a control light at wavelength $\lambda_c = 480\,\text{nm}$, which couples the $|e\rangle$ to $|S\rangle = |44S_{1/2}, m_J = -1/2\rangle$ states with Rabi frequency Ω_c. Applying both beams simultaneously, one creates a transparency window for the probe light via EIT. Transmission is measured by sending the probe light co-propagating with the control light along the $-\hat{z}$ direction through the atomic array. In the end, the control light is filtered out by a combination of a FESH0850 (Thorlabs) and two BLP01-594R-50 (Semrock) filters, allowing only the probe light to reach the EMCCD. The reflection can be measured by reflecting the probe beam along the $+\hat{z}$ direction, counter-propagating it with the control light, and detecting the reflected light from the array to the EMCCD. Both the probe and control lights propagate parallel to the bias field B_z, setting an almost pure circular polarization. The probe light is chosen to be larger than the array size, allowing the driving field to be approximated as a plane wave. The UV excitation pulse with Rabi frequency Ω_{UV} at wavelength $\lambda_{\text{UV}} = 297\,\text{nm}$ couples the ancilla atom from the $|g'\rangle$ to $|P\rangle = |44P_{3/2}, m_J = +3/2\rangle$ states. The large

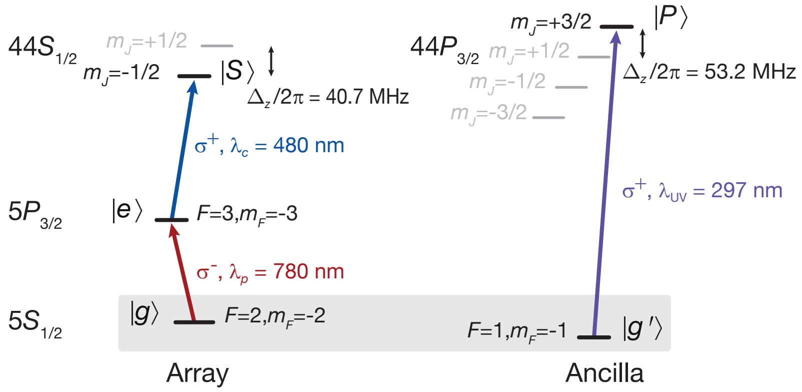

Figure 4.3: Electronic level structure and excitation scheme. The atoms are resonantly coupled to the Rydberg states via the two-photon transition from $|g\rangle = |5S_{1/2}, F = 2, m_F = -2\rangle$ to $|S\rangle = |44S_{1/2}, m_J = -1/2\rangle$ states via the intermediate $|e\rangle = |5P_{3/2}, F = 3, m_F = -3\rangle$ state with σ^-/σ^+ polarized probe/control light. The ancilla atom, initially prepared in $|g'\rangle = |5S_{1/2}, F = 1, m_F = -1\rangle$, is coupled to the $|P\rangle = |44P_{3/2}, m_j = +3/2\rangle$ state using a σ^+ polarization of ultraviolet (UV) light. The $|S\rangle - |P\rangle$ Rydberg states experience a strong interaction, creating a distance-dependent energy shift, $U_{\text{int}}(r)$.

hyperfine separation of approximately $2\pi \times 6.8\,\text{GHz}$ between $|g\rangle$ and $|g'\rangle$ ensures that the UV light only couples with the ancilla without affecting the atomic array. Moreover, the large Zeeman splitting of $\Delta_z = 2\pi \times 53.2\,\text{MHz}$ in the $44P_{3/2}$ manifold isolates the $|P\rangle$ state from the other magnetic sublevels so that a clean polarization of the UV light is not required. We choose $|P\rangle$ over the other magnetic sublevels due to its strong $|S\rangle - |P\rangle$ interaction. With the quantization axis perpendicular to the interatomic distance, the Rydberg interaction between the ancilla and the array atoms is spatially homogeneous in the atomic plane.

4.4.1 Initial state preparation and experimental sequence

We start by preparing a near unity-filled MI trapped in the optical lattices with lattice spacing of $a_{\text{lat}} = 532\,\text{nm}$. The atom number in the array can be tuned to a small array of approximately 250 atoms or a large array of up to approximately 1500 atoms with a filling of $\eta \approx 0.96$ and 0.92, respectively, see Sec. 3.3.1. The atoms are fully polarized in $|g'\rangle$. We then use the addressing technique, see Sec. 3.3.2,to transfer the target ancilla atom to $|g\rangle$. Finally, the global MW transfer flips the states of the array into $|g\rangle$ and the ancilla into $|g'\rangle$, see Fig. 4.4a. However, the diffraction limit of the addressing light leads to partial cross talk on neighboring sites [162], resulting in a finite probability of having more than a single atom flipped to $|g'\rangle$. Note that the effect of having a few ancilla atoms on the switching response can be seen in Sec. 4.6.2. For

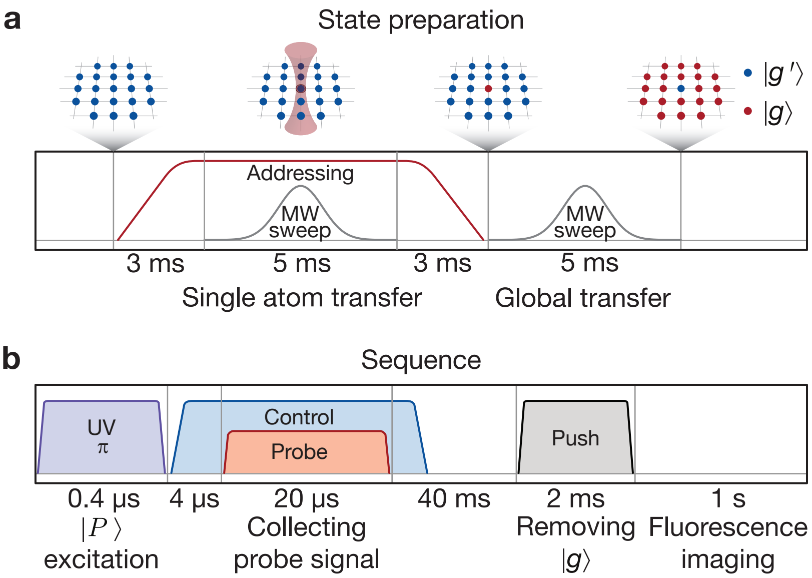

Figure 4.4: State preparation and experimental sequence. (**a**) Starting with a near unity-filled Mott insulator (MI) in $|g'\rangle$, we use a microwave (MW) transfer combined with a tightly focused addressing beam at a wavelength of 787.55 nm to transfer a single ancilla atom to $|g\rangle$. Then, a subsequent global MW sweep prepares the ancilla atom in $|g'\rangle$ and the array atoms in $|g\rangle$. (**b**) Switching of the cooperative mirror is then performed by exciting the ancilla to the $|P\rangle$ state with the UV π-pulse, $\Omega_{\mathrm{UV}}t = \pi$. After switching on the control light and an additional waiting time of 4 µs, the probe light is switched afterwards to monitor the probe signal on the EMCCD. Depending on the state to be detected, the resonant push-out can be added to remove $|g\rangle$ before recording the fluorescence image.

the rest of the measurements, we tune the intensity of the addressing light and the pattern on the digital micromirror device (DMD) to minimize the cross talk while maintaining a substantial amount of the light shift so that the shift is larger than the MW sweep frequency during the population transfer. For our square lattice, we achieve an averaged efficiency of 0.83(4) to prepare the ancilla in $|g'\rangle$ with a negligible probability of having a few additional ancilla atoms.

After the initial state preparation, we ramp up all three lattices to a depth of $100E_r$ to reduce the spatial spread of the atomic wavefunction. Here one needs to keep in mind that further increasing the lattice depth would cause spatial fluctuations, as our optical lattice is anti-trapped for the excited state $|e\rangle$ [78]. We then applied the UV light with pulse area of $\Omega_{\mathrm{UV}}t = \pi$ to controllably excite the ancilla atom from $|g'\rangle$ to the Rydberg state $|P\rangle$. After that, we turn on the control light, 4 µs before the probe light, with a Rabi frequency Ω_c. Then, the array is illuminated by the probe light for a duration of

$t_p = 20\,\mu s$ to collect the transmission (reflection) signal on the EMCCD. Subsequently, we perform site-resolved fluorescence imaging, see Sec. 3.3.3, after removing the array ($|g\rangle$) by using a resonant push-out pulse to observe the presence of the ancilla atom in $|g'\rangle$. In the case of transmission and reflection probing, the EMCCD is operated in a low-noise and short-duration setting, whereas fluorescence imaging collects the scattered light over a much longer duration of approximately 450 ms. These very different demands, we switch the EMCCD setting within the sequence, which requires a switching time on the order of 500 ms. Thus, operating with a reconfigurable EMCCD, we can simultaneously access both the photon properties and the ancilla states in a single measurement. The sequence is summarized in Fig. 4.4b.

4.4.2 Detecting few photons with the EMCCD

Collecting a low photon signal requires a low noise detector. While a single photon detector is capable of detecting single photons with high efficiency, it unfortunately lacks spatial information on the detected field. To observe the switching area, we use the EMCCD. We have optimized various settings of the EMCCD, for instance the read out rate, the shift speed during readout, have operated with binned pixels to improve the region of interest (ROI) ratio. our regular operation of fluorescence imaging, the EMCCD is set to "external" trigger mode, meaning that it waits for a trigger from the experimental control to take images. We found, however, that this mode introduces significant noise to the images. Testing the external trigger mode with a new, identical model, EMCCD shows the same results. However, we are able to reduce the noise level close to the specification, stated in the data sheet, by operating in "internal" trigger mode. With the previous observation, we are able to fully address all challgens by using the "kinematic" mode and setting the trigger to the "external start" trigger mode. In this setting, the EMCCD waits for the external trigger to take the first image and subsequently takes additional images using its internal electronic clock cycle. This results in high noise on the first image (unused) and low noise on the following images (used for the measurements). Since the internal clock is used for the trigger, approximately every (25 ms), we need to adjust the external trigger start time so that the second image matches the activation of the probe light. We set the exposure time to be 2 ms to avoid a time mismatch between the trigger and the probe light. Under our measurement conditions, having a relatively long exposure time of 2 ms compared to $< 100\,\mu s$ does not significantly increase the noise in the images. The optical field at the atomic array is collected by a high-resolution objective with a numerical aperture (NA) of 0.68 and then focused on the EMCCD. A series of filters along the imaging path ensure that only the probe light reaches the EMCCD, while other wavelengths are significantly suppressed. Taking into account all elements of the imaging path along with the quantum efficiency of our EMCCD 0.8, our imaging setup has a photon detection efficiency of approximately 0.61. Transmission and reflection measurements are evaluated over the 11×11 sites around the center of the array.

To measure the directional switching between reflection and transmission, choosing the probe parameters is very critical. The three important factors that constrain the probe parameters are as follows: First, the finite lifetime of the ancilla Rydberg state $|P\rangle$ is in the order of a few ten microsecond. This limits the maximum probe duration of the array. Second, the maximum of the probe power is limited by the Rydberg self-blockade, see Sec. 4.5. This constrains the incident probe Rabi frequency Ω_p for a given control Rabi frequency Ω_c. However, it is not straightforward to increase both Ω_p and Ω_c while keeping the ratio fixed because a larger Ω_c reduces the switching area, see Sec. 4.6.6. Lastly, the number of photons incident on the EMCCD has to overcome the detector's noise floor. To compromise all criteria, we set the probe duration to $t_p = 20\,\mu\text{s}$, which is below the theoretical $|P\rangle$ lifetime of $65\,\mu\text{s}$. The control Rabi frequency of $\Omega_c = 2\pi \times 6.7(6)\text{MHz}$ is chosen to provide a large switching area of $r_b = 4.63\,\mu\text{m}$, see Sec. 4.6.6. Then, we tune the probe Rabi frequency Ω_p to minimize self-blockade for a fixed control power while obtaining enough signal-to-noise ratio in the EMCCD. We empirically end up with an optimum incident probe photon of $0.36(2)$ $(0.44(8))$ photons per lattice site for the transmission (reflection) probe light, which corresponds to $\Omega_p = 2\pi \times 168(5)$ $(189(16))\text{kHz}$. It's important to note that incident photons of the transmission probe light can be directly measured with the EMCCD. In contrast, the reflection probe light propagates in opposite directions away from the EMCCD, therefore, the same calibration method cannot be applied. We instead cross-calibrate with the probe light that used for transmission by comparing the scattering-induced heating on the atomic array [78].

Camera signal to photon conversion

To measure the Rabi frequency of the probe light with the EMCCD, a conversion from the detected signal to the actual impinging photon number is required. We perform two independent calibrations to obtain the conversion factor α from the raw signal c to the impinging photon number N_p, with $\alpha = N_p/c$. In the first method, we measure the amplification gain for a fixed intensity light illuminated on EMCCD by comparing an increase of the signal with and without amplification. We found that the set amplification of 800 in the software yields a measured amplification of 250, resulting in the conversion factor of $\alpha = 0.298(1)$ photon per count. This large discrepancy originates from the well-known degradation of the EMCCD amplification gain [283–285]. The second method exploits the scaling of the photon shot noise, $\Delta N_p = \sqrt{N_p}$. We can derive the relation between the standard deviation of the signal Δc and the signal c as

$$\Delta c = \sqrt{2/\alpha} \cdot \sqrt{c}. \tag{4.4}$$

Note that the factor of $\sqrt{2}$ represents additional noise originating from the amplification process of the EMCCD [286]. By varying the incident light intensity, we capture the

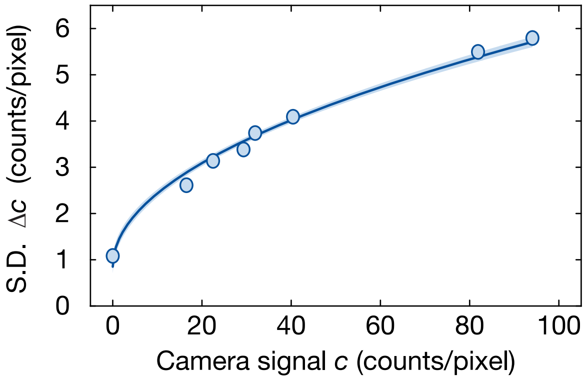

Figure 4.5: Calibration of the EMCCD conversion factor. Standard deviation (S.D.) of detected signal versus mean number of the signal for an intensity-stabilized laser impinging on the EMCCD. Fitting the expected square root scaling provides the conversion factor of $0.32(3)$.

signal and the standard deviation of the signal. Fitting with Eq. (4.4), we obtain the conversion factor of $\alpha = 0.32(3)$, see Fig. 4.5. Both independent calibration methods are in agreement with each other, hence we use their average for analyzing our data.

4.5 Rydberg EIT and optical nonlinearity

Considering the three-level system under the two light fields, as shown in Fig. 4.3, the optical properties of a medium can be dramatically modified in the presence of the strong control light λ_c. This renders a transparent window for the weak probe light λ_p, so-called EIT, which is a consequence of destructive interference between different excitation pathways [212]. The linear response can be described by the first-order susceptibility, which can derived from the polarizability $\chi = 2i\alpha/k_p$. The susceptibility of three-level atoms is given by [212]

$$\chi^{\mathrm{EIT}} = \chi_0 \frac{\Gamma_e}{2i\delta_p - \Gamma_e + \Omega_c^2 \left[2i\Delta_2 - \Gamma_{\mathrm{ryd}}\right]^{-1}}. \tag{4.5}$$

Here, Γ_e and Γ_{ryd} are the natural decay rate of the $|e\rangle$ and $|S\rangle$ states, respectively. We define $\chi_0 = 2\alpha_0/k_p$, and k_p is the wave vector of the probe light. Moreover, $\delta_p = \omega_p - \omega_{\mathrm{eg}}$ and $\delta_c = \omega_c - \omega_{\mathrm{se}}$ are the single-photon detunings of the probe and control lights, respectively, and $\Delta_2 = \delta_p + \delta_c$ is the two-photon detuning. The imaginary part Im $\left[\chi^{\mathrm{EIT}}\right]$ determines the optical response of the medium, whereas the real part Re $\left[\chi^{\mathrm{EIT}}\right]$ determines the dispersion relation. The optical response of the weak probe light in the absence of the control light exhibits a Lorentzian absorption profile with a width of Γ_e. When the strong control light is resonantly coupled, the absorption

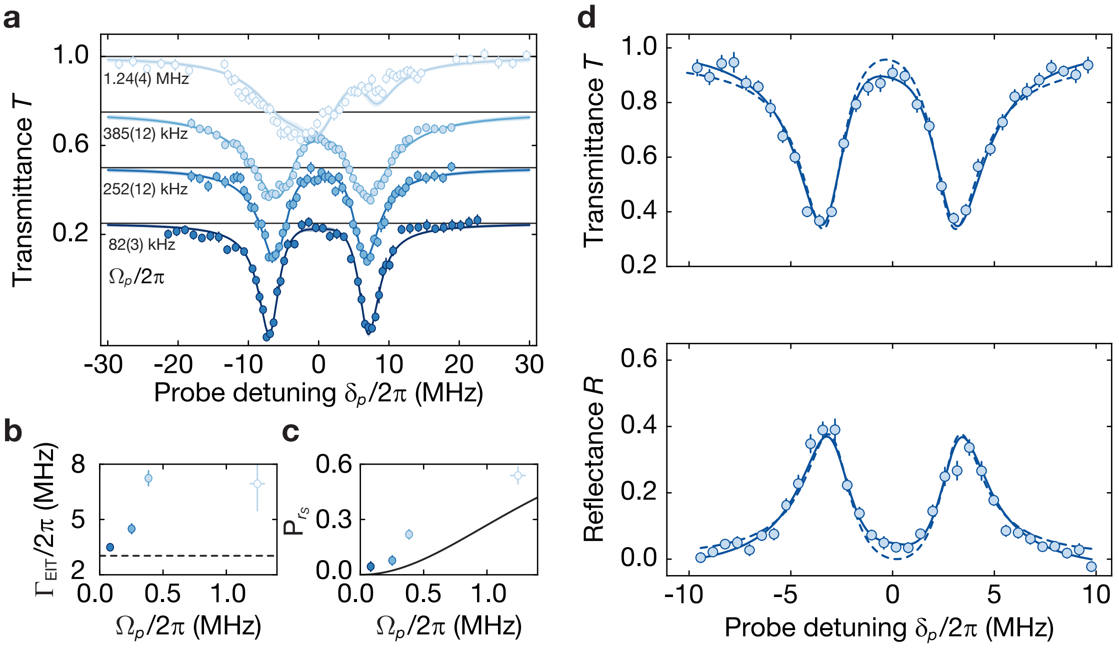

Figure 4.6: EIT nonlinearity due to Rydberg self-blockade. (**a**) EIT spectroscopy for varying probe Rabi frequencies $\Omega_p = 2\pi \times 82(3), 252(8), 385(12)$, and $1245(40)$ kHz with a vertical offset of 0.25 added to each data set for clarity. The incident probe photons are fixed at 39(2) photons with $\Omega_c = 2\pi \times 13.4(6)$ MHz. (**b**) The fitted width of each dips Γ_{EIT} increases with an increase Ω_p. The black dashed line indicates the expected width at $\Gamma_e/2 = 2\pi \times 3.03$ MHz for the single-particle weak-probe limit. (**c**) The Rydberg fraction $P_{|S\rangle}$ extracted from the fits with increasing Ω_p. The black solid line represents the model presented in Eq. (4.8) for comparison. (**d**) The standard single-atom EIT model in Eq. (4.5) (dashed line) and the Rydberg EIT model in Eq. (4.7) (solid line) are fitted to the observed spectroscopic results at low photon flux of 0.32 photons/site. For the fitted Rydberg fraction of $P_{|S\rangle} = 0.16(2)$, we find good agreement using the Rydberg EIT model. The data set was recorded for $\Omega_p = 2\pi \times 168(5)$ kHz and $\Omega_c = 2\pi \times 6.7(6)$ MHz.

dip symmetrically splits into two dips with a separation equal to the control Rabi frequency Ω_c and a width of $\Gamma_e/2$. Therefore, the medium provides the transparent window near the resonance of the probe light, resulting in transmission of the probe photons. By coupling the control light to a Rydberg state, so-called Rydberg EIT, has demonstrated that increasing probe powers lead to a breakdown of the linear optical response in disordered ensembles [267, 287]. A higher probability of the atoms being excited to Rydberg states due to increased probe powers introduces the excitation of a delocalized *Rydberg polariton*, which results in an interaction-induced energy shift

$U_{\text{int}}(r)$ for subsequent excitations of the Rydberg states. Optical nonlinearity emerges when this energy shift significantly breaches the EIT condition. This nonlinearity, known as "Rydberg self-blockade", occurs when the Rydberg fraction, scaling as $\Omega_p^2/(\Omega_p^2+\Omega_c^2)$ in the single particle limit, becomes substantial.

In this section, we study the limit of the Rydberg EIT nonlinearity in subwavelength atomic arrays. We record the EIT transmission for a variable probe Rabi frequency, while maintaining the control Rabi frequency at a constant $\Omega_c = 2\pi \times 13.4(6)$ MHz. The probe Rabi frequency is tuned by keeping the total incident photon fixed at 39(2) photons while varying the illumination time of $t_p = 10\,\text{ms}, 1\,\text{ms}, 400\,\mu\text{s}$, and $40\,\mu\text{s}$. This corresponds to the Rabi frequencies of $\Omega_p = 2\pi \times 82(3), 252(8), 385(12)$, and 1245(40) kHz, respectively. We observe an increase in transmission dips and a broadening of widths with larger probe Rabi frequencies, as seen Fig. 4.6a, consistent with previous studies [288, 289]. The EIT gradually breaks down, most evidently at $\Omega_p = 2\pi \times 1245(40)$ kHz, where the two EIT dips transform into a single dip at the resonance of the probe frequency. To understand the results, we used an EIT model including Rydberg interactions as described in [290, 291]. The model superimposes the susceptibility of a standard two-level atom, which can derive from Eq. (4.1) as

$$\chi^{\text{TA}} = \chi_0 \frac{\Gamma_e}{2i\delta_p - \Gamma_e}, \tag{4.6}$$

with the EIT susceptibility in Eq. (4.5) with the modified two-photon detuning with the Rydberg S state interaction $\Delta_2 + U_{\text{int}}^{\text{SS}}$. This yields the total susceptibility, weighted by the Rydberg (ground) state fraction $P_{|S\rangle}$ $(1 - P_{|S\rangle})$ as

$$\chi^{\text{REIT}} = P_{|S\rangle}\chi^{\text{TA}} + \left(1 - P_{|S\rangle}\right)\chi^{\text{EIT}}. \tag{4.7}$$

The extreme limits of this model are easy to comprehend. If the Rydberg fraction is $P_{|S\rangle} = 0$, the only remaining term is χ^{EIT}, yielding an EIT spectra. Conversely if $P_{|S\rangle} = 1$, when the Rydberg state is fully blockaded, the coupling is shifted out of resonance, retrieving only the two-level atomic response. To extract the spectroscopic line shape, we consider the imaginary part of the total susceptibility, $\text{Im}\left[\chi^{\text{REIT}}\right]$. We fit the modified model of Eq. (4.7) with the amplitude, offset, $P_{|S\rangle}$, Γ_{EIT} and $U_{\text{int}}^{\text{SS}}$ as free parameters. The best fitted results are shown as solid lines in Fig. 4.6a. The fitted EIT width Γ_{EIT} and the Rydberg fraction $P_{|S\rangle}$ both increase with larger probe Rabi frequencies, see Fig. 4.6b,c. We compare the data with the calculated Rydberg fraction derived from a model including the collective enhancement [290],

$$P_{|S\rangle} = \frac{n_{SA}\Omega_p^2\Omega_c^2}{n_{SA}\Omega_p^2\Omega_c^2 + [\Omega_c^2 - 4\delta_p\Delta_2]^2 + 4\Delta_2^2\Gamma_e^2}, \tag{4.8}$$

where $n_{SA} = (1/a_{\mathrm{lat}}^2) \times \pi (r_b^{\mathrm{SS}})^2 \approx 66$ is the atom number in the blockade volume. Here, $r_b^{\mathrm{SS}} = \sqrt[6]{2C_6^{\mathrm{SS}}\Gamma_e/\hbar\Omega_c^2} \approx 2.44\,\mu\mathrm{m}$ is the EIT-blockade radius [292] and $C_6^{\mathrm{SS}} = h \times 3.15\,\mathrm{GHz}\,\mu\mathrm{m}^6$ is the van der Waals coefficient between two atoms in the $|S\rangle$ state. Applying our experimental parameters to Eq. (4.8), this predicts the Rydberg fraction to be below the results obtained from the fits, illustrated by the black solid line in Fig. 4.6c. The discrepancy can be attributed to two main sources: First, the presented model is developed for the weak-probe limit. This is supported in our data, as the reduced Chi-square from the fits increase for larger Ω_p. The model would require further assumptions to capture the essential physics for larger Ω_p, for example using the model including dipole-dipole interaction of subwavelength arrays [293]. Second, the measurements were performed with a relatively high incident photon flux of 39(2) photons/site. After the illumination of the probe light, the atomic filling in the array decreases to approximately 0.7 due to the scattering-induced heating by the probe light, which can influence the transmission detection. In future studies, it would be interesting to repeat the measurements at much lower photon flux, down to 1 photons/site to avoid the heating issue.

Fig. 4.6d shows the EIT spectra at the parameters used in the following sections. The control and probe Rabi frequencies are set to $\Omega_c = 2\pi \times 6.7(6)\,\mathrm{MHz}$ and $\Omega_p = 2\pi \times 168(5)\,\mathrm{kHz}$, respectively. The total incident photons are 0.32 photons for the probe duration of $t_p = 20\,\mu\mathrm{s}$, where the atomic loss from scattering is negligible. In this setting, the minor influence of the Rydberg self-blockade is still evident. The dashed lines represent the fitted results from the simplified EIT model, Eq. (4.5). We observe a noticeable discrepancy, especially at the transparent window near resonance, where the transmittance falls below the fit. Fitting the data with the modified model of Eq. (4.7), shown as solid lines, provides a better agreement with a low Rydberg fraction of $P_{|S\rangle} = 0.16(2)$.

4.6 Switching the subwavelength atomic array

The main concept for controlling our subwavelength atomic array involves transferring the strong interactions between Rydberg states to the optical response of the cooperative array using EIT [212]. We begin with a cooperative atomic array in which emitters are approximately described as two-level systems with the ground state $|g\rangle$ and the excited state $|e\rangle$. On-resonance photons efficiently reflect on the array, see Fig. 4.7a. To induce EIT, the excited $|e\rangle$ state is coupled with a control field Ω_c to a highly excited Rydberg $|S\rangle$ state. Consequently, the cooperative optical response for a weak probe field Ω_p is altered, and the array becomes transparent in the presence of the control field, see Fig. 4.7b. The control field Ω_c inherits the long-range interaction of the $|S\rangle$ state to the excited $|e\rangle$ state. The population of the Rydberg state, determined by Ω_c and Ω_p, is kept sufficiently small to prevent optical nonlinearity caused by Rydberg self-blockade [267, 287]. In order to manipulate the characteristics of the cooperative array, another atom, referred to as the "ancilla", is excited from the ground state $|g'\rangle$ to a neighboring Rydberg $|P\rangle$ state. This results in strong Rydberg interactions between $|S\rangle$ and $|P\rangle$, leading to an energy shift in $|S\rangle$ by $U_{\mathrm{int}}(r)$. The interaction shift exceeds half of the EIT spectral width within a "blockade disc" of radius r_b [146, 294], centered around the location of the ancilla. As a result, the EIT condition is disturbed within the blockade volume, causing the optical properties to switch back to those of the cooperative array, thereby reflecting the probe photons, see Fig. 4.7c.

4.6.1 Spectroscopy signature

In a first set of experiments, we probe the spectroscopic signature of switching the cooperative mirror by the ancilla atom. The measurements are performed with an array of approximately 250 atoms, where the array radius is comparable with the expected blockade radius. We begin by reproducing our previously published results on the cooperative nature of our atomic array by measuring the transmission and reflection response of the probe beam frequency sweep near the $|g\rangle \leftrightarrow |e\rangle$ transition. In comparison to the previous work [78], where the experiment was conducted at the incident photon flux of 20 photons/site, we operate at a much lower flux of 0.36(2) photons/site to avoid Rydberg self-blockade, as discussed in Sec. 4.5. Operating in the weak photon limit, we can reproduce the subradiant Lorentzian lineshape. The extracted width is $\Gamma_{\mathrm{M}} = 2\pi \times 4.40(32)/3.75(14)$MHz for transmission/reflection, which is narrower than the natural linewidth of $\Gamma_e = 2\pi \times 6.06\,$MHz, as shown in Fig. 4.8a. Next, we demonstrate the transparency of the probe light using the EIT. We illuminate the atomic array with the resonance control field on the $|e\rangle \leftrightarrow |S\rangle$ transition simultaneously while collecting the probe light. We observed the characteristic EIT signature, where the transmission dip splits into two dips with a spectral separation on the order of the control Rabi frequency $\Omega_c = 2\pi \times 6.7(6)\,$MHz. This results in

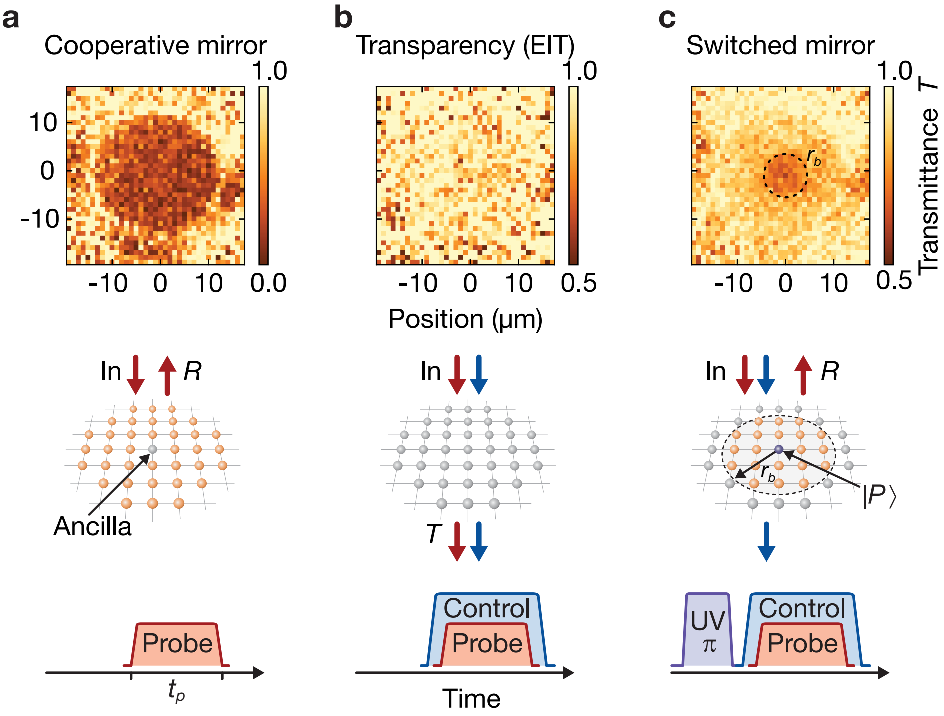

Figure 4.7: Switching subwavelength array. The top, middle, and bottom rows show a spatially resolved optical response in transmission, the atomic array with the relevant light fields, and the corresponding experimental pulse sequences, respectively. (**a**) The cooperative atomic array, consisting of 1500 atoms, strongly reflects the probe photons, causing low transmission over the entire array. (**b**) When the coupling field is activated, the array turns transparent as photons pass through without interacting, leading to complete transmission. (**c**) The ancillary atom is excited to the $|P\rangle$ state using the resonant UV light, resulting in a significant energy shift $U_{\text{int}}(r)$ that interrupts the EIT condition. The probe photons are reflected within the blockade area of radius r_b.

a transparent window for the probe light near the resonance, which means that the atomic array is transparent for the probe photons. Taking a closer look at the reflection, the EIT doublet reveals signatures of a cooperative response with an enhanced high reflectance of $0.37(2)$, exceeding the reflectance signal for isotropic scattering $0.16(3)$, see Sec. 4.6.1. The width of each EIT doublet is $\Gamma_{\text{EIT}} = 2\pi \times 2.95(17)$ MHz, consistent with the expected width from the single-particle limit $\Gamma_e/2$. The parameters were selected to maximize the contrast between the cooperative mirror and the EIT response at the resonance of the probe detuning with a fixed probe duration of $t_p = 20\,\mu\text{s}$. At the same time, the selected parameters must meet the constraints of minimizing Rydberg

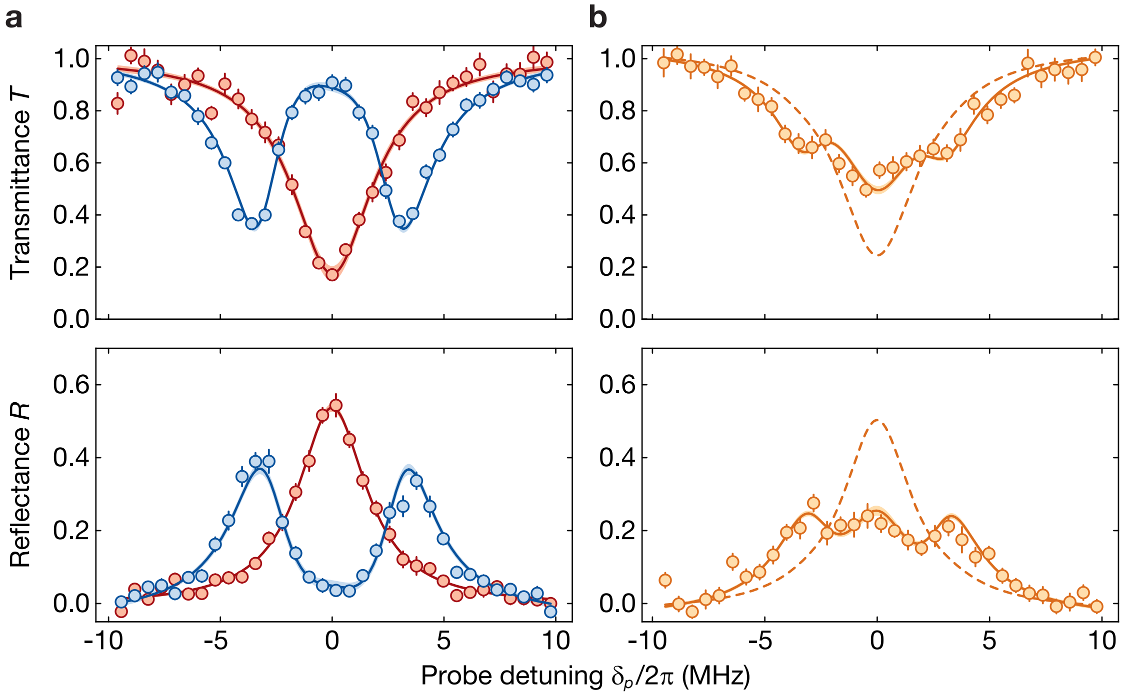

Figure 4.8: Cooperative response in absence and presence of the ancilla Rydberg excitation. (**a**) Cooperative response of the atomic array with (blue) and without (red) control field for a probe duration of $t_p = 20\,\mu\text{s}$, with the ancilla prepared in $|g'\rangle$. Without the control field, we reproduce the cooperative subradiant response of the cooperative array with a reduced transmission/reflection width of $\Gamma_\text{M} = 2\pi \times 4.40(32)/3.75(14)\text{MHz}$. With the control laser present, we observe a splitting of the EIT doublet, where the width of each peak amounts to $\Gamma_\text{EIT} = 2\pi \times 2.95(17)/3.01(28)\text{MHz}$ in transmission/reflection and a minimal/maximal transmittance/reflectance of 0.35(2)/0.37(2) is observed. (**b**) When preparing the ancilla atom in the Rydberg $|P\rangle$ state, the spectrum (orange) changes dramatically and reveals a triple-peak structure, featuring contributions of both the cooperative mirror and EIT spectrum. By superimposing both spectra while having the ancilla Rydberg fraction $P_{|P\rangle}$ and a global offset as free fit parameters, we find excellent agreement with our data set, with $P_{|P\rangle} = 0.61(2)/0.45(2)$ in transmittance/reflectance. The dashed lines illustrate the expected spectra assuming ideal ancilla preparation and substantially shorter probe duration than the Rydberg lifetime ($t_p = 2\,\mu\text{s}$), thereby improving the ancilla Rydberg fraction to $P_{|P\rangle} = 0.96$.

self-blockade and ensuring a sufficient signal-to-noise ratio of the probe light on the EMCCD, as detailed in Sec. 4.4.2. Finally, we demonstrate the switch mechanism using the single ancilla atom by applying a pulse duration of $t = \pi/\Omega_\text{UV}$ on the $|g'\rangle \leftrightarrow |P\rangle$

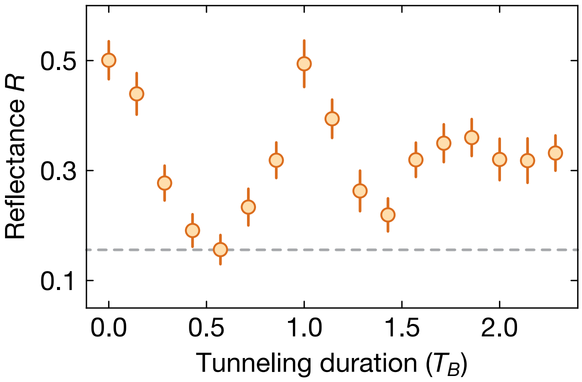

Figure 4.9: Reflectance under vertical Bloch oscillation. At half of the Bloch oscillation period ($0.5T_B$), the cooperative response is disrupted as the atoms are vertically displaced to their maximum extent, leading to isotropic scattering of the disordered atoms. The dashed line shows the reflectance of $0.16(3)$ at the half oscillation period.

transition, and then probing in the same manner as in the EIT measurements. The resulting spectrum consists of three peaks. This triple peak structure arises from a combination of the cooperative array and EIT spectrum, which corresponds to scenarios with and without the ancilla Rydberg atom present. We can fit a simplified model of a statistical mixture of the switched and unswitched cases, weighted according to the probability of finding the ancilla in the Rydberg or ground state, as represented by the solid lines in Fig. 4.8b. From the fit of the transmission/reflection data, we extract the ancilla Rydberg probability of $P_{|P\rangle} = 0.61(2)/0.45(2)$. The results are in a good agreement with an independent reference measurement of $P_{|P\rangle} = 0.52(8)$. The two major limitations in achieving a high ancilla Rydberg probability are attributed to an imperfect initial state preparation of the ancilla in $|g'\rangle$ (Sec. 4.4.1) and the decay of the ancilla Rydberg state during probing (Sec. 4.6.3). Potential improvements could be realized by upgrading the setup to have perfect ancilla preparation in $|g'\rangle$ and substantially shortening the probe duration of $t_p = 2\,\mu s$ with better probe photon detector so that the decay of the Rydberg ancilla becomes negligible. We illustrate the ideal case of expected spectra with dashed lines in Fig. 4.8b assuming all improvements are implemented.

Inducing spatial disorder through Bloch oscillations

We compare the cooperative response with the dissipative free-space scattering from disordered atoms by inducing vertical Bloch oscillations, which introduce a position spread along the propagation direction of the probe light. In this way, the probe light experiences the same optical depth, ensuring that the observed change in the optical response of the array is caused by spatial disorder. We begin with a 2D ordered array at a depth of 15 E_r and 20 E_r in the vertical and horizontal lattices, respectively. The combination of a magnetic field and gravity gradient creates a potential energy difference between adjacent lattice sites of $\Delta_z = \; h \times 360\,\mathrm{Hz}$ along the vertical axis. By instantaneously reducing the vertical lattice depth to $4E_r$, the ordered array spreads vertically and refocuses after the Bloch period of $T_B = h/\Delta_z \sim 2.8\,\mathrm{ms}$. At half period $(0.5T_B)$, the atoms are maximally displaced with a displacement of $d_z = 4Ja_{\mathrm{lat}}/\Delta_z \sim 3.6\,\mathrm{a}_{\mathrm{lat}}$, where J is the tunneling rate in the vertical direction. At this point, we measure the reflectance of 0.16(3) at resonance, which is equivalent to the expected isotropic scattering of approximately 0.13 for a single particle, given our objective's NA of 0.68.

4.6.2 Coherent control of cooperative response

After demonstrating the switching capabilities and studying the spectroscopy signature in the previous section, we proceed to the next step by emphasizing the capability to dynamically alter the optical properties of the array via coherent manipulation of the ancilla atom. Here, we drive the ancilla atom from $|g'\rangle$ to the Rydberg state $|P\rangle$ for variable pulse durations. This results in a coherent Rabi oscillation with Rabi frequency of $\Omega_{\mathrm{UV}} = 2\pi \times 1.22(2)\,\mathrm{MHz}$, see Fig. 4.10a. We measure the population of the ancilla atom in the ground state $|g'\rangle$ after applying the driving field, under the assumption that the Rydberg state is untrapped in the optical lattice. In the same sequence, the recorded transmission/reflection of the probe light shows strong correlation with the ancilla Rabi oscillation. The properties of the array switch from transmitting to reflecting when the ancilla is driven from $|g'\rangle$ to $|P\rangle$ and resume transmitting when the ancilla is driven back to $|g'\rangle$. The solid lines in Fig. 4.10b,c show fits of the transmission and reflection dynamics with a damped sinusoidal function, which is in a good agreement with the data. For these fits, the oscillation frequency is fixed using the fitted result of the ancilla the ancilla Rabi oscillation, while the amplitude and offset are left as free fit parameters. However, we notice some small distortions in the transmission data. We attribute these to a non-vanishing probability of initially having two ancilla atoms before exciting to the Rydberg state, as discussed in Sec. 4.6.2. In particular, the oscillating reflectance is above the single-particle limit of (0.16(3)), which we measured experimentally by introducing vertical disorder through Bloch oscillations, see Sec. 4.6.1. This emphasizes that the cooperative response of the mirror is preserved during the oscillation.

Enhanced Rabi oscillations

We investigate the distortions in Fig. 4.10b more thoroughly by examining the ancilla Rabi oscillation in this dataset. By analyzing the histogram of the fluorescence counts at the position of the ancilla atom, we identify three separated peaks. These peaks represent an occupation of $N_{g'} = 0, 1, 2$ atoms in $|g'\rangle$ from low to high signal counts, respectively, see Fig. 4.11a. The separation of the rightmost peak ($N_{g'} = 2$ atoms) is smaller than the expected equal separation of the discrete atom number. This is because

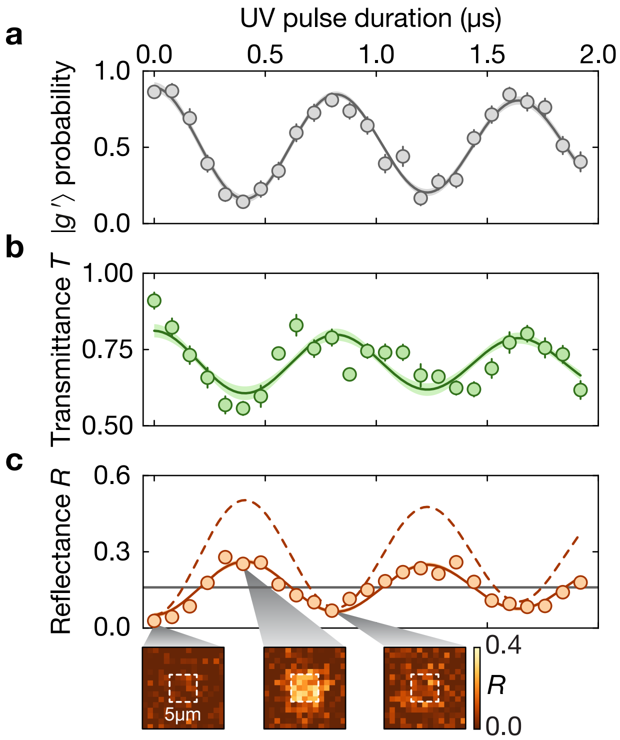

Figure 4.10: Cooperative response while coherently driving the ancilla atom. (**a**) Ancilla $|g'\rangle \leftrightarrow |P\rangle$ Rabi oscillations obtained from ground state $|g'\rangle$ fluorescence detection through varying the length of the UV pulse before probing. Applying a damped sinusoidal fit, we find a Rabi frequency of $\Omega_{\text{UV}} = 2\pi \times 1.22(2)$ MHz and a decay constant of $\tau_{\text{decay}} = 6(3)$ μs. We observe the transmittance (**b**) and reflectance (**c**) data to follow the Rabi oscillation of the ancilla. The solid lines in **b** and **c** represent the best fit results, with the amplitude of the oscillation and overall offset as the only fit parameters, while the oscillation frequency and decay time are fixed and taken from **a**. The three insets in **c** display spatially-averaged reflection images for $\Omega_{\text{UV}}t = 0$, π and 2π, respectively, with an indicated ROI of 5×5 μm. The dashed line in **c** illustrates the expected transmission signal for an ancilla Rydberg fraction of $P_{|P\rangle} = 0.96$. The gray solid line represents the resonance reflection signal (0.16(3)) from isotropic scattering.

the $N_{g'} = 2$ atoms occupy different adjacent sites in the vertical lattice, originating from imperfect preparation of MI in the early stages before ancilla preparation. The adjacent sites are out of focus of the objective, leading to a diminished fluorescence signal during imaging. We verify this by intentionally preparing atoms to occupy two layers at the adjacent site of the vertical lattice, which results in a histogram with an identical distribution spacing. The reduction of the fluorescence signal from the different planes cannot discriminate $N_{g'} = 2$ by our reconstruction script, as it only

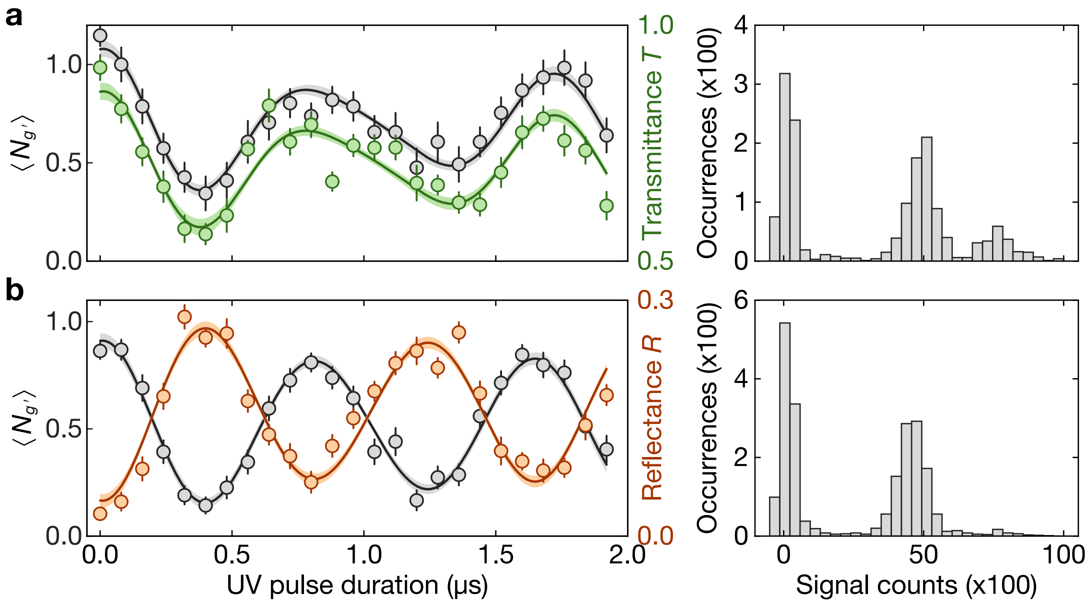

Figure 4.11: Rabi oscillations and related fluorescence histograms. (**a, left**) The average detected atom number in $|g'\rangle$ during the ancilla Rabi oscillation using the new thresholds from **a, right** to differentiate atom number (gray) and the corresponding transmittance oscillation (green). A finite population in $N_{g'} = 2$ gives rise to a beating oscillation between the single-atom frequency and two-atom enhanced Rabi frequency. (**b, left**) The average detected atom number in $|g'\rangle$ during ancilla Rabi oscillation with new thresholds from **b, right** to differentiate atom number (gray) and corresponding reflectance oscillation (brown). This dataset has a negligible population in $N_{g'} = 2$, resulting in clean oscillations featuring a single frequency. (**right**) The histograms of the fluorescence signal, evaluated from ancilla Rabi oscillation data, are shown on the left. These histograms provide the thresholds for differentiating the number of atoms, used in the Rabi oscillation analysis. The transmission dataset has a probability of 0.28(5) for initially having two ancilla atoms. In contrast, the reflection dataset, with its improved preparation fidelities, presents a negligible fraction of two-atom instances.

accounts for the equal spacing of the histogram to identify $N_{g'} = 2$ atoms. Therefore, the $N_{g'} = 2$ peak on the histogram was considered as a single atom occupation. Based on this new histogram in Fig. 4.11a, we defined new thresholds to differentiate between $N_{g'} = 0$, $N_{g'} = 1$ and $N_{g'} = 2$. We obtain ancilla probabilities of 0.42, 0.44, and 0.14 for $N_{g'} = 0, 1, 2$, respectively. Note that the probabilities throughout the entire oscillation experiences a 50% loss due to the Rydberg state being untrapped. We, thus, reevaluate the atom numbers contributing to the Rabi oscillation $\langle N_{g'}(t)\rangle$ shown in Fig. 4.11a. The new evaluation exhibits a deviation from a pure sinusoidal single-frequency oscillation, which significantly improves the agreement with the observed transmittance. Based on the observation of $N_{g'} = 2$ for the ancilla atoms, we extend our model accounting for the additional frequency, which is enhanced by $\sqrt{N_{g'}}$ [131, 134]. The fit model leaves relative amplitudes, which directly connect to the probability of $N_{g'} = 0, 1, 2$ as free fit parameters The fit, represented by the black solid line in Fig. 4.11a, is in excellent agreement with the data. We obtain the initial probability of $P_2(t = 0) = 0.28(5)$ for $N_{g'} = 2$. This initial probability averages to $\langle P_2(t)\rangle = 0.14(3)$, taking into account a 50% loss pf the untrapped Rydberg state during the dynamics, and provides excellent agreement with the population obtained from the histogram. The same model from the Rabi oscillation fit of $\langle N_{g'}\rangle$ is fitted to the transmission data with a global amplitude and offset rescaling, where the oscillation frequency and relative amplitude remain fixed. The presence of the second ancilla atoms manifests itself in the enhanced oscillation frequency and inherits to the atomic array properties. Repeating the measurements with an imrpoved initial state, where $N_{g'} = 2$ from adjacent vertical occupation is suppressed, we obtain a pure single frequency, as seen in Fig. 4.11b.

4.6.3 Detecting the Rydberg ancilla lifetime

After demonstrating the working principle of the switching, we reverse the argument and use the scattered probe photons as a non-destructive detection of the ancilla Rydberg states. After applying the excitation pulse with a duration of $t = \pi/\Omega_{UV}$, exciting the ancilla to the Rydberg $|P\rangle$ state, we vary the time interval δt between the ancilla excitation pulse and the detected transmission of the probe. A schematic of the sequence is shown in Fig. 4.12. We observe an increase in transmittance with a longer delay time δt. This is caused by the Rydberg decay which reduces the Rydberg fraction $P_{|P\rangle}$, so that the properties of the array change from reflecting to transmitting. We can estimate the Rydberg fraction $P_{|P\rangle}$ by

$$P_{|P\rangle}(\delta t) = \frac{\eta_{\text{init}}}{t_p} \int_{\delta t}^{\delta t + t_p} e^{-t'/\tau} dt', \tag{4.9}$$

where η_{init} is the efficiency of initially preparing the ancilla atom in $|P\rangle$. By fitting Eq. (4.9) to the transmission data, we leave the initial preparation efficiency η_{init} and the Rydberg lifetime τ as free fit parameters. The two limits in the fit, at long interval $\delta t > 120\,\mu\text{s}$ and short interval $\delta t = 4\,\mu\text{s}$, are constrained by the transmittance of the EIT and cooperative mirror, respectively. The fitted initial preparation efficiency of $\eta_{\text{init}} = 0.85(10)$ aligns with the independent measurement to prepare the ancilla in $|g'\rangle$, assuming a perfect excitation pulse from $|g'\rangle$ to $|P\rangle$. We extract the Rydberg lifetime of $\tau = 27(5)\,\mu\text{s}$ from the fit. Comparing the Rydberg lifetime τ with a theoretical estimate of 65 µs at $T = 300\,K$ from the "ARC" package [102] and an experimental measurement of 64.2(26) µs of ^{85}Rb atoms in a magneto-optical trap [295], our measured lifetime is lower by approximately a factor of two. We investigate two potential factors that might

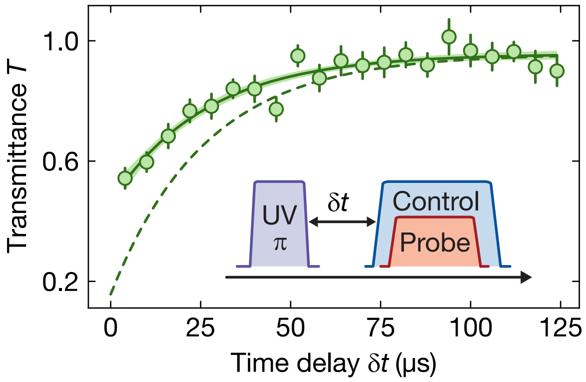

Figure 4.12: Rydberg ancilla lifetime. The transmission signal for variable delay time δt between Rydberg excitation and probe pulse. We extract the Rydberg lifetime $\tau = 27(5)$ μs from an exponential fit (solid line). The dashed line is the expected transmission signal for an ancilla Rydberg fraction of $P_{|P\rangle} = 0.96$.

contribute to this discrepancy: photoionization from the optical lattice light and the motion of the ancilla atom. A previous observation in [113] measured photoionization via the loss rate of the dilute atomic cloud by off-resonant dressing to the Rydberg state, $\delta_{\mathrm{UV}} \gg \Omega_{\mathrm{UV}}$. The results show a negligible effect of photoionization up to lattice depths of 1000 E_r. With regard to the motion of the ancilla atom, we numerically solve the time evolution of the initial wave packet under one-dimensional (1D) optical lattice at a depth of 100 E_r. Due to the anti-trapping of the Rydberg state, the initial wave packet initially localized at a single lattice site expands approximately up to 5.3 μm within $t = 120$ μs. This expansion of the ancilla moves the blockade volume out of the analysis region, resulting in a slightly increased measured transmittance. Due to the momentum kick of the excitation photon, the in-plane motion has a larger influence compared to a vertical expansion. However, the ancilla motion alone can only explain the lifetime shortened of approximately $20 - 30\%$. As a consequence, further possible effects need to be investigated in the future.

4.6.4 Distribution of detected photons

Until now, we have focused on the average properties of the detected photons. In addition, it is also interesting to observe the statistics of the scattered photons, as they provide a further understanding of the correlation between the states of the ancilla and the states of the probe photons. In an ideal case, we expect photons within a detection area to either be only reflected or transmitted, depending on whether the ancilla is excited to the Rydberg state $|P\rangle$ or remains in its ground state $|g'\rangle$. We monitor the reflected photons for a duration of $t_p = 60$ μs, expecting that the histograms of the two cases will be clearly distinguishable. The observed histograms are shown

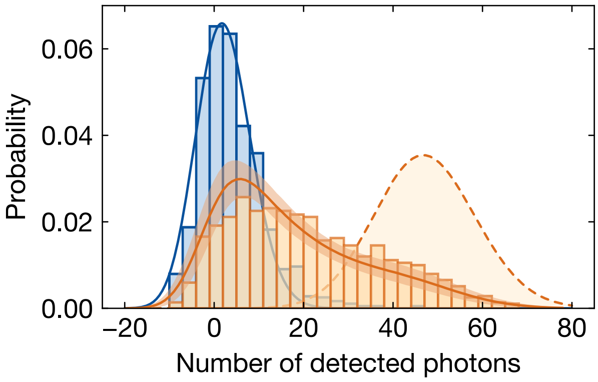

Figure 4.13: Distribution of detected photons. The distribution of detected reflection photons, relative to the mean background photon numbers, in the ROI of 5 × 5 µm. For the ancilla in the $|g'\rangle$ state (blue histogram), we obtain a Poissonian distribution corresponding to the photon counts in the EIT configuration (blue solid line). When the ancilla is prepared in $|P\rangle$ (orange histogram), the histogram acquires a tail toward high photon numbers. This histogram is a combination of photons due to Rydberg-induced reflection (orange dashed line) and photons at low photon numbers due to imperfect Rydberg preparation and Rydberg decay. A Monte-Carlo simulation that includes our experimental uncertainties reproduces the essential features observed in the histogram (orange solid line and shaded region). The orange dashed curve represents an expected histogram which assumes an absence of Rydberg decay and perfect ancilla preparation, providing a clear separation of histogram.

in Fig. 4.13. These have been subtracted with a background of $\mu = 16.0(7)$ photons independently measured without the array. The blue histogram represents the case when the ancilla atom remains in its ground state $|g'\rangle$. We model the probability distribution of the detected photons with a Poissonian distribution, with a variance exceeding the photon shot noise by a factor of two due to the stochastic EMCCD amplification process [286]. The best fit has $\mu = 18.3(7)$ photons, which is slightly higher than the photon background. When the ancilla atom is excited to the Rydberg state $|P\rangle$, we find a broad asymmetric histogram, represented in orange, exhibits a long tail at high photon numbers in addition to a peak at low photon numbers. To explain the detected shape, we repeatedly run the following steps to generate a simulated histogram. We assume the histogram is a combination of two distinct Poissonian distributions corresponding to two ancilla states, $|g'\rangle$ and $|P\rangle$. The first Poissonian has a mean fixed at $\mu = 18.3(7)$ photons, while the second "switched" Poissonian remains to be determined. The relative weight between these two contributions is defined by the preparation fidelity of 0.85(10), see Sec. 4.4.1, and the Rydberg $|P\rangle$ lifetime of $\tau = 27(6)$ µs, see Sec. 4.6.3. We perform a Monte-Carlo simualtion, where we randomly sample the initial Rydberg fraction and the Rydberg decay within their respective error bars for each instance from a Gaussian distribution. After running the aforementioned procedure for 10^5 independent realizations, we varying the mean photon number of the second Poissonian until the simulated histogram is best reproduces our data. The best agreement shows that the second "switched" Poissonian has a mean value of $65(2)$ photons. By performing 5000 independent runs, each containing 10^4 independent sets of photon numbers, we derive a predicted histogram and standard deviation, shown in the orange solid curve and shade area in Fig. 4.13, using the experimental parameters. The orange dashed curve, as a reference, represents an expected histogram which assumes an absence of Rydberg decay and perfect ancilla preparation, providing a proper separation between the Poissonian distributions. Here, the preparation and the short Rydberg lifetime of the ancilla atom are the limitations factor for achieving better switching performance.

4.6.5 Precursor of ancilla-photon correlations

In Fig. 4.10, we coherently drive the Rydberg fraction of the ancilla before probing the optical response of the array. We find, as expected, that the reflection/transmission properties are entirely controllable using the ancilla state. In fact, after applying a pulse area of $\Omega_{\mathrm{UV}} t = \pi/2$ on the ancilla, and subsequent measurement of the optical properties and the ancilla state, we would expect a correlation of the measured ancilla state and the reflection/transmission of the photons. This is due to the entanglement between the ancilla state and the photon,

$$|\Psi\rangle_{\mathrm{ancilla-photon}} = \frac{1}{\sqrt{2}} \left(|g'\rangle \otimes |T\rangle + |P\rangle \otimes |R\rangle \right) , \tag{4.10}$$

where $|g'\rangle/|P\rangle$ represents the Rydberg/ground state of the ancilla and $|T\rangle/|R\rangle$ represents the transmitting/reflecting photonic state. We can clearly see a first indication of this correlation in our data, as illustrated in Fig. 4.14. Here, we post-select for the absence the ancilla atom, denoted as the Rydberg $|P\rangle$ state, revealing the expected increase in reflectance. Conversely, post-selecting on the presence of the ancilla atom, labeled as the ground state $|g'\rangle$, shows the reduction in reflectance. The imperfect correlation signal after applying post-selection can be attributed to the imperfect preparation of the ancilla and the decay of the Rydberg ancilla after probing. For example, a vacant site at the target ancilla due to imperfect preparation can cause false events labelled as $|P\rangle$, as a missing ancilla atom is mapped to the Rydberg state, leading to incorrect labeling of $|P\rangle \otimes |T\rangle$. In a second instance, the decay of the Rydberg ancilla to the ground state after probing leads to incorrect labeling of $|g'\rangle \otimes |R\rangle$. Therefore, future work on atom-photon correlation with an upgraded setup will be intriguing to observe the degree of signal improvement. Therefore, future work on atom-photon entanglement might become visible when operating with an upgraded setup, such as an improved photon detector and a better initial state preparation.

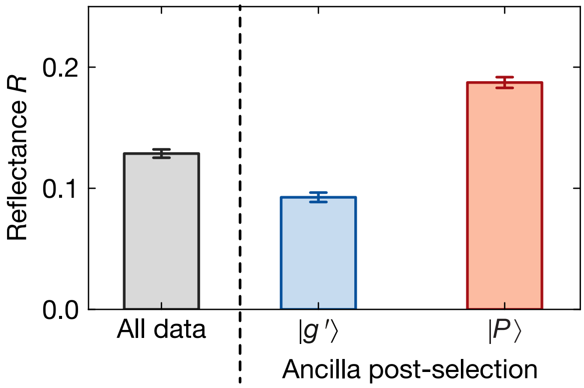

Figure 4.14: Correlation of the ancilla and photonic state. For the presented data set, we first apply the UV $\pi/2$-pulse, preparing the ancilla in a coherent superposition between the ground and the Rydberg state. We then apply the 60 µs probe pulse while detecting the reflection signal, followed by the push out pulse to remove the array atoms. Finally, the ancilla state is detected by fluorescence imaging. Without post-selection ("All data"), we find a reflectance of 0.129(2), which is approximately half the reflectance obtained after the ancilla is excited to the Rydberg state. With post-selection, we can divide the same data into two subsets, where either the presence ("$|g'\rangle$") or absence ("$|P\rangle$") of the ancilla atom at the end of the sequence was observed. Performing this analysis, we observe the correlation, where the ancilla in the $|g'\rangle$ ($|P\rangle$) state resulted in a lower (higher) reflectance, hinting a first indication for atom-photon entanglement.

4.6.6 Spatial switching area

The subwavelength array naturally achieves high cooperative properties from dipolar interactions, where the free space strongly relaxes the mode selection. Our fundamentally new approach can spatially control the mode of single photons that interact with the array over the position of the ancilla atom. In this section, we probe and demonstrate the finite spatial switching area due to the finite Rydberg interactions, discuss the tuning ability of the switching area, and the possible solution to mitigate limitations. To estimate the blockade radius, we assume a van der Waals interaction of $U_{\text{int}} = C_6/r^6$ with C_6 being the interaction strength. The blockade radius $r_b = (2C_6\Gamma_e/\hbar\Omega_c^2)^{1/6}$ is defined at the point where the interaction strength equals the width of the EIT transparency window $\Omega_c^2/(2\Gamma_e)$ [292, 294]. With that, we theoretically estimate the blockade radius of $r_b = 4.6$ µm for our experimental parameters. Interestingly, a more complex model, including all relevant interaction potentials from neighbor states, agrees with this simplified model, see Sec. 4.6.6. We measure the switching area by monitoring the area around the ancilla atom by evaluating a radial average of the transmittance, see Fig. 4.15. We compare the optical response of a small atomic array of

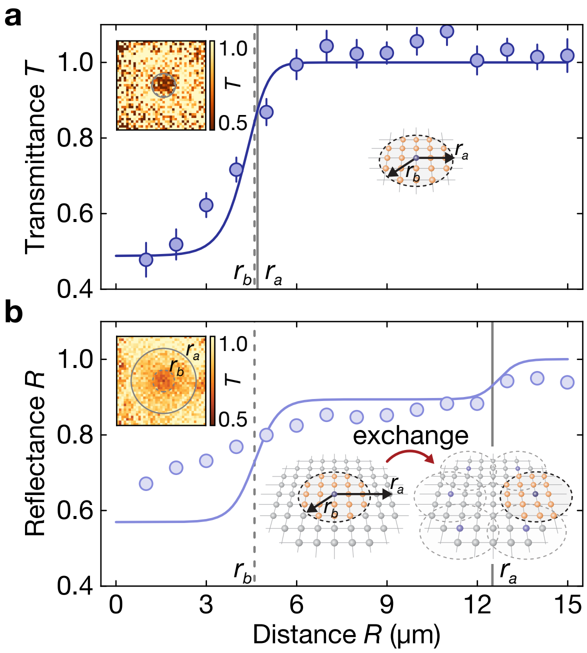

Figure 4.15: Spatially resolved switching area. The radially averaged transmittance over the size of the switched array, centered around the ancilla atom. The solid lines depict the estimated radial profile, taking into account the $|S\rangle - |P\rangle$ blockade, array size and Rydberg fraction of the ancilla $P_{|P\rangle}$. The insets in the upper left corner show the spatially-averaged transmission images. The solid and dashed gray lines mark the array radius r_a and the estimated blockade radius r_b, respectively. (**a**) The transmittance of the array, which contains 250 atoms and is comparable in size ($r_a \approx 4.7\,\mu\text{m}$) to the blockade radius, aligns well with the estimated radial profile. (**b**) The array of 1500 atoms with a radius $r_a \approx 12.5\,\mu\text{m}$, which is large compared to blockade radius, shows a gradual change of the transmittance, deviating from the solid line. This can be explained by long-range exchange processes, where the $|P\rangle$ excitation undergoes $|S\rangle - |P\rangle$ exchange, resulting in the transportation of the excitation and hence a shift of the switching area, as illustrated by the sketch.

radius $r_a = 4.7(7)\,\mu\text{m}$, comparable to an expected blockade radius r_b, and a larger array of radius $r_a = 12.5(5)\,\mu\text{m}$, exceeding the expected blockade radius. In the small array, we observe a relatively sharp edge where the transmission abruptly changes from its central value of $0.48(2)$ to a full transmission. This is attributable to the combination of the finite size of the array r_a and the blockade radius r_b. Unlike the small array, the large array exhibits an increased transmittance at the center and a more gradual increase in transmittance beyond the blockade radius. This reveals the presence of long-range exchange processes between the $|S\rangle$ and $|P\rangle$ state during probing, which has previously been studied in [292, 294]. These exchange processes delocalize the ancilla $|P\rangle$ excitation over the entire system, resulting in a smooth transmittance signal. The derivation and discussion of the exchange processes are explained in more detail in Sec. 4.6.6. Notably, these exchange processes can be mitigated by either operating with shorter probe timescales or reducing the probe Rabi frequency, as the relevant exchange process scales with $\propto \Omega_p^2$ [292]. Access to this regime can be achieved by upgrading to a single-photon detector array, which maps each spatial mode of the light field to an individual detector within the detector array while maintaining spatially resolved parallel detection.

Derivation of the EIT-blockade radius

To estimate the blockade radius, we first calculate the interaction potentials for the $|SP\rangle$ and $|PS\rangle$ pair states under a bias field of $B_z = 28.5\,\mathrm{G}$ used in the measurements. We use the "Pairinteraction" software [98] that performs an exact diagonalization of the electrostatic interaction hamiltonian of numerous pair states $|r', r''\rangle$ that are coupled with the target state $|SP\rangle$. Fig. 4.16a shows the distance-dependent interaction energies $U_{\mathrm{int}}^{r'r''}(r)$ and the relative overlap of the coupling strength $|C_{r'r''}(r)|^2$ with the target $|SP\rangle$ pair state, given by the blue coloring. For the pair states composed of opposite parity, the interactions are typically described by resonant dipole-dipole interactions following a scaling of $\propto 1/r^3$, as discussed in Sec. 2.3.1. However, our chosen Rydberg states of $|S\rangle = |44S_{1/2}, m_J = -1/2\rangle$ and $|P\rangle = |44S_{1/2}, m_J = +3/2\rangle$ have vanishing first-order dipole-dipole matrix elements due to the magnetic quantum numbers differing by $\Delta m_J = 2$. Instead, the interactions are described in second-order perturbation theory by van der Waals interactions $\propto 1/r^6$, which arise from off-resonant coupling to pair states formed by neighboring Zeeman sublevels, as discussed in Sec. 2.3.1. To compare with the simple van der Waals interactions $U_{\mathrm{int}} = C_6^{\mathrm{SP}}/r^6$, we fit the interaction potential for $r > 4\,\mu\mathrm{m}$ and find the van der Waals coefficient of $C_6^{\mathrm{SP}} \approx h \times 35\,\mathrm{GHz}\,\mu\mathrm{m}^6$, as shown by the red dashed line in Fig. 4.16a,b. Next, we derive the EIT-blockade radius r_b by analyzing the single-particle optical response $\mathrm{Im}[\chi]$ of the probe transition using the calculated interaction potentials. The model includes all relevant Rydberg pair states $|r'r''\rangle$ with respect to Rydberg interaction of $U_{\mathrm{int}}^{r'r''}(r)$ at $\delta_p = \delta_c = 0$,

$$\begin{aligned} H =& \frac{\hbar}{2}\Omega_p |e\rangle\langle g| + \frac{\hbar}{2}\sum_{r',r''} \Omega_c C_{r'r''} |r'r''\rangle\langle e| \\ &+ \sum_{r',r''} U_{\mathrm{int}}^{r'r''}(r) |r'r''\rangle\langle r'r''| + h.c.. \end{aligned} \tag{4.11}$$

Here, $C_{r'r''} = \langle r'r''|SP\rangle$ is the overlap of $|r'r''\rangle$ with the bare pair state $|SP\rangle$. By considering only the Rydberg pair states with $|C_{r'r''}|^2 > 0.05$ and $U_{\mathrm{int}}^{r'r''} < h \times 100\,\mathrm{MHz}$, we calculate the steady-state solution of the probe transition density matrix (ρ_{eg}) using the "QuTiP" package [296]. The results for the distance-dependent optical probe

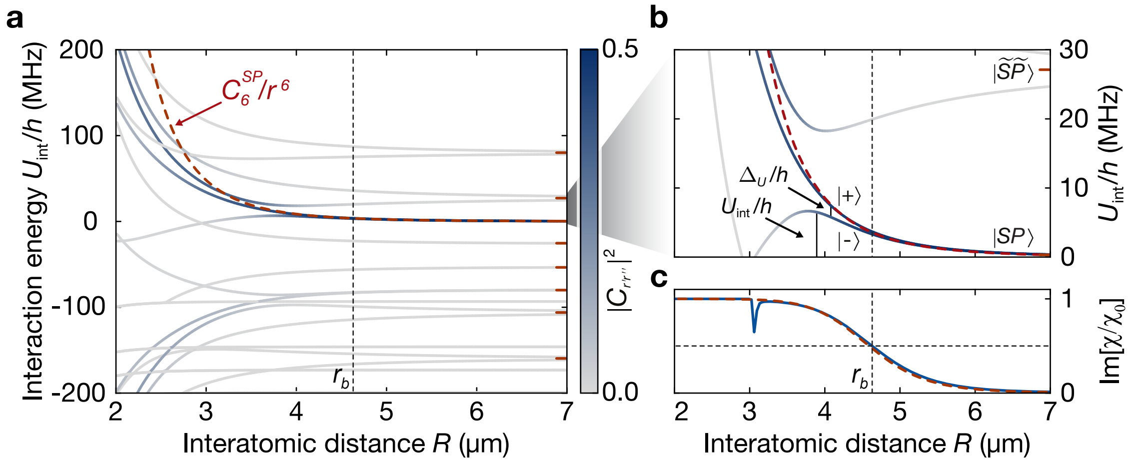

Figure 4.16: Interaction potentials and optical response. (**a**) Potential energy curves relevant for $|r'r''\rangle$ pair state coupling the $44S_{1/2}$ and $44P_{3/2}$ Rydberg states in an external magnetic field of $B_z = 28.5\,\mathrm{G}$. The intensity of the blue coloring indicates the relative optical coupling strength $|C_{r'r''}|^2$. The red ticks at a large distance mark the magnetic sublevel splittings. The red dashed curve resembles the fitted van der Waals potential C_6^{SP}/r^6 with $C_6^{\mathrm{SP}} \approx h \times 35\,\mathrm{GHz}\,\mu\mathrm{m}^6$. (**b**) Potential energy curves in the close vicinity of the EIT-blockade radius r_b (vertically-dashed line). The red ticks mark the asymptotic state $|SP\rangle$ and $|\tilde{S}\tilde{P}\rangle$, where $|\tilde{S}\rangle = |44S_{1/2}, m_J = +1/2\rangle$ and $|\tilde{P}\rangle = |44P_{3/2}, m_J = +1/2\rangle$. The splitting Δ_U/h between the curves marked as $|+\rangle$ and $|-\rangle$ gives rise to the dipolar $|S\rangle - |P\rangle$ exchange. (**c**) Imaginary part of the probe susceptibility ($|g\rangle \leftrightarrow |e\rangle$) for variable interatomic distance assuming $\delta_p = 0$. The blue curve takes the four most relevant Rydberg pair potentials with $|C_{r'r''}|^2 > 0.05$ into account, resulting in the EIT-blockade radius of $r_b = 4.63\,\mu\mathrm{m}$ (vertically-dashed line) where $\mathrm{Im}[\chi/\chi_0](r_b) = 1/2$. Approximating the potentials by the van der Waals potential with $C_6^{\mathrm{SP}} \approx h \times 35\,\mathrm{GHz}\,\mu\mathrm{m}^6$, we find excellent agreement of the optical response, as shown by the red dashed curve. Note that the dipole-dipole interaction coefficient C_3 becomes negligible for $r > 4\,\mu\mathrm{m}$, as resonant dipole-dipole coupling between $|S\rangle$ and $|P\rangle$ is forbidden due to the difference in magnetic quantum number of $\Delta m_J = 2$.

response $\mathrm{Im}[\chi](r)$ with $\chi = -2\chi_0\gamma_e\rho_{eg}/\Omega_p$ are presented in Fig. 4.16c. Defining the EIT-blockade radius r_b as the distance at which $\mathrm{Im}[\chi/\chi_0]$ is reduced to half of its maximum value, we find the EIT-blockade radius of $r_b = 4.63\,\mu\mathrm{m}$. The red dashed line in Fig. 4.16c corresponds to a simplified calculation, where we only consider a single pair state with the fitted van der Waals coefficient of $C_6^{\mathrm{SP}} \approx h \times 35\,\mathrm{GHz}\,\mu\mathrm{m}^6$. Interestingly, the simplified model of the pure van der Waals interaction already provides a good explanation of the optical response of the system. Moreover, calculating the blockade radius using the pure van der Waals interaction yields a good agreement with the derived model, with $r_b = (2C_6\Gamma_e/\hbar\Omega_c^2)^{1/6} = 4.6\,\mu\mathrm{m}$.

Estimating the $|S\rangle - |P\rangle$ dipolar exchange rate

In Fig. 4.15b, the spatial transmission profile for the large atomic array gradually changes over the radius, deviating from the expected sharp blockade radius. In addition, we observed a "halo" of reduced transmittance at the distance beyond the blockade radius r_b. We attribute these observations to dipolar exchange processes between the ancilla atom in the $|P\rangle$ state and the surrounding atoms dressed to the $|S\rangle$ state. The exchange process has been observed in previous works [292, 294, 297], which cause resonant dipole-dipole coupling of different Rydberg parity. In contrast, our chosen Rydberg states cause the exchange by a second-order process, as discussed in Sec. 4.6.6. In this section, we will provide a theoretical model of such processes and a quantitative estimation of the exchange rate for our system. Considering the interaction potentials in Fig. 4.16b, there are two pair-potentials that are relevant for distances $r > 4\,\mu\mathrm{m}$. These potentials can be decomposed into the symmetric $|+\rangle = \frac{1}{\sqrt{2}}(|SP\rangle + |PS\rangle)$ and anti-symmetric $|-\rangle = \frac{1}{\sqrt{2}}(|SP\rangle - |PS\rangle)$ superposition of the $|SP\rangle$ pair basis. Therefore, initializing the atoms in the bare state $|SP\rangle = \frac{1}{\sqrt{2}}(|+\rangle + |-\rangle)$ causes a coherent exchange to the $|PS\rangle$ state. The coherent exchange dynamics of two particles is described by

$$|\Psi\rangle(t) \approx \cos(J_{\mathrm{ex}}t)\,|SP\rangle + e^{i\phi}\sin(J_{\mathrm{ex}}t)\,|PS\rangle, \tag{4.12}$$

where ϕ is a global phase. We can derive the exchange coupling $J_{\mathrm{ex}} = 2\pi\Delta_U/(2h)$, where Δ_U is the energy splitting of the two pair-potentials ($U_{\mathrm{int}}^{r'r''}$ and $U_{\mathrm{int}}^{r'''r''''}$), as shown in Fig. 4.17a. The exchange is restricted to two pair states ($|SP\rangle \leftrightarrow |PS\rangle$) for larger distances, but a multitude of states are contributing for shorter distances, resulting in strong dephasing and possible coupling to other states ($|SP\rangle \rightarrow |r'r''\rangle$) depending on the overlap of the pair states, $|C_{r'r''}C_{r'''r''''}|^2$. In the next step, we estimate the Rydberg probability $P_{|S\rangle}(r)$ of finding atoms around the ancilla atom in the $|S\rangle$ state, which can be quantified using Eq. (4.8). Due to the distance-dependent interaction shift of the Rydberg states, $P_{|S\rangle}(r)$ becomes negligible within the blockade radius r_b and high at large distances, see Fig. 4.17b. Combining the exchange rate $J_{\mathrm{ex}}(r)$ with the Rydberg probability $P_{|S\rangle}(r)$, we get an effective exchange rate by $J_{\mathrm{ex}}^{\mathrm{eff}}(r) = P_{|S\rangle}(r) \times J_{\mathrm{ex}}(r)$ [294]. The effective exchange rate shows a maximum two particle exchange rate of $J_{\mathrm{ex}}^{\mathrm{eff}} \approx 2\pi \times 3.2\,\mathrm{kHz}$, peaked at a distance around $r \approx 3.7\,\mu\mathrm{m}$, as shown in Fig. 4.17c.

To this end, the derivation of the effective exchange rate is for a two-particle model. We extend this to a many-particle description to account for the entire array, where the ancilla atom can coherently exchange with all surrounding atoms, by numerically solving the Lindblad master equation. Here, many particles cause a collective enhanced exchange coupling. We find that the dynamics of the ancilla is well described by an

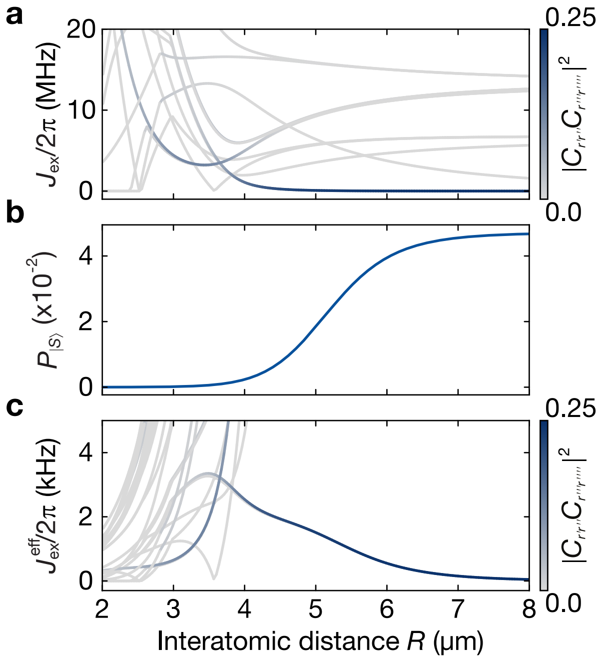

Figure 4.17: Dipolar exchange rate. (**a**) $|S\rangle - |P\rangle$ exchange rate J_{ex}. The rate is calculated from the splitting between neighboring interaction potentials ($U_{\mathrm{int}}^{r'r''}$ and $U_{\mathrm{int}}^{r'''r''''}$), while the intensity of the blue coloring indicates the overlap $|C_{r'r''}C_{r'''r''''}|^2$ with the bare state $|SP\rangle$. (**b**) $|S\rangle$ Rydberg fraction as calculated from Eq. (4.8). (**c**) Effective exchange rate, given by the product of the upper and middle graph $J_{\mathrm{ex}}^{\mathrm{eff}}(r) = P_{|S\rangle}(r) \times J_{\mathrm{ex}}(r)$. For larger distances $r > 4\,\mu\mathrm{m}$, the effective exchange rate is predominantly given by the difference of the symmetric and antisymmetric pair states $|+\rangle$ and $|-\rangle$, respectively. For smaller distances $r < 4\,\mu\mathrm{m}$ however, a multitude of pair states contribute, resulting in strong dephasing.

effective exchange rate of $J_{\mathrm{ex}}^{\mathrm{col}} \approx 2\pi \times 30\,\mathrm{kHz}$. With this rate, a single exchange event occurs at $t = 1/(2 \times 30\,\mathrm{kHz}) \approx 16\,\mu\mathrm{s}$, which is comparable to our probe duration of $t_p = 20\,\mu\mathrm{s}$. Therefore, the ancilla $|P\rangle$ delocalizes to a distance around $r \approx 3.7\,\mu\mathrm{m}$, causing the transmittance to decrease at the center of the original position. The exchange processes can be suppressed by reducing the probe duration or decreasing the probe power, as the exchange process scales with $\propto \Omega_p^2$ in the limit $\Omega_p \ll \Omega_c$ [292].

4.7 Summary

We exploited the strong cooperative response of an array composed of ordered emitters, spaced at subwavelength distances, to realize a photon switch. By utilizing the Rydberg blockade, we manipulated the probe photons interacting with the array to either be transmitted or reflected. We demonstrated that the optical properties of the array can be coherently altered by driving Rabi oscillations on the ancilla into the Rydberg state. We attained spatial control around the ancilla atom, which is deterministically placed within the array, and directly measured the spatial switching area. The residual imperfections are primarily due to the finite Rydberg lifetime and preparation fidelity of the ancilla. These issues are straightforward to address with future upgrades to the experimental setup.

Chapter 5

Extended Bose-Hubbard model using Rydberg dressing

5.0.1 Introduction

The Hubbard model has become an integral part of condensed matter physics, describing the dynamics of strongly correlated particles in a periodic potential [298–301]. Ultra-cold atoms in optical lattices are an ideal platform to realize Hubbard systems [147, 148] due to their clean environment, precise control and tuning capabilities, down to the microscopic level. However, so far the vast majority of work has focused on systems with only on-site interactions [42]. Moving beyond local interactions, including extended-range interactions stretching over several sites in the Hubbard model, the so-called *extended Bose-Hubbard model (eBHM)*, leads to a variety of intriguing phenomena arising from the competition between the long-range, tunneling and local interaction energy scales [43–45]. Near equilibrium, this competition gives rise to the emergence of non-local order [302], supersolids [303–308], spin liquids [309], and exotic cluster Luttinger liquid phases [310–312], while the emergence of repulsively-bound pairs has been predicted out-of-equilibrium [313].

In this chapter, we focus on realizing and studying *itinerant Rydberg models*. Here, we combine Rydberg dressing, as described in Sec. 2.4.2, with the full capabilities of single-site control and read-out of our quantum gas microscope. In the following sections, an overview of experimental platforms featuring long-range interactions is given. We then describe our experimental platform where we achieve itinerant one-dimensional (1D) bosonic systems with extended-range interactions. Most importantly, we demonstrate our findings on stroboscopic Rydberg dressing, which allows us to improve the Rydberg-dressed lifetime by over two orders of magnitude compared with previous measurements [140, 141]. Finally, we probe key features of the eBHM evidenced by the observation of repulsively-bound pairs, quantum hard-rods, and near-equilibrium density ordering. This chapter follows the publication [314]. The theoretical description of the near-equilibrium density ordering was developed in close collaboration with Tizian Blatz and Annabelle Bohrdt.

5.0.2 Long-range interacting quantum systems

Realizing an itinerant long-range interacting quantum system with single-particle control and single-particle read-out is an outstanding experimental challenge and continues to be an active field of research. Over the past decades, considerable effort has been devoted to experimentally incorporate long-range interactions into quantum simulations for itinerant lattice gases [45, 315]. The following list provides an overview of various platforms and their respective state-of-the-art:

- **Light-mediated-interactions in cavity systems:** Long-range interactions can be harnessed from atoms in cavities. The light scattered from an atom into the cavity mode can be rescattered by other atoms, with the photons carrying the information between the atoms [316–319]. Combined with optical lattices, the system captures the extended Hubbard model [320, 321]. The on-site interaction is manipulated by the lattice depth, whereas the long-range interaction is tuned by the resonance frequency of the cavity. The independent control over the short- and long-range interactions allows to observe four distinct quantum phases, including the superfluid (SF), supersolid (SS), Mott insulator (MI), and charge density wave (CDW) [320], and the quench dynamics between two insulating phases [322]. However, dissipation is the primary hurdle in achieving the strongly correlated regime.

- **Semiconductor quantum dots:** Semiconductor quantum dots, formed by a semiconductor two-dimensional (2D) electron gas, are promising candidates to study the Fermi-Hubbard model [323–326]. With long-range Coulomb interactions and electronically tunable Hubbard parameters, the extended Fermi-Hubbard model can be realized [327]. Local control and read-out have been active areas of research. However, significant electrostatic disorder and the challenge to extend the system towards larger systems sizes still persist.

- **Dipolar excitons:** An electron-hole pair in a semiconductor can form quasiparticles [328] in a 2D lattice with spacing of 250 nm, which is created by an array of electrodes. The dipole interactions of quasiparticles within this short lattice are adequate to generate long-range interactions necessary for simulating the eBHM [329]. Here, two Wannier states are confined in the lattice with large on-site interactions compared to the tunneling energy $U \gg J$, and achieve a nearest-neighbor interaction of $V/J \approx 20$. Two incompressible phases of the MI and checkerboard are observed at unity- and half-filling, respectively. The challenge is to perform a site-resolved analysis in the short spacing lattice.

- **Polar molecules:** Ultracold polar molecules feature a strong and tunable electric dipole moment, making them a potential platform for the eBHM [52–56]. Moreover, the rich spectrum of rotational and vibrational degrees of freedom can be utilized for tunability and information storage. However, this complex internal structure causes high collisional losses, known as "sticky collisions" [330]. The latter poses challenges in preparing high phase-space densities near quantum degeneracy, limiting lattice fillings. Nevertheless, there has been impressive progress over the past decade. Recently, the first quantum gas microscopy of dilute molecular samples has been reported [55]. In addition, efficient electric field and microwave (MW) shielding have been developed and implemented [331–334], allowing the loss to be significantly reduced and resulting in the first observation of a molecular dipolar Bose-Einstein condensate (BEC) [335]. In parallel, molecules have been trapped and detected in optical tweezers, which can be achieved by direct cooling of molecules [336–338] or assembly from single atoms [339–342]. However, the pursuit of developing large-scale extended Hubbard systems remains ongoing.

- **Magnetic atoms:** Magnetic atoms naturally have a permanent magnetic dipole moment, which is tunable by an external magnetic field [46–48]. Due to the relatively weak dipolar interaction strengths, achieving sufficiently strong nearest-neighbor interactions requires very small lattice spacing. For example, the first observation of an ^{168}Er-based eBHM in optical lattices with a spacing of 266 nm can reach a nearest-neighbor interaction of $V/J = 10$ [49]. Performing single-site readout or manipulation with short spacing is extremely challenging. To cover the various demands of short-spaced lattices for physics and the long-range spacing for single-site imaging, the latter studies required an accordion lattice with a tunable lattice spacing from 266 nm to 3 µm Here, the single-site detection allows to observe different phases, such as dipolar quantum solids [50].

- **Rydberg atoms:** Rydberg quantum simulators, commonly used for simulating spin models [62] or quantum computing [60, 63] where motional dynamics are frozen, have been employed to simulate itinerant hard-core interacting bosons through a spin-boson mapping [61]. Rydberg dressing, off-resonant optical coupling to Rydberg states, offers an alternative pathway to realize extended-range interactions over micron-scale distances in quantum gas microscopes [137, 191, 311, 343–348]. The optical coupling provides a distinct mechanism for controlling interactions, including quenching the interaction strength in sub-microsecond timescales, periodically modulating the interactions [349], or switching interactions at a specific state of evolution. Furthermore, attractive or repulsive interactions can be realized by employing blue or red detuning [136], and the isotropy of the interactions can be controlled by the external field and the polarization of the coupling light [140, 192]. So far, Rydberg-dressed interactions have been successfully implemented in the absence of motional dynamics to realize spin models [140, 141, 190, 192, 350–352]. Initial efforts have been made to employ Rydberg-dressed interactions for itinerant fermionic systems [197]. Nevertheless, the technique has faced significant challenges from substantial collective losses [140, 353]. These losses result from off-resonant coupling to Rydberg states of opposite parity whose interaction with the dressed state tunes the coupling light into a resonance that can trigger an excitation avalanche [140, 353, 354]. This challenge can be overcome using stroboscopic Rydberg dressing, as detailed in Sec. 2.4.2. Combined with the abilities of local control and single-site read-out of a quantum gas microscope [152], this enables the realization of the eBHM which has been demonstrated for both in- and out-of-equilibrium dynamics [314] with nearest-neighbor interaction up to $V/J \approx 10$.

5.1 Experimental protocol

Beginning with near unity-filled MI of up to 200 atoms in the diagonal lattice, we use our addressing technique, see Sec. 3.3.2, to prepare three parallel atomic chains oriented along the x-direction. We choose a separation distance of three lattice sites between chains to suppress the interaction between the chains, ensuring pure 1D dynamics without any influence from neighboring chains. The diagonal lattice has a lattice spacing of $a_{\mathrm{lat}} = 752\,\mathrm{nm}$ with an approximately fixed repulsive on-site interaction of $U = h \times 225\,\mathrm{Hz}$. The single-photon light in the UV range off-resonantly couples atoms from the ground state $|g\rangle = |F = 2, m_F = +2\rangle$ to the Rydberg manifolds $|30P_{3/2}\rangle$, generating a dressed ground state $|\tilde{g}\rangle$. The characteristic Rydberg properties in $|\tilde{g}\rangle$ feature extended-range interactions with a softcore shape and a strength of V, see Fig. 5.1a.

We choose to operate with the diagonal lattice due to a geometry constrain of the UV propagation direction. Coupling a ground state to a Rydberg state with the single-photon scheme usually generates a potential offset due to the AC-Stark shift. A tightly focused beam of our single-photon coupling light, see Sec. 3.4.1, causes a strong optical gradient orthogonal to its propagation direction, whereas the optical gradient along the preparation direction is negligible. This prevents atomic dynamics in the square lattice because the coupling light propagates along the diagonal direction of the lattice axes. Therefore, we work with the diagonal lattice, as described in Sec. 3.3.5, where the propagation direction aligns with one of the lattice axes, specifically the x-direction, as seen in Fig. 5.1a. In this scenario, the dynamics in 1D are not affected during illumination of the Rydberg dressing light because the potential gradient is absent along the x-direction. However, the dynamics in the diagonal lattice turn into 2D when the coupling light is turned off, there is no independent tuning ability of the tunneling rate between the two orthogonal lattice axes for the diagonal lattice. To constrain the dynamics to 1D along the x-direction, we additionally apply a magnetic gradient along the y-direction ∇B_y, see Sec. 5.1.1.

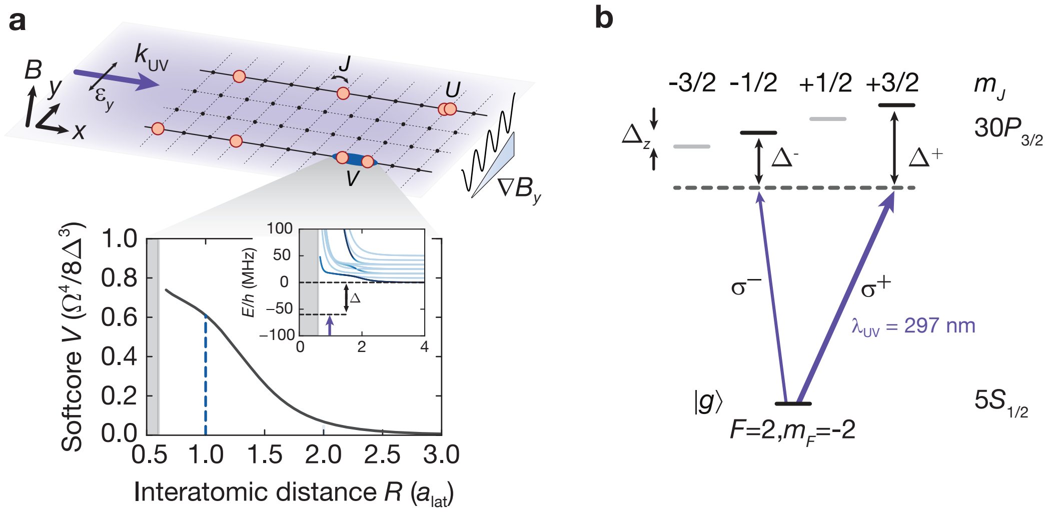

Figure 5.1: Rydberg-dressed extended Bose Hubbard model and excitation scheme. (**a**) Tilted lattice system and softcore interaction. The atoms are allowed to tunnel along 1D chains with a tunneling energy J and experience on-site interactions U. Off-resonant coupling to the Rydberg states generates softcore-shaped interaction with tunable nearest-neighbor interactions $V = \Omega^4/8\Delta^3$. The inset shows Rydberg-Rydberg interaction potentials with their relative optical coupling strength indicated by the intensity of the blue coloring. (**b**) The ultraviolet (UV) light at a wavelength of 297 nm off-resonantly couples the atoms, initially prepared in the $|g\rangle = |F = 2, m_F = +2\rangle$ state, to the Rydberg manifold $|30P_{3/2}\rangle$ with Rabi frequency of $\Omega = 2\pi \times 20\,\text{MHz}$ and detuning of $\Delta^+ = 2\pi \times -(60\,\text{to}\,400)\,\text{MHz}$. The UV laser propagates along the x-direction, with a the bias magnetic field of $B = 4.48\,\text{G}$. Setting a linear polarization on the y-axis for the UV light, we off-resonantly couple to the Rydberg manifold with both the σ^+ and σ^- polarizations.

Fig. 5.1b shows the relevant electronic states and the laser excitation scheme. A magnetic bias field of $B = 4.48\,\text{G}$, near z-direction, provides a Zeeman splitting for the m_J Rydberg manifolds of $\Delta_{\text{Zeeman}} = 2\pi \times 8.36\,\text{MHz}$. Choosing the linear polarization along the y-axis results in σ^+ and σ^- polarizations that couple $|g\rangle$ to both the $|30P_{3/2}, m_J = +3/2\rangle$ and the $|30P_{3/2}, m_J = -1/2\rangle$ states. With our parameters, the coupling strength ratio of these two branches amounts to $\Omega^+ : \Omega^- \simeq 1 : 0.577$. Despite the closer detuning for the σ^- contribution ($|\Delta_-| < |\Delta_+|$), the nearest-neighbor interaction V is predominantly given by the σ^+ contribution, due to the strong scaling ($V \propto \Omega^4$) and the Rydberg-Rydberg interaction potentials at $B = 4.48\,\text{G}$. Note that we intentionally displace the center of the UV beam by a few lattice sites so that the optical gradient from the AC-Stark shifts along the y-direction does not cancel with the magnetic gradient due to drifts of the beam pointing.

5.1.1 One-dimensional dynamics with magnetic gradient

The diagonal lattice is impractical for the independent control of the tunneling rate of each lattice axis. To address this, we apply a potential gradient along one of the lattice axes, generated by Zeeman shifts of a magnetic field gradient. This prevents dynamics along the direction of the gradient, while dynamics in the orthogonal direction remain unaffected. We employ a single coil, in conjunction with a vertical offset field, to generate a quadrupole magnetic field with the magnetic zero set in the atomic plane. Additionally, offset fields on the horizontal plane are used to counteract the quadrupole field, aligning the magnetic gradient to one of the lattice axes. We characterize the magnitude and orientation of the magnetic field gradient using Ramsey interferometry, see Fig. 5.2a. Our procedure begins with a unity-filled 2D MI in the $|\downarrow\rangle = |F = 1, m_F = -1\rangle$ hyperfine ground state. We then apply a MW $\pi/2$ pulse, coupling to the $|\uparrow\rangle = |F = 2, m_F = -2\rangle$ state, preparing the atomic ensemble in the superposition state $(|\downarrow\rangle + |\uparrow\rangle)/\sqrt{2}$. The superposition state undergoes spatially dependent spin precession according to the local magnetic field strength. Finally, we apply a second MW $\pi/2$ pulse to map the accumulated spatial phase to spin population. Subsequently, we measure the $|\uparrow\rangle$ component using the push out to remove the $|\uparrow\rangle$ component before imaging. As the magnetic phase is random, we analyze the connected correlator

$$C_d = \langle \hat{n}_i \hat{n}_{i+d} \rangle - \langle \hat{n}_i \rangle \langle \hat{n}_{i+d} \rangle, \tag{5.1}$$

where d is the correlate distance. For example, the connected correlator $C_{d=1}$ provides the relative phase different with the nearest-neighbor site. The spatial 2D phase profile is shown in the inset of Fig. 5.2a. By fitting a 2D sinusoidal function to the phase profile, we can extract the orientation and strength of the magnetic gradient [355]. In the measurements for this chapter, we operate with a magnetic gradient of $\nabla B_y = h \times 350(3)\,\mathrm{Hz}/a_{\mathrm{lat}}$ and $\nabla B_x = h \times 2(2)\,\mathrm{Hz}/a_{\mathrm{lat}}$. This allows tunneling along the x-direction, while inter-chain tunneling along the y-direction is suppressed due to the large potential gradient $\nabla B_y > U = h \times 225\,\mathrm{Hz}$. At this setting, the magnetic field along the z- and y-direction is $B_z = 4.28\,\mathrm{G}$ and $B_y = 1.31\,\mathrm{G}$, respectively, while B_x is negligible. Furthermore, we find that the vertical potential gradient ∇B_z from the magnetic field cancels the potential gradient caused by gravity. This results in vertical tunneling out of the plane over long dynamical timescales for the atoms in the $|F = 2, m_F = -2\rangle$ state. To overcome this issue, we apply a series of MW transfer to transfer atoms to the $|F = 2, m_F = +2\rangle$ state, in which the vertical potential gradient ∇B_z combines with the potential gradient from gravity. With the optimized B field settings, we verify 1D tunneling by performing single-particle quantum walks [35], see Fig. 5.2b. We observe the characteristic quantum walk within the chain, while the inter-chain tunneling is negligible.

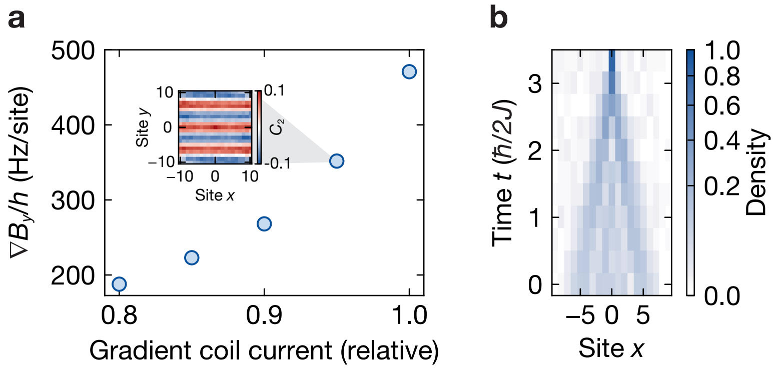

Figure 5.2: Calibrating the potential gradient and benchmarking the 1D dynamics. (**a**) We use Ramsey interferometry to align and calibrate the potential gradient. The spins are encoded in two hyperfine ground states that are coupled by a MW field. The local spin precession accrues a spatially dependent phase due to the local magnetic field. The phase is mapped to the population of the spins and analyzed with the connected correlator $C_{d=2}$, as illustrated in the inset. (**b**) Starting with a single atom within the tilted lattice, we observe quantum walk dynamics with the population confined within the chain, whereas inter-chain tunneling is negligible.

5.1.2 Rydberg-dressed interactions

Theoretical estimation of the softcore interaction

We can estimate the softcore potential V given the set of parameters used in the measurements and focusing solely on the σ^+ coupling to the $|r\rangle = |30\mathrm{P}_{3/2}, m_J = +3/2\rangle$ state. Following the calculation in Sec. 2.4.2 with an extension to multiple pair states, we first calculate the distance-dependent interaction $V_{\mathrm{rr}}^{r'r''}(R)$ between Rydberg pair states using the "pairinteraction" software [98]. The relevant pair states and their respective relative coupling to the ground states are illustrated in the inset of Fig. 5.1a. We then diagonalize the two-atom Hamiltonian coupled to the ground state $|g\rangle$ with Rabi frequency Ω,

$$\begin{aligned} H(R) =& \frac{\hbar}{2}\Omega(|rg\rangle\langle gg| + |gr\rangle\langle gg|) - \hbar\Delta(|rg\rangle\langle rg| + |gr\rangle\langle gr|) \\ &+ \frac{\hbar}{2}\sum_{r',r''} \Omega C_{r'r''}(|r'r''\rangle\langle rg| + |r'r''\rangle\langle gr|) \\ &+ \sum_{r',r''}(-2\hbar\Delta + V_{\mathrm{rr}}^{r'r''}(R))|r'r''\rangle\langle r'r''|. \end{aligned} \tag{5.2}$$

Here, $|r'r''\rangle$ are the Rydberg pair states and $C_{r'r''} = \langle r'r''|rr\rangle$ is the overlap of $|r'r''\rangle$ with the bare Rydberg pair state $|rr\rangle$. We account for all Rydberg states, for which the absolute interaction energy $V_{\mathrm{rr}}^{r'r''}$ is smaller than $h \times 3\,\mathrm{GHz}$, as the overlap becomes negligible for larger energies. The diagonalization results of Eq. (5.2) present both the softcore height (interaction strength V) and the softcore shape (range of the interaction). Given a Rabi frequency of $\Omega = 2\pi \times 20\,\mathrm{MHz}$, a detuning of $\Delta = 2\pi \times -60\,\mathrm{MHz}$, and a pulse duty cycle of $D = 1/600$, we obtain a nearest-neighbor interaction of $V = h \times 94\,\mathrm{Hz}$ and a negligible next-nearest-neighbor interaction. This estimation applies to the peak intensity at the center of the beam. Taking into account our small beam waist of $w_0 \simeq 12\,\mu\mathrm{m}$, measurements with parallel chains and the center offset of the beam, we estimate an average nearest-neighbor interaction of $V \simeq h \times 80\,\mathrm{Hz}$. Repeating the same treatment for σ^- coupling to the $|r\rangle = |30\mathrm{P}_{3/2}, m_J = -1/2\rangle$ state, yields a maximum softcore of $V(\sigma^-) \lesssim h \times 9\,\mathrm{Hz}$. Therefore, the interaction due to the σ^- coupling is much smaller with a fraction of 0.1 compared to the σ^+ coupling.

Softcore calibration with spin echo sequence

We follow previous studies [140, 192, 197, 356] which used a spin-echo sequence to measure the nearest-neighbor interaction V. We operate with two hyperfine ground states $|\uparrow\rangle = |F = 2, m_F = +2\rangle$ and $|\downarrow\rangle = |F = 2, m_F = +1\rangle$, coupled by a MW field. As the UV light is only coupling the $|\uparrow\rangle$ state to the Rydberg state, the two ground states experience differential phase shifts due to both the single-particle AC-Stark shift $\Delta_{AC} = \Omega^2/2\Delta$ and the two-particle interaction shift V. However, an echo pulse with a MW pulse duration of π removes single-particle phase shifts, providing direct access to the two-particle interaction V. To solely probe the effect of the nearest-neighbor interaction without higher-order effects from many particles [141], we prepare isolated pairs using our addressing technique, see Sec. 3.3.2, as an initial state for the measurement. For the spin-echo sequence, we start in the $|\uparrow\rangle$ state and prepare a coherent superposition between the $|\uparrow\rangle$ and $|\downarrow\rangle$ states with a MW pulse with a duration of $\pi/2$. We perform a triple spin-echo scheme with four dressing intervals alternating with the three echo pulses, as illustrated in Fig. 5.3a. This scheme allows us to measure for a longer dressing duration, and the dephasing time due to the magnetic fluctuation also improves with more echo pulses. During each phase accumulation in the echo sequence, we apply eight UV pulses using the stroboscopic scheme to avoid collective losses. At the end of the sequence, we apply a final MW $\pi/2$ pulse to map the detected phase shifts into spin population. In the absence of interaction V, all spins return to the original $|\uparrow\rangle$ state, which is then subsequently removed by a push out pulse before imaging. The interaction V can be derived from the correlated pair flips between the pair states $|\uparrow\uparrow\rangle \leftrightarrow |\downarrow\downarrow\rangle$. In the presence of dephasing, the spins will eventually align randomly, resulting in a damped oscillation. Motivated by the recent observation of damped pair oscillations between dipolar molecules in tweezers [356], we utilize a similar model to derive the interaction V. This model accounts for particle loss τ_{L} and dephasing τ_{D} due to Gaussian noise in the UV pulse area with a doubly damped

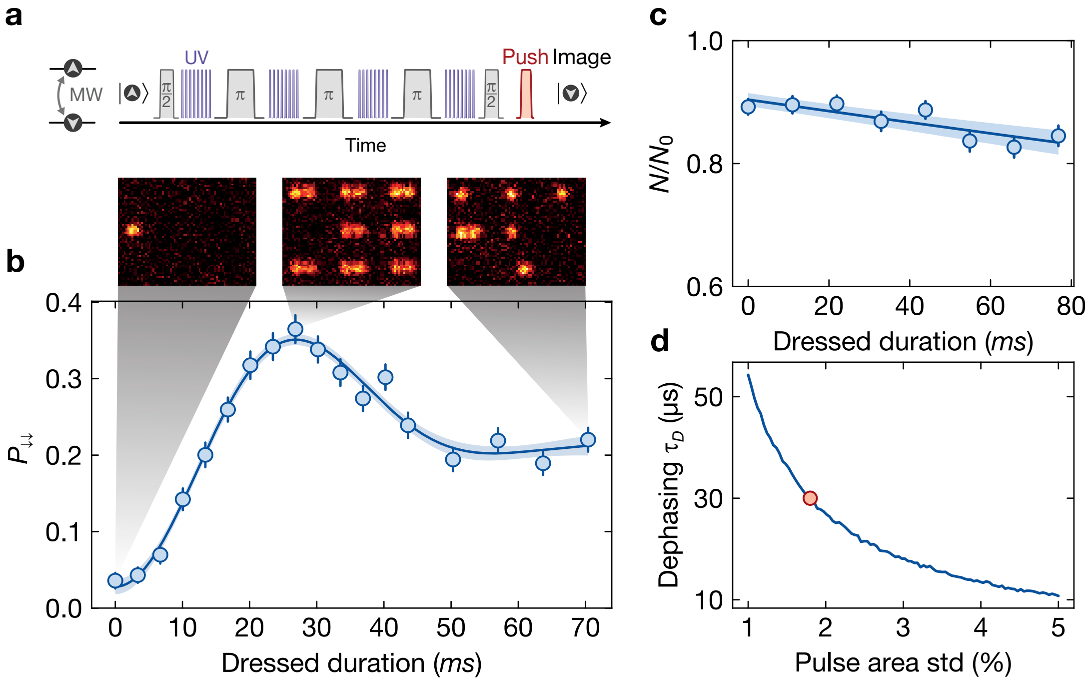

Figure 5.3: Calibration of the nearest-neighbor interaction V using a spin-echo sequence. (**a**) Spin-echo pulse sequence: We begin with spin-polarized isolated pairs in the $|\uparrow\rangle$ state. The MW pulse with a duration of $\pi/2$ prepares a coherent superposition of $|\uparrow\rangle$ and $|\downarrow\rangle$. We then alternate the application of UV pulses for differential phase accumulation with MW echo pulses. This induces a phase shift due to interaction while canceling out the phases acquired from the single-particle light shift. For imaging, we apply a final MW $\pi/2$ pulse, remove the $|\uparrow\rangle$ atoms by a push out pulse, and then detect the $|\downarrow\rangle$ atoms. (**b**) We consider the pair state probability $P_{\downarrow\downarrow}$, over varying total dressing durations. We observe that the spins are randomly aligned, causing the oscillation to be damped at longer dressing durations. The solid line illustrates the best-fit result of our empirical model, see Eq. (5.3). Examples of single shots are displayed in the insets. (**c**) The atomic lifetime is measured during the applied echo sequence. Fitting with an exponential decay, we find a lifetime of 838(213) µs. (**d**) We perform a Monte-Carlo simulation of the dephasing time τ_D in the presence of fluctuating Gaussian noise in the UV pulse area. Comparing the simulation (blue line) with our experimental result (red data point), we estimate an upper bound for the fluctuations in the UV pulse area with a standard deviation of $\lesssim 1.8\,\%$.

oscillation, given by

$$P_{\downarrow\downarrow} = Ae^{-t/\tau_\mathrm{L}} \left(1 - e^{-t^2/(2\tau_\mathrm{D}^2)} \cdot \cos\left(\frac{Vt}{2\hbar}\right)\right). \tag{5.3}$$

Fig. 5.3b shows our experimental measurements of the correlated pairs and the fit results of the model. We obtain a nearest-neighbor interaction of $h \times 34.1(13)$ kHz and a dephasing of $\tau_D = 30(1)\,\mu\text{s}$. With a duty cycle of $D = 1/600$, the nearest-neighbor interaction is averaged to $V = h \times 57(2)\,\text{Hz}$, whereas the theoretical estimation is $V = h \times 80\,\text{Hz}$. The fit results indicate that atomic loss plays a negligible role for the dephasing. This is consistent with the lifetime measurement of $838(213)\,\mu\text{s}$, see Fig. 5.3c. The majority of the dephasing is attributed to a shot-to-shot pulse area fluctuations of the UV light. A few-percent of pulse fluctuations result in strong variations of the induced phase shift $\phi = \delta \cdot t$ [141]. The difference in the accumulated phase shifts between the various echo pulses will eventually dominate, leading to randomly aligned spins in the end. We used a classical Monte-Carlo simulation to simulate this phenomenon and estimate the dephasing time τ_D. The simulatiom assumes the pulse area fluctuations follow a Gaussian distribution with standard deviation σ_P. For each σ_P, we can compute the dephasing time τ_D, see Fig. 5.3d. Consequently, we can establish an upper bound for the relative pulse area fluctuations of $\sigma_p \lesssim 1.8\,\%$.

5.2 Enhanced lifetime with stroboscopic Rydberg dressing

Blackbody radiation can incoherently drive transitions between neighboring opposite parity Rydberg states. This process dominates the natural radiative decay of the Rydberg states for large principle quantum numbers [107]. The strong dipole interactions between these neighboring Rydberg states and the target Rydberg state can tune pair states into resonance with a detuned laser. This subsequently triggers an avalanche excitation of the Rydberg population [81], which is not trapped in the optical lattice. These collective losses are the main limitations to extending Rydberg dressing towards many-body systems. Many experiments have observed substantial losses when driven off-resonantly to the Rydberg states [140, 353, 354]. There is a direction of research that shields the system from the blackbody radiation using cryogenic systems [110, 111, 357]. However, we choose an alternative approach by stroboscopically manipulating the Rydberg dressed coupling, as demonstrated in [105, 140] and confirmed in another study [358]. The long switch-off gaps in the stroboscopic scheme effectively suppress the follow-up Rydberg excitation, minimizing the chance of avalanche excitation and allowing the excited atom to decay before subsequent pulses occur. Therefore, the collective losses are suppressed, as illustrated in Fig. 5.4. In addition, the stroboscopic dressing allows to operate in a larger Rydberg admixture regime, improving the quality factor $Q \propto \Omega^2/\Delta$, see Sec. 2.4.2, while reaching the same interaction strength as the continuous dressing. These two aspects highlight the advantages of the stroboscopic dressing over the continuous dressing.

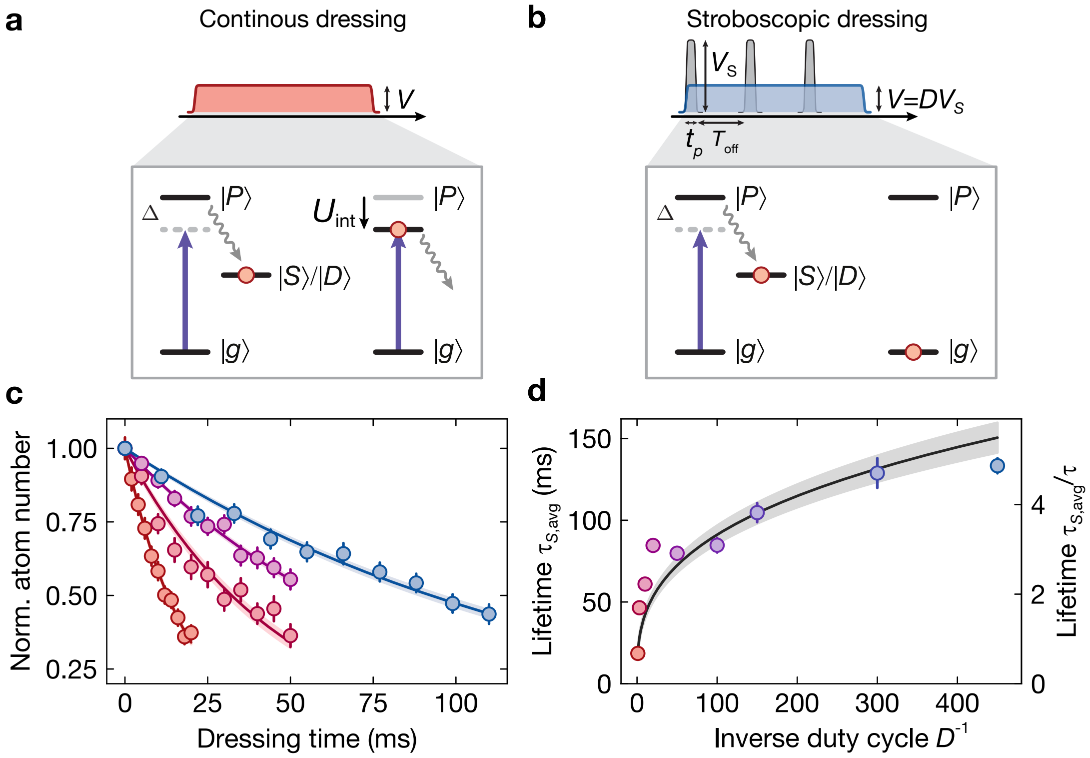

Figure 5.4: Stroboscopic Rydberg-dressed lifetimes. (**a**) In continuous Rydberg dressing, off-resonant scattering followed by blackbody radiation drives transitions to neighboring Rydberg states $|S\rangle$ or $|D\rangle$. The interactions U_{int} between our target Rydberg state and the neighboring Rydberg states can tune the state into resonance. This leads to avalanche excitations, which results in significant losses. (**b**) In stroboscopic Rydberg dressing, the off-resonant light is periodically pulsed with a duration of t_p alternated with an off-time T_{off}. This results in an average interaction $V = DV_S$, where $D = t_p/(t_p + T_{\text{off}})$ is the duty cycle. The off-times T_{off} allow the contaminated atoms to decay before the subsequent pulses occur, thus preventing the avalanche excitation. Therefore, the strong losses are suppressed, while the same interaction V can be achieved as in the continuous Rydberg dressing. (**c**) Atomic loss measurements for different duty cycles with fixed interaction of $V = h \times 114(4)$ Hz in a unity-filled 1D chain of 11 atoms. Here, we apply stroboscopic pulses with pulse durations of $t_p = 0.5 - 1\,\mu\text{s}$ and tunable off-times $T_{\text{off}} = 150 - 300\,\mu\text{s}$. As we decrease the duty cycle from red to blue, the atomic lifetime improves. (**d**) The fitted lifetime for varying duty cycles. Tuning the duty cycle from $D = 1$ (red), through $D = 1/3$ (purple), to $D = 1/450$ (blue), the atomic lifetime increases by a factor of $\sim 7.2(3)$, following the expected scaling $\sqrt[3]{D^{-1}}$. Averaged over all measurements, our experimental lifetimes reach 54(3) % of their respective theoretical off-resonant Rydberg lifetime. Compared with the bare Rydberg state lifetime τ, the stroboscopic dressing improves the lifetimes by a factor of 4.

In the following, we present the working principle of stroboscopic Rydberg dressing as derived in Sec. 2.4.2. The goal is to measure the average dressed lifetime $\tau_{S,\mathrm{avg}}$ for varying duty cycles D while maintaining the same average dressed interaction $V_{S,\mathrm{avg}} = DV_S$, where V_S is the Rydberg-dressed interaction if continuously dressed with the same Rabi frequency and detuning. For that reason, we reduce the detuning to increase the dressed interaction V_S, ensuring that DV_S remains constant while the Rabi frequency Ω is fixed. Note that reducing the detuning is constrained by the requirement to stay in the weak dressing regime $\Delta \gg \Omega$. Moving beyond this point would cause higher-order many-body interactions to emerge. We experimentally measure the lifetime of the dressed ground state $|\tilde{g}\rangle$ by monitoring the atom number for a variable illumination time of the stroboscopic dressing light.

We begin with 1D isolated chains of 11 atoms, trapped in the optical lattice at a depth of $20E_r$ at the $|F = 2, m_F = +2\rangle$ state. We pulse the UV light to couple atoms to the $|30P_{3/2}, mJ = +3/2, +1/2\rangle$ state with durations of $t_p = 0.5 - 1\,\mu\mathrm{s}$ and off-times $T_{\mathrm{off}} = 0 - 225\,\mu\mathrm{s}$, corresponding to a duty cycle of $D = 1 - 1/450$. The UV is operated at a Rabi frequency of $\Omega = 2\pi \times 20.9(9)\,\mathrm{MHz}$ and a detuning of $\Delta = 2\pi \times -60\,\mathrm{MHz}$ (stroboscopic scheme) and $2\pi \times -400\,\mathrm{MHz}$ (continuous scheme). This results in the average dressed interaction of $V_{S,\mathrm{avg}} = DV_S = h \times 114(4)\,\mathrm{Hz}$. Fig. 5.4c shows the atomic loss measurements for varying average dressing durations and different duty cycles. The extracted lifetimes from the exponential decay fit are correspondingly shown in Fig. 5.4d. For the continuous dressing (red), we measure a lifetime of $\tau = 18.6(3)\,\mathrm{ms}$, which is $51(1)\,\%$ of the expected single-particle lifetime and consistent with previous observations in 1D [105, 141, 197]. With a reduction in the duty cycle (from red to blue), the lifetime enhances, which is in the excellent agreement with the expected scaling of $\tau_{S,\mathrm{avg}} = \tau / D^{1/3}$. Compared with the tunneling timescale of approximately 10 ms in the Bose-Hubbard model (BHM) parameters, the improved lifetime beyond 100 ms exceeds tens of tunneling events. For the first time, this allows the incorporation of extended-range interactions into the BHM system using stroboscopic Rydberg dressing. Note that the pulse timescale is much shorter than the tunneling timescale. We typically apply more than 25 pulses during one tunneling timescale.

5.3 Probing key features of the extended Bose-Hubbard model

In the following sections, we realize an effective 1D eBHM using stroboscopic Rydberg dressing of ^{87}Rb atoms in the optical lattice. We induce the nearest-neighbor interaction V, which corresponds to the average stroboscopic dressed interaction $V = V_{S,\mathrm{avg}} = DV_S$, as depicted in Sec. 5.2. Our system is described by the Hamiltonian

$$\hat{H} = -J \sum_{\langle i,j \rangle} \hat{a}_i^\dagger \hat{a}_j + \frac{U}{2} \sum_i \hat{n}_i(\hat{n}_i - 1) + V \sum_i \hat{n}_i \hat{n}_{i+1}, \tag{5.4}$$

where the term V only acts on the nearest-neighboring site. Note that the enhanced lifetimes exceed our typical tunneling times $\hbar/(2J) \simeq 4-7\,\mathrm{ms}$ at least by an order of magnitude with a maximum interaction of $V/J = 10$. Compared with previously reported lifetimes [141, 197], our method shows an improvement of approximately two orders of magnitude. This allows us to experimentally probe the microscopic features of the eBHM. With excellent control over the extended interaction strength V and microscopic control over single atoms, we explore various in- and out-of-equilibrium regimes, thereby highlighting the impact of this new energy scale on the emerging many-body physics. First, we observe the existence and dynamics of repulsively-bound pairs in which atoms occupying neighboring lattice sites are bound and exhibit slower dynamics. Second, increasing to half-filling, we realize a gas of "hard-rods" at large nearest-neighbor interaction. We find a striking difference in the density relaxation between an initial charge-density wave of such hard-rods and the case of hard-core bosons. Finally, we probe the nature of the low-energy states of the eBHM by gradually increasing the nearest-neighbor interaction V and observing the emergence of density-ordering.

5.3.1 Repulsively-bound pair states

In the 1D eBHM, bound pair states have been predicted for atoms in two adjacent sites, when the nearest-neighbor interaction V exceeds a critical value. The complete derivation of two-particle solutions in the 1D eBHM can be found in [313]. Here, the two atom wavefunction can be expanded in a non-symmetrized basis $|x_1, x_2\rangle$ as $|\Psi\rangle = \sum_{x_1,x_2} \Psi(x_1, x_2)|x_1, x_2\rangle$, where x_i is the atomic position of the atom i. We introduce the relative coordinate $x = x_1 - x_2 = a_{\mathrm{lat}}\Delta x$ and the center of mass $R = (x_1 + x_2)/2$, where a_{lat} is the lattice constant. The two atom wavefunction can be separated using the ansatz $\Psi(x_1, x_2) = e^{KR}\phi_K(x)$, where K is the center-of-mass quasimomentum $K \in [-\pi/a_{\mathrm{lat}}, \pi/a_{\mathrm{lat}}]$. This simplifies the problem to a single particle problem in the relative coordinate. This yields the eigenvalue problem of the Schrödinger equation of the Hamiltonian in Eq. (5.4),

$$J_K \left[\phi_K(x-1) + \phi_K(x+1)\right] + \left[U\delta_{x,0} + V(\delta_{x,1} + \delta_{x,-1}) - E_K\right] \phi_K(x) = 0, \tag{5.5}$$

where $J_K = 2J\cos Ka_{\mathrm{lat}}/2$. Eq. (5.5) can be divided into two cases: the scattering states of free atoms and the bound states of atomic pairs.

Scattering states

The analysis of the scattering solution of Eq. (5.5) can be obtained with the ansatz of plane wave scattering with phase shift $\delta_{K,k}$, represented as $\phi_{K,k}(x \neq 0) \propto e^{-ik|x|} + e^{2i\delta_{K,k}}e^{ik|x|}$. This generates eigenenergies $E_{K,k} = -2J_K \cos ka_{\mathrm{lat}}$, equivalent to the sum of the Bloch bands of two free atoms [359, 360]. The energies $E_{K,k}$ form a continuum, with the lowest value $E_{K,0} = -4J$ and highest value $E_{K,\pi} = 4J$ at $k = 0$ and $k = \pi/a_{\mathrm{lat}}$, respectively (see gray curve in Fig. 5.5a).

Bound states

We now apply the exponential ansatz $\phi_K(x \neq 0) \propto \alpha_K^{|x|-1}$ in Eq. (5.5) and obtain

$$J_K V\alpha_K^3 + \left(VU - J_K^2\right)\alpha_K^2 + J_K(V+U)\alpha_K + J_K^2 = 0. \tag{5.6}$$

The solutions of Eq. (5.6) have been proven in [313, 361] and there are at most two bound states, $\phi_K(x=0)$ and $\phi_K(x \neq 0)$. We emphasize some of the interesting limits for the existence of the bound states:

- For $U = V = 0$: The noninteracting particles do not have a bound state.
- For $U \neq 0$ and $V = 0$: There is a bound state $\phi_K(x=0)$ with $\alpha_K = (U - E_K)/2J_K$ and corresponding energy of $E_K = \mathrm{sgn}(U)\sqrt{U^2 + 4J_K^2}$. This is equivalent to atoms located at the same site with additional energy U, which has been observed before [362, 363].
- For any value of U and $V \neq 0$: The first bound state is the same as the previous case, where two atoms are located at the same site. The second bound state of $\phi_K(x = -1, 1)$ exists only if $W \geq 2J$ with $W = UV/(U + 2V)$. This corresponds to two atoms located in adjacent sites with the additional energy V. In the hard-core boson limit[363–365] where $U \gg J$, the second bound state simplifies to $\alpha_K = -J_K/V$ with the corresponding energy of $E_K = V + J_K^2/V = V + 4J^2/V\cos(Ka_{\mathrm{lat}}/2)$. The condition for the existence of the bound state in this case is $V \geq 2J$, see the red lines in Fig. 5.5a. The bound states can be interpreted as an isolated state separated from the continuum of free single-particle states by the additional energy U (V) and featuring a bandwidth set by the reduced tunneling energy $J_b = J^2/U$ ($J_b = J^2/V$). This reduced tunneling energy of the bound pair can be intuitively understood as a hopping of the bound state that occurs perturbatively in J/U (J/V) through a second-order process that couples off-resonantly to the continuum of free states.

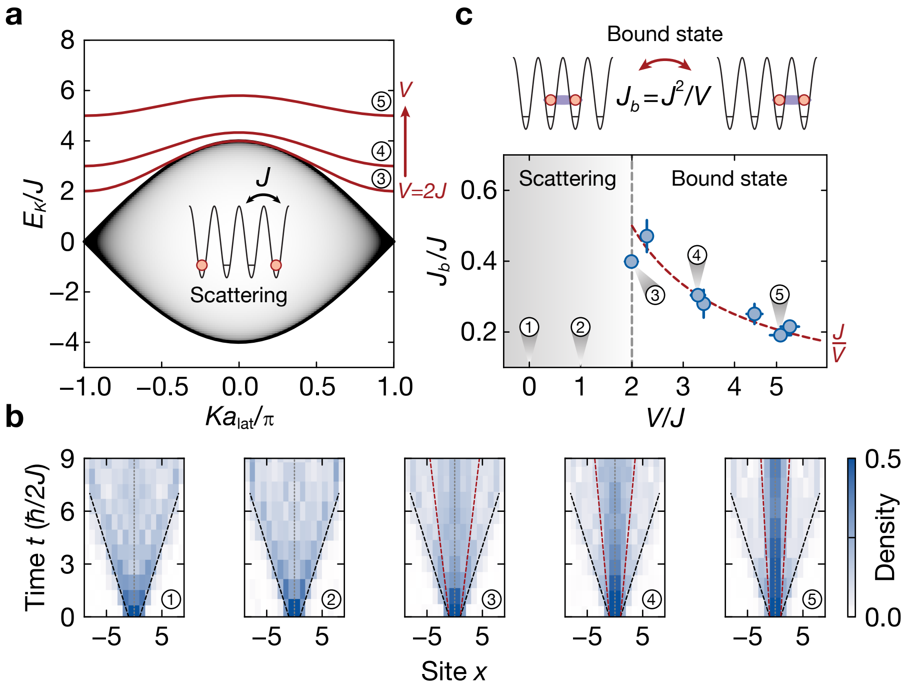

Figure 5.5: Repulsively-bound pair states in the extended Bose-Hubbard model. (**a**) Two-particle energy spectrums of the 1D eBHM as a function of center-of-mass quasimomentum K for the hard-core boson limit. The scattering state features an energy continuum represented by the gray area. For $V \geq 2J$, a bound state $\phi_K(x=-1,1)$ exists, shown by the red lines for different interaction strength V. (**b**) Symmetrized two-particle density dynamics for $V/J = [0, 1.0(1), 2.0(2), 3.3(1), 4.9(2)]$ (cases ①-⑤, respectively). We post-select on two atoms being present in the 1D system. For the cases ① and ② when $V < 2J$, the atoms spread independently with a ballistic light-cone velocity of $2Ja_{\mathrm{lat}}/\hbar$, see black dashed lines. For $V \geq 2J$, an additional slower light-cone emerges. The best fitted results of the bound pair's expansion according to Eq. (5.8) are shown as red dashed lines for $V/J = [2.0(2), 3.3(1), 4.9(2)]$. (**c**) The extracted tunneling energy of the bound pair J_b is shown for varying nearest-neighbor interactions V. As V increases, the tunneling energy of the bound pair decreases, demonstrating excellent agreement with the exact solution $J_b = J^2/V$ derived in [313], illustrated by red dashed line.

To experimentally probe the existence of the bound state due to eBHM, we focus on the hard-core boson limit of $U \to \infty$ and the repulsive nearest-neighbor interaction $V > 0$, where the occupation of two atoms in a single site is strongly suppressed. We measure the out-of-equilibrium dynamics of the bound state by preparing two atoms on neighboring sites in the 1D system and quenching the tunneling energy to finite values J. We use our addressing technique, see Sec. 3.3.2, to prepare three atomic pairs in a separated chain, with each pair spaced three lattice sites apart. These pairs are aligned along the x-direction with the dynamics axis, prepared by the magnetic gradient, see Sec. 5.1.1. The atomic pairs are initially in the $|1,-1\rangle$ state before applying a series of MW transfers into the $|2,+2\rangle$ state. The $|2,+2\rangle$ state is chosen to eliminate the vertical tunneling due to the magnetic gradient conditions. At this stage, the atomic pairs are trapped in the optical lattices at the depth of $40/40/60E_r$ ($x/y/z$-direction) where their motional dynamics are frozen. To initiate the dynamics, we quench the depth of the lattices to $12-13E_r$, corresponding to a tunneling energy of $J = h \times 17 - 20$Hz, which allows us to reach the hard-core limit $U/J \gtrsim 11$. Simultaneously, we apply stroboscopic dressing pulses, enabling the atomic pairs to undergo dynamics with the nearest-neighbor interaction V. Finally, we freeze the dynamics by quenching the optical lattice depth to the atomic limit before imaging.

In the absence of nearest-neighbor interactions ($V = 0$; case ① in Fig. 5.5b), we observe a characteristic light-cone indicating the free expansion of the two atoms. This is expected for the hard-core boson limit [363–365]. The expansion speed of the wavefront is consistent with the Lieb-Robinson bound given by $2Ja_{\mathrm{lat}}/\hbar$, see black dashed lines in Fig. 5.5b. When the nearest-neighbor interaction strength is introduced beyond the critical value $V \geq 2J$ [313], a second light-cone with a slower wavefront expansion emerges. Moreover, at higher interaction strengths V, the pair's density at the original position remains high. To qualitatively study the dynamics of the bound pair, we introduce a model that describes the wavefront propagation. The coherent interference of all pathways of the single-particle quantum walk results in a ballistic expansion with a group velocity of $2Jt/\hbar$. Here, the probability density ρ is described by $\rho_i(t) = |\mathcal{J}_i(2Jt)|^2$, where $\mathcal{J}_i$ is the Bessel function of the first kind on the lattice site i. Initializing a pair state in the hard-core boson limit in absence of the nearest-neighbor interactions, we describe the probability density by the incoherent sum of two Bessel functions as

$$\rho_i(t) = (|\mathcal{J}_i(2Jt)|^2 + |\mathcal{J}_{i+1}(2Jt)|^2)/2. \tag{5.7}$$

Here, the density continues to spread ballistically with $2Jt/\hbar$, but the central interference pattern vanishes. This model is in perfect agreement with a hard-core bosons simulation and is in good agreement with our experimental data in Fig. 5.5b (case ① and ②). We extend the model to include the ballistic expansion of the bound pair [37, 366, 367] by following Eq. (5.7) with a reduced tunneling energy J_b compared to the tunneling energy of the free pair $J_f = J$. To fit the model to our data, we further incorporate the relative amplitude of the free pair A_f and the bound state A_b with $A_f + A_b = 1$, resulting in:

$$\begin{aligned} \rho_i(t) = A_f \cdot (|\mathcal{J}_i(2J_f t)|^2 + |\mathcal{J}_{i+1}(2J_f t)|^2)/2 \\ + A_b \cdot (|\mathcal{J}_i(2J_b t)|^2 + |\mathcal{J}_{i+1}(2J_b t)|^2)/2. \end{aligned} \tag{5.8}$$

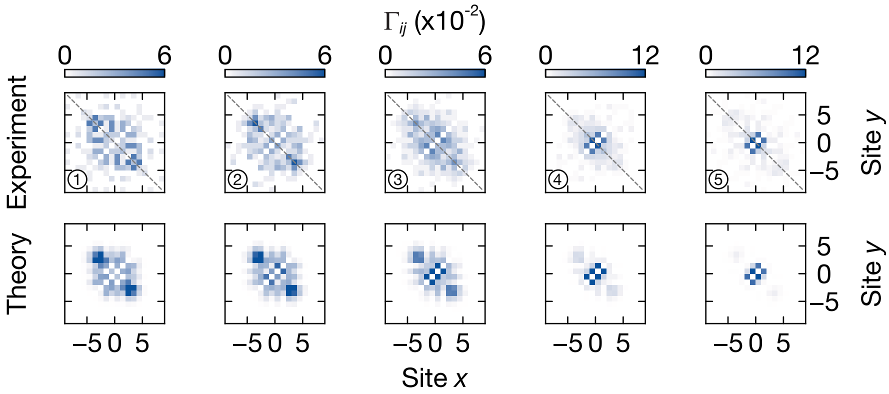

Figure 5.6: Symmetrized two-particle correlators. We analyze the two-particle correlator $\Gamma_{i,j} = \langle a_i^\dagger a_j^\dagger a_i a_j \rangle$ for the datasets in Fig. 5.5c at a fixed evolution time of $t = 3.8\,\hbar/2J$. The upper row shows the measured correlator, while the lower row is the correlator obtained with exact diagonalization for comparison. For $V = 0$, we observe strong anti-bunching on the off-diagonal due to the fermionization of the hard-core bosons. However, for $V \geq 2J$, the strong nearest-neighbor correlators on the diagonal begin to appear, indicating correlated pair tunneling. These results are in good agreement with the theoretical simulation. The gray dashed lines illustrate the symmetrization axis of data averaging.

Increasing the nearest-neighbor interaction strength $V/J = 2.0(2) - 4.9(2)$ (cases ③-⑤), we find a reduced velocity for the bound pairs (red dashed lines in Fig. 5.5b) while the light-cone of the free atoms remains stable (shown by black dashed lines). Comparing the fitted bound pair tunneling energy J_b with the exact solution derived in [313], we find excellent agreement with the expected bound pair tunneling energy of $J_b = J^2/V$, see Fig. 5.5c. To definitively prove the existence of the repulsively-bound pairs, we additionally examine the microscopic two-particle correlators, $\Gamma_{i,j} = \langle a_i^\dagger a_j^\dagger a_i a_j \rangle$ [37, 363]. Fig. 5.6 shows the experimental data and the exact diagonalization simulation of the two-particle correlations $\Gamma_{i,j}$ for varying nearest-neighbor interaction V. In the absence of nearest-neighbor interactions $V = 0$, the hard-core bosons effectively behave as noninteracting spinless fermions and show long-range correlations on the anti-diagonal. This is a direct consequence of Hanbury Brown and Twiss interference for fermions, leading to characteristic anti-bunching [363, 365, 368]. However, when the nearest-neighbor interactions are present, $V \geq 2J$, we observe correlated pair-tunneling, which results in strong nearest-neighbor correlations along the diagonal [369].

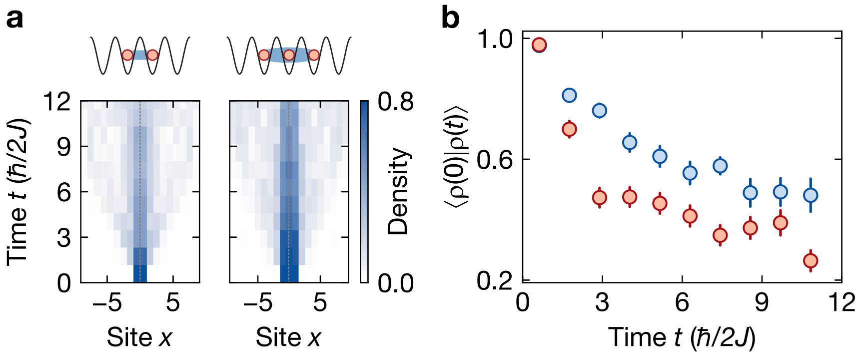

Figure 5.7: Repulsively-bound dimers and trimers. (**a**) Symmetrized probability density of two-particle $l = 2$ and three-particle $l = 3$ dynamics at $V/J = 4.9(2)$. The vertical gray dashed lines show the symmetrization axis. (**b**) We analyze the atomic density of the two (three) central sites for the string of length $l = 2$ ($l = 3$), shown in red (blue). The three-atom bound state experiences an effective larger repulsion and has a lower group velocity, resulting in larger density at the center positions.

Three-atom bound state

We extend the repulsively-bound atomic pair to larger many-particle bound states. The dynamics of these strings are often referred to as "l-bits" or "l-strings" where l refers to the length of the string. These strings have been extensively studied in theory [366, 367] and have recently been observed experimentally with MW photons [370]. The exact band structure of these larger many-particle bound states can be derived by using the Bethe ansatz [367]. The tunneling dynamics of the strings is exponentially suppressed, and follows $J_b \propto e^{-l}$, indicating that longer strings become increasingly localized.

In our measurements, we probe the dynamics of three-atom linear strings ($l = 3$) and compare with two-atom linear strings ($l = 2$), which have been studied in the previous Sec. 5.3.1. For both cases, we operate with the same interaction of $V/J = 4.9(2)$, which gives us direct insight into the influence of l. Fig. 5.7a shows the symmetrized probability density evolution for the string of length $l = 2$ and $l = 3$. For the strings of length $l = 2$, a clear double light-cone was observed, featuring the free-particle light-cone and the slowly spreading light-cone of the bound string. For the strings of length $l = 3$, the double light-cone still remains. Given our measured timescale of $t < 12\hbar/2J$, it is challenging to extract the light-cone velocity of $l = 3$ since their dynamics are almost frozen on this timescale. Instead, we compare the probability density at the origin of the string position by evaluating the time evolution of the mean atomic density at their original sites $\langle\rho(0)\rho(t)\rangle$, see Fig. 5.7b. We observe that the mean density for $l = 3$ is strongly localized on its original sites, as anticipated from the theoretical predictions [366, 367] and prior experimental observations [370].

5.3.2 Constrained "hard-rods" dynamics

We proceed from the two-particle low-density regime to the higher density of half-filling. We use a CDW pattern, a periodic structure of atoms and holes, as an initial state. The CDW state with a period of $2a_{\mathrm{lat}}$ has the same energy, independent of the nearest-neighbor interaction V. Therefore, we can measure the effect of the eBHM over the BHM using the initial state, which has the same energy in both models. To keep the density stable during the dynamics, we place repulsive potential walls with a height larger than the on-site interaction U at the boundary of the system. These walls are generated by off-resonant light at a wavelength of 670 nm, whose shape and potential height can be fully controlled by a digital micromirror device (DMD). We prepare the CDW pattern with a size of 18 lattice sites using our addressing technique, see Sec. 3.3.2. We then subsequently quench the optical lattices and apply the stroboscopic Rydberg dressing to the hard-core limit to examine the dynamics in 1D.

We first investigate the many-body dynamics of the CDW in the absence of the nearest-neighbor interaction $V = 0$. In the hard-core boson limit, the local mean density of the CDW exhibits an oscillatory phase during the dynamics while maintaining the crystalline-like structure. The atomic density occupies the even or the odd sites alternately over the dynamics, see top row in Fig. 5.8a. We quantify this oscillation by introducing the imbalance, given by

$$\mathcal{I} = \frac{N_e - N_o}{N_e + N_o}, \tag{5.9}$$

where N_e (N_o) are the number of atoms occupying in the the even (odd) sites. Comparing our data to the exact diagonalization calculations, which includes a reduced density $\bar{n} = 0.44 - 0.50$, we find excellent agreement, see Fig. 5.8b. For the strong nearest-neighbor interacting $V/J = 11.3(6)$, the hard-core bosons become "hard-rods". The nearest-neighbor interaction V prevents the dynamics of the atoms, featuring an extended exclusion volume and thus inhibiting the occupation of neighboring sites [371]. This can also be explained by the energy gap induced by the bound state, as discussed in Fig. 5.5a. The stabilized CDW under the eBHM has been experimentally observed with the CDW of two-particle per period [197]. However, one can observe the dynamics of a defect, beginning at the edge where the site is unoccupied, see the left side of Fig. 5.8c. At this edge, the atom is unimpeded and can tunnel without paying any extra energy, leaving an additional free volume for the subsequent atom to propagate freely. As time evolves, the defect will propagate through the system to the opposite edge, leaving behind a CDW density pattern phase-shifted by one site. This is equivalent to flipping the sign of the imbalance $\mathcal{I}$ in a area through which the defect propagates. We quantify this characteristic signature of the defect trace by evaluating the imbalance $\mathcal{I}$ of two subsystems, separated by a maximum propagation distance of the defect within our observation timescale, see the vertical dashed line of Fig. 5.8c.

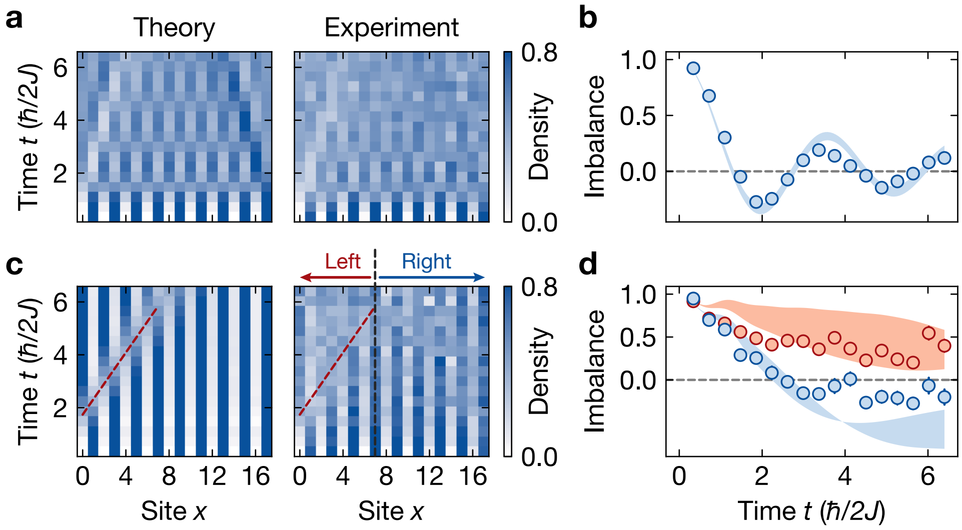

Figure 5.8: Charge density wave dynamics of hard-core bosons and hard-rods. (**a**) Many-body dynamics of a CDW in the hard-core boson limit obtained from exact diagonalization (left) and our measurements (right). The CDW exhibits oscillations between two phases in the density over the course of evolution. The measurements are post-selected for a mean desity of $\bar{n} = 0.44 - 0.50$ (**b**) The imbalance analysis of the CDW in the hard-core boson limit oscillates around 0, resulting from the alternating CDW phases. The shaded area is obtained from exact diagonalization calculations for $\bar{n} = 0.44 - 0.50$. (**c**) The CDW evolution, under the nearest-neighbor interaction of $V/J = 11.3(6)$, preserves its initial phase, in agreement between both theory (left) and measurements (right). The red dashed line highlights the defect dynamics through the stabilized CDW, leaving a trace by flipping the phase of the CDW. (**d**) When analyzing the imbalance on the left subsystem ($x < 7$), we observe a sign change from positive to negative, indicating the phase flip due to defect motion. Whereas, the imbalance of the right subsystem ($x \geq 7$) remains positive, preserving the original CDW phase. The shaded areas are obtained from the exact diagonalization calculations for $\bar{n} = 0.44 - 0.50$.

The imbalance $\mathcal{I}$ of the left subsystem ($x < 7$) undergoes a sign change, resulting in the switching of the CDW phase due to the defect motion. In contrast, for the right subsystem ($x \geq 7$), the imbalance $\mathcal{I}$ remains positive, preserving the original CDW phase. The imbalance $\mathcal{I}$ of the left and right subsystems has a qualitative agreement with exact diagonal calculations, see Fig. 5.8d. The remaining deviations are attributed to Rydberg decay and imperfections in the CDW preparation and the trapping potential. These can cause individual atom loss, which generates many defects in the system, leading to more complex dynamics.

5.3.3 Near-equilibrium density ordering

In the previous sections, we have studied the eBHM features in out-of-equilibrium dynamics. In this section, we examine the eBHM near equilibrium where we anticipate numerous interesting quantum phases intimately connected to the long-range interactions [50]. Specifically, we investigate atomic density ordering and the accumulation of long-range density-density correlations when the nearest-neighbor interaction V increases adiabatically from zero to $V \gg J$, crossing the critical value $V = 2J$. As a prerequisite, we initially establish a 1D low-energy state at half-filling in the absence of long-range interactions.

Preparation of low-energy ensemble

We first describe and characterize the preparation of a half-filling low-energy ensemble on a single 1D chain, which will subsequently be used for long-range equilibrium dynamics. Beginning with a unity-filled MI in 2D, we utilize our site-resolved addressing technique to prepare a single chain of 9 atoms. To confine the system to a stable half-filled system of 17 sites, we create repulsive potential walls at the system boundaries. Throughout the entire measurements, these walls remain stable, with a potential height of approximately $1.4U$, where $U \approx h \times 250\,\text{Hz}$ represents the on-site interaction. Next, we implement repulsive tapered potentials on both sides of the chain, starting from empty lattice sites next to the edge atoms and increasing towards the system boundaries, as illustrated in Fig. 5.9a. The repulsive tapered potentials use a separate set of off-resonant light and DMD, independent of the set used for the repulsive walls. The tapered profile is empirically chosen so that the potential different of the adjacent site approximates the band gap of $4J$, thus potentials linearly escalate from 0 to $20J$ over 5 lattice sites. At this point, the atoms remain pinned by the lattices, see stage ① in Fig. 5.9. We continue by reducing the lattice depth from $60E_r$ to the hard-core limit of $14.8E_r$ corresponding to tunneling energy of $J = h \times 11.6(3)$. We then linearly decrease the repulsive tapered potentials over a duration of δt, thereby connecting the atoms to the vacant sites across the entire system, see stage ②. Ideally, this procedure should prepare the ensemble in the many-body ground state at a mean filling of $\bar{n} = 0.53$. We characterize the efficiency of the preparation by observing the mean density of the reverse process back to the original point, which should restore the original state of the 9 atoms chain, see stage ③. Fig. 5.9b shows the spatial density profile of the initial state (gray, ①), the expected many-body ground state (blue, ②), and after the reversal of the process (red, ③). The corresponding mean atom number $\bar{n}$ is shown in Fig. 5.9c. After the preparation (stage ②), the mean density profile is spread over the entire system, leading to a reduced density from the initial state. The remaining density modulation is attributed to local potential disoder. The reduced density observed at the boundaries could be caused by the repulsive walls occupying the space within the system due to phase drifts between the optical lattices and the walls over the course of

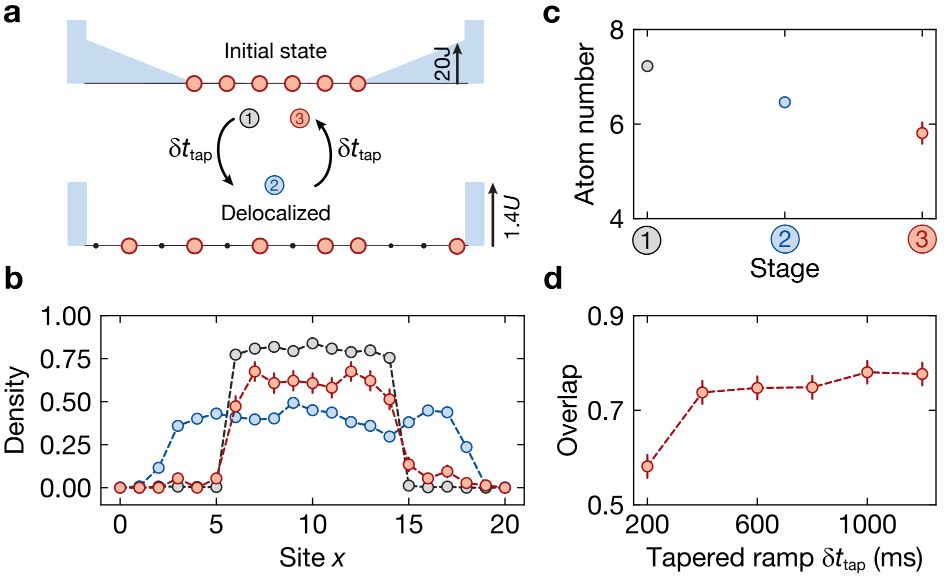

Figure 5.9: Preparation and characterization of the low-energy ensemble. (**a**) Simplified experimental protocol to prepare the low-energy ensemble. Beginning with a 1D chain of 9 atoms in 17 sites within the potential walls, repulsive tapered potentials are applied to the unoccupied sites. We then lower the lattice depth to the hard-core boson limit, which allows the atoms to tunnel. Subsequently, the tapered potentials are ramped down over a timescale of $\delta t_{\mathrm{tap}} \approx 120\hbar/2J$ to adiabatically delocalize the atoms, preparing the half-filling many-body state. Finally, reversing the procedure, we estimate the preparation efficiency by the revival of its original density. (**b**) The spatial density profiles during the three stages of the protocol. We start with a uniform average density of 0.76(1). Lowering the repulsive tapered potentials, the atoms delocalize over the entire system of 17 sites with a reduced density of 0.3(1). Ramping up the repulsive tapered potentials, we observe the revival of the initial density with an overlap of 0.78(2). (**c**) The average atom number at the three stages of the protocol. The preparation in stage ② causes loss of 0.7(1) atoms. (**d**) The density overlap with the original density for varying repulsive tapered ramp durations δt_{tap}. The overlap increases for longer ramp durations and only slightly improves after 400 ms. We operate with the repulsive tapered ramp duration of 800 ms for the following measurements.

measurements. Reversing the process (stage ③), the density distribution resembles its original configuration of the 9 atom chain with lower mean density. Comparing the mean atom number, before and after the preparation, we lose approximately 0.7(1) atoms. The reduction in atom number is likely due to imperfections in the adiabatic preparation, which consequently leads to the formation of doublons. These are then removed in our detection scheme due to parity projection [150–152]. We evaluate the density overlap between the initial with the revived states for varying durations of the tapered potential δt_{tap}, see Fig. 5.9d. The density overlap increases for longer durations. However, the improvement is marginal once the duration exceeds 400 ms. We decide to ramp the tapered repulsive potentials for $\delta t_{\mathrm{tap}} = 800\,\mathrm{ms}$, corresponding to $\approx 120\,\hbar/2J$, in subsequent measurements. With this ramp, we find an overlap of $78(2)\,\%$ after the reverse process (stage ③). We estimate the overlap of the half-filled state with the many-body ground state at stage ② to be approximately $88(2)\,\%$. Note that a similar overlap has been reported when adiabatically connecting individual atoms, localized in tweezer light, to the lattice ground state [372]. Excitations resulting from imperfections in the preparation ramps contribute to a finite temperature of the ensemble. By comparing our correlators C_d from Eq. (5.1) at post-selected densities $\bar{n} = 0.35 - 0.52$ with an in-equilibrium density-matrix renormalization group (DMRG) calculation, we are able to estimate an upper bound on the temperature to be $k_{\mathrm{B}}T \sim 2J$. One can obtain a similar energy scale that is introduced by initial holes. With our initial filling of $76(1)\,\%$, we expect an average of 2 holes, with each localized hole carrying an energy of $4J$. Assuming a fully-equilibrated system after the half-filling preparation protocol, the total energy of $E \sim 8J$ is evenly distributed among the 7 atoms. This means that each atom carries an energy of $E \sim 1.1J$. Additional heating might be caused by imperfections of the shape of the tapered potential and the partially diabatic ramp used during the preparation process. In the future, the low-energy ensembles can be achieved by better optimization of the initial filling and the parameters of the preparation ramp.

Experimental realizing of density ordering

Upon preparing the half-filled low-energy ensemble, we proceed to linearly increase the nearest-neighbor interaction from $V = 0$ to $V = 10.0(6)J$ over a timescale corresponding to $\approx 2.9\,\hbar/2J$. Matrix-product-state (MPS) simulations [373] predict that this linear ramp-up of the interaction V results in a significant overlap with the final many-body ground state of approximately $62\,\%$, if the ensemble starts in the many-body ground state before the interaction ramp. As the nearest-neighbor interaction strength increases, non-local density-density correlations are expected to emerge, as the strong nearest-neighbor repulsion results in crystalline-like structures. We investigate this effect by analyzing the connected correlator, see Eq. (5.1), for a distance d at various points along the interaction ramp, see Fig. 5.10. With increasing nearest-neighbor interaction V, both the nearest- ($C_{d=1}$) and next-nearest- ($C_{d=2}$) neighbor correlation strengths decrease and increase, respectively, which signifies the development of density-ordering in the system. The observed correlators $C_{d=1}$ and $C_{d=2}$ agree with time-dependent MPS calculations at $k_{\mathrm{B}}T = 1.5J$ across most interaction strengths, see Fig. 5.10b. Fig. 5.10c displays spatial correlators at various stages of the ramp. We observe no significant correlations for distances $d \gtrsim 3$, which is expected

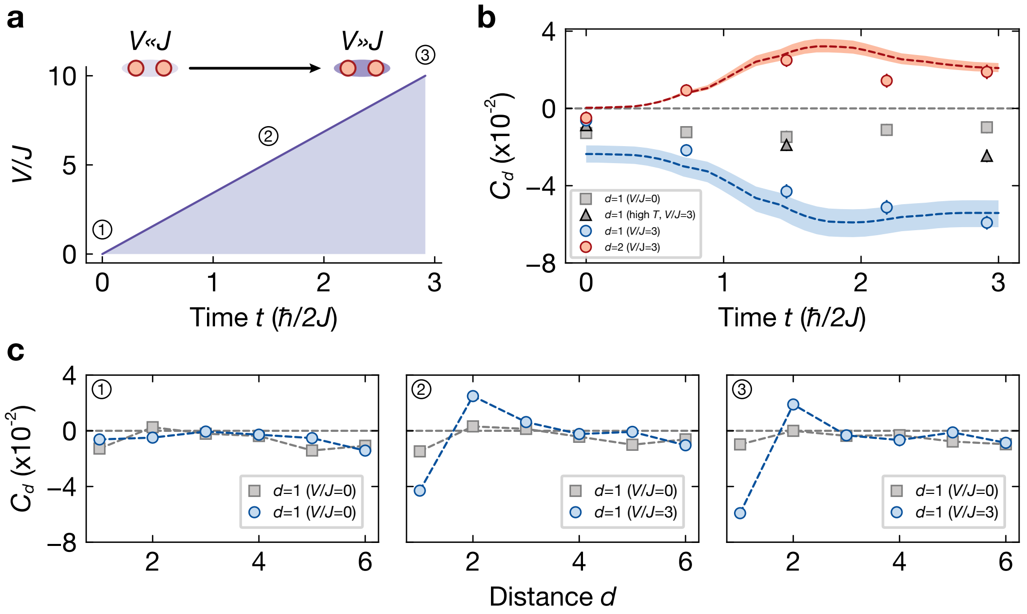

Figure 5.10: Near-equilibrium density-ordering via long-range interactions. (**a**) Illustration of the nearest-neighbor interaction ramp. Beginning with the low-energy ensemble from the preparation stage, we linearly increase the nearest-neighbor interactions up to $V/J = 10.0(6)$ within $t = 2.9\,\hbar/2J$. After that, we freeze the dynamics and evaluate the density-density correlations. (**b**) Observed correlations C_d for $d = 1$ (blue) and $d = 2$ (red) during the interaction ramp. The dashed lines (shaded areas) represent the theoretical correlations for $k_{\mathrm{B}}T = 1.5J$ ($k_{\mathrm{B}}T = 1.3 - 1.7J$) derived by a simulation of time-dependent MPS. For the high temperature ensemble measurements, the correlations remain unchanged over the course of the interaction ramp, see black triangular plot. The gray squares are a reference in the absence of interactions $V = 0$, resulting in no significant correlations. (**c**) Distance-dependent connected correlator C_d for different stages during the interaction ramp. The measurements are post-selected for mean densities $\bar{n} = 0.35 - 0.52$. The blue points (gray squares) show the respective correlation strength in the presence (absence) of Rydberg-dressed interactions.

from the simulations for our mean densities of $\bar{n} = 0.35 - 0.52$ and the chosen ramp duration. The energy ensemble is constrained by the initial state preparation, whose energy is independently estimated to be at $k_{\mathrm{B}}T \lesssim 2J$ in Sec. 5.3.3. We also perform a cross-reference measurement in which the ensemble starts at a high-energy. To generate this state, the repulsive tapered potentials are excluded during the preparation stage, while the rest of the protocol remains unchanged, see Sec. 5.3.3. As a result, the initial product state cannot follow the many-body ground state adiabatically, resulting in a substantial energy increase. Using this high-energy ensemble with an identical linear

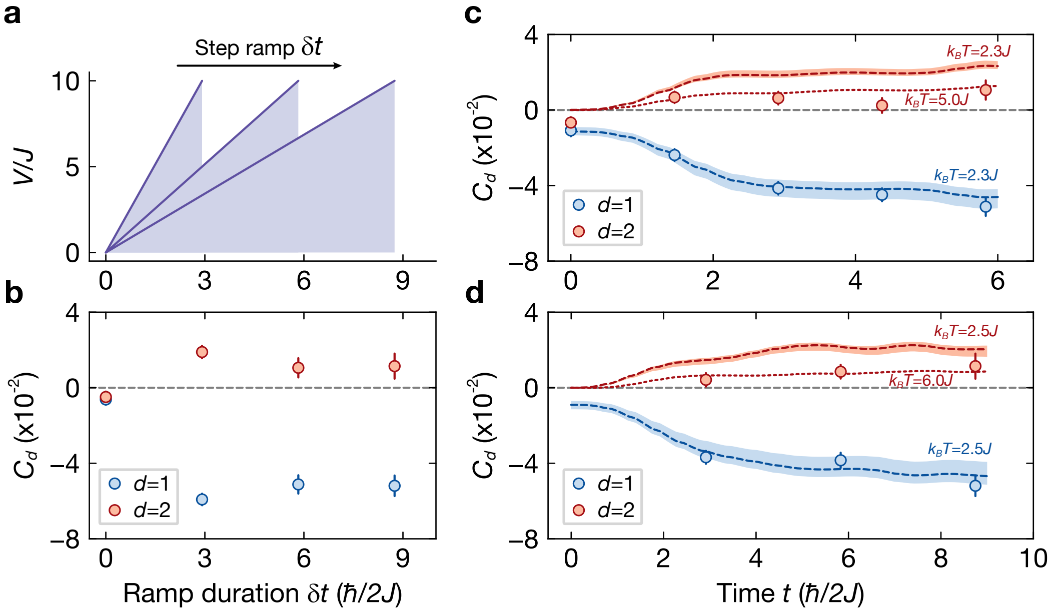

Figure 5.11: Dynamically-induced density-ordering for longer ramp durations. (**a**) Illustration of the experimental protocol. We operate with different ramp durations of $\delta t = [2.9, 5.8, 9.7]\,\hbar/2J$, ramping up to the same nearest-neighbor interaction of $V/J = 10.0(6)$. (**b**) The correlations for $d = 1$ (blue) and $d = 2$ (red) for each ramp duration at $V/J = 10.0(6)$. We observe slightly decreasing correlations for longer ramp durations. (**c**) The build-up of correlations during the ramp for a ramp duration of $\delta t = 5.8\,\hbar/2J$. The dashed (dotted) lines represent the theoretical correlations for $k_{\mathrm{B}}T = 2.3J$ ($k_{\mathrm{B}}T = 5.0J$) simulated using DMRG, with the shaded areas specify a range of $k_{\mathrm{B}}T = 2.0 - 2.5J$. (**d**) The build-up of correlations during the ramp for the ramp duration of $\delta t = 9.7\,\hbar/2J$. The dashed (dotted) lines represent the theoretical correlations for $k_{\mathrm{B}}T = 2.5J$ ($k_{\mathrm{B}}T = 6.0J$) simulated using DMRG, with the shaded areas specify a range of $k_{\mathrm{B}}T = 2.3 - 3.0J$. All measurements are post-selected for mean densities $\bar{n} = 0.35 - 0.52$

increase of the interactions V, see the triangular plot in Fig. 5.10c, we find that the correlations vanish.

We continue to investigate the influence of the nearest-neighbor interaction V for longer ramp timescales. In the absence of any imperfection such as Rydberg-losses and heating, we would expect a longer ramp duration to result in a larger overlap with the many-body ground state. This would feature stronger nearest-neighbor ($C_{d=1}$) and next-nearest-neighbor correlations ($C_{d=2}$). We extend our measurements to longer durations for the ramp of the nearest-neighbor interaction V, specifically $\delta t = 5.8\,\hbar/2J$ and $\delta t = 8.7\,\hbar/2J$. The final interaction strength remains constant at $V/J = 10.0(6)$, see Fig. 5.11a. We compare the correlators at the end of each ramp duration, shown in Fig. 5.11b. Interestingly, the correlators are strongest for the shorter ramp duration and decrease slightly for the longer ramps. This could potentially be explained by an overall energy increase in the ensemble due to Rydberg losses. We observe an average atom loss of approximately 0.9 atoms for the ramp duration of $\delta t = 2.9\,\hbar/2J$ and approximately 2.0 atoms for the longer ramp duration of $\delta t = 8.7\,\hbar/2J$. To quantify the heating effect, we compare the experimental data with dynamical DMRG calculations in Fig. 5.11c,d. From these observations, we can draw two main conclusions: First, focusing on the nearest-neighbor correlation $C_{d=1}$, we see that the longer ramp agrees with the calculation at an ensemble temperature of $k_\mathrm{B}T = 2.5J$. This indicates a monotonic temperature increase with an extended duration. Second, we observe a temperature mismatch between $C_{d=1}$ and $C_{d=2}$, where the $C_{d=2}$ agree better with higher temperature calculations. This can be explained by the fact that the ensemble does not fully re-thermalize when an atom-loss event occurs during the interaction V ramp. There are several open directions to explore this processes in the future. Experimentally, it would be worth investigating ramps with lower nearest-neighbor interaction at the final of the ramps. An ideal point would be slightly above the critical point at $V = 2J$ where the nearest-neighbor interaction V remains dominant. Moreover, improving the initial state preparation will increase the correlator strength due to a better ground state overlap with the ground state of eBHM. On the theoretical side, extending the model to include an open quantum system and Rydberg losses, would offer more understanding and provide further insights to explain the results.

5.4 Summary

We exploited Rydberg dressing to introduce long-range interactions in a quantum system. Through stroboscopic Rydberg dressing, the atomic lifetime can be extended over 100 ms, surpassing the tunneling timescale in the BHM. Consequently, we realized long-range interactions in the itinerant regime. Together with our quantum gas microscope, which provides excellent single-site control and readout, we then demonstrated key features of the eBHM using stroboscopic Rydberg dressing: We probed the existence of two-particle repulsively-bound pair states in out-of-equilibrium dynamics. In a half-filled system, we observed striking different dynamics for a CDW due to the nearest-neighbor interactions and identify defect dynamics causing a phase shift of the CDW pattern. Finally, we investigated the near-equilibrium state of the half-filled ensemble. By slowly increasing the nearest-neighbor interactions, the density-density correlations are observed.

Chapter 6

Conclusion and outlook

Conclusion

In this dissertation, we have studied long-range interactions of Rydberg atoms in strongly correlated systems of ultracold gases. Microscopic insights and controls over quantum states due to our quantum gas microscope enabled the study of both in- and out-of-equilibrium dynamics. The long-range interactions were controlled via independent optical coupling schemes to two distinct Rydberg states.

We utilized strong Rydberg interactions to control a light-matter interface based on subwavelength atomic arrays. The high-efficiency light-matter coupling of the array, a prior resulting in strong reflection of probe photons, was altered to be transparent via a Rydberg state electromagnetically induced transparency (EIT). Exploring the regime of high Rydberg population, we observed that the transmissive array was restored to reflective for the probe photons. The switching mechanism was also alternatively demonstrated using a single controlled Rydberg atom. Here, the transparent array was returned to being reflective for the probe photons around the controlled Rydberg atom through the Rydberg blockade. By simultaneously detecting the controlled atom and the probe photons, we observed correlations that are indications for the entanglement between them.

Moving towards off-resonant coupling to Rydberg states, we tuned the long-range interactions to the relevant parameters of the Hubbard model. Using stroboscopic Rydberg dressing, we improved the Rydberg lifetimes to exceed Hubbard tunneling timescales by approximately a factor of ten. This pioneering scheme allowed us to merge long-range Rydberg-dressed interactions into itinerant Hubbard systems. We then explored the out-of-equilibrium dynamics of this system and observed repulsively-bound states of atomic pairs and the stabilization of a charge density wave (CDW) state. In the near equilibrium when ramping the long-range interactions, the observation of density ordering indicates a phase transition to the predicted quantum solid.

Outlook

Switchable atomic arrays

We demonstrated the optical switching for single photons by manipulating individual single atoms in a subwavelength array. The switching efficiency is limited by the long required detection time of the EMCCD, a consequence of the low signal-to-noise ratio (SNR), compared to the finite Rydberg lifetime and the dipolar exchange processes. This could be improved by modifying the imaging system to map the photons within the blockaded area to a detector with single photon sensitivity. Consequently, the probe duration can be significantly shortened, suppressing the Rydberg lifetime and dipolar exchange processes.

Our results demonstrate a fundamental component for high-efficiency control over individual atoms and photons, thereby paving the way towards several applications: the detection of atom-photon entanglement, generating entangled photonic states such as multiple-photon entangled Greengerber-Horne-Zeilinger (GHZ) state [156], or using single atoms to generate a spatial photon mode via dipole-dipole interactions [281, 282]. The same procedure can be utilized for the direct detection of Rydberg atoms, where the reflected photon mode is mapped to the presence of Rydberg atoms. Given the free space nature of the subwavelength arrays, scaling to multimode operation with multiple controlled single atoms over the arrays is straightforward, enabling the parallelization of quantum operations on multiple qubits [156]. In addition, coupling the arrays to Rydberg states offers high fidelity for photon storage [275, 277] and photon-photon gates [156, 275]. Furthermore, extending to three-dimensional (3D) subwavelength arrays might provide further advantages [374].

Rydberg dressing

The combination of local microscopic control for initial state preparation, along with temporal control over extended-range interactions and the flexibility in tuning Rydberg-dressed interactions via external fields, provides numerous possibilities that are challenging to attain on other platforms. For example, we can extend to higher dimensions using ladder systems [310]. Operating with two components, where only one component has long-range interactions, presents the supersolid (SS) formation [375]. When moving beyond the hard-core boson limit, the full $V/J - U/J$ phase diagram of the one-dimensional (1D) extended Bose-Hubbard model (eBHM) predicts the existence of the Haldane insulator [302, 376]. Exploring low-energy physics of extended-range interacting fermions could provide insights relevant for understanding 1D cuprate chains [377]. Additionally, the constrained dynamics of the hard-rods model is an intriguing area for exploration [371], and the ability to dynamically control the interaction strength could open new opportunities towards mixed analog-digital quantum simulation approaches [63, 348].

In the frozen gas regime, the transverse field in Rydberg-dressed Ising models is typically small due to weak microwave (MW) coupling between hyperfine states. Optical coupling between these states with a Raman setup, as mentioned in Sec. 3.5.4, offers strong coupling of the transverse field to Rydberg-dressed Ising models, providing for stability or melting of initial state dynamics [378, 379]. Finally, our capability of parallel spin-dependent coupling to Rydberg states can be utilized to create multi-qubit gates [380].

Bibliography

[1] H. J. Metcalf and P. Van der Straten. *Laser cooling and trapping*. Springer, New York (1999). ISBN 978-0-387-98747-7 978-0-387-98728-6. (Cited on page **1**)

[2] A. Ashkin. *Trapping of Atoms by Resonance Radiation Pressure*. Phys. Rev. Lett. **40**, 729–732 (1978). (Cited on page **1**)

[3] W. D. Phillips and H. Metcalf. *Laser Deceleration of an Atomic Beam*. Phys. Rev. Lett. **48**, 596–599 (1982). (Cited on page **1**)

[4] S. Chu, L. Hollberg, J. E. Bjorkholm, A. Cable, and A. Ashkin. *Three-dimensional viscous confinement and cooling of atoms by resonance radiation pressure*. Phys. Rev. Lett. **55**, 48–51 (1985). (Cited on page **1**)

[5] S. Chu, J. E. Bjorkholm, A. Ashkin, and A. Cable. *Experimental Observation of Optically Trapped Atoms*. Phys. Rev. Lett. **57**, 314–317 (1986). (Cited on page **1**)

[6] M. H. Anderson, J. R. Ensher, M. R. Matthews, C. E. Wieman, and E. A. Cornell. *Observation of Bose-Einstein Condensation in a Dilute Atomic Vapor*. Science **269**, 198–201 (1995). (Cited on page **1**)

[7] C. C. Bradley, C. A. Sackett, J. J. Tollett, and R. G. Hulet. *Evidence of Bose-Einstein Condensation in an Atomic Gas with Attractive Interactions*. Phys. Rev. Lett. **75**, 1687–1690 (1995). (Cited on page **1**)

[8] K. B. Davis, M. O. Mewes, M. R. Andrews, N. J. Van Druten, D. S. Durfee, D. M. Kurn, and W. Ketterle. *Bose-Einstein Condensation in a Gas of Sodium Atoms*. Phys. Rev. Lett. **75**, 3969–3973 (1995). (Cited on page **1**)

[9] B. DeMarco and D. S. Jin. *Onset of Fermi Degeneracy in a Trapped Atomic Gas*. Science **285**, 1703–1706 (1999). (Cited on page **1**)

[10] F. Schreck, L. Khaykovich, K. L. Corwin, G. Ferrari, T. Bourdel, J. Cubizolles, and C. Salomon. *Quasipure Bose-Einstein Condensate Immersed in a Fermi Sea*. Phys. Rev. Lett. **87** (2001). (Cited on page **1**)

[11] A. G. Truscott, K. E. Strecker, W. I. McAlexander, G. B. Partridge, and R. G. Hulet. *Observation of Fermi Pressure in a Gas of Trapped Atoms*. Science **291**, 2570–2572 (2001). (Cited on page **1**)

[12] I. Buluta and F. Nori. *Quantum Simulators*. Science **326**, 108–111 (2009). (Cited on page **1**)

[13] I. Bloch, J. Dalibard, and S. Nascimbène. *Quantum simulations with ultracold quantum gases*. Nat. Phys. **8**, 267–276 (2012). (Cited on pages **1** and **25**)

[14] I. Georgescu, S. Ashhab, and F. Nori. *Quantum simulation*. Rev. Mod. Phys. **86**, 153–185 (2014). (Cited on pages **1** and **25**)

[15] F. Schäfer, T. Fukuhara, S. Sugawa, Y. Takasu, and Y. Takahashi. *Tools for quantum simulation with ultracold atoms in optical lattices*. Nat. Rev. Phys. **2**, 411–425 (2020). (Cited on page **1**)

[16] M. Greiner, O. Mandel, T. Esslinger, T. W. Hänsch, and I. Bloch. *Quantum Phase Transition from a Superfluid to a Mott Insulator in a Gas of Ultracold Atoms*. Nature **415**, 39–44 (2002). (Cited on pages **1** and **25**)

[17] J. J. García-Ripoll, M. A. Martin-Delgado, and J. I. Cirac. *Implementation of Spin Hamiltonians in Optical Lattices*. Phys. Rev. Lett. **93** (2004). (Cited on page **1**)

[18] C. A. Regal, M. Greiner, and D. S. Jin. *Observation of Resonance Condensation of Fermionic Atom Pairs*. Phys. Rev. Lett. **92** (2004). (Cited on page **1**)

[19] M. W. Zwierlein, J. R. Abo-Shaeer, A. Schirotzek, C. H. Schunck, and W. Ketterle. *Vortices and superfluidity in a strongly interacting Fermi gas*. Nature **435**, 1047–1051 (2005). (Cited on page **1**)

[20] M. Aguado, G. K. Brennen, F. Verstraete, and J. I. Cirac. *Creation, Manipulation, and Detection of Abelian and Non-Abelian Anyons in Optical Lattices*. Phys. Rev. Lett. **101** (2008). (Cited on page **1**)

[21] H. P. Büchler, M. Hermele, S. D. Huber, M. P. A. Fisher, and P. Zoller. *Atomic Quantum Simulator for Lattice Gauge Theories and Ring Exchange Models*. Phys. Rev. Lett. **95** (2005). (Cited on page **1**)

[22] E. Zohar, J. I. Cirac, and B. Reznik. *Quantum simulations of lattice gauge theories using ultracold atoms in optical lattices*. Rep. Prog. Phys. **79**, 014401 (2016). (Cited on page **1**)

[23] U. Fischer and R. Schützhold. *Quantum simulation of cosmic inflation in two-component Bose-Einstein condensates*. Phys. Rev. A **70** (2004). (Cited on page **1**)

[24] S. Giovanazzi. *Hawking Radiation in Sonic Black Holes*. Phys. Rev. Lett. **94** (2005). (Cited on page **1**)

[25] M. Endres, M. Cheneau, T. Fukuhara, C. Weitenberg, P. Schauß, C. Gross, L. Mazza, M. C. Bañuls, L. Pollet, I. Bloch, and S. Kuhr. *Observation of Correlated Particle-Hole Pairs and String Order in Low-Dimensional Mott Insulators*. Science **334**, 200–203 (2011). (Cited on page **1**)

[26] J. Simon, W. S. Bakr, R. Ma, M. E. Tai, P. M. Preiss, and M. Greiner. *Quantum simulation of antiferromagnetic spin chains in an optical lattice*. Nature **472**, 307–312 (2011). (Cited on page **1**)

[27] M. Cheneau, P. Barmettler, D. Poletti, M. Endres, P. Schauß, T. Fukuhara, C. Gross, I. Bloch, C. Kollath, and S. Kuhr. *Light-cone-like spreading of correlations in a quantum many-body system*. Nature **481**, 484–487 (2012). (Cited on page **1**)

[28] M. F. Parsons, A. Mazurenko, C. S. Chiu, G. Ji, D. Greif, and M. Greiner. *Site-resolved measurement of the spin-correlation function in the Fermi-Hubbard model*. Science **353**, 1253–1256 (2016). (Cited on page **1**)

[29] M. Boll, T. A. Hilker, G. Salomon, A. Omran, J. Nespolo, L. Pollet, I. Bloch, and C. Gross. *Spin- and density-resolved microscopy of antiferromagnetic correlations in Fermi-Hubbard chains*. Science **353**, 1257–1260 (2016). (Cited on page **1**)

[30] L. W. Cheuk, M. A. Nichols, K. R. Lawrence, M. Okan, H. Zhang, E. Khatami, N. Trivedi, T. Paiva, M. Rigol, and M. W. Zwierlein. *Observation of spatial charge and spin correlations in the 2D Fermi-Hubbard model*. Science **353**, 1260–1264 (2016). (Cited on page **1**)

[31] A. Mazurenko, C. S. Chiu, G. Ji, M. F. Parsons, M. Kanász-Nagy, R. Schmidt, F. Grusdt, E. Demler, D. Greif, and M. Greiner. *A cold-atom Fermi–Hubbard antiferromagnet*. Nature **545**, 462–466 (2017). (Cited on page **1**)

[32] T. A. Hilker, G. Salomon, F. Grusdt, A. Omran, M. Boll, E. Demler, I. Bloch, and C. Gross. *Revealing hidden antiferromagnetic correlations in doped Hubbard chains via string correlators*. Science **357**, 484–487 (2017). (Cited on page **1**)

[33] M. Holten, L. Bayha, K. Subramanian, S. Brandstetter, C. Heintze, P. Lunt, P. M. Preiss, and S. Jochim. *Observation of Cooper pairs in a mesoscopic two-dimensional Fermi gas*. Nature **606**, 287–291 (2022). (Cited on page **1**)

[34] M. Lebrat, M. Xu, L. H. Kendrick, A. Kale, Y. Gang, P. Seetharaman, I. Morera, E. Khatami, E. Demler, and M. Greiner. *Observation of Nagaoka polarons in a Fermi–Hubbard quantum simulator*. Nature **629**, 317–322 (2024). (Cited on page **1**)

[35] C. Weitenberg, M. Endres, J. F. Sherson, M. Cheneau, P. Schauß, T. Fukuhara, I. Bloch, and S. Kuhr. *Single-Spin Addressing in an Atomic Mott Insulator*. Nature **471**, 319–324 (2011). (Cited on pages **1**, **28**, **62**, and **96**)

[36] T. Fukuhara, A. Kantian, M. Endres, M. Cheneau, P. Schauß, S. Hild, D. Bellem, U. Schollwöck, T. Giamarchi, C. Gross, I. Bloch, and S. Kuhr. *Quantum Dynamics of a Mobile Spin Impurity*. Nat. Phys. **9**, 235–241 (2013). (Cited on pages **1**, **25**, and **62**)

[37] T. Fukuhara, P. Schauß, M. Endres, S. Hild, M. Cheneau, I. Bloch, and C. Gross. *Microscopic Observation of Magnon Bound States and Their Dynamics*. Nature **502**, 76–79 (2013). (Cited on pages **1**, **25**, **106**, and **107**)

[38] J.-y. Choi, S. Hild, J. Zeiher, P. Schauß, A. Rubio-Abadal, T. Yefsah, V. Khemani, D. A. Huse, I. Bloch, and C. Gross. *Exploring the many-body localization transition in two dimensions*. Science **352**, 1547–1552 (2016). (Cited on page **1**)

[39] A. M. Kaufman, M. E. Tai, A. Lukin, M. Rispoli, R. Schittko, P. M. Preiss, and M. Greiner. *Quantum thermalization through entanglement in an isolated many-body system*. Science **353**, 794–800 (2016). (Cited on page **1**)

[40] D. Wei, A. Rubio-Abadal, B. Ye, F. Machado, J. Kemp, K. Srakaew, S. Hollerith, J. Rui, S. Gopalakrishnan, N. Y. Yao, I. Bloch, and J. Zeiher. *Quantum gas microscopy of Kardar-Parisi-Zhang superdiffusion*. Science **376**, 716–720 (2022). (Cited on pages **1** and **25**)

[41] J. Léonard, S. Kim, J. Kwan, P. Segura, F. Grusdt, C. Repellin, N. Goldman, and M. Greiner. *Realization of a fractional quantum Hall state with ultracold atoms*. Nature **619**, 495–499 (2023). (Cited on page **1**)

[42] C. Chin, R. Grimm, P. Julienne, and E. Tiesinga. *Feshbach Resonances in Ultracold Gases*. Rev. Mod. Phys. **82**, 1225–1286 (2010). (Cited on pages **1** and **91**)

[43] D. Rossini and R. Fazio. *Phase diagram of the extended Bose–Hubbard model*. New J. Phys. **14**, 065012 (2012). (Cited on pages **1** and **91**)

[44] O. Dutta, M. Gajda, P. Hauke, M. Lewenstein, D.-S. Lühmann, B. A. Malomed, T. Sowiński, and J. Zakrzewski. *Non-Standard Hubbard Models in Optical Lattices: A Review*. Rep. Prog. Phys. **78**, 066001 (2015). (Cited on pages **1** and **91**)

[45] N. Defenu, T. Donner, T. Macrì, G. Pagano, S. Ruffo, and A. Trombettoni. *Long-Range Interacting Quantum Systems*. Rev. Mod. Phys. **95**, 035002 (2023). (Cited on pages **1**, **91**, and **92**)

[46] L. Chomaz, I. Ferrier-Barbut, F. Ferlaino, B. Laburthe-Tolra, B. L. Lev, and T. Pfau. *Dipolar physics: a review of experiments with magnetic quantum gases*. Rep. Prog. Phys. **86**, 026401 (2023). (Cited on pages **1** and **93**)

[47] J. Stuhler, A. Griesmaier, T. Koch, M. Fattori, T. Pfau, S. Giovanazzi, P. Pedri, and L. Santos. *Observation of Dipole-Dipole Interaction in a Degenerate Quantum Gas*. Phys. Rev. Lett. **95**, 150406 (2005). (Cited on pages **1** and **93**)

[48] H. Kadau, M. Schmitt, M. Wenzel, C. Wink, T. Maier, I. Ferrier-Barbut, and T. Pfau. *Observing the Rosensweig Instability of a Quantum Ferrofluid*. Nature **530**, 194–197 (2016). (Cited on pages **1** and **93**)

[49] S. Baier, M. J. Mark, D. Petter, K. Aikawa, L. Chomaz, Z. Cai, M. Baranov, P. Zoller, and F. Ferlaino. *Extended Bose-Hubbard Models with Ultracold Magnetic Atoms*. Science **352**, 201–205 (2016). (Cited on pages **1** and **93**)

[50] L. Su, A. Douglas, M. Szurek, R. Groth, S. F. Ozturk, A. Krahn, A. H. Hébert, G. A. Phelps, S. Ebadi, S. Dickerson, F. Ferlaino, O. Marković, and M. Greiner. *Dipolar Quantum Solids Emerging in a Hubbard Quantum Simulator*. Nature **622**, 724–729 (2023). (Cited on pages **1**, **93**, and **111**)

[51] K.-K. Ni, S. Ospelkaus, M. H. G. De Miranda, A. Pe'er, B. Neyenhuis, J. J. Zirbel, S. Kotochigova, P. S. Julienne, D. S. Jin, and J. Ye. *A High Phase-Space-Density Gas of Polar Molecules*. Science **322**, 231–235 (2008). (Cited on page **1**)

[52] B. Yan, S. A. Moses, B. Gadway, J. P. Covey, K. R. A. Hazzard, A. M. Rey, D. S. Jin, and J. Ye. *Observation of Dipolar Spin-Exchange Interactions with Lattice-Confined Polar Molecules*. Nature **501**, 521–525 (2013). (Cited on pages **1** and **92**)

[53] S. A. Moses, J. P. Covey, M. T. Miecnikowski, D. S. Jin, and J. Ye. *New Frontiers for Quantum Gases of Polar Molecules*. Nat. Phys. **13**, 13–20 (2017). (Cited on pages **1** and **92**)

[54] J. S. Rosenberg, L. Christakis, E. Guardado-Sanchez, Z. Z. Yan, and W. S. Bakr. *Observation of the Hanbury Brown–Twiss Effect with Ultracold Molecules*. Nat. Phys. **18**, 1062–1066 (2022). (Cited on pages **1** and **92**)

[55] L. Christakis, J. S. Rosenberg, R. Raj, S. Chi, A. Morningstar, D. A. Huse, Z. Z. Yan, and W. S. Bakr. *Probing Site-Resolved Correlations in a Spin System of Ultracold Molecules*. Nature **614**, 64–69 (2023). (Cited on pages **1**, **92**, and **93**)

[56] A. N. Carroll, H. Hirzler, C. Miller, D. Wellnitz, S. R. Muleady, J. Lin, K. P. Zamarski, R. R. Wang, J. L. Bohn, and A. M. Rey. *Observation of Generalized tJ Spin Dynamics with Tunable Dipolar Interactions*. arXiv:2404.18916 (2024). (Cited on pages **1** and **92**)

[57] T. F. Gallagher. *Rydberg Atoms*. Cambridge University Press (1994). ISBN 978-0-521-38531-2 978-0-521-02166-1 978-0-511-52453-0. (Cited on pages **1**, **5**, **6**, **10**, and **11**)

[58] H. Weimer, M. Müller, I. Lesanovsky, P. Zoller, and H. P. Büchler. *A Rydberg quantum simulator*. Nat. Phys. **6**, 382–388 (2010). (Cited on page **1**)

[59] R. Löw, H. Weimer, J. Nipper, J. B. Balewski, B. Butscher, H. P. Büchler, and T. Pfau. *An experimental and theoretical guide to strongly interacting Rydberg gases*. J. Phys. B: At. Mol. Opt. Phys. **45**, 113001 (2012). (Cited on pages **1**, **9**, **10**, and **36**)

[60] M. Saffman. *Quantum Computing with Atomic Qubits and Rydberg Interactions: Progress and Challenges*. J. Phys. B: At. Mol. Opt. Phys. **49**, 202001 (2016). (Cited on pages **1** and **93**)

[61] S. De Léséleuc, V. Lienhard, P. Scholl, D. Barredo, S. Weber, N. Lang, H. P. Büchler, T. Lahaye, and A. Browaeys. *Observation of a symmetry-protected topological phase of interacting bosons with Rydberg atoms*. Science **365**, 775–780 (2019). (Cited on pages **1**, **25**, and **93**)

[62] A. Browaeys and T. Lahaye. *Many-Body Physics with Individually Controlled Rydberg Atoms*. Nat. Phys. **16**, 132–142 (2020). (Cited on pages **1** and **93**)

[63] M. Morgado and S. Whitlock. *Quantum Simulation and Computing with Rydberg-interacting Qubits*. AVS Quantum Sci. **3**, 023501 (2021). (Cited on pages **1**, **19**, **93**, and **118**)

[64] H. Bernien, S. Schwartz, A. Keesling, H. Levine, A. Omran, H. Pichler, S. Choi, A. S. Zibrov, M. Endres, M. Greiner, V. Vuletić, and M. D. Lukin. *Probing many-body dynamics on a 51-atom quantum simulator*. Nature **551**, 579–584 (2017). (Cited on pages **1**, **5**, **23**, **25**, and **43**)

[65] G. Semeghini, H. Levine, A. Keesling, S. Ebadi, T. T. Wang, D. Bluvstein, R. Verresen, H. Pichler, M. Kalinowski, R. Samajdar, A. Omran, S. Sachdev, A. Vishwanath, M. Greiner, V. Vuletić, and M. D. Lukin. *Probing topological spin liquids on a programmable quantum simulator*. Science **374**, 1242–1247 (2021). (Cited on pages **1**, **23**, and **25**)

[66] S. Ebadi, T. T. Wang, H. Levine, A. Keesling, G. Semeghini, A. Omran, D. Bluvstein, R. Samajdar, H. Pichler, W. W. Ho, S. Choi, S. Sachdev, M. Greiner, V. Vuletić, and M. D. Lukin. *Quantum phases of matter on a 256-atom programmable quantum simulator*. Nature **595**, 227–232 (2021). (Cited on pages **1** and **23**)

[67] S. Ebadi, A. Keesling, M. Cain, T. T. Wang, H. Levine, D. Bluvstein, G. Semeghini, A. Omran, J.-G. Liu, R. Samajdar, X.-Z. Luo, B. Nash, X. Gao, B. Barak, E. Farhi, S. Sachdev, N. Gemelke, L. Zhou, S. Choi, H. Pichler, S.-T. Wang, M. Greiner, V. Vuletić, and M. D. Lukin. *Quantum optimization of maximum independent set using Rydberg atom arrays*. Science **376**, 1209–1215 (2022). (Cited on pages **1** and **23**)

[68] M. D. Lukin, M. Fleischhauer, R. Cote, L. M. Duan, D. Jaksch, J. I. Cirac, and P. Zoller. *Dipole Blockade and Quantum Information Processing in Mesoscopic Atomic Ensembles*. Phys. Rev. Lett. **87**, 037901 (2001). (Cited on pages **1**, **23**, **25**, and **44**)

[69] L. Isenhower, E. Urban, X. L. Zhang, A. T. Gill, T. Henage, T. A. Johnson, T. G. Walker, and M. Saffman. *Demonstration of a Neutral Atom Controlled-NOT Quantum Gate*. Phys. Rev. Lett. **104**, 010503 (2010). (Cited on pages **1** and **23**)

[70] T. Wilk, A. Gaëtan, C. Evellin, J. Wolters, Y. Miroshnychenko, P. Grangier, and A. Browaeys. *Entanglement of Two Individual Neutral Atoms Using Rydberg Blockade*. Phys. Rev. Lett. **104**, 010502 (2010). (Cited on pages **1** and **23**)

[71] T. Graham, M. Kwon, B. Grinkemeyer, Z. Marra, X. Jiang, M. Lichtman, Y. Sun, M. Ebert, and M. Saffman. *Rydberg-Mediated Entanglement in a Two-Dimensional Neutral Atom Qubit Array*. Phys. Rev. Lett. **123**, 230501 (2019). (Cited on pages **1** and **23**)

[72] H. Levine, A. Keesling, G. Semeghini, A. Omran, T. T. Wang, S. Ebadi, H. Bernien, M. Greiner, V. Vuletić, H. Pichler, and M. D. Lukin. *Parallel Implementation of High-Fidelity Multiqubit Gates with Neutral Atoms*. Phys. Rev. Lett. **123**, 170503 (2019). (Cited on pages **1**, **19**, **23**, and **50**)

[73] I. S. Madjarov, J. P. Covey, A. L. Shaw, J. Choi, A. Kale, A. Cooper, H. Pichler, V. Schkolnik, J. R. Williams, and M. Endres. *High-fidelity entanglement and detection of alkaline-earth Rydberg atoms*. Nat. Phys. **16**, 857–861 (2020). (Cited on pages **1** and **23**)

[74] S. Ma, A. P. Burgers, G. Liu, J. Wilson, B. Zhang, and J. D. Thompson. *Universal Gate Operations on Nuclear Spin Qubits in an Optical Tweezer Array of Yb 171 Atoms*. Phys. Rev. X **12**, 021028 (2022). (Cited on pages **1** and **23**)

[75] J. Kumlin, C. Braun, C. Tresp, N. Stiesdal, S. Hofferberth, and A. Paris-Mandoki. *Quantum optics with Rydberg superatoms*. J. Phys. Commun. **7**, 052001 (2023). (Cited on page **1**)

[76] R. J. Bettles, S. A. Gardiner, and C. S. Adams. *Enhanced optical cross section via collective coupling of atomic dipoles in a 2D array*. Phys. Rev. Lett. **116**, 103602 (2016). (Cited on pages **1** and **61**)

[77] E. Shahmoon, D. S. Wild, M. D. Lukin, and S. F. Yelin. *Cooperative resonances in light scattering from two-dimensional atomic arrays*. Phys. Rev. Lett. **118**, 113601 (2017). (Cited on pages **1**, **59**, **60**, and **61**)

[78] J. Rui, D. Wei, A. Rubio-Abadal, S. Hollerith, J. Zeiher, D. M. Stamper-Kurn, C. Gross, and I. Bloch. *A subradiant optical mirror formed by a single structured atomic layer*. Nature **583**, 369–374 (2020). (Cited on pages **1**, **60**, **61**, **62**, **65**, **67**, and **72**)

[79] I. Mourachko, D. Comparat, F. De Tomasi, A. Fioretti, P. Nosbaum, V. M. Akulin, and P. Pillet. *Many-Body Effects in a Frozen Rydberg Gas*. Phys. Rev. Lett. **80**, 253–256 (1998). (Cited on page **2**)

[80] W. R. Anderson, J. R. Veale, and T. F. Gallagher. *Resonant Dipole-Dipole Energy Transfer in a Nearly Frozen Rydberg Gas*. Phys. Rev. Lett. **80**, 249–252 (1998). (Cited on page **2**)

[81] C. Simonelli, M. M. Valado, G. Masella, L. Asteria, E. Arimondo, D. Ciampini, and O. Morsch. *Seeded excitation avalanches in off-resonantly driven Rydberg gases*. J. Phys. B: At. Mol. Opt. Phys. **49**, 154002 (2016). (Cited on pages **2** and **100**)

[82] C. S. Adams, J. D. Pritchard, and J. P. Shaffer. *Rydberg atom quantum technologies*. J. Phys. B: At. Mol. Opt. Phys. **53**, 012002 (2020). (Cited on pages **5** and **36**)

[83] P. Scholl, M. Schuler, H. J. Williams, A. A. Eberharter, D. Barredo, K.-N. Schymik, V. Lienhard, L.-P. Henry, T. C. Lang, T. Lahaye, A. M. Läuchli, and A. Browaeys. *Quantum simulation of 2D antiferromagnets with hundreds of Rydberg atoms*. Nature **595**, 233–238 (2021). (Cited on page **5**)

[84] D. Bluvstein, S. J. Evered, A. A. Geim, S. H. Li, H. Zhou, T. Manovitz, S. Ebadi, M. Cain, M. Kalinowski, D. Hangleiter, J. P. Bonilla Ataides, N. Maskara, I. Cong, X. Gao, P. Sales Rodriguez, T. Karolyshyn, G. Semeghini, M. J. Gullans, M. Greiner, V. Vuletić, and M. D. Lukin. *Logical quantum processor based on reconfigurable atom arrays*. Nature (2023). (Cited on page **5**)

[85] M. Saffman, T. G. Walker, and K. Mølmer. *Quantum information with Rydberg atoms*. Rev. Mod. Phys. **82**, 2313–2363 (2010). (Cited on pages **5** and **25**)

[86] O. Firstenberg, C. S. Adams, and S. Hofferberth. *Nonlinear quantum optics mediated by Rydberg interactions*. J. Phys. B: At. Mol. Opt. Phys. **49**, 152003 (2016). (Cited on pages **5**, **25**, and **61**)

[87] J. A. Sedlacek, A. Schwettmann, H. Kübler, R. Löw, T. Pfau, and J. P. Shaffer. *Microwave electrometry with Rydberg atoms in a vapour cell using bright atomic resonances*. Nat. Phys. **8**, 819–824 (2012). (Cited on pages **5** and **42**)

[88] H. Fan, S. Kumar, J. Sedlacek, H. Kübler, S. Karimkashi, and J. P. Shaffer. *Atom based RF electric field sensing*. J. Phys. B: At. Mol. Opt. Phys. **48**, 202001 (2015). (Cited on page **5**)

[89] C. G. Wade, N. Šibalić, N. R. De Melo, J. M. Kondo, C. S. Adams, and K. J. Weatherill. *Real-time near-field terahertz imaging with atomic optical fluorescence*. Nat. Photonics **11**, 40–43 (2017). (Cited on page **5**)

[90] E. K. Dietsche, A. Larrouy, S. Haroche, J. M. Raimond, M. Brune, and S. Gleyzes. *High-sensitivity magnetometry with a single atom in a superposition of two circular Rydberg states*. Nat. Phys. **15**, 326–329 (2019). (Cited on pages **5** and **42**)

[91] M. M. Müller, A. Kölle, R. Löw, T. Pfau, T. Calarco, and S. Montangero. *Room-temperature Rydberg single-photon source*. Phys. Rev. A **87**, 053412 (2013). (Cited on page **5**)

[92] G. W. F. Drake and R. A. Swainson. *Quantum defects and the 1/ n dependence of Rydberg energies: Second-order polarization effects*. Phys. Rev. A **44**, 5448–5459 (1991). (Cited on page **6**)

[93] M. J. Seaton. *Quantum defect theory*. Rep. Prog. Phys. **46**, 167–257 (1983). (Cited on page **6**)

[94] C.-J. Lorenzen and K. Niemax. *Quantum Defects of the* $n\ ^2P_{1/2,3/2}$ *Levels in* ^{39}*K I and* ^{85}*Rb I*. Phys. Scr. **27**, 300–305 (1983). (Cited on page **6**)

[95] M. J. Seaton. *The Quantum Defect Method*. Mon. Not. R. Astron. Soc. **118**, 504–518 (1958). (Cited on page **6**)

[96] M. Mack, F. Karlewski, H. Hattermann, S. Höckh, F. Jessen, D. Cano, and J. Fortágh. *Measurement of absolute transition frequencies of Rb 87 to nS and nD Rydberg states by means of electromagnetically induced transparency*. Phys. Rev. A **83**, 052515 (2011). (Cited on page **6**)

[97] W. Li, I. Mourachko, M. W. Noel, and T. F. Gallagher. *Millimeter-wave spectroscopy of cold Rb Rydberg atoms in a magneto-optical trap: Quantum defects of the ns , np , and nd series*. Phys. Rev. A **67**, 052502 (2003). (Cited on page **6**)

[98] S. Weber, C. Tresp, H. Menke, A. Urvoy, O. Firstenberg, H. P. Büchler, and S. Hofferberth. *Calculation of Rydberg interaction potentials*. J. Phys. B: At. Mol. Opt. Phys. **50**, 133001 (2017). (Cited on pages **7**, **8**, **11**, **23**, **85**, and **97**)

[99] C. E. Theodosiou. *Lifetimes of alkali-metal—atom Rydberg states*. Phys. Rev. A **30**, 2881–2909 (1984). (Cited on page **7**)

[100] M. Marinescu, H. R. Sadeghpour, and A. Dalgarno. *Dispersion coefficients for alkali-metal dimers*. Phys. Rev. A **49**, 982–988 (1994). (Cited on page **7**)

[101] C. H. Greene and M. Aymar. *Spin-orbit effects in the heavy alkaline-earth atoms*. Phys. Rev. A **44**, 1773–1790 (1991). (Cited on page **7**)

[102] N. Šibalić, J. Pritchard, C. Adams, and K. Weatherill. *ARC: An open-source library for calculating properties of alkali Rydberg atoms*. Comput. Phys. Commun. **220**, 319–331 (2017). (Cited on pages **8**, **11**, **23**, and **79**)

[103] M. Auzinsh, D. Budker, and S. Rochester. *Optically polarized atoms: understanding light-atom interactions*. New York : Oxford University Press, Oxford (2010). ISBN 978-0-19-956512-2. (Cited on page **8**)

[104] B. E. King. *Angular Momentum Coupling and Rabi Frequencies for Simple Atomic Transitions*. arXiv:0804.4528 (2008). (Cited on page **8**)

[105] J. Zeiher. *Realization of Rydberg-dressed quantum magnets*. Ph.D. thesis, Ludwig-Maximilians-Universität München (2017). (Cited on pages **9**, **19**, **22**, **25**, **44**, **100**, and **102**)

[106] T. F. Gallagher, S. A. Edelstein, and R. M. Hill. *Radiative lifetimes of the S and D Rydberg levels of Na*. Phys. Rev. A **11**, 1504–1506 (1975). (Cited on page **10**)

[107] I. I. Beterov, I. I. Ryabtsev, D. B. Tretyakov, and V. M. Entin. *Quasiclassical calculations of blackbody-radiation-induced depopulation rates and effective lifetimes of Rydberg n S , n P , and n D alkali-metal atoms with* $n \leq 80$. Phys. Rev. A **79**, 052504 (2009). (Cited on pages **10**, **11**, and **100**)

[108] S. R. Cohen and J. D. Thompson. *Quantum Computing with Circular Rydberg Atoms*. PRX Quantum **2**, 030322 (2021). (Cited on page **11**)

[109] R. G. Hulet and D. Kleppner. *Rydberg Atoms in "Circular" States*. Phys. Rev. Lett. **51**, 1430–1433 (1983). (Cited on page **11**)

[110] T. Cantat-Moltrecht, R. Cortiñas, B. Ravon, P. Méhaignerie, S. Haroche, J. M. Raimond, M. Favier, M. Brune, and C. Sayrin. *Long-lived circular Rydberg states of laser-cooled rubidium atoms in a cryostat*. Phys. Rev. Res. **2**, 022032 (2020). (Cited on pages **11** and **100**)

[111] K.-N. Schymik, S. Pancaldi, F. Nogrette, D. Barredo, J. Paris, A. Browaeys, and T. Lahaye. *Single Atoms with 6000-Second Trapping Lifetimes in Optical-Tweezer Arrays at Cryogenic Temperatures*. Phys. Rev. Applied **16**, 034013 (2021). (Cited on pages **11** and **100**)

[112] M. Mack, J. Grimmel, F. Karlewski, L. Sárkány, H. Hattermann, and J. Fortágh. *All-optical measurement of Rydberg-state lifetimes*. Phys. Rev. A **92**, 012517 (2015). (Cited on page **11**)

[113] S. J. Hollerith. *A microscopically and vibrationally resolved study of Rydberg macrodimers*. Ph.D. thesis, Ludwig-Maximilians-Universität München (2022). (Cited on pages **11**, **25**, **38**, and **80**)

[114] J. Deiglmayr. *Long-range interactions between Rydberg atoms*. Phys. Scr. **91**, 104007 (2016). (Cited on page **11**)

[115] M. R. Flannery, D. Vrinceanu, and V. N. Ostrovsky. *Long-range interaction between polar Rydberg atoms*. J. Phys. B: At. Mol. Opt. Phys. **38**, S279–S293 (2005). (Cited on page **11**)

[116] K. Singer, J. Stanojevic, M. Weidemüller, and R. Côté. *Long-range interactions between alkali Rydberg atom pairs correlated to the n s– n s, n p– n p and n d– n d asymptotes*. J. Phys. B: At. Mol. Opt. Phys. **38**, S295–S307 (2005). (Cited on page **11**)

[117] M. E. Rose. *The Electrostatic Interaction of Two Arbitrary Charge Distributions*. J. Math. Phys. **37**, 215–222 (1958). (Cited on page **12**)

[118] P. R. Fontana. *Theory of Long-Range Interatomic Forces. I. Dispersion Energies between Unexcited Atoms*. Phys. Rev. **123**, 1865–1870 (1961). (Cited on page **12**)

[119] A. Dalgarno and W. Davison. *The Calculation of Van Der Waals Interactions*. Adv. At. Mol. Phys. **2**, 1–32 (1966). (Cited on page **12**)

[120] S. Ravets, H. Labuhn, D. Barredo, L. Béguin, T. Lahaye, and A. Browaeys. *Coherent dipole–dipole coupling between two single Rydberg atoms at an electrically-tuned Förster resonance*. Nat. Phys. **10**, 914–917 (2014). (Cited on page **14**)

[121] S. Ravets, H. Labuhn, D. Barredo, T. Lahaye, and A. Browaeys. *Measurement of the angular dependence of the dipole-dipole interaction between two individual Rydberg atoms at a Förster resonance*. Phys. Rev. A **92**, 020701 (2015). (Cited on page **14**)

[122] D. Barredo, H. Labuhn, S. Ravets, T. Lahaye, A. Browaeys, and C. S. Adams. *Coherent Excitation Transfer in a Spin Chain of Three Rydberg Atoms*. Phys. Rev. Lett. **114**, 113002 (2015). (Cited on page **14**)

[123] Y. Chew, T. Tomita, T. P. Mahesh, S. Sugawa, S. De Léséleuc, and K. Ohmori. *Ultrafast energy exchange between two single Rydberg atoms on a nanosecond timescale*. Nat. Photonics **16**, 724–729 (2022). (Cited on page **14**)

[124] T. G. Walker and M. Saffman. *Consequences of Zeeman degeneracy for the van der Waals blockade between Rydberg atoms*. Phys. Rev. A **77**, 032723 (2008). (Cited on pages **15** and **16**)

[125] B. Vermersch, A. W. Glaetzle, and P. Zoller. *Magic distances in the blockade mechanism of Rydberg p and d states*. Phys. Rev. A **91**, 023411 (2015). (Cited on page **15**)

[126] D. Barredo, S. Ravets, H. Labuhn, L. Béguin, A. Vernier, F. Nogrette, T. Lahaye, and A. Browaeys. *Demonstration of a Strong Rydberg Blockade in Three-Atom Systems with Anisotropic Interactions*. Phys. Rev. Lett. **112**, 183002 (2014). (Cited on page **16**)

[127] P. Schauß, M. Cheneau, M. Endres, T. Fukuhara, S. Hild, A. Omran, T. Pohl, C. Gross, S. Kuhr, and I. Bloch. *Observation of spatially ordered structures in a two-dimensional Rydberg gas*. Nature **491**, 87–91 (2012). (Cited on pages **17**, **19**, and **25**)

[128] P. Schauß, J. Zeiher, T. Fukuhara, S. Hild, M. Cheneau, T. Macrì, T. Pohl, I. Bloch, and C. Gross. *Crystallization in Ising quantum magnets*. Science **347**, 1455–1458 (2015). (Cited on pages **17** and **25**)

[129] H. Weimer, R. Löw, T. Pfau, and H. P. Büchler. *Quantum Critical Behavior in Strongly Interacting Rydberg Gases*. Phys. Rev. Lett. **101**, 250601 (2008). (Cited on page **17**)

[130] J. Schachenmayer, I. Lesanovsky, A. Micheli, and A. J. Daley. *Dynamical crystal creation with polar molecules or Rydberg atoms in optical lattices*. New J. Phys. **12**, 103044 (2010). (Cited on page **17**)

[131] A. Gaëtan, Y. Miroshnychenko, T. Wilk, A. Chotia, M. Viteau, D. Comparat, P. Pillet, A. Browaeys, and P. Grangier. *Observation of collective excitation of two individual atoms in the Rydberg blockade regime*. Nat. Phys. **5**, 115–118 (2009). (Cited on pages **19** and **79**)

[132] E. Urban, T. A. Johnson, T. Henage, L. Isenhower, D. D. Yavuz, T. G. Walker, and M. Saffman. *Observation of Rydberg blockade between two atoms*. Nat. Phys. **5**, 110–114 (2009). (Cited on page **19**)

[133] H. Labuhn, D. Barredo, S. Ravets, S. De Léséleuc, T. Macrì, T. Lahaye, and A. Browaeys. *Tunable two-dimensional arrays of single Rydberg atoms for realizing quantum Ising models*. Nature **534**, 667–670 (2016). (Cited on page **19**)

[134] J. Zeiher, P. Schauß, S. Hild, T. Macrì, I. Bloch, and C. Gross. *Microscopic Characterization of Scalable Coherent Rydberg Superatoms*. Phys. Rev. X **5**, 031015 (2015). (Cited on pages **19**, **44**, and **79**)

[135] J. E. Johnson and S. L. Rolston. *Interactions between Rydberg-dressed atoms*. Phys. Rev. A **82**, 033412 (2010). (Cited on page **19**)

[136] J. B. Balewski, A. T. Krupp, A. Gaj, S. Hofferberth, R. Löw, and T. Pfau. *Rydberg Dressing: Understanding of Collective Many-Body Effects and Implications for Experiments*. New J. Phys. **16**, 063012 (2014). (Cited on pages **19** and **93**)

[137] N. Henkel, R. Nath, and T. Pohl. *Three-Dimensional Roton Excitations and Supersolid Formation in Rydberg-Excited Bose-Einstein Condensates*. Phys. Rev. Lett. **104**, 195302 (2010). (Cited on pages **19** and **93**)

[138] N. Henkel. *Rydberg-dressed Bose-Einstein condensates*. Ph.D. thesis, Technische Universität Dresden Dresden (2014). (Cited on page **19**)

[139] E. Guardado-Sanchez. *Exploring many-body quantum dynamics with Rydberg dressed fermions and tilted Hubbard systems*. Ph.D. thesis, Princeton University (2021). (Cited on page **19**)

[140] J. Zeiher, R. van Bijnen, P. Schauß, S. Hild, J.-y. Choi, T. Pohl, I. Bloch, and C. Gross. *Many-Body Interferometry of a Rydberg-dressed Spin Lattice*. Nat. Phys. **12**, 1095–1099 (2016). (Cited on pages **21**, **25**, **91**, **93**, **94**, **98**, and **100**)

[141] J. Zeiher, J.-y. Choi, A. Rubio-Abadal, T. Pohl, R. van Bijnen, I. Bloch, and C. Gross. *Coherent Many-Body Spin Dynamics in a Long-Range Interacting Ising Chain*. Phys. Rev. X **7**, 041063 (2017). (Cited on pages **22**, **91**, **93**, **98**, **100**, **102**, and **103**)

[142] W. Xu, A. V. Venkatramani, S. H. Cantú, T. Šumarac, V. Klüsener, M. D. Lukin, and V. Vuletić. *Fast Preparation and Detection of a Rydberg Qubit Using Atomic Ensembles*. Phys. Rev. Lett. **127**, 050501 (2021). (Cited on pages **23** and **61**)

[143] S. Baur, D. Tiarks, G. Rempe, and S. Dürr. *Single-Photon Switch Based on Rydberg Blockade*. Phys. Rev. Lett. **112**, 073901 (2014). (Cited on pages **23**, **61**, and **62**)

[144] H. Gorniaczyk, C. Tresp, J. Schmidt, H. Fedder, and S. Hofferberth. *Single-Photon Transistor Mediated by Interstate Rydberg Interactions*. Phys. Rev. Lett. **113**, 053601 (2014). (Cited on pages **23** and **61**)

[145] J. D. Thompson, T. L. Nicholson, Q.-Y. Liang, S. H. Cantu, A. V. Venkatramani, S. Choi, I. A. Fedorov, D. Viscor, T. Pohl, M. D. Lukin, and V. Vuletić. *Symmetry-protected collisions between strongly interacting photons*. Nature **542**, 206–209 (2017). (Cited on page **23**)

[146] G. Günter, M. Robert-de Saint-Vincent, H. Schempp, C. S. Hofmann, S. Whitlock, and M. Weidemüller. *Interaction Enhanced Imaging of Individual Rydberg Atoms in Dense Gases*. p **108**, 013002 (2012). (Cited on pages **23** and **72**)

[147] I. Bloch, J. Dalibard, and W. Zwerger. *Many-Body Physics with Ultracold Gases*. Rev. Mod. Phys. **80**, 885–964 (2008). (Cited on pages **25**, **26**, and **91**)

[148] C. Gross and I. Bloch. *Quantum Simulations with Ultracold Atoms in Optical Lattices*. Science **357**, 995–1001 (2017). (Cited on pages **25** and **91**)

[149] R. Jördens, N. Strohmaier, K. Günter, H. Moritz, and T. Esslinger. *A Mott insulator of fermionic atoms in an optical lattice*. Nature **455**, 204–207 (2008). (Cited on page **25**)

[150] W. S. Bakr, J. I. Gillen, A. Peng, S. Fölling, and M. Greiner. *A Quantum Gas Microscope for Detecting Single Atoms in a Hubbard-regime Optical Lattice*. Nature **462**, 74–77 (2009). (Cited on pages **25**, **27**, and **113**)

[151] J. F. Sherson, C. Weitenberg, M. Endres, M. Cheneau, I. Bloch, and S. Kuhr. *Single-Atom-Resolved Fluorescence Imaging of an Atomic Mott Insulator*. Nature **467**, 68–72 (2010). (Cited on pages **25**, **27**, and **113**)

[152] C. Gross and W. S. Bakr. *Quantum Gas Microscopy for Single Atom and Spin Detection*. Nat. Phys. **17**, 1316–1323 (2021). (Cited on pages **25**, **27**, **94**, and **113**)

[153] M. Greiner, O. Mandel, T. W. Hänsch, and I. Bloch. *Collapse and revival of the matter wave field of a Bose–Einstein condensate*. Nature **419**, 51–54 (2002). (Cited on page **25**)

[154] S. Will, T. Best, U. Schneider, L. Hackermüller, D.-S. Lühmann, and I. Bloch. *Time-resolved observation of coherent multi-body interactions in quantum phase revivals*. Nature **465**, 197–201 (2010). (Cited on page **25**)

[155] D. Adler, D. Wei, M. Will, K. Srakaew, S. Agrawal, P. Weckesser, R. Moessner, F. Pollmann, I. Bloch, and J. Zeiher. *Observation of Hilbert-space fragmentation and fractonic excitations in two-dimensional Hubbard systems*. arXiv:2404.14896 (2024). (Cited on page **25**)

[156] R. Bekenstein, I. Pikovski, H. Pichler, E. Shahmoon, S. F. Yelin, and M. D. Lukin. *Quantum metasurfaces with atom arrays*. Nat. Phys. **16**, 676–681 (2020). (Cited on pages **25**, **61**, **62**, and **118**)

[157] C. Weitenberg. *Single-Atom Resolved Imaging and Manipulation in an Atomic Mott Insulator*. Ph.D. thesis, Ludwig-Maximilians-Universität München (2011). (Cited on pages **25** and **28**)

[158] M. Endres. *Probing correlated quantum many-body systems at the single-particle level*. Ph.D. thesis, Ludwig-Maximilians-Universität München (2013). (Cited on page **25**)

[159] P. Schauss. *High-resolution imaging of ordering in Rydberg many-body systems*. Ph.D. thesis, Ludwig-Maximilians-Universität München (2015). (Cited on pages **25**, **29**, **36**, and **46**)

[160] S. Hild. *Microscopy of quantum many-body systems out of equilibrium*. Ph.D. thesis, Ludwig-Maximilians-Universität München (2016). (Cited on page **25**)

[161] A. Rubio Abadal. *Probing quantum thermalization and localization in Bose-Hubbard systems*. Ph.D. thesis, Ludwig-Maximilians-Universität München (2020). (Cited on pages **25** and **28**)

[162] D. Wei. *Microscopy of spin hydrodynamics and cooperative light scattering in atomic Hubbard systems*. Ph.D. thesis, Ludwig-Maximilians-Universität München (2023). (Cited on pages **25**, **28**, **29**, **31**, **35**, and **64**)

[163] M. P. A. Fisher, P. B. Weichman, G. Grinstein, and D. S. Fisher. *Boson localization and the superfluid-insulator transition*. Phys. Rev. B **40**, 546–570 (1989). (Cited on page **26**)

[164] W. Zwerger. *Mott Hubbard transition of cold atoms in optical lattices*. J. Opt. B: Quantum Semiclass. Opt. **5**, S9–S16 (2003). (Cited on pages **26** and **28**)

[165] S. Sachdev. *Quantum Phase Transitions*. Cambridge University Press (2011). ISBN 978-0-521-51468-2 978-0-511-97376-5. (Cited on pages **26** and **28**)

[166] F. Gerbier, A. Widera, S. Fölling, O. Mandel, T. Gericke, and I. Bloch. *Phase Coherence of an Atomic Mott Insulator*. Phys. Rev. Lett. **95**, 050404 (2005). (Cited on page **26**)

[167] M. F. Parsons, F. Huber, A. Mazurenko, C. S. Chiu, W. Setiawan, K. Wooley-Brown, S. Blatt, and M. Greiner. *Site-Resolved Imaging of Fermionic Li 6 in an Optical Lattice*. Phys. Rev. Lett. **114**, 213002 (2015). (Cited on page **27**)

[168] E. Haller, J. Hudson, A. Kelly, D. A. Cotta, B. Peaudecerf, G. D. Bruce, and S. Kuhr. *Single-atom imaging of fermions in a quantum-gas microscope*. Nat. Phys. **11**, 738–742 (2015). (Cited on page **27**)

[169] L. W. Cheuk, M. A. Nichols, M. Okan, T. Gersdorf, V. V. Ramasesh, W. S. Bakr, T. Lompe, and M. W. Zwierlein. *Quantum-Gas Microscope for Fermionic Atoms*. Phys. Rev. Lett. **114**, 193001 (2015). (Cited on page **27**)

[170] A. Omran, M. Boll, T. A. Hilker, K. Kleinlein, G. Salomon, I. Bloch, and C. Gross. *Microscopic Observation of Pauli Blocking in Degenerate Fermionic Lattice Gases*. Phys. Rev. Lett. **115**, 263001 (2015). (Cited on page **27**)

[171] R. Yamamoto, J. Kobayashi, T. Kuno, K. Kato, and Y. Takahashi. *An ytterbium quantum gas microscope with narrow-line laser cooling*. New J. Phys. **18**, 023016 (2016). (Cited on page **27**)

[172] J. Mongkolkiattichai, L. Liu, D. Garwood, J. Yang, and P. Schauss. *Quantum gas microscopy of fermionic triangular-lattice Mott insulators*. Phys. Rev. A **108**, L061301 (2023). (Cited on page **27**)

[173] S. Buob, J. Höschele, V. Makhalov, A. Rubio-Abadal, and L. Tarruell. *A Strontium Quantum-Gas Microscope*. PRX Quantum **5**, 020316 (2024). (Cited on page **27**)

[174] C. S. Chiu, G. Ji, A. Mazurenko, D. Greif, and M. Greiner. *Quantum State Engineering of a Hubbard System with Ultracold Fermions*. Phys. Rev. Lett. **120**, 243201 (2018). (Cited on page **28**)

[175] B. Yang, H. Sun, C.-J. Huang, H.-Y. Wang, Y. Deng, H.-N. Dai, Z.-S. Yuan, and J.-W. Pan. *Cooling and entangling ultracold atoms in optical lattices*. Science **369**, 550–553 (2020). (Cited on page **28**)

[176] A. Rubio-Abadal, J.-y. Choi, J. Zeiher, S. Hollerith, J. Rui, I. Bloch, and C. Gross. *Many-Body Delocalization in the Presence of a Quantum Bath*. Phys. Rev. X **9**, 041014 (2019). (Cited on page **28**)

[177] W. S. Bakr, A. Peng, M. E. Tai, R. Ma, J. Simon, J. I. Gillen, S. Fölling, L. Pollet, and M. Greiner. *Probing the Superfluid–to–Mott Insulator Transition at the Single-Atom Level*. Science **329**, 547–550 (2010). (Cited on page **29**)

[178] N. Schlosser, G. Reymond, I. Protsenko, and P. Grangier. *Sub-poissonian loading of single atoms in a microscopic dipole trap*. Nature **411**, 1024–1027 (2001). (Cited on page **29**)

[179] A. Fuhrmanek, R. Bourgain, Y. R. P. Sortais, and A. Browaeys. *Light-assisted collisions between a few cold atoms in a microscopic dipole trap*. Phys. Rev. A **85**, 062708 (2012). (Cited on page **29**)

[180] Y. H. Fung and M. F. Andersen. *Efficient collisional blockade loading of a single atom into a tight microtrap*. New J. Phys. **17**, 073011 (2015). (Cited on page **29**)

[181] D. Wei, D. Adler, K. Srakaew, S. Agrawal, P. Weckesser, I. Bloch, and J. Zeiher. *Observation of Brane Parity Order in Programmable Optical Lattices*. Phys. Rev. X **13**, 021042 (2023). (Cited on page **31**)

[182] J. Sebby-Strabley, M. Anderlini, P. S. Jessen, and J. V. Porto. *Lattice of double wells for manipulating pairs of cold atoms*. Phys. Rev. A **73**, 033605 (2006). (Cited on page **34**)

[183] D. A. Tate and T. F. Gallagher. *Microwave-optical two-photon excitation of Rydberg states*. Phys. Rev. A **97**, 033410 (2018). (Cited on page **36**)

[184] C. Carr, M. Tanasittikosol, A. Sargsyan, D. Sarkisyan, C. S. Adams, and K. J. Weatherill. *Three-photon electromagnetically induced transparency using Rydberg states*. Opt. Lett. **37**, 3858 (2012). (Cited on page **36**)

[185] B. Ravon, P. Méhaignerie, Y. Machu, A. D. Hernández, M. Favier, J. Raimond, M. Brune, and C. Sayrin. *Array of Individual Circular Rydberg Atoms Trapped in Optical Tweezers*. Phys. Rev. Lett. **131**, 093401 (2023). (Cited on page **36**)

[186] S. De Léséleuc, S. Weber, V. Lienhard, D. Barredo, H. P. Büchler, T. Lahaye, and A. Browaeys. *Accurate Mapping of Multilevel Rydberg Atoms on Interacting Spin- 1 / 2 Particles for the Quantum Simulation of Ising Models*. Phys. Rev. Lett. **120**, 113602 (2018). (Cited on page **36**)

[187] J. D. Pritchard. *Cooperative Optical Non-linearity in a blockaded Rydberg Ensemble*. Ph.D. thesis, Durham University (2011). (Cited on page **36**)

[188] D. A. Steck. *Quantum and Atom Optics*. available online at http://steck.us/teaching (2024). (revision 0.16.1, 16 June 2024). (Cited on page **36**)

[189] S. Hollerith, J. Zeiher, J. Rui, A. Rubio-Abadal, V. Walther, T. Pohl, D. M. Stamper-Kurn, I. Bloch, and C. Gross. *Quantum gas microscopy of Rydberg macrodimers*. Science **364**, 664–667 (2019). (Cited on page **38**)

[190] S. Hollerith, K. Srakaew, D. Wei, A. Rubio-Abadal, D. Adler, P. Weckesser, A. Kruckenhauser, V. Walther, R. van Bijnen, J. Rui, C. Gross, I. Bloch, and J. Zeiher. *Realizing Distance-Selective Interactions in a Rydberg-Dressed Atom Array*. Phys. Rev. Lett. **128**, 113602 (2022). (Cited on pages **38** and **93**)

[191] M. Barbier, S. Hollerith, and W. Hofstetter. *Extended Bose-Hubbard models with Rydberg macrodimer dressing*. Phys. Rev. A **104**, 053304 (2021). (Cited on pages **38** and **93**)

[192] L.-M. Steinert, P. Osterholz, R. Eberhard, L. Festa, N. Lorenz, Z. Chen, A. Trautmann, and C. Gross. *Spatially Tunable Spin Interactions in Neutral Atom Arrays*. Phys. Rev. Lett. **130**, 243001 (2023). (Cited on pages **38**, **93**, and **98**)

[193] A. M. Hankin, Y.-Y. Jau, L. P. Parazzoli, C. W. Chou, D. J. Armstrong, A. J. Landahl, and G. W. Biedermann. *Two-atom Rydberg blockade using direct 6 S to n P excitation*. Phys. Rev. A **89**, 033416 (2014). (Cited on page **38**)

[194] J. Bai, J. Wang, J. He, and J. Wang. *Electronic sideband locking of a broadly tunable 318.6 nm ultraviolet laser to an ultra-stable optical cavity*. J. Opt. **19**, 045501 (2017). (Cited on page **38**)

[195] E. M. Bridge, N. C. Keegan, A. D. Bounds, D. Boddy, D. P. Sadler, and M. P. A. Jones. *Tunable cw UV laser with <35 kHz absolute frequency instability for precision spectroscopy of Sr Rydberg states*. Opt. Express **24**, 2281 (2016). (Cited on page **38**)

[196] T. Manthey, T. M. Weber, T. Niederprüm, P. Langer, V. Guarrera, G. Barontini, and H. Ott. *Scanning electron microscopy of Rydberg-excited Bose–Einstein condensates*. New J. Phys. **16**, 083034 (2014). (Cited on page **38**)

[197] E. Guardado-Sanchez, B. M. Spar, P. Schauss, R. Belyansky, J. T. Young, P. Bienias, A. V. Gorshkov, T. Iadecola, and W. S. Bakr. *Quench Dynamics of a Fermi Gas with Strong Nonlocal Interactions*. Phys. Rev. X **11**, 021036 (2021). (Cited on pages **38**, **94**, **98**, **102**, **103**, and **109**)

[198] S. Hannig, J. Mielke, J. A. Fenske, M. Misera, N. Beev, C. Ospelkaus, and P. O. Schmidt. *A highly stable monolithic enhancement cavity for second harmonic generation in the ultraviolet*. Rev. Sci. Instrum. **89**, 013106 (2018). (Cited on page **38**)

[199] H. Abitan and T. Skettrup. *Laser resonators with several mirrors and lenses with the bow-tie laser resonator with compensation for astigmatism and thermal lens effects as an example*. J. Opt. A: Pure Appl. Opt. **7**, 7–20 (2005). (Cited on page **38**)

[200] R. W. P. Drever, J. L. Hall, F. V. Kowalski, J. Hough, G. M. Ford, A. J. Munley, and H. Ward. *Laser phase and frequency stabilization using an optical resonator*. Appl. Phys. B **31**, 97–105 (1983). (Cited on page **38**)

[201] K. Huang, H. Le Jeannic, J. Ruaudel, O. Morin, and J. Laurat. *Microcontroller-based locking in optics experiments*. Rev. Sci. Instrum. **85**, 123112 (2014). (Cited on page **38**)

[202] B. M. Sparkes, H. M. Chrzanowski, D. P. Parrain, B. C. Buchler, P. K. Lam, and T. Symul. *A scalable, self-analyzing digital locking system for use on quantum optics experiments*. Rev. Sci. Instrum. **82**, 075113 (2011). (Cited on page **38**)

[203] T. Preuschoff, M. Schlosser, and G. Birkl. *Digital laser frequency and intensity stabilization based on the STEMlab platform (originally Red Pitaya)*. Rev. Sci. Instrum. **91**, 083001 (2020). (Cited on page **38**)

[204] F. Schmid. *rp-lockbox*. GitHub repository (2019). (Cited on page **39**)

[205] L.-M. Steinert. *Spatially tunable spin interactions with Rydberg atoms in optical tweezers*. Ph.D. thesis, Universität Tübingen (2024). (Cited on page **39**)

[206] L. Festa. *Black-body radiation induced correlated excitation of Potassium Rydberg atoms in tweezer arrays*. Ph.D. thesis, Ludwig-Maximilians-Universität München (2021). (Cited on page **39**)

[207] N. Lorenz. *A Rydberg tweezer platform with potassium atoms*. Ph.D. thesis, Ludwig-Maximilians-Universität München (2021). (Cited on page **39**)

[208] L. Beguin. *Measurement of the van der Waals interaction between two Rydberg atoms*. Ph.D. thesis, Institut d'Optique Graduate School (2013). (Cited on page **42**)

[209] H. J. Levine. *Quantum Information Processing and Quantum Simulation with Programmable Rydberg Atom Arrays*. Ph.D. thesis, Harvard University (2021). (Cited on pages **43**, **49**, **50**, and **54**)

[210] M. Viteau, M. G. Bason, J. Radogostowicz, N. Malossi, D. Ciampini, O. Morsch, and E. Arimondo. *Rydberg Excitations in Bose-Einstein Condensates in Quasi-One-Dimensional Potentials and Optical Lattices*. Phys. Rev. Lett. **107**, 060402 (2011). (Cited on page **43**)

[211] M. Ebert, M. Kwon, T. Walker, and M. Saffman. *Coherence and Rydberg Blockade of Atomic Ensemble Qubits*. Phys. Rev. Lett. **115**, 093601 (2015). (Cited on page **44**)

[212] M. Fleischhauer, A. Imamoglu, and J. P. Marangos. *Electromagnetically induced transparency: Optics in coherent media*. Rev. Mod. Phys. **77**, 633–673 (2005). (Cited on pages **45**, **61**, **68**, and **72**)

[213] H. Levine, D. Bluvstein, A. Keesling, T. T. Wang, S. Ebadi, G. Semeghini, A. Omran, M. Greiner, V. Vuletić, and M. D. Lukin. *Dispersive optical systems for scalable Raman driving of hyperfine qubits*. Phys. Rev. A **105**, 032618 (2022). (Cited on pages **48**, **50**, **51**, and **54**)

[214] D. L. Hayes. *Remote and Local Entanglement of Ions using Photons and Phonons*. Ph.D. thesis, University of Maryland (2012). (Cited on page **49**)

[215] D. Hayes, D. N. Matsukevich, P. Maunz, D. Hucul, Q. Quraishi, S. Olmschenk, W. Campbell, J. Mizrahi, C. Senko, and C. Monroe. *Entanglement of Atomic Qubits Using an Optical Frequency Comb*. Phys. Rev. Lett. **104**, 140501 (2010). (Cited on page **49**)

[216] D. F. James and J. Jerke. *Effective Hamiltonian theory and its applications in quantum information*. Can. J. Phys. **85**, 625–632 (2007). (Cited on page **49**)

[217] C. Cohen-Tannoudji and J. Dupont-Roc. *Experimental Study of Zeeman Light Shifts in Weak Magnetic Fields*. Phys. Rev. A **5**, 968–984 (1972). (Cited on page **49**)

[218] F. Le Kien, P. Schneeweiss, and A. Rauschenbeutel. *Dynamical polarizability of atoms in arbitrary light fields: general theory and application to cesium*. Eur. Phys. J. D **67**, 92 (2013). (Cited on page **49**)

[219] J. Kobayashi, K. Shibata, T. Aoki, M. Kumakura, and Y. Takahashi. *Fictitious magnetic resonance by quasielectrostatic field*. Appl. Phys. B **95**, 361–365 (2009). (Cited on page **49**)

[220] M. Zielonkowski, J. Steiger, U. Schünemann, M. DeKieviet, and R. Grimm. *Optically induced spin precession and echo in an atomic beam*. Phys. Rev. A **58**, 3993–3998 (1998). (Cited on page **49**)

[221] C. Y. Park, H. Noh, C. M. Lee, and D. Cho. *Measurement of the Zeeman-like ac Stark shift*. Phys. Rev. A **63**, 032512 (2001). (Cited on page **49**)

[222] N. Arias, V. Abediyeh, S. Hamzeloui, and E. Gomez. *Low phase noise beams for Raman transitions with a phase modulator and a highly birefringent crystal*. Opt. Express **25**, 5290 (2017). (Cited on page **50**)

[223] D. D. Yavuz, P. B. Kulatunga, E. Urban, T. A. Johnson, N. Proite, T. Henage, T. G. Walker, and M. Saffman. *Fast Ground State Manipulation of Neutral Atoms in Microscopic Optical Traps*. Phys. Rev. Lett. **96**, 063001 (2006). (Cited on page **50**)

[224] P. J. Lee, B. B. Blinov, K. Brickman, L. Deslauriers, M. J. Madsen, R. Miller, D. L. Moehring, D. Stick, and C. Monroe. *Atomic qubit manipulations with an electro-optic modulator*. Opt. Lett. **28**, 1582 (2003). (Cited on page **50**)

[225] J. K. Ranka, R. S. Windeler, and A. J. Stentz. *Visible continuum generation in air–silica microstructure optical fibers with anomalous dispersion at 800 nm*. Opt. Lett. **25**, 25 (2000). (Cited on page **52**)

[226] ITU. *Characteristics of a single-mode optical fibre and cable.* , International Telecommunication Union standard G.652 (2017). (Cited on page **52**)

[227] L. Glebov, V. Smirnov, E. Rotari, I. Cohanoschi, L. Glebova, O. Smolski, J. Lumeau, C. Lantigua, and A. Glebov. *Volume-chirped Bragg gratings: monolithic components for stretching and compression of ultrashort laser pulses*. Opt. Eng. **53**, 051514 (2014). (Cited on page **52**)

[228] S. Kaim, S. Mokhov, B. Y. Zeldovich, and L. B. Glebov. *Stretching and compressing of short laser pulses by chirped volume Bragg gratings: analytic and numerical modeling*. Opt. Eng. **53**, 051509 (2013). (Cited on page **52**)

[229] D. Bluvstein, H. Levine, G. Semeghini, T. T. Wang, S. Ebadi, M. Kalinowski, A. Keesling, N. Maskara, H. Pichler, M. Greiner, V. Vuletić, and M. D. Lukin. *A quantum processor based on coherent transport of entangled atom arrays*. Nature **604**, 451–456 (2022). (Cited on page **55**)

[230] J. W. Lis, A. Senoo, W. F. McGrew, F. Rönchen, A. Jenkins, and A. M. Kaufman. *Midcircuit Operations Using the omg Architecture in Neutral Atom Arrays*. Phys. Rev. X **13**, 041035 (2023). (Cited on page **55**)

[231] P. Calabrese, F. H. L. Essler, and M. Fagotti. *Quantum Quench in the Transverse-Field Ising Chain*. Phys. Rev. Lett. **106**, 227203 (2011). (Cited on page **55**)

[232] J. Schachenmayer, B. P. Lanyon, C. F. Roos, and A. J. Daley. *Entanglement Growth in Quench Dynamics with Variable Range Interactions*. Phys. Rev. X **3**, 031015 (2013). (Cited on page **55**)

[233] K. R. A. Hazzard, M. Van Den Worm, M. Foss-Feig, S. R. Manmana, E. G. Dalla Torre, T. Pfau, M. Kastner, and A. M. Rey. *Quantum correlations and entanglement in far-from-equilibrium spin systems*. Phys. Rev. A **90**, 063622 (2014). (Cited on page **55**)

[234] M. Schmitt, M. M. Rams, J. Dziarmaga, M. Heyl, and W. H. Zurek. *Quantum phase transition dynamics in the two-dimensional transverse-field Ising model*. Sci. Adv. **8**, eabl6850 (2022). (Cited on page **55**)

[235] K. Srakaew, P. Weckesser, S. Hollerith, D. Wei, D. Adler, I. Bloch, and J. Zeiher. *A subwavelength atomic array switched by a single Rydberg atom*. Nat. Phys. **19**, 714–719 (2023). (Cited on page **59**)

[236] D. E. Chang, J. S. Douglas, A. González-Tudela, C.-L. Hung, and H. J. Kimble. *Colloquium: Quantum matter built from nanoscopic lattices of atoms and photons*. Rev. Mod. Phys. **90**, 031002 (2018). (Cited on pages **59** and **61**)

[237] P. Lambropoulos and D. Petrosyan. *Fundamentals of Quantum Optics and Quantum Information*. Springer Berlin Heidelberg, Berlin, Heidelberg (2007). ISBN 978-3-540-34571-8. (Cited on page **59**)

[238] A. Asenjo-Garcia, M. Moreno-Cardoner, A. Albrecht, H. J. Kimble, and D. E. Chang. *Exponential improvement in photon storage fidelities using subradiance and "selective radiance" in atomic arrays*. Phys. Rev. X **7**, 031024 (2017). (Cited on pages **60** and **61**)

[239] R. J. Bettles. *Cooperative Interactions in Lattices of Atomic Dipoles*. Ph.D. thesis, Durham University (2016). (Cited on page **60**)

[240] D. E. Chang, V. Vuletić, and M. D. Lukin. *Quantum nonlinear optics — photon by photon*. Nat. Photonics **8**, 685–694 (2014). (Cited on page **61**)

[241] G. Wrigge, I. Gerhardt, J. Hwang, G. Zumofen, and V. Sandoghdar. *Efficient coupling of photons to a single molecule and the observation of its resonance fluorescence*. Nat. Phys. **4**, 60–66 (2008). (Cited on page **61**)

[242] B. Darquié, M. P. A. Jones, J. Dingjan, J. Beugnon, S. Bergamini, Y. Sortais, G. Messin, A. Browaeys, and P. Grangier. *Controlled Single-Photon Emission from a Single Trapped Two-Level Atom*. Science **309**, 454–456 (2005). (Cited on page **61**)

[243] M. K. Tey, Z. Chen, S. A. Aljunid, B. Chng, F. Huber, G. Maslennikov, and C. Kurtsiefer. *Strong interaction between light and a single trapped atom without the need for a cavity*. Nat. Phys. **4**, 924–927 (2008). (Cited on page **61**)

[244] G. Hétet, L. Slodička, M. Hennrich, and R. Blatt. *Single Atom as a Mirror of an Optical Cavity*. Phys. Rev. A **107**, 133002 (2011). (Cited on page **61**)

[245] N. Piro, F. Rohde, C. Schuck, M. Almendros, J. Huwer, J. Ghosh, A. Haase, M. Hennrich, F. Dubin, and J. Eschner. *Heralded single-photon absorption by a single atom*. Nat. Phys. **7**, 17–20 (2011). (Cited on page **61**)

[246] A. N. Vamivakas, M. Atatüre, J. Dreiser, S. T. Yilmaz, A. Badolato, A. K. Swan, B. B. Goldberg, A. Imamoğlu, and M. S. Ünlü. *Strong Extinction of a Far-Field Laser Beam by a Single Quantum Dot*. Nano Lett. **7**, 2892–2896 (2007). (Cited on page **61**)

[247] M. K. Tey, G. Maslennikov, T. C H Liew, S. A. Aljunid, F. Huber, B. Chng, Z. Chen, V. Scarani, and C. Kurtsiefer. *Interfacing light and single atoms with a lens*. New J. Phys. **11**, 043011 (2009). (Cited on page **61**)

[248] H. J. Kimble. *Strong interactions of single atoms and photons in cavity QED*. Phys. Scr. **T76**, 127 (1998). (Cited on page **61**)

[249] J. McKeever, A. Boca, A. D. Boozer, R. Miller, J. R. Buck, A. Kuzmich, and H. J. Kimble. *Deterministic generation of single photons from one atom trapped in a cavity*. Science **303**, 1992–1994 (2004). (Cited on page **61**)

[250] K. M. Birnbaum, A. Boca, R. Miller, A. D. Boozer, T. E. Northup, and H. J. Kimble. *Photon blockade in an optical cavity with one trapped atom*. Nature **436**, 87–90 (2005). (Cited on page **61**)

[251] T. Wilk, S. C. Webster, A. Kuhn, and G. Rempe. *Single-Atom Single-Photon Quantum Interface*. Science **317**, 488–490 (2007). (Cited on page **61**)

[252] B. Dayan, A. S. Parkins, T. Aoki, E. P. Ostby, K. J. Vahala, and H. J. Kimble. *A Photon Turnstile Dynamically Regulated by One Atom*. Science **319**, 1062–1065 (2008). (Cited on page **61**)

[253] M. Mücke, E. Figueroa, J. Bochmann, C. Hahn, K. Murr, S. Ritter, C. J. Villas-Boas, and G. Rempe. *Electromagnetically induced transparency with single atoms in a cavity*. Nature **465**, 755–758 (2010). (Cited on page **61**)

[254] A. Reiserer and G. Rempe. *Cavity-based quantum networks with single atoms and optical photons*. Rev. Mod. Phys. **87**, 1379–1418 (2015). (Cited on page **61**)

[255] C. Junge, D. O'Shea, J. Volz, and A. Rauschenbeutel. *Strong coupling between single atoms and nontransversal photons*. Phys. Rev. Lett. **110**, 213604 (2013). (Cited on page **61**)

[256] J. D. Thompson, T. G. Tiecke, N. P. de Leon, J. Feist, A. V. Akimov, M. Gullans, A. S. Zibrov, V. Vuletić, and M. D. Lukin. *Coupling a single trapped atom to a nanoscale optical cavity*. Science **340**, 1202–1205 (2013). (Cited on page **61**)

[257] P. Lodahl, S. Mahmoodian, and S. Stobbe. *Interfacing single photons and single quantum dots with photonic nanostructures*. Rev. Mod. Phys. **87**, 347–400 (2015). (Cited on page **61**)

[258] P. Lodahl, S. Mahmoodian, S. Stobbe, A. Rauschenbeutel, P. Schneeweiss, J. Volz, H. Pichler, and P. Zoller. *Chiral quantum optics*. Nature **541**, 473–480 (2016). (Cited on page **61**)

[259] L.-M. Duan and H. J. Kimble. *Scalable photonic quantum computation through cavity-assisted interactions*. Phys. Rev. Lett. **92**, 127902 (2004). (Cited on page **61**)

[260] B. Hacker, S. Welte, G. Rempe, and S. Ritter. *A photon–photon quantum gate based on a single atom in an optical resonator*. Nature **536**, 193–196 (2016). (Cited on page **61**)

[261] T. Stolz, H. Hegels, M. Winter, B. Röhr, Y.-F. Hsiao, L. Husel, G. Rempe, and S. Dürr. *Quantum-logic gate between two optical photons with an average efficiency above 40%*. Phys. Rev. X **12**, 021035 (2022). (Cited on page **61**)

[262] K. Hammerer, A. S. Sørensen, and E. S. Polzik. *Quantum interface between light and atomic ensembles*. Rev. Mod. Phys. **82**, 1041–1093 (2010). (Cited on page **61**)

[263] K. S. Choi, H. Deng, J. Laurat, and H. J. Kimble. *Mapping photonic entanglement into and out of a quantum memory*. Nature **452**, 67–71 (2008). (Cited on page **61**)

[264] J. Keaveney, A. Sargsyan, U. Krohn, I. G. Hughes, D. Sarkisyan, and C. S. Adams. *Cooperative Lamb Shift in an Atomic Vapor Layer of Nanometer Thickness*. Phys. Rev. Lett. **108**, 173601 (2012). (Cited on page **61**)

[265] J. Pellegrino, R. Bourgain, S. Jennewein, Y. Sortais, A. Browaeys, S. Jenkins, and J. Ruostekoski. *Observation of Suppression of Light Scattering Induced by Dipole-Dipole Interactions in a Cold-Atom Ensemble*. Phys. Rev. Lett. **113**, 133602 (2014). (Cited on page **61**)

[266] M. Bajcsy, S. Hofferberth, V. Balic, T. Peyronel, M. Hafezi, A. S. Zibrov, V. Vuletic, and M. D. Lukin. *Efficient All-Optical Switching Using Slow Light within a Hollow Fiber*. Phys. Rev. Lett. **102**, 203902 (2009). (Cited on page **61**)

[267] T. Peyronel, O. Firstenberg, Q.-Y. Liang, S. Hofferberth, A. V. Gorshkov, T. Pohl, M. D. Lukin, and V. Vuletić. *Quantum nonlinear optics with single photons enabled by strongly interacting atoms*. Nature **488**, 57–60 (2012). (Cited on pages **61**, **69**, and **72**)

[268] Y. O. Dudin and A. Kuzmich. *Strongly interacting Rydberg excitations of a cold atomic gas*. Science **336**, 887–889 (2012). (Cited on page **61**)

[269] D. Maxwell, D. J. Szwer, D. Paredes-Barato, H. Busche, J. D. Pritchard, A. Gauguet, K. J. Weatherill, M. P. A. Jones, and C. S. Adams. *Storage and Control of Optical Photons Using Rydberg Polaritons*. Phys. Rev. Lett. **110**, 103001 (2013). (Cited on page **61**)

[270] D. Porras and J. I. Cirac. *Collective generation of quantum states of light by entangled atoms*. Phys. Rev. A **78**, 053816 (2008). (Cited on page **61**)

[271] S. D. Jenkins and J. Ruostekoski. *Controlled manipulation of light by cooperative response of atoms in an optical lattice*. Phys. Rev. A **86**, 031602 (2012). (Cited on page **61**)

[272] S. D. Jenkins and J. Ruostekoski. *Metamaterial transparency induced by cooperative electromagnetic interactions*. Phys. Rev. Lett. **111**, 147401 (2013). (Cited on page **61**)

[273] G. Facchinetti, S. D. Jenkins, and J. Ruostekoski. *Storing light with subradiant correlations in arrays of atoms*. Phys. Rev. Lett. **117**, 243601 (2016). (Cited on page **61**)

[274] J. Ruostekoski. *Cooperative quantum-optical planar arrays of atoms*. Phys. Rev. A **108**, 030101 (2023). (Cited on page **61**)

[275] M. Moreno-Cardoner, D. Goncalves, and D. E. Chang. *Quantum nonlinear optics based on two-dimensional Rydberg atom arrays*. Phys. Rev. Lett. **127**, 263602 (2021). (Cited on pages **61**, **62**, and **118**)

[276] L. Zhang, V. Walther, K. Mølmer, and T. Pohl. *Photon-photon interactions in Rydberg-atom arrays*. Quantum **6**, 674 (2022). (Cited on page **61**)

[277] M. T. Manzoni, M. Moreno-Cardoner, A. Asenjo-Garcia, J. V. Porto, A. V. Gorshkov, and D. E. Chang. *Optimization of photon storage fidelity in ordered atomic arrays*. New J. Phys. **20**, 083048 (2018). (Cited on pages **62** and **118**)

[278] D. Tiarks, S. Schmidt-Eberle, T. Stolz, G. Rempe, and S. Dürr. *A photon–photon quantum gate based on Rydberg interactions*. Nat. Phys. **15**, 124–126 (2019). (Cited on page **62**)

[279] E. Shahmoon, M. D. Lukin, and S. F. Yelin. *Quantum optomechanics of a two-dimensional atomic array*. Phys. Rev. A **101**, 063833 (2020). (Cited on page **62**)

[280] Y. Solomons, R. Ben-Maimon, and E. Shahmoon. *Universal Approach for Quantum Interfaces with Atomic Arrays*. PRX Quantum **5**, 020329 (2024). (Cited on page **62**)

[281] D. Petrosyan and K. Mølmer. *Deterministic free-space source of single photons using Rydberg atoms*. Phys. Rev. Lett. **121**, 123605 (2018). (Cited on pages **62** and **118**)

[282] A. Grankin, P. O. Guimond, D. V. Vasilyev, B. Vermersch, and P. Zoller. *Free-space photonic quantum link and chiral quantum optics*. Phys. Rev. A **98**, 043825 (2018). (Cited on pages **62** and **118**)

[283] A. M. Evagora, N. J. Murray, A. D. Holland, D. Burt, and J. Endicott. *Novel method for identifying the cause of inherent ageing in Electron Multiplying Charge Coupled Devices*. J. Inst. **7**, C01023–C01023 (2012). (Cited on page **67**)

[284] E. Stevens, J. Clayhold, H. Doan, R. Fabinski, J. Hynecek, S. Kosman, and C. Parks. *Recent Enhancements to Interline and Electron Multiplying CCD Image Sensors*. Sensors **17**, 2841 (2017). (Cited on page **67**)

[285] A. Dunford, K. Stefanov, and A. Holland. *Ageing and proton irradiation damage of a low voltage EMCCD in a CMOS process*. J. Instrum. **13**, C02059–C02059 (2018). (Cited on page **67**)

[286] M. Robbins and B. Hadwen. *The noise performance of electron multiplying charge-coupled devices*. IEEE Trans. Electron Devices **50**, 1227–1232 (2003). (Cited on pages **67** and **81**)

[287] J. D. Pritchard, D. Maxwell, A. Gauguet, K. J. Weatherill, M. P. A. Jones, and C. S. Adams. *Cooperative atom-light interaction in a blockaded Rydberg ensemble*. Phys. Rev. Lett. **105**, 193603 (2010). (Cited on pages **69** and **72**)

[288] B. J. DeSalvo, J. A. Aman, C. Gaul, T. Pohl, S. Yoshida, J. Burgdörfer, K. R. A. Hazzard, F. B. Dunning, and T. C. Killian. *Rydberg-blockade effects in Autler-Townes spectra of ultracold strontium*. Phys. Rev. A **93**, 022709 (2016). (Cited on page **70**)

[289] A. Tebben, C. Hainaut, A. Salzinger, S. Geier, T. Franz, T. Pohl, M. Gärttner, G. Zürn, and M. Weidemüller. *Nonlinear absorption in interacting Rydberg electromagnetically-induced-transparency spectra on two-photon resonance*. Phys. Rev. A **103**, 063710 (2021). (Cited on page **70**)

[290] D. Petrosyan, J. Otterbach, and M. Fleischhauer. *Electromagnetically induced transparency with Rydberg atoms*. Phys. Rev. Lett. **107**, 213601 (2011). (Cited on page **70**)

[291] M. Gärttner, S. Whitlock, D. W. Schönleber, and J. Evers. *Semianalytical model for nonlinear absorption in strongly interacting Rydberg gases*. Phys. Rev. A **89**, 063407 (2014). (Cited on page **70**)

[292] H. Schempp, G. Günter, S. Wüster, M. Weidemüller, and S. Whitlock. *Correlated exciton transport in Rydberg-dressed-atom spin chains*. Phys. Rev. Lett. **115**, 093002 (2015). (Cited on pages **71**, **83**, **85**, **87**, and **88**)

[293] Y. Solomons and E. Shahmoon. *Multichannel waveguide QED with atomic arrays in free space*. Phys. Rev. A **107**, 033709 (2023). (Cited on page **71**)

[294] G. Günter, H. Schempp, M. Robert-de Saint-Vincent, V. Gavryusev, S. Helmrich, C. S. Hofmann, S. Whitlock, and M. Weidemüller. *Observing the dynamics of dipole-mediated energy transport by interaction-enhanced imaging*. Science **342**, 954–956 (2013). (Cited on pages **72**, **83**, **85**, and **87**)

[295] D. B. Branden, T. Juhasz, T. Mahlokozera, C. Vesa, R. O. Wilson, M. Zheng, A. Kortyna, and D. A. Tate. *Radiative lifetime measurements of rubidium Rydberg states*. J. Phys. B: At. Mol. Opt. Phys. **43**, 015002 (2009). (Cited on page **79**)

[296] J. Johansson, P. Nation, and F. Nori. *QuTiP 2: A Python framework for the dynamics of open quantum systems*. Comput. Phys. Commun **184**, 1234–1240 (2013). (Cited on page **85**)

[297] D. W. Schönleber, A. Eisfeld, M. Genkin, S. Whitlock, and S. Wüster. *Quantum simulation of energy transport with embedded Rydberg aggregates*. Phys. Rev. Lett. **114**, 123005 (2015). (Cited on page **87**)

[298] J. Hubbard. *Electron correlations in narrow energy bands*. Proc. R. Soc. Lond. A **276**, 238–257 (1963). (Cited on page **91**)

[299] J. Hubbard. *Electron correlations in narrow energy bands. II. The degenerate band case*. Proc. R. Soc. Lond. A **277**, 237–259 (1964). (Cited on page **91**)

[300] E. H. Lieb and F. Wu. *The one-dimensional Hubbard model: a reminiscence*. Phys. A: Stat. Mech. Appl. **321**, 1–27 (2003). (Cited on page **91**)

[301] F. H. L. Essler, H. Frahm, F. Göhmann, A. Klümper, and V. E. Korepin. *The One-Dimensional Hubbard Model*. Cambridge University Press (2005). ISBN 978-0-521-80262-8 978-0-521-14394-3 978-0-511-53484-3. (Cited on page **91**)

[302] E. Berg, E. G. Dalla Torre, T. Giamarchi, and E. Altman. *Rise and Fall of Hidden String Order of Lattice Bosons*. Phys. Rev. B **77**, 245119 (2008). (Cited on pages **91** and **118**)

[303] G. G. Batrouni, R. T. Scalettar, G. T. Zimanyi, and A. P. Kampf. *Supersolids in the Bose-Hubbard Hamiltonian*. Phys. Rev. Lett. **74**, 2527–2530 (1995). (Cited on page **91**)

[304] M. Boninsegni and N. V. Prokof'ev. *Colloquium: Supersolids: What and Where Are They?* Rev. Mod. Phys. **84**, 759–776 (2012). (Cited on page **91**)

[305] F. Cinti, T. Macrì, W. Lechner, G. Pupillo, and T. Pohl. *Defect-Induced Supersolidity with Soft-Core Bosons*. Nat. Commun. **5**, 3235 (2014). (Cited on page **91**)

[306] A. Geißler, I. Vasić, and W. Hofstetter. *Condensation versus Long-Range Interaction: Competing Quantum Phases in Bosonic Optical Lattice Systems at near-Resonant Rydberg Dressing*. Phys. Rev. A **95**, 063608 (2017). (Cited on page **91**)

[307] H.-K. Wu and W.-L. Tu. *Competing quantum phases of hard-core bosons with tilted dipole-dipole interaction*. Phys. Rev. A **102**, 053306 (2020). (Cited on page **91**)

[308] B. Capogrosso-Sansone, C. Trefzger, M. Lewenstein, P. Zoller, and G. Pupillo. *Quantum Phases of Cold Polar Molecules in 2D Optical Lattices*. Phys. Rev. Lett. **104**, 125301 (2010). (Cited on page **91**)

[309] N. Y. Yao, M. P. Zaletel, D. M. Stamper-Kurn, and A. Vishwanath. *A quantum dipolar spin liquid*. Nat. Phys. **14**, 405–410 (2018). (Cited on page **91**)

[310] C. Kollath, J. S. Meyer, and T. Giamarchi. *Dipolar Bosons in a Planar Array of One-Dimensional Tubes*. Phys. Rev. Lett. **100**, 130403 (2008). (Cited on pages **91** and **118**)

[311] M. Mattioli, M. Dalmonte, W. Lechner, and G. Pupillo. *Cluster Luttinger Liquids of Rydberg-Dressed Atoms in Optical Lattices*. Phys. Rev. Lett. **111**, 165302 (2013). (Cited on pages **91** and **93**)

[312] M. Dalmonte, W. Lechner, Z. Cai, M. Mattioli, A. M. Läuchli, and G. Pupillo. *Cluster Luttinger Liquids and Emergent Supersymmetric Conformal Critical Points in the One-Dimensional Soft-Shoulder Hubbard Model*. Phys. Rev. B **92**, 045106 (2015). (Cited on page **91**)

[313] M. Valiente and D. Petrosyan. *Scattering Resonances and Two-Particle Bound States of the Extended Hubbard Model*. J. Phys. B: At. Mol. Opt. Phys. **42**, 121001 (2009). (Cited on pages **91**, **103**, **104**, **105**, **106**, and **107**)

[314] P. Weckesser, K. Srakaew, T. Blatz, D. Wei, D. Adler, S. Agrawal, A. Bohrdt, I. Bloch, and J. Zeiher. *Realization of a Rydberg-dressed extended Bose Hubbard model*. arXiv:2405.20128 (2024). (Cited on pages **91** and **94**)

[315] T. Chanda, L. Barbiero, M. Lewenstein, M. J. Mark, and J. Zakrzewski. *Recent progress on quantum simulations of non-standard Bose-Hubbard models*. arXiv:2405.07775 (2024). (Cited on page **92**)

[316] S. Welte, B. Hacker, S. Daiss, S. Ritter, and G. Rempe. *Photon-Mediated Quantum Gate between Two Neutral Atoms in an Optical Cavity*. Phys. Rev. X **8**, 011018 (2018). (Cited on page **92**)

[317] A. Periwal, E. S. Cooper, P. Kunkel, J. F. Wienand, E. J. Davis, and M. Schleier-Smith. *Programmable interactions and emergent geometry in an array of atom clouds*. Nature **600**, 630–635 (2021). (Cited on page **92**)

[318] F. Mivehvar, F. Piazza, T. Donner, and H. Ritsch. *Cavity QED with quantum gases: new paradigms in many-body physics*. Adv. Phys. **70**, 1–153 (2021). (Cited on page **92**)

[319] V. Helson, T. Zwettler, F. Mivehvar, E. Colella, K. Roux, H. Konishi, H. Ritsch, and J.-P. Brantut. *Density-wave ordering in a unitary Fermi gas with photon-mediated interactions*. Nature **618**, 716–720 (2023). (Cited on page **92**)

[320] R. Landig, L. Hruby, N. Dogra, M. Landini, R. Mottl, T. Donner, and T. Esslinger. *Quantum Phases from Competing Short- and Long-Range Interactions in an Optical Lattice*. Nature **532**, 476–479 (2016). (Cited on page **92**)

[321] J. Léonard, A. Morales, P. Zupancic, T. Esslinger, and T. Donner. *Supersolid formation in a quantum gas breaking a continuous translational symmetry*. Nature **543**, 87–90 (2017). (Cited on page **92**)

[322] L. Hruby, N. Dogra, M. Landini, T. Donner, and T. Esslinger. *Metastability and avalanche dynamics in strongly correlated gases with long-range interactions*. Proc. Natl. Acad. Sci. U. S. A. **115**, 3279–3284 (2018). (Cited on page **92**)

[323] T. Byrnes, N. Y. Kim, K. Kusudo, and Y. Yamamoto. *Quantum simulation of Fermi-Hubbard models in semiconductor quantum-dot arrays*. Phys. Rev. B **78**, 075320 (2008). (Cited on page **92**)

[324] A. Singha, M. Gibertini, B. Karmakar, S. Yuan, M. Polini, G. Vignale, M. I. Katsnelson, A. Pinczuk, L. N. Pfeiffer, K. W. West, and V. Pellegrini. *Two-Dimensional Mott-Hubbard Electrons in an Artificial Honeycomb Lattice*. Science **332**, 1176–1179 (2011). (Cited on page **92**)

[325] P. Barthelemy and L. M. K. Vandersypen. *Quantum Dot Systems: a versatile platform for quantum simulations*. Ann. Phys. **525**, 808–826 (2013). (Cited on page **92**)

[326] J. Salfi, J. A. Mol, R. Rahman, G. Klimeck, M. Y. Simmons, L. C. L. Hollenberg, and S. Rogge. *Quantum simulation of the Hubbard model with dopant atoms in silicon*. Nat. Commun. **7**, 11342 (2016). (Cited on page **92**)

[327] T. Hensgens, T. Fujita, L. Janssen, X. Li, C. J. Van Diepen, C. Reichl, W. Wegscheider, S. Das Sarma, and L. M. K. Vandersypen. *Quantum simulation of a Fermi–Hubbard model using a semiconductor quantum dot array*. Nature **548**, 70–73 (2017). (Cited on page **92**)

[328] M. Combescot, R. Combescot, and F. Dubin. *Bose–Einstein condensation and indirect excitons: a review*. Rep. Prog. Phys. **80**, 066501 (2017). (Cited on page **92**)

[329] C. Lagoin, U. Bhattacharya, T. Grass, R. W. Chhajlany, T. Salamon, K. Baldwin, L. Pfeiffer, M. Lewenstein, M. Holzmann, and F. Dubin. *Extended Bose–Hubbard model with dipolar excitons*. Nature **609**, 485–489 (2022). (Cited on page **92**)

[330] R. Bause, A. Christianen, A. Schindewolf, I. Bloch, and X.-Y. Luo. *Ultracold Sticky Collisions: Theoretical and Experimental Status*. J. Phys. Chem. A **127**, 729–741 (2023). (Cited on page **93**)

[331] G. Valtolina, K. Matsuda, W. G. Tobias, J.-R. Li, L. De Marco, and J. Ye. *Dipolar evaporation of reactive molecules to below the Fermi temperature*. Nature **588**, 239–243 (2020). (Cited on page **93**)

[332] K. Matsuda, L. De Marco, J.-R. Li, W. G. Tobias, G. Valtolina, G. Quéméner, and J. Ye. *Resonant collisional shielding of reactive molecules using electric fields*. Science **370**, 1324–1327 (2020). (Cited on page **93**)

[333] A. Schindewolf, R. Bause, X.-Y. Chen, M. Duda, T. Karman, I. Bloch, and X.-Y. Luo. *Evaporation of Microwave-Shielded Polar Molecules to Quantum Degeneracy*. Nature **607**, 677–681 (2022). (Cited on page **93**)

[334] J. Lin, G. Chen, M. Jin, Z. Shi, F. Deng, W. Zhang, G. Quéméner, T. Shi, S. Yi, and D. Wang. *Microwave Shielding of Bosonic NaRb Molecules*. Phys. Rev. X **13**, 031032 (2023). (Cited on page **93**)

[335] N. Bigagli, W. Yuan, S. Zhang, B. Bulatovic, T. Karman, I. Stevenson, and S. Will. *Observation of Bose–Einstein condensation of dipolar molecules*. Nature **631**, 289–293 (2024). (Cited on page **93**)

[336] L. Anderegg, L. W. Cheuk, Y. Bao, S. Burchesky, W. Ketterle, K.-K. Ni, and J. M. Doyle. *An optical tweezer array of ultracold molecules*. Science **365**, 1156–1158 (2019). (Cited on page **93**)

[337] C. M. Holland, Y. Lu, and L. W. Cheuk. *Bichromatic Imaging of Single Molecules in an Optical Tweezer Array*. Phys. Rev. Lett. **131**, 053202 (2023). (Cited on page **93**)

[338] N. B. Vilas, P. Robichaud, C. Hallas, G. K. Li, L. Anderegg, and J. M. Doyle. *An optical tweezer array of ultracold polyatomic molecules*. Nature **628**, 282–286 (2024). (Cited on page **93**)

[339] L. R. Liu, J. D. Hood, Y. Yu, J. T. Zhang, N. R. Hutzler, T. Rosenband, and K.-K. Ni. *Building one molecule from a reservoir of two atoms*. Science **360**, 900–903 (2018). (Cited on page **93**)

[340] W. B. Cairncross, J. T. Zhang, L. R. Picard, Y. Yu, K. Wang, and K.-K. Ni. *Assembly of a Rovibrational Ground State Molecule in an Optical Tweezer*. Phys. Rev. Lett. **126**, 123402 (2021). (Cited on page **93**)

[341] X. He, K. Wang, J. Zhuang, P. Xu, X. Gao, R. Guo, C. Sheng, M. Liu, J. Wang, J. Li, G. V. Shlyapnikov, and M. Zhan. *Coherently forming a single molecule in an optical trap*. Science **370**, 331–335 (2020). (Cited on page **93**)

[342] D. K. Ruttley, A. Guttridge, T. R. Hepworth, and S. L. Cornish. *Enhanced Quantum Control of Individual Ultracold Molecules Using Optical Tweezer Arrays*. PRX Quantum **5**, 020333 (2024). (Cited on page **93**)

[343] I. Bouchoule and K. Mølmer. *Spin Squeezing of Atoms by the Dipole Interaction in Virtually Excited Rydberg States*. Phys. Rev. A **65**, 041803 (2002). (Cited on page **93**)

[344] G. Pupillo, A. Micheli, M. Boninsegni, I. Lesanovsky, and P. Zoller. *Strongly Correlated Gases of Rydberg-Dressed Atoms: Quantum and Classical Dynamics*. Phys. Rev. Lett. **104**, 223002 (2010). (Cited on page **93**)

[345] T. Macrì and T. Pohl. *Rydberg Dressing of Atoms in Optical Lattices*. Phys. Rev. A **89**, 011402 (2014). (Cited on page **93**)

[346] R. M. W. Van Bijnen and T. Pohl. *Quantum Magnetism and Topological Ordering via Rydberg Dressing near Förster Resonances*. Phys. Rev. Lett. **114**, 243002 (2015). (Cited on page **93**)

[347] Y. Zhou, Y. Li, R. Nath, and W. Li. *Quench Dynamics of Rydberg-dressed Bosons on Two-Dimensional Square Lattices*. Phys. Rev. A **101**, 013427 (2020). (Cited on page **93**)

[348] D. Malz and J. I. Cirac. *Few-Body Analog Quantum Simulation with Rydberg-Dressed Atoms in Optical Lattices*. PRX Quantum **4** (2023). (Cited on pages **93** and **118**)

[349] A. Rapp, X. Deng, and L. Santos. *Ultracold lattice gases with periodically modulated interactions*. Phys. Rev. Lett. **109**, 203005 (2012). (Cited on page **93**)

[350] Y.-Y. Jau, A. M. Hankin, T. Keating, I. H. Deutsch, and G. W. Biedermann. *Entangling Atomic Spins with a Rydberg-dressed Spin-Flip Blockade*. Nat. Phys. **12**, 71–74 (2016). (Cited on page **93**)

[351] N. Schine, A. W. Young, W. J. Eckner, M. J. Martin, and A. M. Kaufman. *Long-Lived Bell States in an Array of Optical Clock Qubits*. Nat. Phys. **18**, 1067–1073 (2022). (Cited on page **93**)

[352] W. J. Eckner, N. Darkwah Oppong, A. Cao, A. W. Young, W. R. Milner, J. M. Robinson, J. Ye, and A. M. Kaufman. *Realizing Spin Squeezing with Rydberg Interactions in an Optical Clock*. Nature **621**, 734–739 (2023). (Cited on page **93**)

[353] E. A. Goldschmidt, T. Boulier, R. C. Brown, S. B. Koller, J. T. Young, A. V. Gorshkov, S. L. Rolston, and J. V. Porto. *Anomalous Broadening in Driven Dissipative Rydberg Systems*. Phys. Rev. Lett. **116**, 113001 (2016). (Cited on pages **94** and **100**)

[354] L. Festa, N. Lorenz, L.-M. Steinert, Z. Chen, P. Osterholz, R. Eberhard, and C. Gross. *Blackbody-Radiation-Induced Facilitated Excitation of Rydberg Atoms in Optical Tweezers*. Phys. Rev. A **105**, 013109 (2022). (Cited on pages **94** and **100**)

[355] S. Hild, T. Fukuhara, P. Schauß, J. Zeiher, M. Knap, E. Demler, I. Bloch, and C. Gross. *Far-from-Equilibrium Spin Transport in Heisenberg Quantum Magnets*. Phys. Rev. Lett. **113**, 147205 (2014). (Cited on page **96**)

[356] C. M. Holland, Y. Lu, and L. W. Cheuk. *On-Demand Entanglement of Molecules in a Reconfigurable Optical Tweezer Array*. Science **382**, 1143–1147 (2023). (Cited on page **98**)

[357] G. Pichard, D. Lim, E. Bloch, J. Vaneecloo, L. Bourachot, G.-J. Both, G. Mériaux, S. Dutartre, R. Hostein, J. Paris, B. Ximenez, A. Signoles, A. Browaeys, T. Lahaye, and D. Dreon. *Rearrangement of individual atoms in a 2000-site optical-tweezer array at cryogenic temperatures*. Phys. Rev. Applied **22**, 024073 (2024). (Cited on page **100**)

[358] J. A. Hines, S. V. Rajagopal, G. L. Moreau, M. D. Wahrman, N. A. Lewis, O. Marković, and M. Schleier-Smith. *Spin Squeezing by Rydberg Dressing in an Array of Atomic Ensembles*. Phys. Rev. Lett. **131**, 063401 (2023). (Cited on page **100**)

[359] M. Valiente and D. Petrosyan. *Two-particle states in the Hubbard model*. J. Phys. B: At. Mol. Opt. Phys. **41**, 161002 (2008). (Cited on page **104**)

[360] K. Winkler. *Ultracold Molecules and Atom Pairs in Optical Lattice Potentials*. Ph.D. thesis, University of Innsbruck (2007). (Cited on page **104**)

[361] M. Valiente. *Few quantum particles on one dimensional lattices*. Ph.D. thesis, Humboldt-Universität zu Berlin, Mathematisch-Naturwissenschaftliche Fakultät I (2010). (Cited on page **104**)

[362] K. Winkler, G. Thalhammer, F. Lang, R. Grimm, J. Hecker Denschlag, A. J. Daley, A. Kantian, H. P. Büchler, and P. Zoller. *Repulsively Bound Atom Pairs in an Optical Lattice*. Nature **441**, 853–856 (2006). (Cited on page **104**)

[363] P. M. Preiss, R. Ma, M. E. Tai, A. Lukin, M. Rispoli, P. Zupancic, Y. Lahini, R. Islam, and M. Greiner. *Strongly Correlated Quantum Walks in Optical Lattices*. Science **347**, 1229–1233 (2015). (Cited on pages **104**, **106**, and **107**)

[364] M. Karski, L. Förster, J.-M. Choi, A. Steffen, W. Alt, D. Meschede, and A. Widera. *Quantum Walk in Position Space with Single Optically Trapped Atoms*. Science **325**, 174–177 (2009). (Cited on pages **104** and **106**)

[365] L. Sansoni, F. Sciarrino, G. Vallone, P. Mataloni, A. Crespi, R. Ramponi, and R. Osellame. *Two-Particle Bosonic-Fermionic Quantum Walk via Integrated Photonics*. Phys. Rev. Lett. **108**, 010502 (2012). (Cited on pages **104**, **106**, and **107**)

[366] M. Ganahl, E. Rabel, F. H. L. Essler, and H. G. Evertz. *Observation of Complex Bound States in the Spin-1/2 Heisenberg XXZ Chain Using Local Quantum Quenches*. Phys. Rev. Lett. **108**, 077206 (2012). (Cited on pages **106** and **108**)

[367] I. L. Aleiner. *Bethe Ansatz Solutions for Certain Periodic Quantum Circuits*. Ann. Phys. **433**, 168593 (2021). (Cited on pages **106** and **108**)

[368] T. Jeltes, J. M. McNamara, W. Hogervorst, W. Vassen, V. Krachmalnicoff, M. Schellekens, A. Perrin, H. Chang, D. Boiron, A. Aspect, and C. I. Westbrook. *Comparison of the Hanbury Brown–Twiss effect for bosons and fermions*. Nature **445**, 402–405 (2007). (Cited on page **107**)

[369] X. Qin, Y. Ke, X. Guan, Z. Li, N. Andrei, and C. Lee. *Quantum Walks of Two Interacting Particles in One Dimension*. arXiv:1402.3349 (2014). (Cited on page **107**)

[370] A. Morvan, T. I. Andersen, X. Mi, C. Neill, A. Petukhov, K. Kechedzhi, D. A. Abanin, A. Michailidis, R. Acharya, F. Arute, K. Arya, A. Asfaw, J. Atalaya, J. C. Bardin, J. Basso, A. Bengtsson, G. Bortoli, A. Bourassa, J. Bovaird, L. Brill, M. Broughton, B. B. Buckley, D. A. Buell, T. Burger, B. Burkett, N. Bushnell, Z. Chen, B. Chiaro, R. Collins, P. Conner, W. Courtney, A. L. Crook, B. Curtin, D. M. Debroy, A. Del Toro Barba, S. Demura, A. Dunsworth, D. Eppens, C. Erickson, L. Faoro, E. Farhi, R. Fatemi, L. Flores Burgos, E. Forati, A. G. Fowler, B. Foxen, W. Giang, C. Gidney, D. Gilboa, M. Giustina, A. Grajales Dau, J. A. Gross, S. Habegger, M. C. Hamilton, M. P. Harrigan, S. D. Harrington, M. Hoffmann, S. Hong, T. Huang, A. Huff, W. J. Huggins, S. V. Isakov, J. Iveland, E. Jeffrey, Z. Jiang, C. Jones, P. Juhas, D. Kafri, T. Khattar, M. Khezri, M. Kieferová, S. Kim, A. Y. Kitaev, P. V. Klimov, A. R. Klots, A. N. Korotkov, F. Kostritsa, J. M. Kreikebaum, D. Landhuis, P. Laptev, K.-M. Lau, L. Laws, J. Lee, K. W. Lee, B. J. Lester, A. T. Lill, W. Liu, A. Locharla, F. Malone, O. Martin, J. R. McClean, M. McEwen, B. Meurer Costa, K. C. Miao, M. Mohseni, S. Montazeri, E. Mount, W. Mruczkiewicz, O. Naaman, M. Neeley, A. Nersisyan, M. Newman, A. Nguyen, M. Nguyen, M. Y. Niu, T. E. O'Brien, R. Olenewa, A. Opremcak, R. Potter, C. Quintana, N. C. Rubin, N. Saei, D. Sank, K. Sankaragomathi, K. J. Satzinger, H. F. Schurkus, C. Schuster, M. J. Shearn, A. Shorter, V. Shvarts, J. Skruzny, W. C. Smith, D. Strain, G. Sterling, Y. Su, M. Szalay, A. Torres, G. Vidal, B. Villalonga, C. Vollgraff-Heidweiller, T. White, C. Xing, Z. Yao, P. Yeh, J. Yoo, A. Zalcman, Y. Zhang, N. Zhu, H. Neven, D. Bacon, J. Hilton, E. Lucero, R. Babbush, S. Boixo, A. Megrant, J. Kelly, Y. Chen, V. Smelyanskiy, I. Aleiner, L. B. Ioffe, and P. Roushan. *Formation of Robust Bound States of Interacting Microwave Photons*. Nature **612**, 240–245 (2022). (Cited on page **108**)

[371] V. D. Naik, F. B. Trigueros, and M. Heyl. *Quantum Hard Disks on a Lattice*. arXiv:2311.16240 (2024). (Cited on pages **109** and **118**)

[372] A. W. Young, W. J. Eckner, N. Schine, A. M. Childs, and A. M. Kaufman. *Tweezer-Programmable 2D Quantum Walks in a Hubbard-regime Lattice*. Science **377**, 885–889 (2022). (Cited on page **113**)

[373] U. Schollwöck. *The density-matrix renormalization group in the age of matrix product states*. Ann. Phys. **326** (2011). (Cited on page **113**)

[374] C.-R. Mann, F. Andreoli, V. Protsenko, Z. Lenarčič, and D. Chang. *Selective Radiance in Super-Wavelength Atomic Arrays*. arXiv:2402.06439 (2024). (Cited on page **118**)

[375] Y. Li, A. Geißler, W. Hofstetter, and W. Li. *Supersolidity of Lattice Bosons Immersed in Strongly Correlated Rydberg Dressed Atoms*. Phys. Rev. A **97**, 023619 (2018). (Cited on page **118**)

[376] E. G. Dalla Torre, E. Berg, and E. Altman. *Hidden Order in 1D Bose Insulators*. Phys. Rev. Lett. **97**, 260401 (2006). (Cited on page **118**)

[377] Z. Chen, Y. Wang, S. N. Rebec, T. Jia, M. Hashimoto, D. Lu, B. Moritz, R. G. Moore, T. P. Devereaux, and Z.-X. Shen. *Anomalously strong near-neighbor attraction in doped 1D cuprate chains*. Science **373**, 1235–1239 (2021). (Cited on page **118**)

[378] H. Weimer and H. P. Büchler. *Two-Stage Melting in Systems of Strongly Interacting Rydberg Atoms*. Phys. Rev. Lett. **105**, 230403 (2010). (Cited on page **119**)

[379] E. Sela, M. Punk, and M. Garst. *Dislocation-mediated melting of one-dimensional Rydberg crystals*. Phys. Rev. B **84**, 085434 (2011). (Cited on page **119**)

[380] D. Petrosyan, S. Norrell, C. Poole, and M. Saffman. *Fast measurements and multiqubit gates in dual species atomic arrays*. arXiv:2406.07356 (2024). (Cited on page **119**)

List of figures

List of tables

List of abbreviations

1D	one-dimensional. v, 2, 80, 91, 94–96, 101–103, 105, 109, 111, 112, 118
2D	two-dimensional. 25, 27, 30, 41, 59, 60, 75, 92, 94, 96, 111
3D	three-dimensional. 15, 27, 34, 118
AOM	acousto-optical modulator. 31–33, 38, 39, 52, 53
BEC	Bose-Einstein condensate. 1, 26, 27, 93
BHM	Bose-Hubbard model. 25, 26, 34, 102, 109, 116
CBG	chirped Bragg grating. 50–55
CDW	charge density wave. 2, 3, 92, 109, 110, 116, 117
DMD	digital micromirror device. 28, 29, 34, 35, 55, 65, 109, 111
DMRG	density-matrix renormalization group. 113, 115, 116
eBHM	extended Bose-Hubbard model. v, 2, 91–94, 103, 105, 109, 111, 116, 118
EIT	electromagnetically induced transparency. v, 1, 2, 45, 59, 61–63, 68–75, 79, 81, 83, 85, 86, 117
EMCCD	electron multiplying charge-coupled device. 29, 63, 65–68, 74, 81, 118
EOM	electro-optic modulator. 38, 48, 50–55
FPGA	field programmable gate array. 38, 39
FWHM	full width at half maximum. 40, 44
GDD	group delay dispersion. 50, 52
GHZ	Greengerber-Horne-Zeilinger. 118
MI	Mott insulator. 26–28, 34, 35, 40, 43, 44, 64, 65, 77, 92, 94, 96, 111
MOT	magneto-optical trap. 27
MPS	matrix-product-state. 113, 114
MW	microwave. 10, 27–29, 41, 45, 48, 55, 56, 64, 65, 93, 96–99, 106, 108, 119

NA	numerical aperture. 29, 66, 76
NPBS	non-polarizing beam splitter. 33, 34
PDH	Pound-Drever-Hall. 38, 39
PID	proportional-integral-derivative. 38, 39
RF	radio frequency. 38, 52–54
ROI	region of interest. 66, 77, 81
SF	superfluid. 26, 28, 92
SHG	second harmonic generation. 38, 39
SNR	signal-to-noise ratio. 118
SS	supersolid. 92, 118
ULE	ultra-low expansion. 38, 39
UV	ultraviolet. 10, 36, 38–41, 63–65, 73, 77, 83, 94, 95, 98–100, 102

Acknowledgements

Ph.D., one-sixteenth of lifespan, is a significant chapter in my life. I traveled a long way from my homeland and reside in Garching, meeting many wonderful people and gaining many remarkable experiences. My Ph.D. accomplishment would not have been possible without the dedication, knowledge, and support of the people around me. I would like to express my appreciation to all supports and companies.

First, I would like to thank my supervisor, Immanuel Bloch, for letting me enjoy the journey and exploration of frontier science. His guidance offered insights for the next steps when obstacles were encountered. I and the team were able to share and try new ideas with the laboratory support and opportunities to attend conferences.

I would like to thank Johannes Zeiher as a direct supervisor. His physical and technical knowledge can answer and solve my questions and lab problems instantly. I always get stimulated ideas from discussions with him. His optimistic attitude always turns my problems into interesting destinations.

I would also like to thank Christian Groß, who was the first person I contacted and foresaw my potential and encouraged me to study Ph.D. at MPQ. His leading of the team at the start of my Ph.D. inspired me and helped me build confidence in my abilities.

I would like to give credit to the "Single atom" team from generation to generation who contribute all the building blocks. I would not have had success without their dedication to the setup. I would like to thank Simon Hollerith who taught me how to operate the setup and brought me into Rydberg physics business. His expertise and valuable discussion shape my understanding on Rydberg physics, which further drives my work on Rydberg projects. The one who can handle spicier food more than me. I would also like to thank Antonio Rubio Abadal, who spent time explaining the details of the setup and physics to me from basic concepts. I appreciate his support during my illness, drove me to the hospital for emergency surgery during the pandemic. I would like to thanks Jun Rui who was a postdoc during my early Ph.D., taught me optical designs and planned ahead the lattices upgrade design.

I have a great lab partner, David Wei, who overlapped with me the most during my Ph.D.. His talent in programming motivates me to continue learning and practice coding skill. Furthermore, his deep knowledge in physics sparks many interesting discussions. I enjoyed working with him, especially throughout the lattices upgrade, which two new Ph.D. students dismantled the setup during the pandemic. I would like to thank our postdoc of the week, Pascal Weckesser, for his ambition and for encouraging me to change the world again and again. His experience and knowledge motivate me to keep working with energy. I have a great time with him on the Rydberg project. I still try to convince him of how delicious the real authentic Thai food is. I was blessed to work with Daniel Adler, who joined Ph.D. after me, for his meticulous detail in technical and physics discussions that make me think and avoid wrong decision. I appreciate his valuable time to keep the lab clean and organized. I am also very grateful to Suchita Agrawal, who is in an early stage of her Ph.D. and enthusiastic about learning new things. I, for the first time, learn different between Naan, Roti, and Paratha breads from her. Very recently David Gröters also joined our team as a Ph.D. I wish all of them, Daniel, Suchita, and David a lot of success in their Ph.D. at MPQ. The lab has been technically supported by many master students and interns, Simon Evered, Martin Link, Pierre Cussenot, Sarah Rößle and Anwei Zhu. I wish them a great success on their carrier paths.

I would like to thank my team, especially Daniel, for support in German translation and helping me go through the bureaucracy procedure. I thank Daniel, Simon, and Anwei for their time in joining me in Landkreis to extend my Visa.

I continue by thanking Kristina Schuldt, who helped me everything even not a part of her work, and also the administrative team, Doreen Seidl, Veronika Seidl, and Ildiko Kecskes for the great administrative support, organizing group events, seminars, and talks that bring people together, forming a great collaborations and friendships. I also thank Anton Mayer, who helped in getting the mechanical design to live during the lattice upgrade, and also the knowledgeable team Milan Antic and Felix Friedrich for mechanical support. I would like to also thank Karsten Förster, Olivia Mödl, and Thomas Klink, who solved/fixed my electronic problem to meet demand in the lab.

I would like to express my gratitude to all the members at MPQ, LMU and my collaborators for their invaluable contributions, support, and exchange of ideas, which have greatly propelled our research forward.

Finally, I would like to express my thanks to my friends for the time we spent in the EU, my family for the constant support since I was born, and for letting me seek out my own journey and pursue my Ph.D.

Thank you very much.